Title

Search for high-mass dimuon resonances and study of endcap muon system neutron-induced background hits with the Compact Muon Solenoid detector

Author

Schnaible, Christian

Publication Date

2019

Peer reviewed|Thesis/dissertation

UNIVERSITY OF CALIFORNIA

Los Angeles

Search for high-mass dimuon resonances and study of endcap muon system neutron-induced background hits with the Compact Muon Solenoid detector

A dissertation submitted in partial satisfaction
of the requirements for the degree
Doctor of Philosophy in Physics

by

Christian John Schnaible

2019

ABSTRACT OF THE DISSERTATION

Search for high-mass dimuon resonances and study of endcap muon system neutron-induced background hits with the Compact Muon Solenoid detector

by

Christian John Schnaible
Doctor of Philosophy in Physics
University of California, Los Angeles, 2019
Professor Robert D. Cousins, Chair

This thesis presents a search for narrow resonances in the dimuon invariant mass spectrum using data obtained from proton-proton collisions at $\sqrt{s} = 13\,\text{TeV}$ collected by the CMS detector at the CERN LHC. We describe the analysis and results of the data collected in 2018, which corresponds to an integrated luminosity of $63.1\,\text{fb}^{-1}$. We also present results of the combination of the 2016, 2017, and 2018 data sets, as well as the results of the combination with the dielectron analysis, which correspond to a total integrated luminosity of up to $140\,\text{fb}^{-1}$. The results are interpreted in terms of the upper limit on the ratio of the cross section of a new resonance to that of the Z boson. We also compute the corresponding lower limits on the masses of various benchmark resonances. No evidence for beyond the standard model physics is observed in the 2018 data set, or in any of the combined data sets. Relevant for the high masses where we perform our search, we also discuss the reconstruction and performance of high momentum muons in CMS. In the appendix, we present a study of neutron-induced background hits in CMS endcap muon chambers.

The dissertation of Christian John Schnaible is approved.

Per Kraus

Huan Huang

Michail Bachtis

Robert D. Cousins, Committee Chair

University of California, Los Angeles

2019

To my wife, Grace, for your patience, support, and love

TABLE OF CONTENTS

LIST OF FIGURES

LIST OF TABLES

ACKNOWLEDGMENTS

First, thank you to my advisor, Bob Cousins. His wisdom, guidance, and support has helped me grow as a scientist and has challenged me in unexpected and exciting ways. I am truly all the better for it.

Thank you to Alice Florent for continually encouraging me and for always expecting the best from me in our work together. *Alice, tu es la meilleure et la plus intelligente postdoc que j'aie jamais rencontrée.*

Thank you to Riju Dasgupta. I have particularly valued our friendship and our shared experience. The work we have done together has also been both enlightening and rewarding.

Thank you to my friends and collaborators in the CMS High-p_{T} Muon Physics Object Group. Thank you to my friends and collaborators from the CMS $Z' \to \mu^+\mu^-$ analysis group: the groups at the University of Florida, UCLA, British University in Egypt, Joint Institute for Nuclear Research in Russia, Purdue University, and Seoul National University. Thanks especially to those who have helped me and whose work I have relied upon: Benjamin Radburn-Smith, Minesok Oh, Jan-Frederik Schulte, and Alice Florent.

Thank you to everyone from the UCLA CMS group for all of your ideas, comments, and friendship. Thank you also to my friends and collaborators in CMS.

Thank you to my family. To my brothers, Jack and Mitch, for instilling in me a sense of friendly competition that has allowed me to push myself to achieve all that I can. A special thank you to my parents, Mark and Jenny, for encouraging and enabling me to succeed in my education and in my life.

Finally, special thanks to my wife, Grace. Although your contributions to this thesis are innumerable, thanks especially for creating the standard model diagram in Fig. 2.1. You inspire me every single day and none of this was achievable without you.

The work described in Appendix A was performed in full collaboration with fellow UCLA graduate student Abhigyan Dasgupta under the supervision of our common advisor, Prof. Robert Cousins. Together the two students wrote a detailed draft internal CMS Detec-

tor Note DN-2017/019, reproduced below. Prof. Cousins also provided editing assistance, particularly in Section A.5. Abhigyan Dasgupta presented this work in a poster session at 2017 European Physical Society Conference on High-Energy Physics (EPS-HEP), and wrote a conference note for the Proceedings. Christian Schnaible presented this work in a talk at the the 2017 American Physical Society Meeting of the Division of Particles & Fields (APS-DPF).

For the work described in Appendix A, we would like to thank everyone on the CSC GIF++ team, the CMS UCLA group, and everyone whose work we have built on or partially reproduced and who have contributed valuable knowledge and advice, including Cameron Bravo, Tim Cox, Alice Florent, Jay Hauser, Misha Ignatenko, Vladimir Ivantchenko, Evaldas Juska, Alexey Kamenev, Andrey Korytov, Katerina Kuznetsova, Armando Lanaro, Paul Lujan, Alex Madorsky, Nick McColl, Hualin Mei, Yuriy Pakhotin, Vladimir Palchik, Victor Perelygin, Jian Wang, Wells Wuslin, and Piet Verwilligen.

This thesis includes material that is based upon work supported by the U.S. Department of Energy under Award Number DE-SC0009937.

VITA

2011–2013	Undergraduate Research Assistant, Department of Physics, The Ohio State University
2013	B.S. (Physics) The Ohio State University.
2013–2015	Teaching Assistant, Department of Physics, University of California, Los Angeles
2014	M.S. (Physics), University of California, Los Angeles
2015–present	Graduate Research Assistant, Department of Physics, University of California, Los Angeles

CHAPTER 1

Introduction

Particle physics is the field of study that examines the properties and interactions among the smallest known fundamental units of the universe. These fundamental units, known as particles, have led to a rich history of theoretical and experimental breakthroughs. Experimentally, the field of particle physics began in 1897 with J. J. Thomson's discovery of the first fundamental particle, the electron [1]. Theoretically, the properties of and interactions between the particles are described by a successful theory known as the standard model (SM). The SM was invented piece by piece over many decades; beginning with the theory of quantum electrodynamics in the 1930s and ending with experimental confirmation of the quark theory in the mid-1970s. The final undiscovered particle predicted by the SM, the Higgs boson, was discovered in 2012 at the Large Hadron Collider (LHC) by the Compact Muon Solenoid (CMS) [2] and ATLAS experiments [3].

However successful, the SM is an incomplete theory. It does not provide a description of the gravitational interaction, it does not predict the matter-antimatter asymmetry in the universe, and it does not explain the presence of dark matter. Theories that are beyond the SM (BSM) attempt to explain some of the shortcomings. One such possible signature of BSM physics would be the observation of a new narrow resonance in the invariant mass spectrum of muon pairs, as many BSM theories predict such resonances.

The final state of two back-to-back high transverse momentum muon pairs is experimentally advantageous as it provides us with a clean detector signature that has a large signal acceptance, high reconstruction efficiency, and low relative background at high mass. This specific experimental technique—searching for a resonance in the dilepton invariant mass

spectrum—also has ample historical precedent in experimental particle physics. The first example of a new dilepton resonance was in 1974 with the simultaneous discovery at SLAC and Brookhaven of the J/ψ meson in the e^+e^- final state [4, 5]. This discovery led to the famous "November revolution" of particle physics as the discovery of the J/ψ meson implied the existence of a fourth quark, the charm quark, which provided convincing evidence of the quark theory. The 1976 Nobel Prize in Physics was awarded in recognition of this discovery. The next example of a dilepton discovery was at Fermilab in 1977, with the observation of the Υ meson decaying to muon pairs [6]. Again, the discovery of the Υ implied the existence of an additional fifth quark, the bottom quark. The most recent example of a dilepton discovery was at the CERN SPS collider in 1983 with the observation of the Z boson in both the $\mu^+\mu^-$ and e^+e^- final states [7, 8]. The 1984 Nobel Prize in Physics was awarded, in part, for the discovery of the Z boson. In this thesis, we continue this tradition by examining the 2018 proton-proton (pp) collision data collected by the CMS detector at the LHC in search of a new narrow resonance in the dimuon invariant mass spectrum.

We outline this thesis in the following chapters. In Chapter 2, we present a simple description of the SM and describe some of the BSM theories that motivate the search for an additional dimuon resonance. In Chapter 3, we describe the experimental apparatus used to collect the data in this thesis; the LHC accelerator and CMS detector. In Chapter 4, we present a discussion of the relevant challenges related to the identification and reconstruction of high-energy muons in CMS. In Chapter 5, we present the search for high-mass dimuon resonances. Finally, in Appendix A we present a study of the neutron-induced background in CMS endcap muon chambers.

CHAPTER 2

Theoretical Considerations for the Z' Search

2.1 Introduction

In Section 2.2, we present a brief review of the relevant facets of the SM of particle physics in the search for high-mass dimuon resonances. In Section 2.3, we discuss various shortcomings of the SM and potential BSM scenarios that solve these shortcomings and also predict high-mass dimuon resonances.

2.2 The standard model of particle physics

The SM of particle physics is a quantum field theory describing the interactions and properties of all fundamental particles known to exist. Currently, the theory consists of six pairs of fermions. Of the six pairs, three pairs are named quarks and the other three are named leptons. These quarks and leptons interact via the exchange of four gauge boson according to three of the four known fundamental interactions, the electromagnetic, the weak, and the strong interaction. The fourth interaction, gravity, is not incorporated into the SM.

2.2.1 Quarks, leptons, gauge bosons, and interactions

The quarks and leptons make up all the ordinary matter in the universe and are split into three generations and two doublets within each generation. The "up"-type quarks in each quark doublet (u, c, and t quarks) all have an electric charge of $+2/3$, while the "down"-type quarks in each doublet (d, s, and b quarks) all have an electric charge of $-1/3$. For the

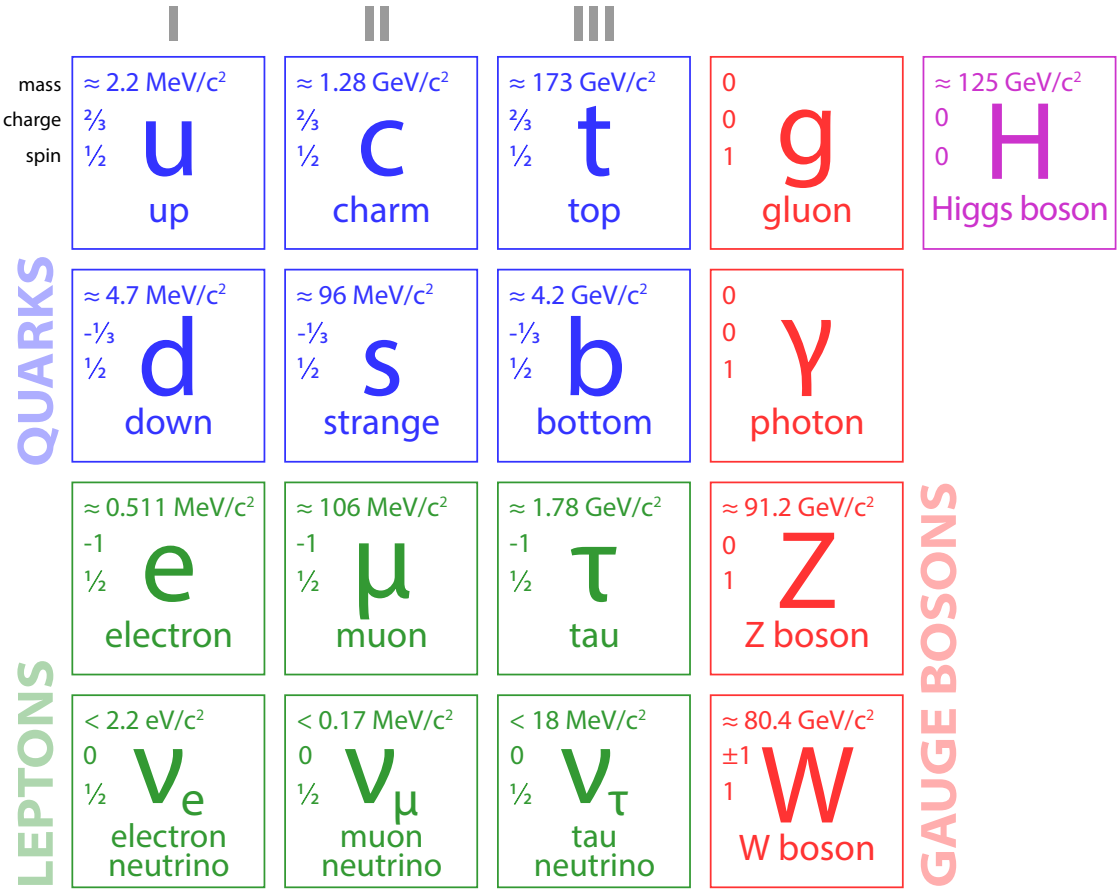

Figure 2.1: Diagram with all of the fundamental fermions and bosons in the SM grouped by generation and type. Quarks are outlined in blue, leptons are outlined in green, gauge bosons are outlined in red, and the Higgs boson is outlined in purple. Labeled are the masses, electric charge, and spin of each particle.

leptons, each generation contains an electrically charged lepton (e, μ, and τ leptons) and an electrically neutral lepton named a neutrino (ν_e, ν_μ, and ν_τ leptons). Each of the 12 fermions has a corresponding antiparticle with opposite quantum numbers. Figure 2.1 is a diagram displaying all the SM fundamental particles.

Mathematically, the SM is formulated as a gauge theory, which is described by the symmetry group,

$$SU(3)_C \times SU(2)_L \times U(1)_Y, \tag{2.1}$$

where $\times$ denotes the direct product of each of the symmetry groups. From Noether's theorem, each of the symmetry groups above has an associated conservation law, which yields a conserved charge. The subscripts on each symmetry group denote the conserved charges. For the $SU(3)_C$ group, which describes the theory known as quantum chromodynamics (QCD) and the strong interaction, the conserved charge is known as color, C. In this interaction, only the particles that carry color, the quarks and the gauge bosons known as gluons, can interact. The $SU(2)_L \times U(1)_Y$ group is described by the electroweak (EWK) theory, which is a combined symmetry of two interactions, the weak and the electromagnetic interactions. For the electroweak interaction, the conserved charges are the weak isospin and the weak hypercharge. Both quarks and leptons carry these electroweak charges, and they can therefore interact via exchange of the electroweak gauge bosons.

In the SM, the SM fermions and gauge bosons do not intrinsically have mass and must acquire mass via the process known as the Higgs mechanism. The Higgs mechanism describes how a scalar field, known as the Higgs field, exists with a potential that causes the ground state to spontaneously break the electroweak symmetry. As a result, the originally massless electroweak gauge bosons mix and thus become the observed weak and electromagnetic gauge bosons. The weak gauge bosons, the Z and W bosons, gain mass, while the electromagnetic gauge boson, the photon, remains massless. In addition, a massive scalar boson, known as the Higgs boson, is also predicted. For the fermions to gain mass, Yukawa interactions terms with the scalar Higgs field are put into the SM.

2.2.2 Parton distribution functions and Drell-Yan

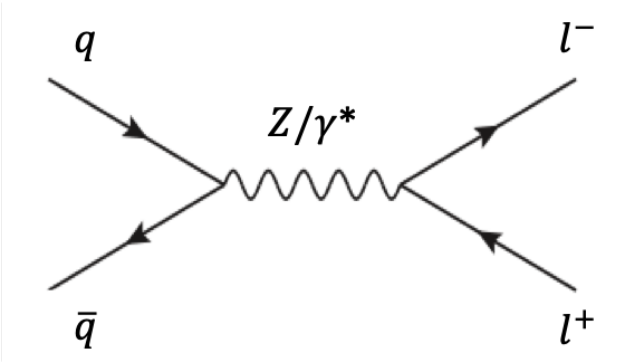

Figure 2.2: Feynman diagram of the tree level DY process.

Of interest to the search for a high mass dimuon resonance is the SM Drell-Yan (DY) process, $q\bar{q} \rightarrow Z/\gamma^* \rightarrow \mu^+\mu^- + X$. The DY process constitutes an irreducible source of background dimuons at both low and high dimuon mass. Figure 2.2 depicts a Feynman diagram of the tree level DY process, which is the annihilation of a quark and antiquark pair into an off-shell Z/γ^* that decays to a pair of charged leptons. For the analysis presented in this thesis, we assume the leptons to be muons when we refer to the DY process.

In pp collisions, the typical process for DY production is a valence quark annihilating with an antiquark from quantum vacuum $q\bar{q}$ fluctuations. These quantum vacuum $q\bar{q}$ fluctuations, known as "sea" quarks, will typically have a lower probability than the valence quarks to carry a large fraction of the proton momentum. Thus, to precisely determine the DY background, it is crucial to understand the probability density to find a parton inside the proton with fraction x of the longitudinal proton momentum, known as the parton distribution function (PDF). PDFs cannot be determined from perturbative QCD so they must be obtained by fits to experimental data. For large x, the PDFs are computed by extrapolations from smaller x. At high energies, where the momentum fractions of the incoming quarks are necessarily large, the PDFs and their associated uncertainties are therefore less well known and play an important role.

2.3 Beyond the standard model

Despite its many successes, the SM is not a theory of everything. As mentioned above in Chapter 1, the SM does not provide a description of the gravitational interaction at a fundamental level, it does not explain the asymmetry of matter and anti-matter in the universe, and it also does not explain the presence of dark matter. Many BSM theories have been proposed in an attempt to explain, in part, some of these shortcomings.

One such class of theories are known as the Grand Unified Theories (GUT). GUTs hypothesize that at very large energy scales, known as the grand unification energy or the GUT scale, the SM interactions unify into a single interaction described by one single gauge group. This idea of low-energy theories unifying at high-energies is partially inspired by existing physics theories. An example of this exists in classical physics with Maxwell's unification of electricity and magnetism into a combined theory of electromagnetism. Another example of this also exists within the SM itself. At low energies ($< 100\,\text{GeV}$), the electromagnetic and the weak interactions appear to be separate, but above the the electroweak symmetry breaking scale, the interactions unify into a single interaction. Thus, in some GUTs, the SM gauge groups defined in Eq. 2.1 become the low-energy approximations of a single interaction described by some unified gauge group.

The first historical example of a proposed GUT gauge group is the simplest larger gauge group that also contains the SM: the $SU(5)$ gauge group [9]. The $SU(5)$ theory combines leptons and quarks into single irreducible representations and therefore may have interactions that do not not conserve baryon number, B, while still conserving the baryon minus lepton number, $B - L$. This provides a mechanism and a prediction for the rate of proton decay. However, experimental limits on the lifetime of the proton soon contradicted the theoretical predictions of the $SU(5)$ GUT [9]. Thus, other GUTs have also been proposed with more complex higher gauge groups.

Examples of models that we consider can be grouped into three general classes; those based on the E_6 gauge group, those based on left-right (LR) symmetric extensions to the SM,

and those based on generalizations of the SM. Each of these classes predict additional $U^{'}(1)$ gauge groups that, under the right circumstances, are spontaneously broken and produce an electrically neutral, spin-1, gauge boson near to the TeV scale. These new gauge bosons, referred to as Z' bosons, can then be potentially detectable in LHC collisions.

In the E_6 case, the additional $U^{'}(1)$ gauge groups follow from the chain,

$$E_6 \rightarrow SO(10) \times U^{'}(1)_{\psi} \rightarrow SU(5) \times U^{'}(1)_{\psi} \times U^{'}(1)_{\chi} \rightarrow SM \times U^{'}(1)_{\theta_{E_6}}. \tag{2.2}$$

At low energies we assume that only one linear combination of the two additional gauge groups $U^{'}(1)_{\chi}$ and $U^{'}(1)_{\psi}$ exists with their charges mixing according to mixing angle θ_{E_6}. (Here, low-energy means low relative to the GUT scale.) The charges of the $U^{'}(1)_{\theta_{E_6}}$ are then given by the linear combination,

$$Q(\theta_{E_6}) = \cos\theta_{E_6}\ Q(\chi) + \sin\theta_{E_6}\ Q(\psi). \tag{2.3}$$

Some commonly studied special cases are the ψ model ($\theta_{E_6} = \pi/2$), which corresponds to the extra Z' of the E_6 symmetry breaking and the χ model ($\theta_{E_6} = 0$), which corresponds to the extra Z' of the $SO(10)$ symmetry breaking. Other E_6 models, η, I, S, and N, are presented in Section 5.10 and involve specific choices of the angle θ_{E_6} [10, 11, 12, 13]. They are not studied in much detail in this thesis, so we do not discuss them further.

Models based on introducing an additional left-right handed symmetric extension to the SM hypothesize that at higher energies, parity symmetry is restored. Generally, the necessary gauge groups can arise from higher gauge groups like $SO(10)$ or E_6, but all involve the general symmetry breaking,

$$SU(2)_L \times SU(2)_R \times U(1)_{B-L} \rightarrow SU(2)_L \times U(1)_Y \times U^{'}(1) \tag{2.4}$$

Thus, in addition to predicting an additional $U^{'}(1)$ gauge group, there is also an additional $SU(2)$ gauge group that predicts an additional W boson-like gauge boson. In general, the $U(1)_R$ coming from the $SU(2)_R$ gauge group can mix with the $U(1)_{B-L}$ and several benchmarks are considered in Section 5.10. In this thesis, we do not study these models in

detail so we do not discuss them further. More discussion can be found elsewhere [10, 11, 12, 13].

The final case discussed in this thesis are Z' based the generalization of the SM. In these models, the SM charges Q, the electric charge, and T_{3L}, the weak isospin, are generalized such that,

$$Q(GSM) = \cos\alpha \; T_{3L} + \sin\alpha \; Q, \tag{2.5}$$

where α is some general mixing angle between the two SM charges. As special case of the angle α is the sequential SM (SSM), where the couplings of the Z' to all SM particles are identical to those of the SM Z boson. Other cases, like $\alpha = 0$ or $\alpha = \pi/2$, have properties that allow for very large decay widths, large production cross sections, and large $Z'/Z/\gamma^*$ interference effects. Interference of a new Z' with the SM DY process is discussed further in Section 5.10.

In each case above, the couplings, and therefore the production cross sections, of the each of the Z' bosons predicted are defined by the specific model. No predictions on the mass of the Z' exist, so, an upper bound on the mass exists at the particular GUT scale (approximately 10^{16} GeV) and the lower bound on the mass being the subject of the measurement described in Chapter 5 of this thesis. If a discovery is made, then other observable are measured, such as the couplings to its observed decay products, the intrinsic width, and decay product angular distributions.

We choose two models to be used as benchmarks when presenting the results of this thesis. The first is the sequential SM, Z'_{SSM}. Compared to the sets of models described above, this model has a wide width (2.5% of the Z' mass) and has a relatively large production cross section times branching fraction to muons. The second model is the Z'_{ψ} boson from the E_6 GUT theory discussed above. This particular Z' has a narrower width compared to the sets of models described above and also has a relatively small production cross section times branching fraction to muons. In addition to these benchmark models used for results of the resonance search, a third model, Z'_Q from the generalized SM models above, is used for tests of $Z'/Z/\gamma^*$ interference. This model is notable for its large width, large production

cross section times branching fraction, as well as its large negative interference effects. More discussion of theoretical aspects of $Z'/Z/\gamma^*$ interference, including more discussion of the Z'_Q model, can be found in Section 5.10.

CHAPTER 3

Experimental Apparatus

3.1 Introduction

As mentioned in Chapter 2, this thesis presents a search for BSM physics at high energy scales where the production cross section is typically small. Thus, to achieve an event rate of BSM physics where discovery is possible, it is necessary to consider a particle collider that can provide beams that are both intense and high in energy. If the collisions are produced in large enough numbers, it is possible to probe these small cross sections in hopes of discovering a previously unknown particles. To do this, it is also necessary to construct complex particle detectors that are able to detect, identify, and measure the decay products of the unknown particles.

In this chapter, we describe the experimental setup of such a particle collider and particle detector. In Section 3.2 we describe the Large Hadron Collider (LHC) machine and in Section 3.3 we describe the Compact Muon Solenoid experiment (CMS).

3.2 The Large Hadron Collider

The Large Hadron Collider (LHC) is the world's largest hadron accelerator and collider. It straddles the border between France and Switzerland, just outside of Geneva, Switzerland at the European Organization for Nuclear Research (CERN). The LHC is located about 100 m underground and is approximately 27 km in circumference. It consists of two counter-rotating beams of protons that provide collisions at a center of mass energy of 13 TeV to four large-scale experiments, which are located at various points along the LHC ring. The LHC

can also be configured to deliver proton-lead collisions, as well as lead-lead collisions. Of the four major experiments, the two smaller experiments (small in a relative sense, as both of these experiments are still large), LHCb and ALICE, focus on more specialized physics programs. LHCb is built in the forward region to focus on b-quark physics and CP violation, while ALICE focuses on studies of the quark gluon plasma that occurs in lead-lead collisions. The two large-scale experiments, ATLAS and CMS, are built as general-purpose detectors with full detection coverage. ATLAS and CMS have similar physics programs, namely, the discovery of the Higgs boson, which was accomplished in the summer of 2012 [2, 3], many precision measurements, and broad programs of many searches for potential signs of BSM physics. This thesis presents an analysis of proton-proton collision data collected by the CMS detector.

The protons used for collisions in the LHC originate from bottled hydrogen gas and pass through a large accelerator complex before reaching their final collision energies. Figure 3.1 shows the CERN accelerator complex. First, the hydrogen is stripped of its electrons and the resulting protons are sent through a linear accelerator, the Linac2, which accelerates the protons to an energy of 50 MeV with radiofrequency (RF) cavities. The protons are then sent through a series of synchrotrons that progressively accelerate the beams of protons with additional RF cavities to higher and higher energies before being injected into the LHC. The first synchrotron is the Proton Synchrotron Booster (PSB), which receives the protons from the Linac2 and accelerates them to an energy of 1.4 GeV. Next, the protons pass into the Proton Synchrotron (PS), which accelerates them to an energy of 26 GeV. The PS also splits the beams into desired the proton bunch structure. For much of Run 2, the beams are typically configured with a 25 ns bunch spacing. In the final step before injection into the LHC, the beams pass into the Super Proton Synchrotron (SPS), which accelerates the beams to an energy of 450 GeV.

The LHC itself is used for the final step in the proton acceleration. For Run 2, the final energy of the beams of protons is 6.5 TeV. The beams are steered around the LHC ring with 1232 dipole superconducting magnets and 392 quadrupole magnets additionally steer

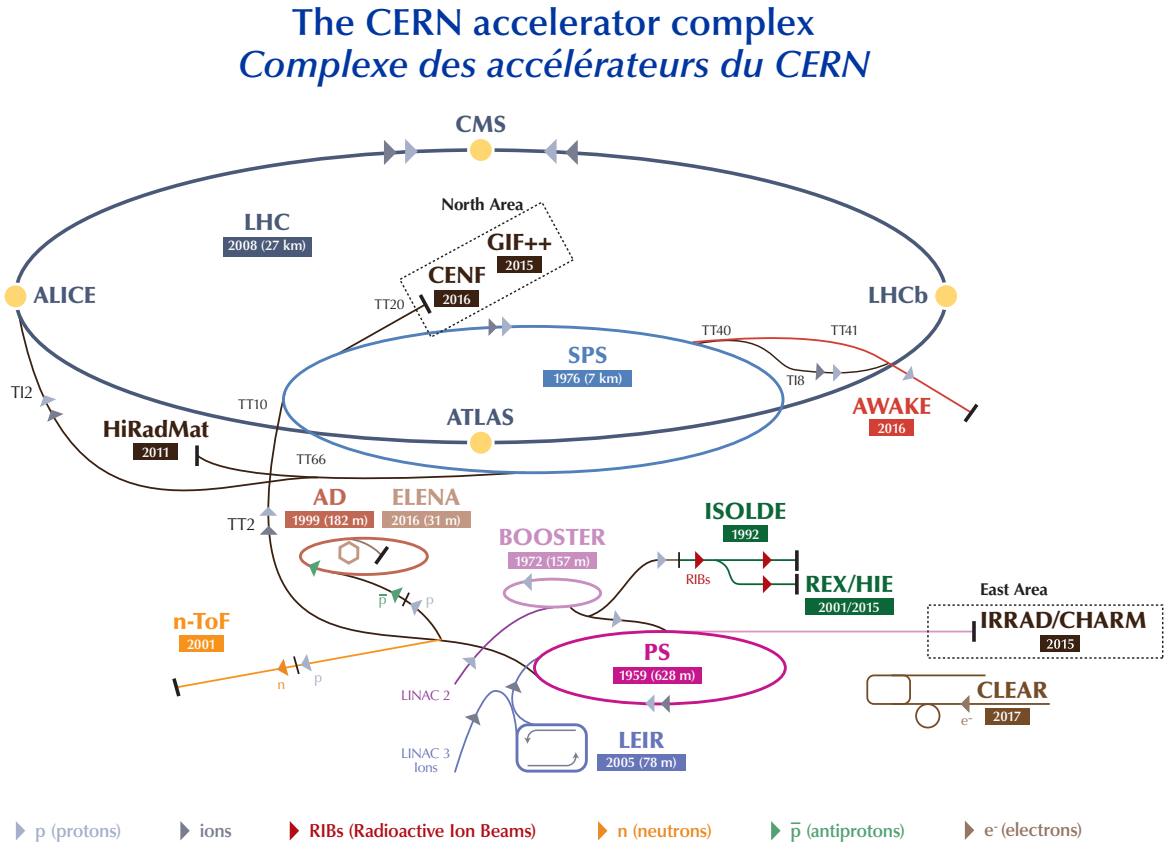

Figure 3.1: The CERN accelerator complex. Shown is the configuration for the 2018 data taking period [14].

the beams. Some special high-field quadrupoles focus the beams to several collision points around the ring. Higher order multipole magnets are also used to further stabilize the beams.

In addition to providing collisions with a large center of mass energy, the LHC also provides collisions with a large instantaneous luminosity. The instantaneous luminosity depends only on parameters specific to the beams and can be written as,

$$\mathcal{L} = \frac{N_b^2 n_b f_{\text{rev}} \gamma_r}{4\pi \epsilon_n \beta^*} F, \tag{3.1}$$

where N_b is the number of protons per bunch, n_b is the total number of bunches in each beam, f_{rev} is the revolution frequency, γ_r is the relativistic factor, ϵ_n is the normalized transverse beam emittance, β^* is the beta function at the collision point, and F is a geometrical factor arising from the angle between the colliding beams at the interaction point [15]. For the 2018 data-taking period, the LHC achieved a maximum instantaneous luminosity of approximately $2.1 \times \times 10^{34}\,\text{cm}^{-2}\,\text{s}^{-1}$. The time-integral of the instantaneous luminosity during LHC operation is the integrated luminosity.

3.3 The Compact Muon Solenoid experiment

In this section, we present an overview of the CMS detector. We provide a description of each of the CMS subdetectors and subsystems . For a detailed description of the CMS detector, see Ref. [16].

3.3.1 Overview of the CMS detector

The central feature of the CMS detector is a superconducting solenoid. The solenoid provides a roughly uniform axial magnetic field of 3.8 T and due to the large radius and volume of the return yoke, the magnetic field strength is between 1–2 T in the iron return yoke. Such a large magnetic field was chosen to achieve good momentum resolution for high energy charged particles.

The solenoid is 6 m in diameter and is large enough to enclose an inner silicon tracker,

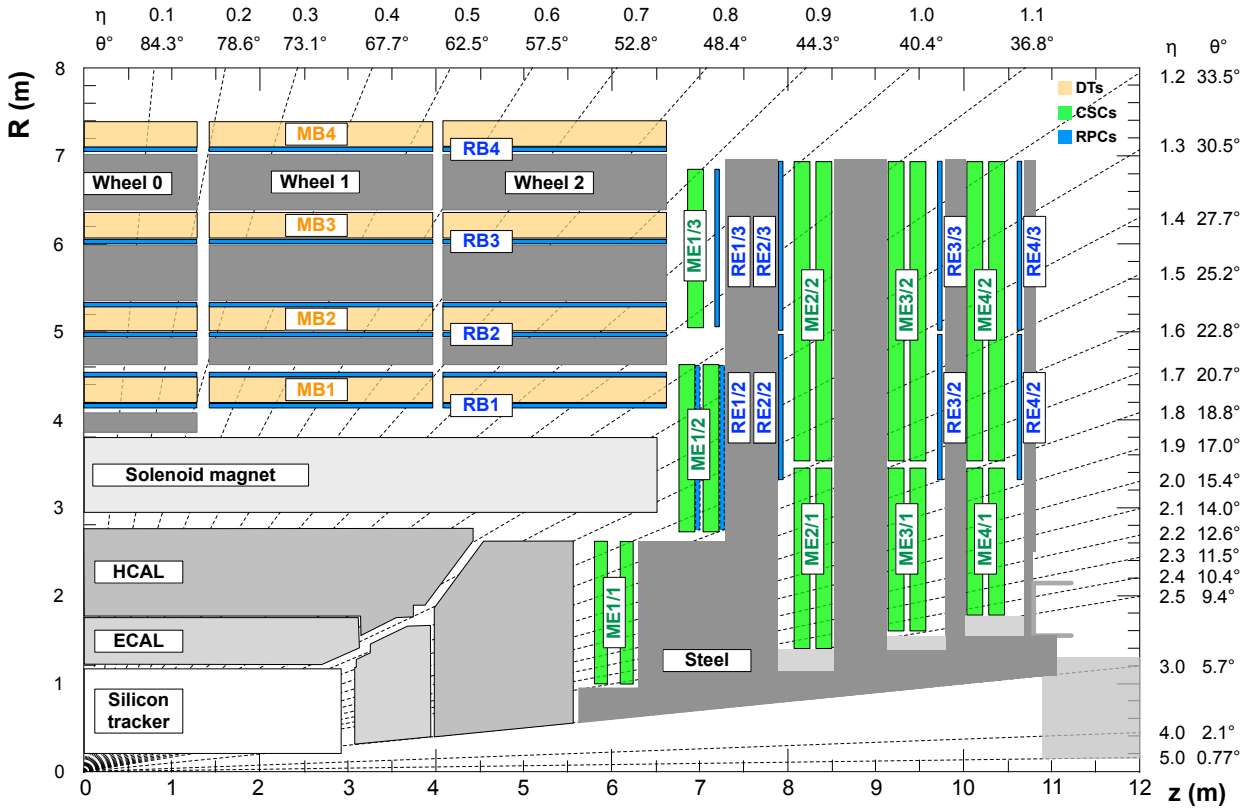

Figure 3.2: An r-z cross section of a quadrant of the CMS detector with the axis parallel to the beam running horizontally (z) and the radius r increasing upward. The interaction point is at the lower left corner. Labeled are each of the subdetectors in CMS; the inner tracker, the ECAL, the HCAL, the solenoid, the muon system, and the iron return yoke. The figure taken from Ref. [17].

as well as electromagnetic and hadronic calorimeters. Outside of the solenoid are four barrel and four endcap muon stations interspersed in the iron return yoke. Figure 3.2 depicts one quadrant of the CMS detector in its Run 2 configuration with the muon detectors in color. Labels denote each of the axis definitions, pseudorapidity values, and various subdetectors.

We use a coordinate system with the origin at the nominal collision point, the y-axis oriented vertically upward, and the x-axis oriented toward the center of the LHC. The z-axis points along the beamline coincident with the solenoid axis in the counterclockwise direction. Radial distance from the beamline is denoted by r. We take the azimuthal angle ϕ to be measured from the x-axis in the x-y plane. The polar angle θ is measured from the positive z-axis. Kinematic quantities measured transverse or parallel to the beamline are denoted by a subscript T or Z, respectively, e.g. transverse momentum p_{T}, or longitudinal momentum p_{Z}. Pseudorapidity is defined as $\eta = -\ln\tan(\theta/2)$, which in the limit of particle energies much greater than their rest mass is equivalent to rapidity, $y = 0.5\ln((E + p_{\mathrm{Z}})/(E - p_{\mathrm{Z}}))$; where E is the particle energy. The imbalance of energy in the transverse plane is denoted by $E_{\mathrm{T}}^{\mathrm{miss}}$.

The remaining subsections in this section describe the construction and operation of each CMS subsystem. We emphasize the relevant properties of each detector that are necessary for the detection and measurement of muons.

3.3.2 CMS inner tracker

The CMS inner tracker is comprised of two separate subdetectors; an inner pixel detector and an outer silicon strip detector. It is the detector closest to the interaction point (IP) and is therefore designed to operate in extremely high particle flux conditions. To handle the high flux the detectors are highly granular. This high granularity provides a low enough hit occupancy that ensures enough separation of hits from individual particles to enable high particle trajectory reconstruction efficiency. The pixel detector is the closest to the beamline and therefore is the most granular detector with silicon pixels. The silicon strip detector is further away, so silicon micro-strip detectors are used. Being inside the solenoid the in-

ner tracker is also primarily responsible for measuring the position of charged particles as they pass through the detector. These signals (or hits) are later reconstructed into particle trajectories, which provide estimates of a particle's charge, p_{T}, η, ϕ, and impact parameters. For example, the inner tracker alone measures p_{T} to approximately 1.6% for muons with $p_{\mathrm{T}} < 200\,\mathrm{GeV}$. The inner tracker is also used for interaction vertex identification and reconstruction.

The pixel detector is the the part of the inner tracker that is closest to the interaction region. It has four barrel layers, the closest of which is at a radial distance of 2.9 cm from the beamline, and three endcap disks, the closest of which is at a longitudinal distance of 29.1 cm from the nominal interaction point. This layout provides redundancy in particle detection and pseudorapidity coverage up to $|\eta| < 2.5$. Single hit resolution is determined by the size of the 124 million pixel sensors, which have an area of $100 \times 150\,\mu\mathrm{m}^2$ in both the barrel layers and endcap disks. The spatial resolution of hits from charged particles is measured to be $10\,\mu$m for the r-ϕ position measurement and about $20\,\mu$m for the z position measurement. In total, the sensitive area of the pixel detector is $1.86\,\mathrm{m}^2$. This description describes the upgraded pixel detector, which replaced the original CMS pixel detector between the data taking years of 2016 and 2017. The original pixel detector had three barrel layers and two endcap disks. See Ref. [18] and references therein for more details about the upgraded pixel detector.

The silicon strip tracker is divided into two parts, a barrel region and an endcap region. The barrel strip tracker region is divided into an inner radial region (the tracker inner barrel or TIB) and an outer radial region (the tracker outer barrel or TOB). The TIB surrounds the pixel detector and is made of 4 layers that extend longitudinally up to $|z| < 65\,\mathrm{cm}$. The outer radial layer in the TIB has a radius of 55 cm. The TOB surrounds the TIB and is made of 6 layers that extend longitudinally up to $|z| < 110\,\mathrm{cm}$. The outer radial layer has a radius of 110 cm. The first 2 layers in both the TIB and the TOB contain "stereo" modules, which provide position measurements for both the r-ϕ and r-z coordinates. For these inner layers, the single hit position resolution is $23\,\mu$m in r-ϕ and $23\,\mu$m in r-z. The remaining

layers in the TIB and the TOB have the single hit position resolutions of 35 μm in r-ϕ and 52 μm in r-z. The endcap strip tracker is also divided into two regions; a larger forward region (the tracker endcap or TEC) and a smaller central region (the tracker inner disks or TID). Each TEC is made of 9 disks that cover the region between $120 < |z| < 280$ cm. The TEC also has an outer radial distance of 110 cm and an inner radius that varies from 20 cm to 50 cm that provides coverage to $|\eta| < 2.5$. Each TID is made with 3 smaller disks that fill the gap between the TIB and the TEC. The TEC and TID modules are arranged in concentric rings centered around the beamline. The strips in the TEC and the TID point toward the beamline and provide position measurements in r, ϕ, and z. In total, the silicon strip tracker covers approximately 200 m^2 of active detection surface.

3.3.3 CMS calorimeters

The CMS electromagnetic calorimeter (ECAL) measures photons and electrons and allows for their identification. It surrounds the inner tracker and is comprised of 61200 lead-tungstate crystals in the barrel region and 7324 crystals in each endcap. Lead-tungstate scintillation crystals were chosen for their high density (8.3 g/cm^3), low radiation length ($X_0 = 0.89$ cm), low Moliere radius (2.2 cm), and quick scintillation response. The high density of the lead-tungstate crystal enables a compact design, which allows the ECAL to fit within the solenoid. The lead-tungstate crystals also have a relatively low light yield and have specially developed photodetectors for both the barrel and endcaps. In the barrel, the crystals are 23 cm long (25.8 X_0) and are laid out in an η-ϕ grid. Each barrel crystal has a front face cross section of 2.2×2.2 cm and uses silicon photodiodes as photodetectors. In the endcap, crystals are 22 cm long (24.7 X_0) and are laid out in an x-y grid. Each endcap crystal has a front facing cross section of $2.86 \times 2.86\,\mathrm{cm}^2$ and uses vacuum phototriodes as photodetectors. The chosen size front face area of the crystals in the barrel and endcap ensure the core of an electromagnetic shower will be contained within a 2×2 crystal area. The barrel region provides pseudorapidity coverage up to $|\eta| < 1.479$, while the endcap region provides pseudorapidity coverage between to $1.479 < |\eta| < 3.0$. A preshower detector (PS) is placed in

front of part of the ECAL endcap region ($1.653 < |\eta| < 2.6$) and consists of two layers of lead absorber and silicon strip sensors. The PS helps to provide precision position measurements of photons and electrons and to distinguish photons from two-photon decays of neutral pions.

The CMS hadronic calorimeter (HCAL) measures the energies of hadrons. It surrounds the ECAL and is comprised of alternating layers of brass as an absorber and plastic tile scintillator to detect the scintillation light. The scintillation light is then read out with embedded wavelength-shifting fibers. Most of the HCAL is installed inside the solenoid and surrounds the ECAL, while additional parts of it are installed outside the magnet and in the forward region. In the region $|\eta| < 1.6$, scintillator tiles are laid out in a rectangular η-ϕ grid and have an area of 0.087×0.087. In the region $|\eta| > 1.6$, the scintillator tiles are larger with an η-ϕ area of 0.17×0.17. The main HCAL provides pseudorapidity coverage up to $|\eta| < 3.0$ and the forward HCAL provides pseudorapidity coverage between $3 < |\eta| < 5.2$. The forward HCAL sits outside the muon system 11.2 m from the interaction point. For the forward HCAL, steel is used as the main absorber and quartz fibers that emit Cherenkov light are used as scintillators.

3.3.4 CMS muon system

The CMS muon system measures the positions of muon trajectories, which are typically the only particles from collisions to reach the outermost chambers. It is located primarily outside of the solenoid and is comprised of four stations of barrel and endcap muon chambers embedded in the iron return yoke. Three types of gaseous detector technologies are used as they can cover a large detection surface, which in total cover approximately 25000 m^2 of active detection planes. In the barrel region drift tube (DT) chambers are used, in the endcap region cathode strip chambers (CSC) are used, and in both the barrel and the endcap regions resistive plate chambers (RPC) are also used.

The DT system is constructed in the barrel region of CMS and consists of four radial stations, five wheels, and a total of 250 chambers. DT chambers in each station are overlapped in ϕ to avoid detection gaps. Pseudorapidity coverage is provided up to $|\eta| < 1.2$. In

Fig. 3.2, the DT chambers are labeled with "MB" (Muon Barrel). In the three innermost stations, 12 layers of drift tubes are divided into three groups of four consecutive layers. The inner and outer groups record the r-ϕ coordinate in the bending plane with drift tubes that are parallel to the beamline. The middle group has drift tubes that are perpendicular to the beamline that records the z coordinate. The outermost DY station only has two groupings of four consecutive layers of drift tubes that measure the r-ϕ coordinate.

Each individual drift tube records the drift time from the ionization induced by a charged particle, which is then translated into a radial distance from the wire. The maximum drift length in each tube is 2.0 cm and the single hit resolution is approximately 200 μm. Hit positions in each station are determined by fits to straight lines in both detection planes, r-ϕ and r-z. These segments typically have a position resolution of approximately 100 μm in position and and angular resolution of 1 mrad.

The CSC system is described in detail in Appendix A.2, so we provide only a brief description here. The CSC system consists of 540 individual multi-wire proportional chambers arranged in four disks on either side of the CMS endcaps. The first disk in each endcap contains three rings of chambers, with the innermost ring (denoted by "ME1/1" in Fig. 3.2) uniquely located inside the solenoid while all other rings located outside the solenoid. The second, third, and fourth stations all contain two rings of chambers. Each chamber consists of six gas gaps that have radial cathode strips that have a roughly constant $\Delta\phi$ and anode wires that run perpendicular to the strips.

As a charged particle passes through a gas gap, the induced ionization charge collects on the anode wires, which is quickly read out for a coarse η measurement. At the same time, an image charge forms on the cathode strips, the shape of which is interpolated to precisely determine the ϕ coordinate. These two dimensional hits are then fit to a straight line in both the ϕ-z and η-z plane (also called segments). These segments provide precision single-hit ϕ position measurements of charged particles with a resolution of about 10 mrad (or 200 μm). The ME1/1 ring has narrower strips and has a hit resolution of about 5 mrad (or 100 μm).

The RPC system is embedded throughout the barrel and endcap muon systems. These

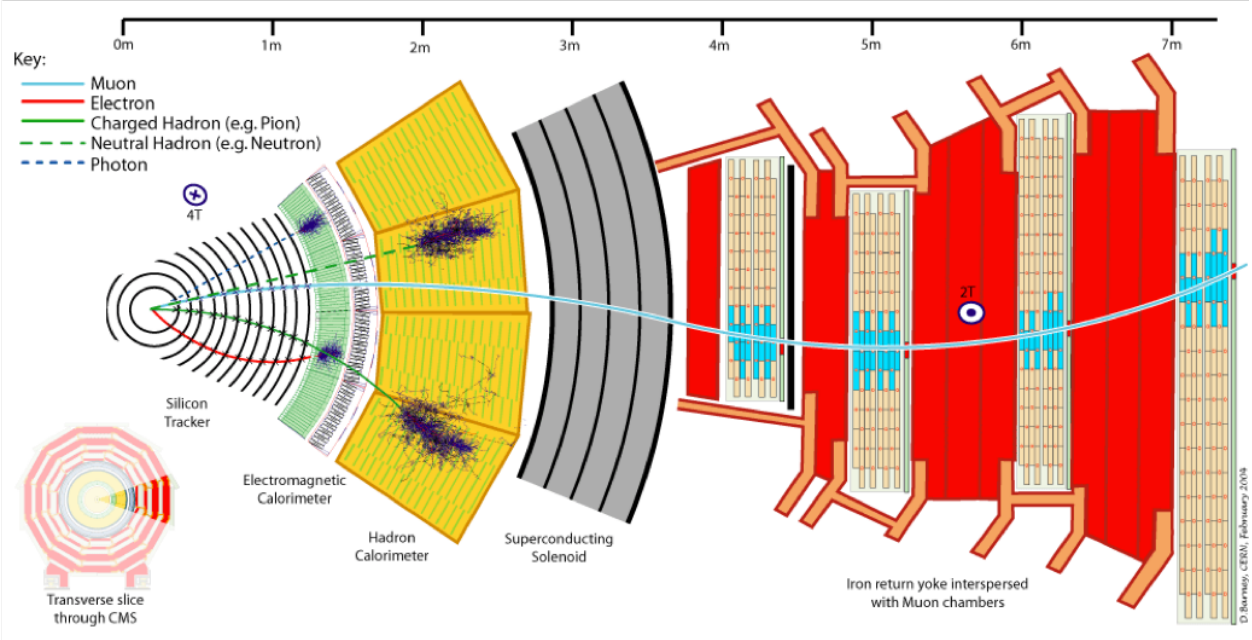

Figure 3.3: Transverse view of a slice of the CMS detector in the barrel region. Labeled are each of the subdetectors with illustrations of the interactions of specific particles relevant to each subdetector [19].

chambers provide imprecise position measurements compared to the CSC and DT detectors, but are much faster and primarily used for muon triggering. In the barrel, the RPCs are placed in front of and behind the DT chambers in the first barrel station and in front of the remaining three barrel stations. In the endcap, RPCs are placed behind all CSCs except for those in the innermost ring.

Figure 3.3 displays transverse slice of the CMS detector in an r-ϕ view. Labeled are each of the subdetectors with an illustration of the interactions of the specific particles that each subdetector is responsible for detecting. Relevant for this thesis is the blue curve denoting the trajectory of a typical low-energy muon that traverses CMS. The muon passes through and leaves hits in each layer of the inner tracker. It eventually also passes through the solenoid and reaches the barrel muon system, leaving hits in each station of the DT muon system.

3.3.5 CMS trigger system

At the LHC, pp bunches cross at a rate of 40 MHz. This high rate leads to approximately 10^9 interactions/sec at the instantaneous luminosities achieved during the 2018 data taking. Thus, an online event selection is designed to select interesting events at a reasonable enough rate such that we can write the events to tape. This is done with a two-level trigger system that consists of a hardware-based first level, referred to as Level 1 or L1, and a software-based second level, referred to as the high-level-trigger or HLT. The two levels of the trigger together reduce the rate of events by a factor of 10^6, such that the eventual rate of events written to tape is only a few hundred per second.

The L1 trigger consists of custom hardware processors that use coarsely segmented data from the calorimeters and the muon system. The coarsely segmented data, also called trigger primitives, are detector-level energy deposits in calorimeters or hit patterns in muon chambers. These trigger primitives are combined to form trigger objects, such as candidate electrons, photons, tau leptons, or muons, in regional triggers. The trigger objects are sorted by the Global Calorimeter and Global Muon triggers that use pattern logic to sort the trigger objects. The sorting rank is determined as a function of energy or momentum and object quality. Trigger object quality is typically a measure of uncertainty in the L1 measurements, angular quantities, or isolation from other trigger objects. In total, the allowed latency between a given bunch crossing and a L1 trigger accept signal is 3.2 μs. During this time, the high-resolution data is held in pipelined memory in the front-end electronics.

Once a L1 accept signal is generated, the high-resolution data from the full detector are collected and sent to the HLT for further evaluation. The HLT consists of software algorithms that are similar to the full offline reconstruction. In this thesis, only the muon parts of the L1 trigger and HLT are used. The specific HLT algorithms used are described in Chapter 5.

CHAPTER 4

TeV Muon Reconstruction in CMS

4.1 Introduction

As we introduced in Chapter 1, we are interested in searching for a dimuon resonance with a mass in the TeV regime. To determine the invariant mass of these high-mass dimuon candidates, precise knowledge is required of the issues relevant for muons at high p_{T}. In this chapter, we discuss the physics, reconstruction, and performance of high-p_{T} muons with the CMS detector.

This chapter begins in Sec. 4.2 with a discussion of the specific challenges due to the physics of high-p_{T} muons in identification and reconstruction of high-p_{T} muons in CMS. In Section 4.3, we describe the specific set of algorithms used to reconstruct high-p_{T} muons and discuss their performance. In Section 4.4, we describe studies of the calibration of the muon momentum scale relevant for the high-mass dimuon search. Finally, in Section 4.5, we present a study on the the probability at which the charge is misassigned to muon candidates. For a full description of the reconstruction of muons in CMS see Ref. [20]. Reference [21] is to be published and contains a full description of the reconstruction and identification of high-p_{T} muons for Run 2.

4.2 Physics of TeV Muons

Experimentally, high-p_{T} muons have important differences with respect to their low-p_{T} counterparts. At low p_{T}, muon momentum resolution is primarily limited by multiple Coulomb scattering. Multiple Coulomb scattering is the process by which a charged particle is de-

flected in its trajectory by the Coulomb interaction with atomic nuclei. If a charged particle undergoes many small-angle Coulomb scatters, then the net scattering angular and displacement distributions approach a Gaussian distribution via the central limit theorem. From Moliere [22], the RMS of the net scattering angle distribution is proportional to the inverse of the momentum of the particle and also depends on the square root of the thickness of the material in radiation lengths. In CMS, potential for large multiple scattering for tracks with low-p_{T} exists where the amount of material is largest: outside the CMS tracker volume in the CMS calorimeters, solenoid, and iron return yoke. Therefore, hits recorded in muon stations that are induced by low-p_{T} muons can be potentially affected by large Coulomb scatters. For cases when the thickness of the material is such that the number of Coulomb scatters is not large or the charged particle undergoes a large-angle Coulomb scatter, then the net scattering angle distributions become non-Gaussian. The other effect at low-p_{T} is energy loss through ionization interactions with the detector material. Ionization energy losses are described by the Bethe-Bloch formula [22] and are taken into account in the track fit model described below.

High-p_{T} muon reconstruction is additionally affected by radiative losses, which affect both the muon momentum scale and resolution. In CMS, the critical energy, where radiative losses become greater than the energy losses due to ionization, for muons in iron is approximately 350 GeV [22]. Radiative processes for muons include interactions with material, e.g. bremsstrahlung, direct pair production, and photonuclear interactions. Among these, large losses in energy are most probable in muon bremsstrahlung. Issues for the reconstruction of particle tracks include the associated generation of electromagnetic showers, which are typically reconstructed by CMS as a large multiplicity of extra hits and segments near to the incident muon trajectory. If the energy loss is large enough, then the muon's trajectory can also be deflected from its original course. For high-p_{T} tracks, special care is taken to ensure that these processes do not spoil the track measurement; we discuss this further in the next section.

4.3 Reconstruction of TeV Muons

4.3.1 Momentum measurement in CMS

As discussed in Section 3.3, the central feature of CMS is a 3.8 T solenoid. This choice of magnetic field configuration facilitates precise measurement of the momenta of charged particles. From the Lorentz force law, the trajectory of a charged particle in a uniform magnetic field is a helix. From this, momentum of a charged particle in a uniform magnetic field is given by

$$p\cos\lambda = p_{\mathrm{T}} = 0.3BR, \tag{4.1}$$

where λ is the angle measured in the x-y plane measured from the y axis (also referred to as the "dip angle"), B is the magnetic field strength in tesla, R is the helix radius in meters. The 0.3 is a unit conversion factor proportional to the speed of light.

It is convenient to restate this Eq. 4.1 in terms of the track sagitta s and signed curvature of the track, $\kappa = q/p_{\mathrm{T}}$,

$$\kappa = \frac{q}{0.3BR} = \frac{8q}{0.3BL^2}s \tag{4.2}$$

where $s \approx L^2/8R$ in the approximation that R, the helix radius, is much larger than L, the arc length of the trajectory.

As uncertainties in s are proportional to the approximately Gaussian hit position uncertainties, this implies that uncertainties in κ are also Gaussian. Thus, we use the variable κ to assess the performance of tracking in CMS. Relative uncertainties in κ due to hit positions uncertainties are then given by,

$$\frac{\delta\kappa}{\kappa} = \frac{1}{\kappa}\frac{8q}{0.3BL^2}\delta s, \tag{4.3}$$

where $\delta\kappa$ and δs are the uncertainties on the signed curvature and track sagitta. By including effects due to multiple Coulomb scattering, the full uncertainty on the curvature is given by

$$(\delta\kappa)^2 = (\delta\kappa_{\mathrm{res}})^2 + (\delta\kappa_{\mathrm{ms}})^2, \tag{4.4}$$

where $\delta\kappa_{\mathrm{res}}$ is given by Eq. 4.3 and $\delta\kappa_{\mathrm{ms}}$ is the curvature due to multiple Coulomb scattering. As stated above, $\delta\kappa_{\mathrm{ms}}$ is proportional to the inverse of the particle momentum, so the

uncertainty due to position resolution becomes the dominant uncertainty for high-p_{T} muons.

From Eq. 4.3, we can understand many of the features involved in CMS tracking. As curvature decreases (or, equivalently, as p_{T} increases) the relative uncertainty in the measurement increases. For muons at high p_{T}, the growing uncertainty can be can be countered by requiring tracks with a large BL^2. In CMS, the magnetic field strength, although large, is fixed, so improvement on the measurement must be done by increasing the length of the track. We do this by adding hits from the muon system to the track.

As a simple, but illustrative, example, we compare the BL^2 for tracks reconstructed from the primary vertex to the outer layer of the inner tracker and from the primary vertex to the inner coil of the solenoid. For tracks with high enough p_{T}, we approximate the arc lengths L as the radial distances from the center of CMS to the outer layer of the inner tracker and the inner coil of the solenoid, which are approximately 1.2 m and 3 m respectively. Thus, for the longer track that extends to the inner coil of the solenoid, the BL^2 is approximately $(L(\text{inner tracker})/L(\text{inner solenoid coil}))^2 = (3/1.2)^2 = 6.25$ times larger.

The following subsections discuss specific algorithms used in CMS to add muon hits to the track.

4.3.2 Muon tracking in CMS

In CMS, a five-dimensional curvilinear track model is used to describe particle tracks. Track model parameters are $\kappa = q/p_{\mathrm{T}}$, the signed inverse of transverse momentum; λ, the "dip angle" measured from the y-axis in the y-z plane; ϕ, the azimuthal angle measured in the x-y plane; and two vertex parameters: d_{XY} and d_Z.

In the remaining discussion about performance of muon momentum measurements in this thesis, we note that the transverse component to the momentum measurement is the dominant source of uncertainty, and not the measurement of the directions or vertex positions. This is close to exactly valid for particles traversing the central barrel region of the detector and less so in the endcaps where the magnetic field is non-uniform and the transverse

component to the total momentum is smaller compared to the longitudinal component.

To fit the sets of hits to the track model, we use a Kalman filter technique [23]. The standard CMS reconstruction sequence independently reconstructs tracks in the inner tracker and in the muon systems. Tracks reconstructed in the inner tracker are referred to as "Tracker tracks" and tracks reconstructed in the muon system are referred to as "Stand-alone tracks". We also define a "Tracker muon" to be a Tracker track that has at least one compatible and matching muon station segment based on the propagation of the fit to the muon system. Tracker tracks that are matched to Stand-alone tracks with compatible directions, positions, and p_{T} are also considered. The combined set of hits from the Tracker track and Stand-alone track are refit and the resulting track is referred to as a "Global track" or a "Global muon".

For muons at low p_{T}, the Tracker track achieves the best performance, as the radius curvature is large enough such that the addition of muon system information to lengthen the track only marginally improves the resolution. As mentioned above, hits in the muon system for muons at low-p_{T} are also significantly affected by multiple scattering in CMS calorimeters, the solenoid, and the iron return yoke, further reducing the gain by including them.

For muons at high p_{T} where uncertainties due to multiple scattering are small compared to hit position uncertainties, lengthening the track by including the muon system information can significantly improve the performance of the muon momentum measurement. However, special care must be taken to select hits that are not negatively affected by radiative effects. As mentioned above, radiative losses can produce large electromagnetic showers, which produce large multiplicity and additional segments that can degrade the quality of the true segment left by the muon. Track fits that include these low quality hits or segments can then degrade the quality of the estimate of the muon's momentum. These effects primarily contribute to the tails of the muon momentum resolution.

In CMS, we employ several algorithms to include hits from the muon system; the "tracker-plus-first-muon-station" (TPFMS) fit, the "Picky" fit, and the "Dynamic Truncation" (DYT) fit. We refer to these algorithms as "TeV refits" in discussions in this thesis.

The TPFMS refit begins with the set of hits from the global track and refits the track using the hits in the tracker plus the hits from the innermost muon station containing hits. This strategy takes advantage of the muon system to lengthen the track, but avoids hits in the outer muon stations, which reduces the potential for contamination from electromagnetic showers. However, this refit is especially sensitive to cases where there is a shower in the first station, so its use alone is not optimal.

The Picky refit also begins with the set of hits from the global track. For this refit, each muon station with hits along the trajectory of the muon is examined to check for the presence of an electromagnetic shower, where a shower is identified by the hit multiplicity in the chamber or station in question. If a shower is identified and the χ^2 of the fit is increased by too much by including the hits, then the segment from that station is excluded from the refit. However, this refit is still sensitive to cases when a large shower occurs and the energy of the muon is significantly decreases. That is, including hits in the track fit from before and after a large radiative energy loss can potentially bias the momentum measurement.

The DYT refit takes ideas from both the TPFMS and Picky refits for cases when a muon undergoes a large energy loss. The DYT algorithm re-performs the pattern recognition by re-adding muon system hits to the trajectory and once a large energy loss is identified it stops adding muon system hits. This approach avoids biasing the momentum measurement with the remaining hits in the trajectory after an energy loss identified. The algorithm begins by extrapolating the Tracker track's trajectory into the muon system and systematically checking for energy losses. The reconstructed segments in each successive muon station are examined and compared to the extrapolated direction of the muon trajectory. If the directions are compatible, then the segments are added to the fit and the trajectory is propagated to the next station and the direction comparison is repeated. However, if the muon's energy has changed due to a radiative loss in the iron yoke, then the segment in question will have a direction inconsistent with the extrapolated muon direction. The DYT algorithm ends the fit if two successive stations are found to have segment directions incompatible with the muon extrapolated trajectory.

To find the optimal track among the TeV refits and the Global and Tracker tracks for each muon candidate, CMS uses an algorithm named TuneP. For each muon candidate, each track is compared to each other based on χ^2/dof tail probability; σ_{p_T}/p_T, the relative p_T uncertainty; and the p_T itself. The end result is the "best" track based on these criteria. TuneP starts by selecting between Picky and DYT based on which track has a smaller σ_{p_T}/p_T. This choice is then compared to the Tracker track and selects between the two based on χ^2/dof tail probability. The χ^2/dof tail probability comparison is done again with the output of the previous choice and the TPFMS track. If in cases where the final track candidate has a p_T less than 200 GeV, then the Tracker tracks is always used. In rare cases, the Global track is chosen if none of the Picky, DYT, or TPFMS tracks are valid and Tracker track p_T is greater than 200 GeV. In CMS muon reconstruction, we use the term "high-p_T" to refer to muons with $p_T > 200$ GeV as muons with this p_T benefit from including muon hits in the track fit.

The performance of muon tracking is evaluated by measuring the relative resolution in simulated events. The relative resolution can be obtained from the relative residual distribution in muon q/p,

$$R_{\text{RECO-GEN}} = \frac{(q/p)_{\text{RECO}} - (q/p)_{\text{GEN}}}{(q/p)_{\text{GEN}}}. \tag{4.5}$$

To extract the resolution as a function of muon p, we fit a Gaussian function to the core of the $R_{\text{RECO-GEN}}$ distribution. We use muons that pass the selection described in Section 5.3 that come from the the DY simulations described in Section 5.2. Figure 4.1 displays the relative muon momentum resolution for the various track fits that include muon system information in the track fit. Shown are the relative resolutions in the (top) barrel and (bottom) endcap regions for the Global, TPFMS, Picky, DYT, and TuneP track fits.

4.4 TeV Muon Scale

The scale of the muon p_T measurement is sensitive not only to energy losses and the exact magnetic field knowledge, but also to the exact knowledge of the detector alignment. CMS

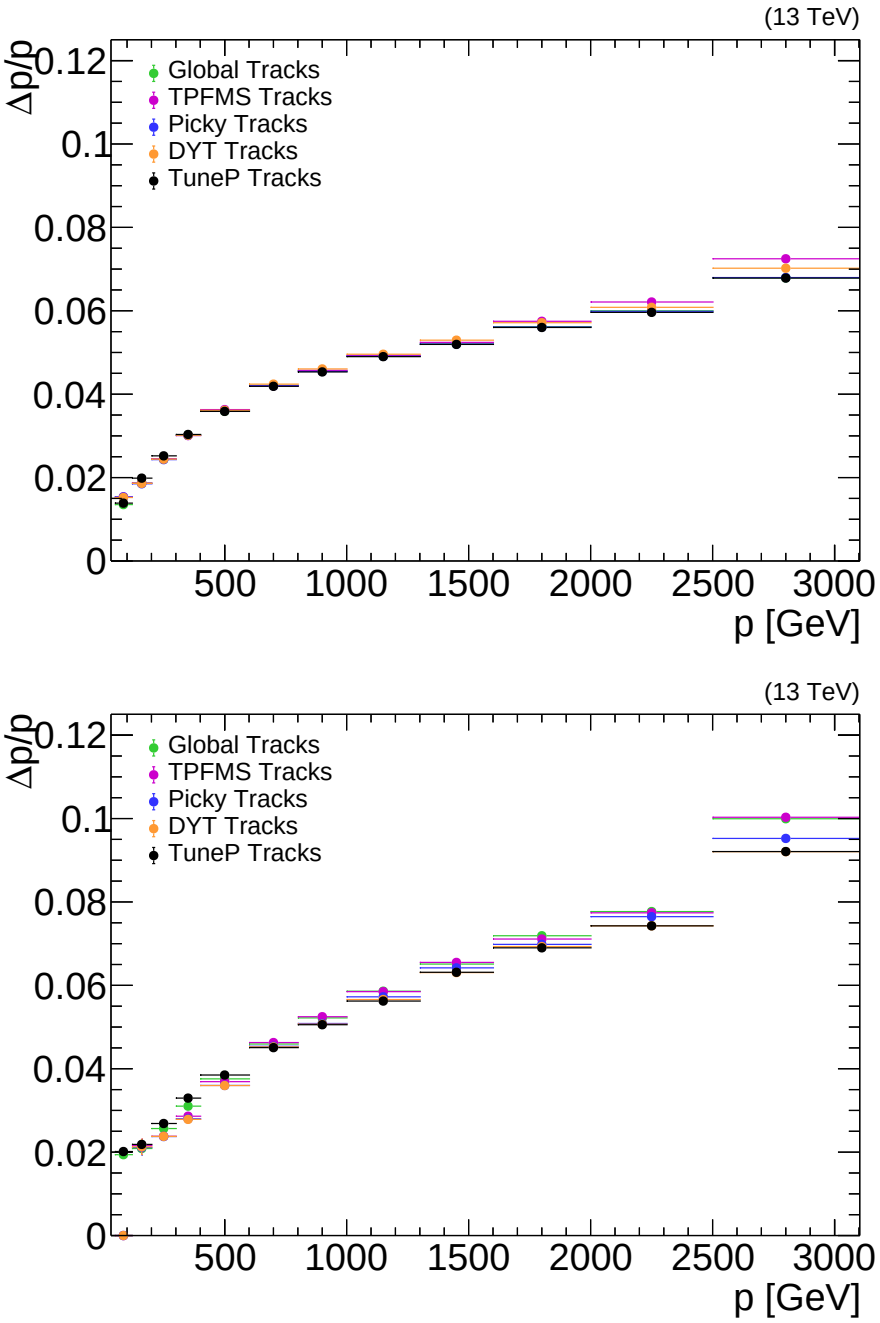

Figure 4.1: Comparison of relative momentum resolution as a function of muon p for different muon fits. Shown is the resolution for the Global tracks, TPFMS tracks, Picky tracks, DYT tracks, and TuneP tracks for (top) muons in the barrel region ($|\eta| \leq 1.2$) and (bottom) muons in the endcap region ($|\eta| > 1.2$).

muon momentum scale calibration accounts for all three of these effects. Energy losses, like those described the Bethe-Bloch equation, are modeled with an additive term that increases with muon momentum. Corrections caused by inexact magnetic field knowledge are modeled as a multiplicative factor on the curvature. Detector misalignment is modeled as a constant additive factor to the signed curvature that depends on muon η and ϕ.

For low-p_{T} measurements, all three of these effects are important. In CMS, we use two dedicated calibration algorithms to calibrate Tracker track curvature measurements. One method uses muons from Z decays and derives correction factors based on detector alignment and magnetic field. The correction factors are computed from comparisons of the averages of the curvature distributions and measured Z mass in bins of η and ϕ in data and simulation to that of a reference sample of events with optimal detector alignment and magnetic field knowledge [24]. The second method uses muons from Z, J/ψ, and $Y(1S)$ and derives corrections for all three effects; energy loss, magnetic field modeling, and detector misalignment. The corrections are computed with a Kalman filter by comparing the reconstructed resonance mass to the known resonance mass.

However, for high-p_{T} muons, the momentum estimate depends on hits in both the inner tracker and the muon system. In the above calibration methods for low-p_{T} muons, which only consider tracks from the inner tracker, the alignment between the inner tracker and the muon system—and also within the muon system—are not accounted for in the calibration. To measure the detector misalignment effect on momentum scale bias at high-p_{T}, we use the Generalized Endpoint (GE) method. The GE method uses DY events in data and simulation to derive corrections based on comparisons of the signed curvature distributions. In bins of muon η and ϕ, the GE method tests the compatibility of the signed curvature distributions in data and simulation by injecting a constant additive term, κ_b, to the simulated distributions. As various values of κ_b are scanned, the simulated curvature distribution is altered as $\kappa \to \kappa + \kappa_b$. Thus, the curvatures of muons with positive and negative charge are muons increase or decrease in opposite according to the sign of κ_b. The value of κ_b found to minimize χ^2 between data and simulation in each bin of muon η and ϕ is taken as the value of the constant

additive factor that models the detector misalignment.

In the 2017 and 2018 data-taking years, the GE method was evaluated at high p_{T} with both Tracker tracks and TuneP tracks for muons with $p_{\mathrm{T}} > 200\,\mathrm{GeV}$ by the CMS Muon Physics Object Group. Within the limited sample size of high-p_{T} muons in data, the additive term was found to not be significantly different between the Tracker and TuneP tracks. Thus, the misalignment mostly comes from the inner tracker, while the muon system does not contribute significantly. The largest misalignment effects were found to occur in the forward endcap regions $|\eta| > 2.1$ and in the barrel regions to be consistent with zero scale bias.

4.5 Muon charge assignment at high-p_{T}

The sign of muon candidate electric charge is assigned according to the direction of the track curvature in the CMS magnetic field. At low muon energies the charge is well determined due to the large amount of bending. However, in the limit of large muon energies the amount of bending in the transverse plane becomes smaller and muon tracks become nearly straight. In this limit, the size of the sagitta also becomes approximately equal to the size of the hit position uncertainties. For these tracks with small deflections, detector-specific effects like non-ideal detector alignment conditions also play an important role in precision track measurements. In addition, at high enough energies large electromagnetic showers in muon detectors caused by muon bremsstrahlung further increases the difficulty of measuring the muon tracks precisely. Thus, at high muon energy the probability to misreconstruct the muon charge becomes non-negligible and is therefore an important quantity to measure.

To illustrate the effect of detector resolution and muon bremsstrahlung on high energy muons tracks, Figure 4.2 displays the distribution of reconstructed q/p computed from the TuneP algorithm and the Picky algorithm for simulated muons generated with a positive charge, $q = +1$, and a fixed momentum, $p = 4000\,\mathrm{GeV}$. The core of the distribution is approximately Gaussian as expected from the reconstructed hit position resolution and peaks at the value the muons were generated, $q/p = +1/4000$, with units of $1/\,\mathrm{GeV}$. The tails are

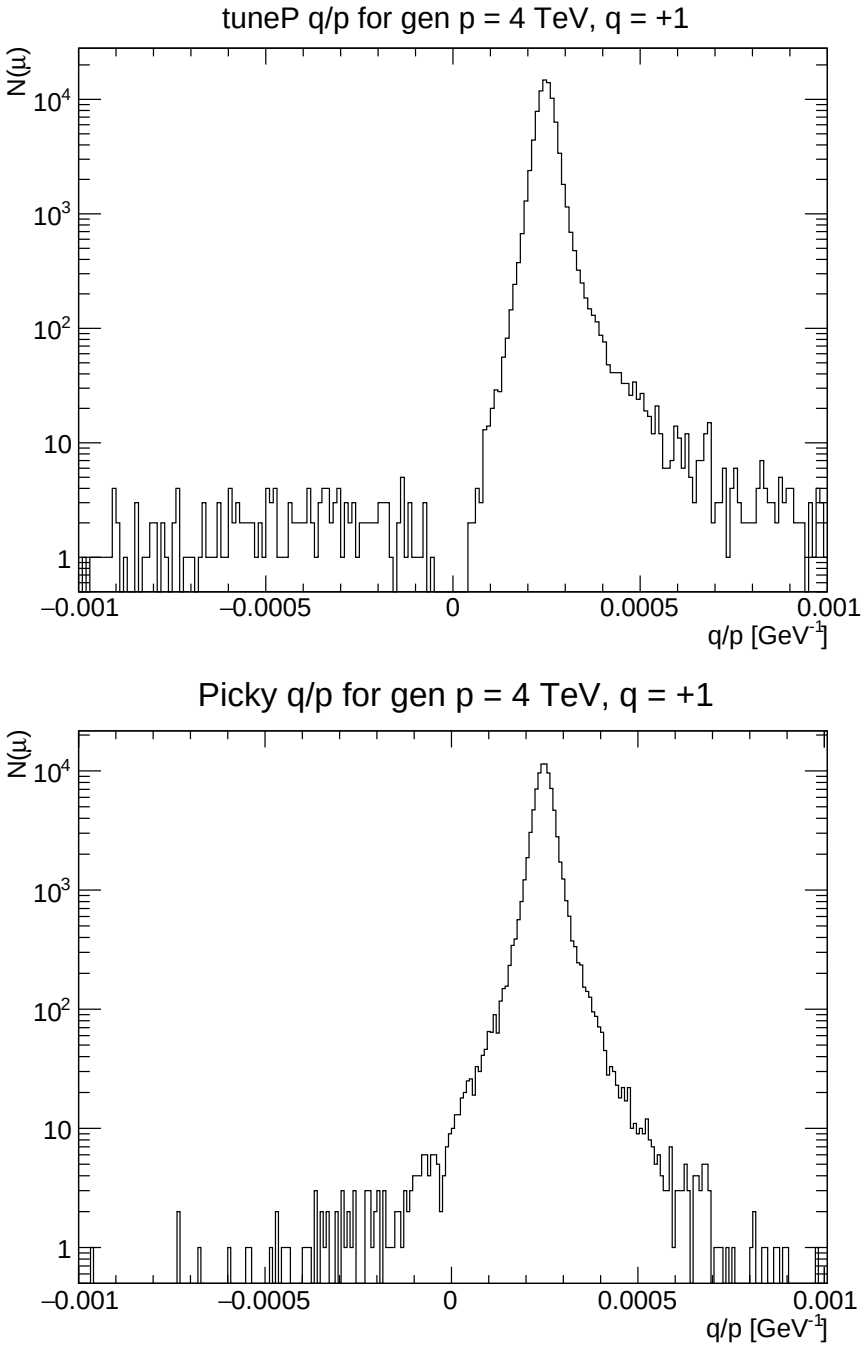

Figure 4.2: Histogram of reconstructed muon q/p in units of $1/\,\mathrm{GeV}$ computed by (top) the TuneP algorithm and (bottom) the Picky algorithm, for positively charged muons generated at $p = 4000\,\mathrm{GeV}$.

non-Gaussian and are caused by muon interactions with detector material. Specifically, muon bremsstrahlung and multiple scattering are effects that contribute non-Gaussian effects. The charge misassignment probability for this sample of simulated muons is then the fraction of the distribution of q/p for muons reconstructed on the wrong size of zero, that is, with negative values of q/p in this histogram. The gap in the distribution near to $q/p = 0$ (very high energy muons) for TuneP is caused by an upper bound on the relative track fit uncertainty, $\Delta p_{\mathrm{T}}/p_{\mathrm{T}}$, of the track candidates implemented in the TuneP algorithm. The Picky algorithm does not have a selection on the relative track fit uncertainty and is a continuous distribution without a gap near $q/p = 0$.

The charge misassignment probability of muon track candidates is studied in two separate simulations; muon candidates from simulated $pp \to Z/\gamma^* \to \mu^+\mu^-$ events, and muon candidates simulated with a "muon-gun". The muon-gun simulation generates muons with fixed values of p and is uniformly distributed in muon η and ϕ. Results are reported in bins of muon p, p_{T}, η, and ϕ. Muons are required to pass the High-p_{T} ID described in 5.3 and are triggered by a single muon trigger with a threshold of 50 GeV.

Figure 4.3 shows the charge misassignment probability vs. muon p_{T} in (left) 2016 MC and (right) 2017 MC separately for muons in the barrel ($|\eta|$ <0.9) and combined positive and negative endcaps ($|\eta|$ >1.2). (In Fig. 4.3 and in the following figures measuring the charge misassignment probability the vertical axis is labeled with "rate" rather than probability. In the context of this section, we define the rate of charge misassignment to be equivalent to the probability of charge misassignment.) The charge misassignment probability is 10^{-5} for muons with $p_{\mathrm{T}} < 250$ GeV and rises to 10^{-3} for muons with $p_{\mathrm{T}} > 1600$ GeV with the probability in the barrel consistently lower than the probability in the endcap for muons with the same p_{T}. Figure 4.4 shows the misassignment probability as a function of muon p. Within the statistical precision of the simulation the charge misassignment probabilities are the same for muons in the barrel and in the endcaps for muons below 2 TeV in p.

As described above, the charge misassignment probability is also measured for muons not coming from a physical process, but simulated at fixed p and flat in detector η and ϕ. These

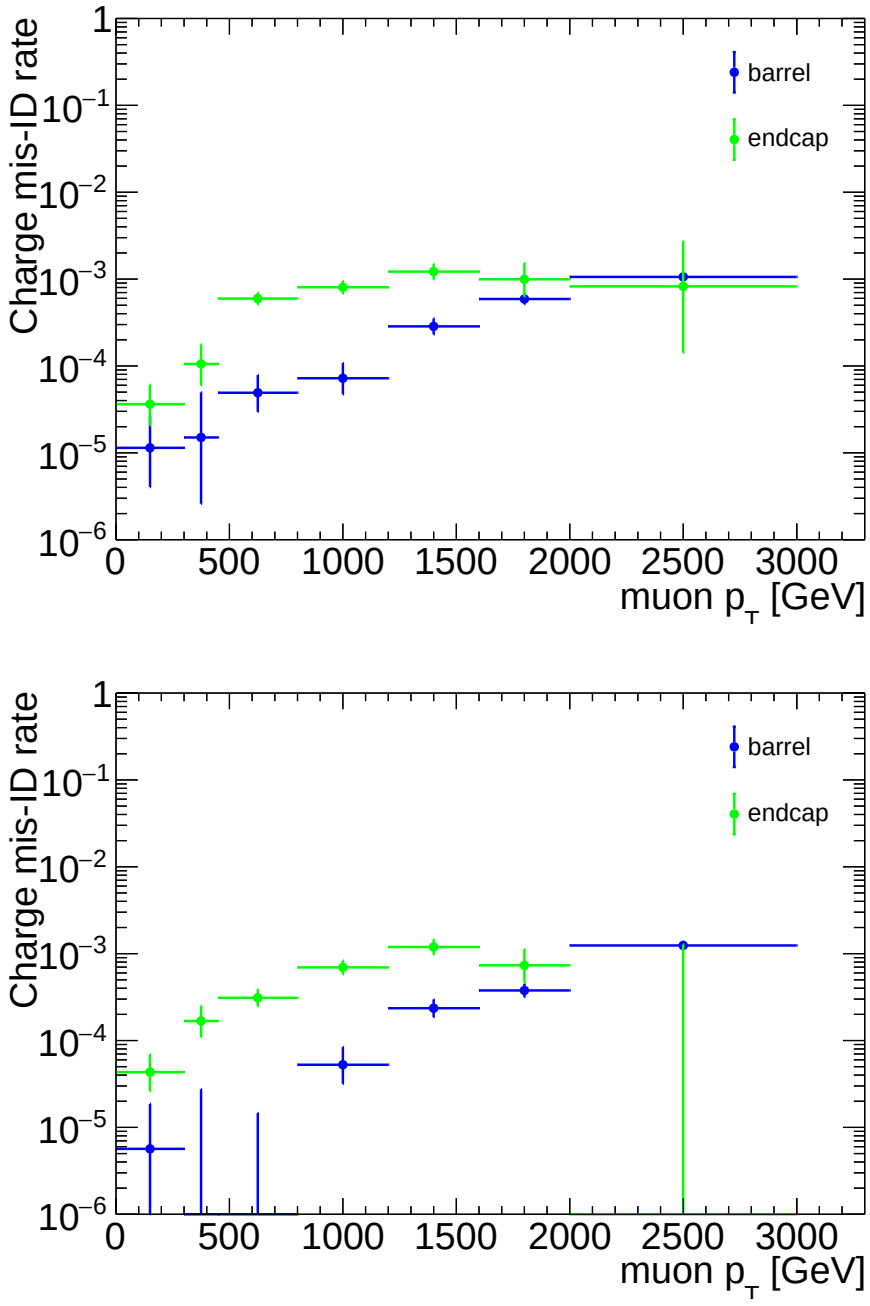

Figure 4.3: Probability (rate) of muon charge misassignment plotted vs. muon p_{T} in DY simulation for (left) 2016 and (right) 2017 data taking conditions, separated for barrel (blue), and endcap (green).

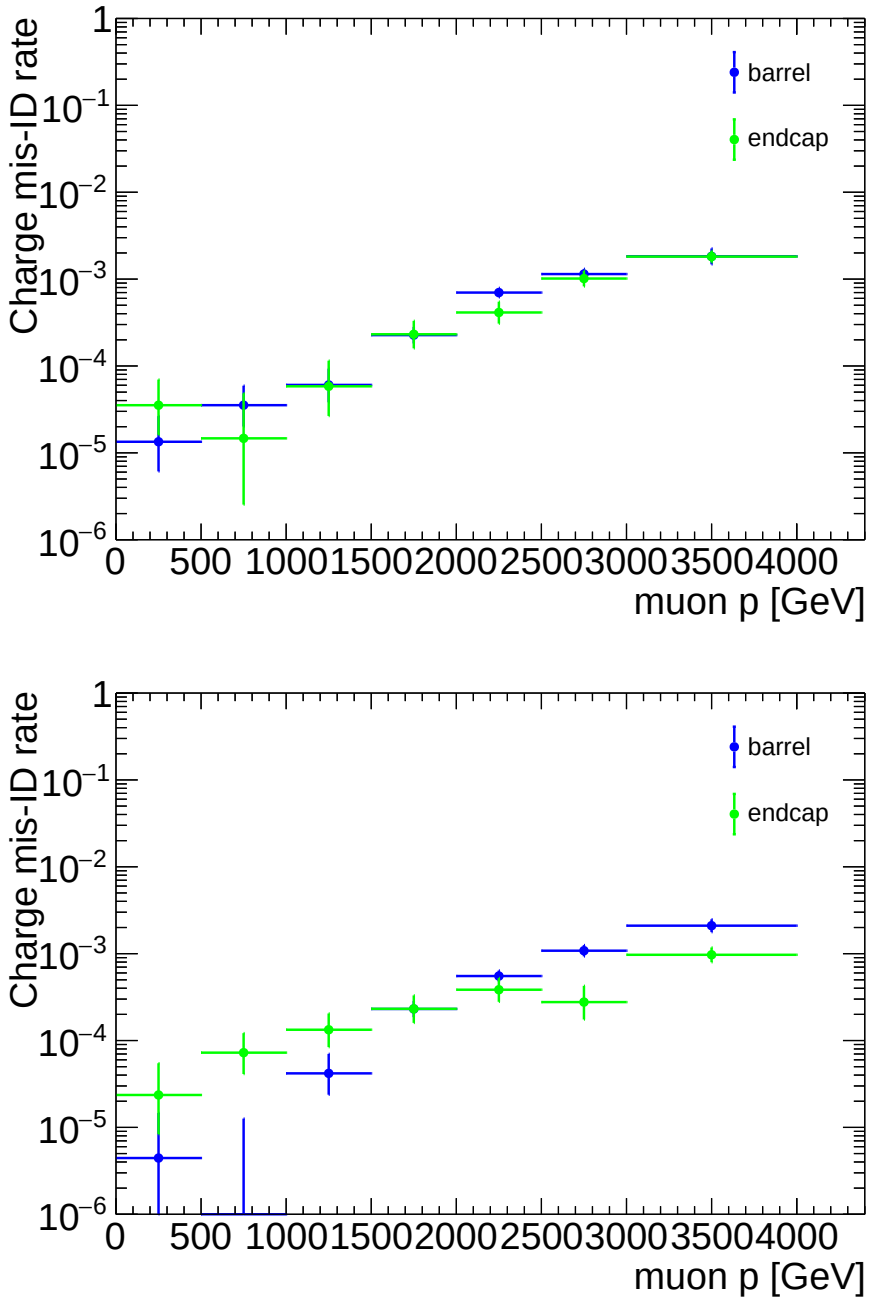

Figure 4.4: Probability (rate) of muon charge misassignment plotted vs. muon p in Drell-Yan MC in (left) 2016 and (right) 2017 data conditions, separated for barrel (blue), and endcap (green).

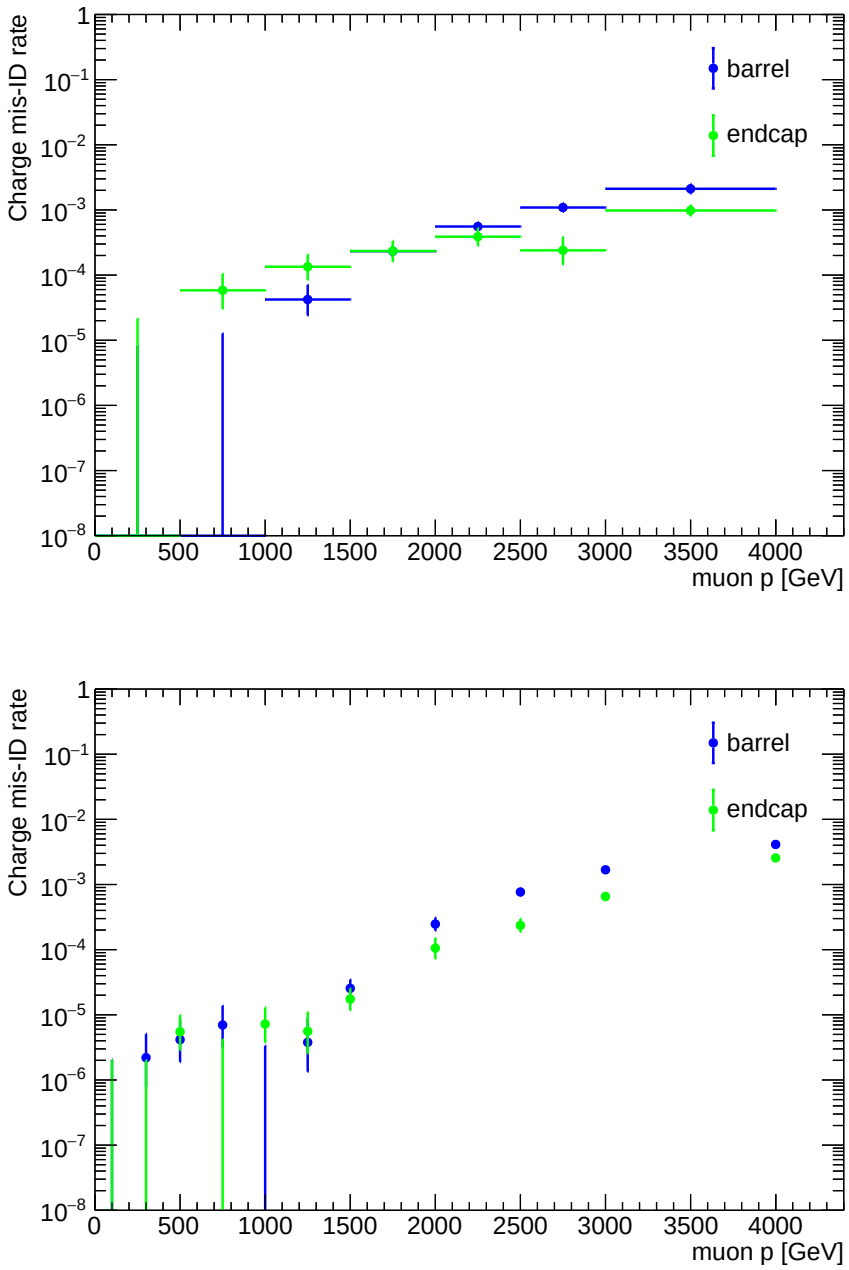

Figure 4.5: Probability (rate) of muon charge misassignment as a function of muon p in (left) Drell-Yan MC and (right) muon gun MC, both for 2017 conditions, separated for (blue) barrel, and (green) endcap.

simulations are referred to as a muon-gun. The muon-gun simulations have the advantage of being independent of any features arising from the specific physical process creating the muons. For this study, we generate muon-gun simulations at fixed values in muon p: 50, 100, 300, 500, 750, 1000, 1250, 1500, 2000, 2500, 3000, and 4000 GeV.

Figure 4.5 compares the charge misassignment obtained with (left) Drell-Yan MC and (right) muon gun MC, for similar detector reconstruction conditions. For muons above 1 TeV, the charge misassignment probabilities are similar. For muons below 1 TeV, the charge misassignment probabilities are smaller, typically less than 10^{-5} in both kinds of samples, and consistent within the MC statistical uncertainties. Figure 4.6 shows the charge misassignment probabilities for positive and negative muons separately. Within the statistical precision of the muon-gun simulations, the probabilities for positive and negative muons are similar.

The muon-gun simulations are also used to compare the charge misassignment probabilities under different detector alignment scenarios. Figure 4.7 compares the charge misassignment probability for (left) muons in the barrel and (right) muons in the endcaps, for two scenarios. The green points represent a detector alignment scenario referred to as "start-up". The start-up alignment is intended to be used at the beginning of the data taking year and therefore has large uncertainties in the detector alignment positions. The purple points represent a detector alignment scenario referred to as "asymptotic". The asymptotic alignment is representative of the end-of-year knowledge of the detector alignment after many calibration runs. The asymptotic alignment therefore has smaller uncertainties in detector alignment positions. The bottom panel in each plot in the figure is a ratio of the asymptotic and start-up detector alignment scenarios. Within the statistical precision of the muon-gun simulations, the detector alignment scenario does not have a significant effect on the charge misassignment probability.

The charge misassignment probability is also studied as a function of the specific TeV refit algorithm selected by TuneP using muons from the muon-gun simulations. Figure 4.8 shows for muons simulated at p = 300, 500, 750, 1000, and 1500 GeV (left) the fraction of of the number of times TuneP chooses each TeV refit and (right) the charge misassignment

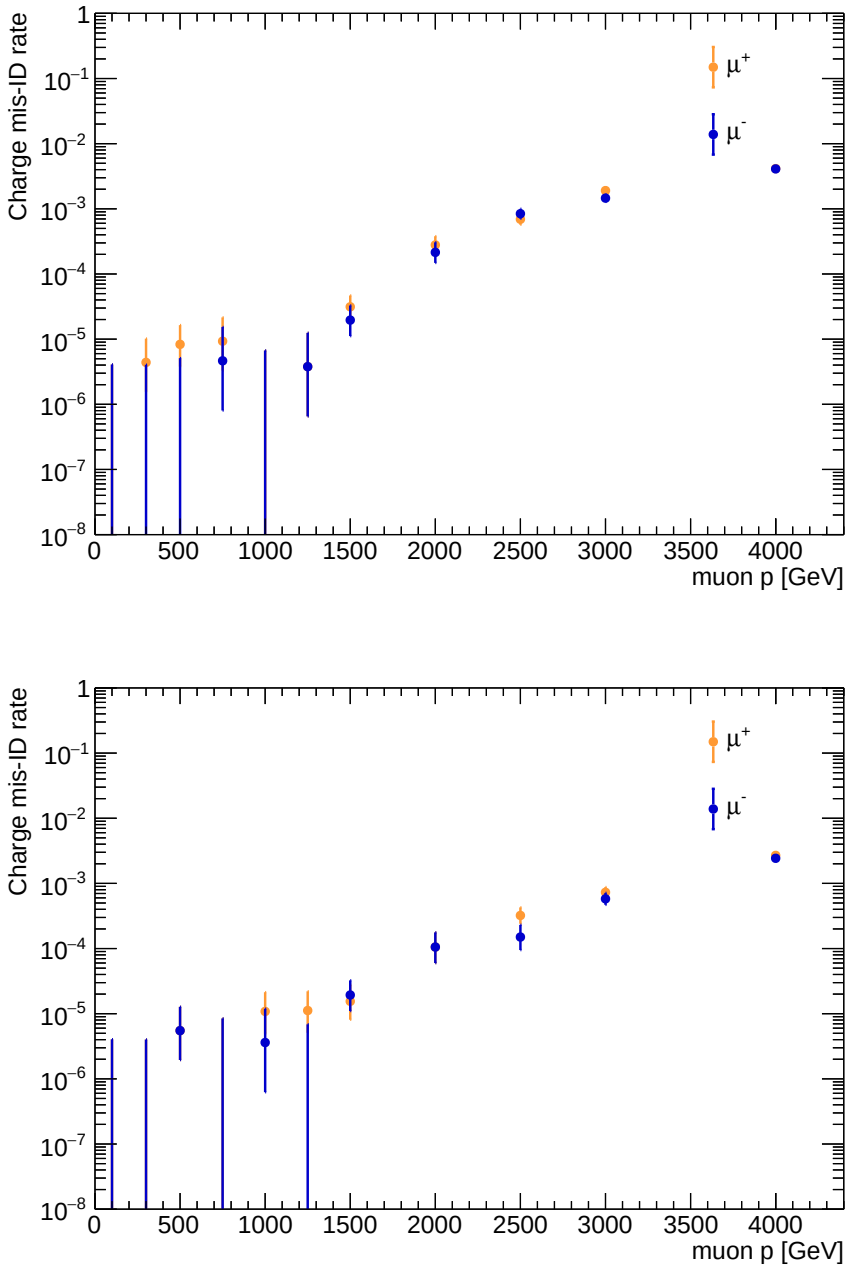

Figure 4.6: Probability (rate) of muon charge misassignment plotted vs. muon p for (left) muons in the barrel ($|\eta| < 1.2$) and (right) muons in the endcap ($|\eta| > 1.2$). Positive muons are plotted in orange and negative muons in blue.

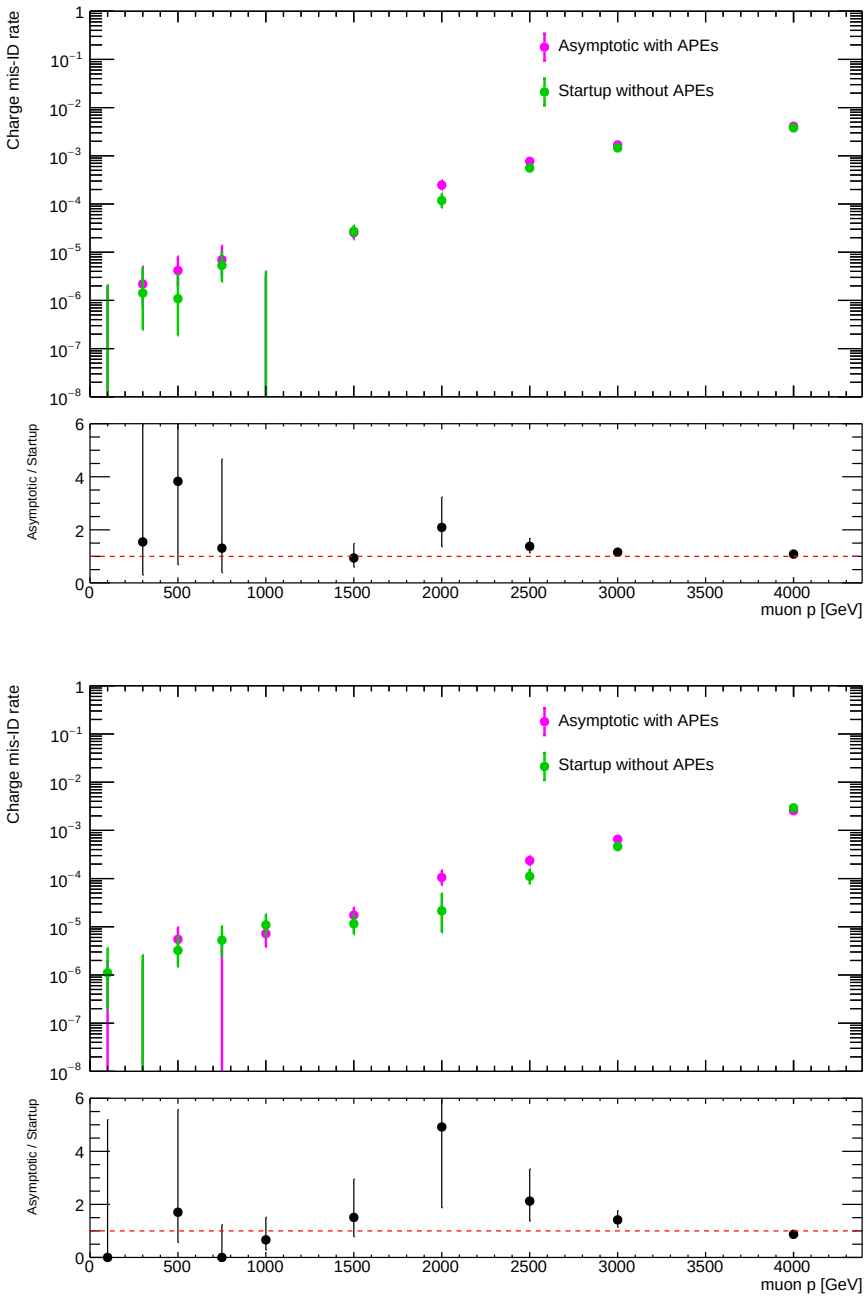

Figure 4.7: Probability (rate) of muon charge misassignment plotted vs. muon p for (top) muons in the barrel and (bottom) muons in the endcap. Muons simulated under asymptotic conditions and detector alignment positions are plotted in purple and muons simulated under startup conditions and detector alignment position errors set to zero are plotted in green.

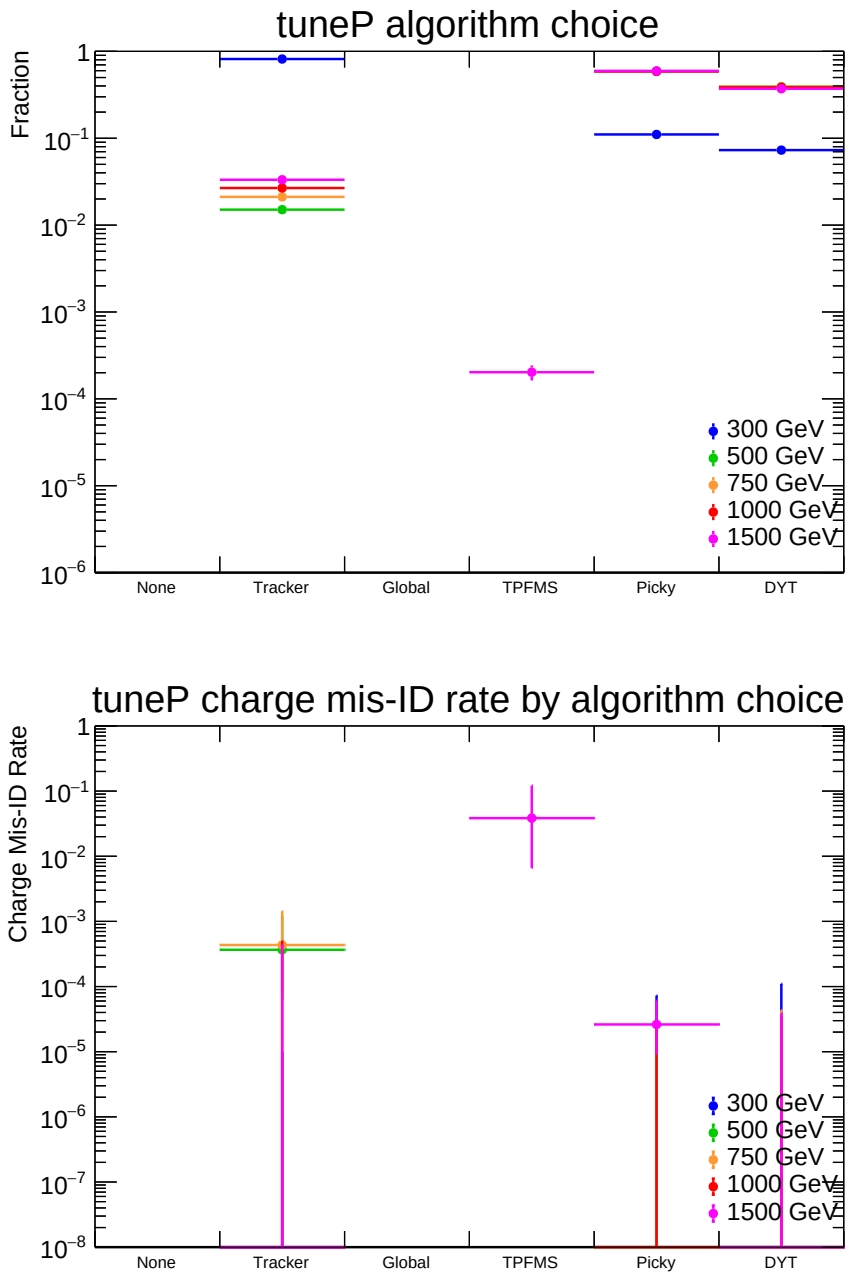

Figure 4.8: (Left) fraction of the number of times TuneP selects each TeV refit algorithm. (Right) Probability (rate) of muon charge misassignment for each selected TeV refit algorithm. Muons with p between 300 and 1500 GeV are considered.

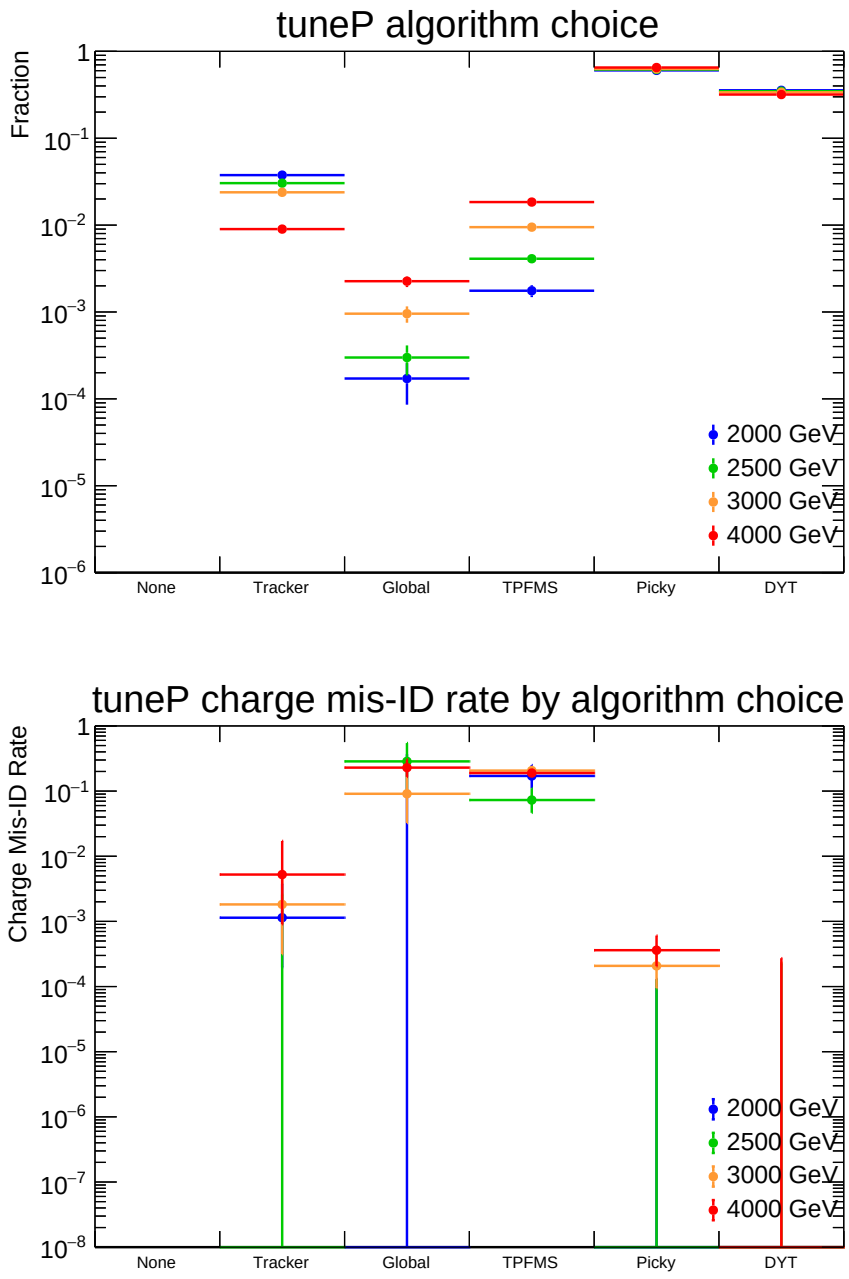

Figure 4.9: (Left) fraction of the number of times TuneP selects each TeV refit algorithm. (Right) Probability (rate) of muon charge misassignment for each selected TeV refit algorithm. Muons with p between 2000 and 4000 GeV are considered.

probability for when TuneP selects each TeV refit. For muons simulated at (blue points) $p = 300\,\text{GeV}$, TuneP selects the Tracker Track roughly 80% of the time, Picky 13% of the time, and DYT the remaining 7% of the time. Global and TPFMS tracks are a negligible contribution. The charge misassignment probability is negligible for tracks with 300 GeV.

As muon momentum increases, the fraction of the time that TuneP selects the Picky or DYT track refits increases to greater than 95%. The charge misassignment probability for these tracks remains negligible for muon p up to 1500 GeV. For tracker tracks, the charge misassignment probability increases to less than 0.01% at 1500 GeV. The TPFMS track has a charge misassignment probability of a few percent at 1500 GeV and is the leading contribution to the total TuneP charge misassignment, despite being selected by TuneP at the lowest rate.

Figure 4.9 shows the same information as in Fig. 4.8, but presents muon-gun simulations at higher muon momentum; p = 2000, 2500, 3000, and 4000 GeV. As muon momentum increases from 2000 GeV to 4000 GeV, the fraction of times that TuneP selects one of the dedicated TeV refit tracks, Picky or DYT, is roughly constant at 95%. The charge misassignment fraction also remains negligible for the Picky and DYT tracks above 2000 GeV. For the remaining 5% of the time, TuneP is split between the Tracker, TPFMS, and Global tracks. For the Tracker track, the fraction of times it is selected by TuneP decreases from approximately 4% at 2 TeV to 1% at 4 TeV while the charge misassignment fraction is between is less than 1%. For the TPFMS track and the Global tracks the charge misassignment fraction is non-negligible and is the dominant source of TuneP tracks with an incorrect charge. For these tracks, the charge misassignment probability is measured to be between 10–20%. However these two tracks are selected by TuneP at the lowest fractions. For the TPFMS track the fraction of times it is selected by TuneP increases from 0.1% for 2 TeV muons and increases to approximately 2% at 4 TeV and for the Global track, the fraction increases over the same range from 0.01% to 0.1%.

To summarize: for muons below 2 TeV, the TuneP charge misassignment probability is negligible. For muons at or above 2 TeV, the charge misassignment probability for all TuneP

tracks primarily comes from TPFMS and Global tracks despite being selected by TuneP at the lowest probability.

CHAPTER 5

A search for high-mass dimuon resonances with CMS

5.1 Introduction

This chapter describes a general search for physics beyond the standard model (BSM) using the dimuon invariant mass spectra obtained from $\sqrt{s} = 13\,\text{TeV}$ proton-proton (pp) collision data collected by the CMS detector at the CERN LHC. As discussed in Chapter 2, many BSM theories predict additional $U'(1)$ gauge groups that, if spontaneously broken near the TeV scale, produce new neutrally charged, spin-1 gauge bosons that can be detectable in LHC collisions. If a new gauge boson, referred to as a Z' boson in all that follows, couples to muons then it may be possible to find it by searching for a narrow resonance in the dimuon invariant mass spectrum. Examples of specific benchmark models that predict a Z' include: Left-Right symmetric models [25], E6 gauge group GUT models [10, 11], and the trivial sequential-standard model [26]. Models that predict spin-2 resonances, such as those predicting gravitons and large extra dimensions [27, 28], can also be interpreted using these results. These results are designed to be model-independent and can be interpreted with any new-physics model that predicts a neutral spin-1 or spin-2 narrow resonance.

Previous searches for a new Z' resonance in the dimuon invariant mass spectrum at the LHC have been performed by the CMS and ATLAS collaborations with data collected at $\sqrt{s} = 7\,\text{TeV}$ [29, 30, 31], at 8 TeV [32, 33, 34], and at 13 TeV [35, 36, 37, 38]. These searches did not find signs of BSM physics and lower mass limits were set for resonances in various BSM models. Reference [39] presents the ATLAS result using a similar data set to the data set we present here and set lower mass limits on a Z'_{SSM} and Z'_{ψ} decaying to dimuons at 4.5 and 4.0 TeV respectively. This chapter presents the results of the analysis of $61.3\,\text{fb}^{-1}$

of data collected by the CMS detector in 2018 [40]. The methods we describe here are also used in the analysis of the 2017 data, which we do not explicitly show here. However, we do present the results of the combination of the full CMS Run 2 data set (2016, 2017, and 2018), which totals $139.7\,\text{fb}^{-1}$. These results are described in CMS Physics Analysis Summary EXO-19-019 [41].

The basic method that we use is to search for a narrow resonant peak in the dimuon mass spectrum on top of a smoothly falling background continuum. We use events selected based on criteria that ensures that the dimuons we consider are well measured. The results of the analysis are presented in terms of the ratio of the measured cross section times branching fraction into dimuons of the Z' boson to that of the Z boson. The ratio is thus defined as:

$$R_\sigma = \frac{\sigma(pp \to Z' + X \to \mu^+\mu^- + X)}{\sigma(pp \to Z + X \to \mu^+\mu^- + X)}, \tag{5.1}$$

where σ in the numerator and denominator of this equation represents the inclusive production cross sections of Z' and Z bosons from pp collisions and decay to opposite-sign dimuon pairs. We choose to use the cross section ratio as the primary result as it reduces many experimental and theoretical uncertainties common to both the Z-peak and high-mass dimuon regimes. Specifically, the ratio reduces known uncertainties such as the uncertainty based on the calculation of the integrated luminosity; the experimental acceptance; and trigger and offline reconstruction efficiencies, in addition to any unknown systematic effects. We are left to consider only the uncertainties that depend on invariant mass. Inputs to the cross section calculations, such as the reconstruction efficiency and experimental acceptance, are calculated separately for events at the Z-peak, defined here as the invariant masses between 60 and 120 GeV, and at high mass, defined as $m_{\mu^+\mu^-} > 120\,\text{GeV}$.

As described in Chapter 4, muon momentum resolution, momentum scale, and reconstruction efficiency vary as a function of the muon pseudorapidity. These differences due to muon pseudorapidity propagate to the calculation of dimuon quantities such as the invariant mass. We therefore perform the analysis separately in two pseudorapidity categories to better characterize the data. The categories are events with two muons in the CMS barrel region and events with at least one muon in a CMS endcap. In all that follows below, the

barrel-barrel pseudorapidity analysis category is referred to as BB and the barrel-endcap and endcap-endcap pseudorapidity category is referred to as BE+EE. (We use this nomenclature for the BE+EE category to make it clear that while one muon is required to be in the endcap, the other can be in either of the barrel or endcap region.) We use the $|\eta| = 1.2$ boundary between the CMS barrel muon detectors and endcap muon detectors to separate our analysis categories. Each input for the calculation of the cross section ratio is studied for the two analysis categories separately and later combined during the statistical computation. We also present merged histograms and for the inclusive pseudorapidity category.

In Section 5.2, we discuss the data set used in the analysis. The triggers that we use to collect data and the event selections that we use to obtain the set of dimuons for the search are described in Section 5.3. In Section 5.4, we describe our methods for estimating the SM backgrounds. Then, in Section 5.5, we show comparisons of data and SM simulation prediction. We describe the highest-mass events in Section 5.6. In Section 5.7, we describe the procedure to compute the relevant quantities for the Z peak normalization. In Section 5.8, we define the signal and background models, the likelihood function, and the parameter of interest. We also discuss the methods to calculate the results. In Section 5.9, we present the results of the search. Investigations of $Z'/Z/\gamma^* \to \mu^+\mu^-$ interference to complement the resonant search are presented in Section 5.10. We conclude in Section 5.11.

5.2 CMS data sets considered and data certification

In this search, we use a data set of pp collisions at a center-of-mass energy of 13 TeV collected by the CMS detector during the 2018 LHC running. As mentioned in Chapter 3, the collected event data are first processed in real-time by hardware-based triggers and are later fully reconstructed for analysis use by CMS offline software. This analysis uses data that has been reprocessed using the best available detector alignment, alignment uncertainties, and calibrations to reconstruct physics objects for the 2018 data-taking year.

The data used are studied and certified according to the CMS Data Quality Management

CMS Data Set Name	CMS Run Range
/SingleMuon/Run2018A-17Sep2018-v2/MINIAOD	315252–316995
/SingleMuon/Run2018B-17Sep2018-v1/MINIAOD	317080–319310
/SingleMuon/Run2018C-17Sep2018-v1/MINIAOD	319337–320065
/SingleMuon/Run2018D-22Jan2019-v2/MINIAOD	320673–325175

Table 5.1: CMS data sets used in this analysis and their corresponding run number ranges.

(DQM) group. The DQM group receives information from each corresponding subdetector group about whether that subdetector was fully operational and about the quality of the data collected for each individual data-taking period. For example, data can be certified as bad if a subdetector is turned off or if the data-taking conditions are problematic. In addition to detector-level information, the reconstruction quality of the offline physics objects are also monitored and used to certify data as good. This analysis uses a set of data-taking periods that are optimized for muon physics. That is, only the CMS subdetectors, conditions, and reconstruction quality necessary to reconstruct muon candidates are considered when declaring data good or bad to use. The integrated luminosity of the data declared good for muon physics in 2018 was $61.3\,\text{fb}^{-1}$ with an uncertainty of 2.5% [40]. For the entirety of Run 2 the integrated luminosity of the muon physics data is $139.7\,\text{fb}^{-1}$, with $36.3\,\text{fb}^{-1}$ collected in 2016 with an uncertainty of 2.5% [42] and $42.1\,\text{fb}^{-1}$ collected in 2017 with an uncertainty of 2.3% [43].

We consider the set of events that were triggered by a single muon trigger. (For computational purposes in addition to other considerations, CMS splits the full data set into smaller data sets according to the primary triggers that collected the data.) These data sets are reported in Table 5.1 along with their specific CMS run number ranges. Each entry in the table represents a specific data-taking "era" where the data collected were collected and processed under similar conditions.

5.3 Trigger and event selection

5.3.1 Trigger

We require that events be selected by at least one of three different High Level Trigger (HLT) paths, all of which trigger events based on muon p_{T}. The main trigger path that we use is the lowest p_{T} unprescaled path, which has a p_{T} threshold of 50 GeV. The CMS Muon Physics Object group measures the efficiency of these triggers in data and simulation using a sample of dimuon decays from Z candidates.

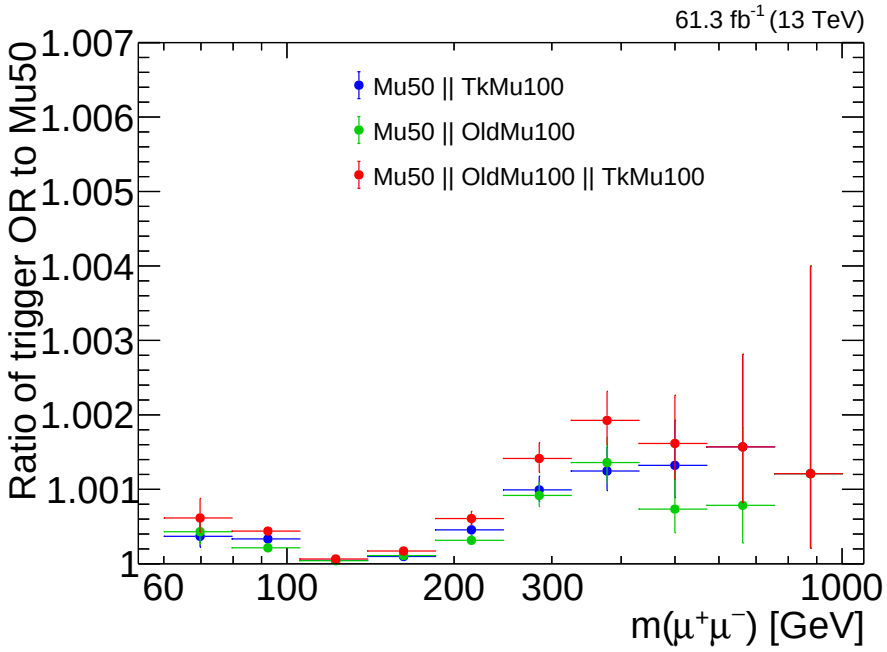

Figure 5.1: Ratio of the number of dimuon events that pass the primary trigger or any of the backup triggers to the number of dimuon events that pass only the primary trigger. The technical name of the main analysis trigger is Mu50 and names of the two backup triggers are OldMu100 and TkMu100. The legend describes the logic of the numerator of each point. The red points are the relative gain in number of events due to using all three triggers. The green and blue points are the relative gain due to adding only one of the backup triggers.

In 2018, the CMS HLT group responsible for developing, commissioning, and maintaining muon triggers updated the algorithm to identify muon tracks. Among the improvements

made was an additional requirement on the track fit χ^2 of the HLT muon track candidates. For muons at high p_{T}, this becomes problematic, as these muons can have a systematically large track fit χ^2 because of high-energy muon interactions with the detector material, which can corrupt hits used in the muon candidate track fit due to the subsequent electromagnetic showers. Therefore, we also consider events triggered by two additional backup triggers that do not have the aforementioned track fit χ^2 requirement. One trigger uses the algorithm previously used during the 2016 and 2017 data-taking periods and has a p_{T} threshold of 100 GeV; the other trigger uses only tracks reconstructed with the inner tracker and has a p_{T} threshold 100 GeV. The gain in efficiency as measured in DY simulation with these two back-up triggers on dimuon events—where we have two chances to trigger the event—was found to be less than 1% for both the BB and BE+EE categories. By including these backup triggers, we recover 192 events with $m_{\mu^+\mu^-} > 120\,\mathrm{GeV}$ in the data; with the highest mass event recovered at a mass of 810 GeV. Figure 5.1 shows the ratio of the number events that we recover with various combinations backup and main analysis triggers to the number of events that pass only the main analysis trigger. The red points are the relative gain in the number of events as a function of dimuon mass by using all three triggers. We gain an additional 0.4% of events in data after summing the additional events over the entire mass spectrum.

5.3.2 Event selection

To obtain a collection of events with clean and well-measured dimuon candidates, we select events that satisfy the following criteria:

The primary vertex (PV) is required to have at least four associated tracks reconstructed in the tracker and to be located within the nominal pp interaction region in CMS, $|r| < 2\,\mathrm{cm}$ and $|z| < 24\,\mathrm{cm}$. These selections on the PV reject events triggered by cosmic muons in empty LHC bunch-crossings and also rejects events triggered by accelerator induced muons traveling parallel to the beamline.

Muons at high energy ($> 200\,\mathrm{GeV}$) are reconstructed using the dedicated TeV-refit al-

gorithms described Chapter 4.3 to account for radiative effects due to interactions with the detector material [20].

Muon candidates are considered with the following criteria:

- The muon has $p_{\mathrm{T}} > 53\,\mathrm{GeV}$,
  - This p_{T} threshold is chosen to be above the minimum HLT threshold used, 50 GeV.
- The muon has $|\eta| < 2.4$.
  - This ensures that the muon is within the detector acceptance.

We refer to the combination of muon p_{T} and muon η selections as the acceptance.

The muon candidate track fits must pass the following selections optimized for high efficiency at high p_{T}:

- The muon must be identified as a "Tracker muon" as described in Chapter 4.3.
- The muon must be identified as a "Global muon" as described in Chapter 4.3.
- The tracker track must have at least 5 tracker layers used for measurement
  - A minimum number of measurements from the inner tracker helps to ensure a good p_{T} measurement as well as suppresses muons from decays in flight.
- The tracker track must have least 1 valid hit from the pixel detector.
  - A valid hit from the pixel detector suppresses muons from decays in flight.
- The TuneP or the Global tracks must have at least 1 valid hit from the muon system used in the track fit.
  - A valid hit from the muon system suppresses hadronic punch-through and muons from decays in flight.

- The impact parameter of the tracker track with respect to the PV must be less than 0.2 cm, $|d_{XY}| < 0.2\,\text{cm}$.
  - Tracks that are required to be close to the PV suppress contributions from cosmic ray muons, muons from decays in flight, and tracks from additional interactions in the event.
- The longitudinal distance of the tracker track with respect to the PV must be less than 0.5 cm, $|d_z| < 0.5\,\text{cm}$.
  - Tracks that are required to be close to the PV suppress contributions from cosmic ray muons, muons from decays in flight, and tracks from additional interactions in the event.
- The tracker track must be matched to at least two muon stations.
  - Two matched stations in the track fit suppresses muons from hadronic punch through and accidental track-to-segment matches. Additional care for muon tracks with only one matched station accounts is considered for cases when muon passes through a gap in the detector. To recover inefficiencies caused by these gaps between detector subsystems we impose a looser criterion if the track candidate does not have at least two matched muon stations. If the tracker track has only one matched station, then at least one of the following must also be satisfied: the tracker track must be matched to a station that is not the first station, matched to at last two RPC layers, or has less than two expected matched stations based on the extrapolation of the tracker track.
- The relative track fit p_{T} uncertainty $\sigma_{p_{\text{T}}}/p_{\text{T}}$ must be less than 30%
  - This selection rejects grossly mismeasured tracks by requiring that the uncertainty $\sigma_{p_{\text{T}}}$ from the internal fit of the muon track candidate does not exceed a fraction of the muon's p_{T}. For muons at high p_{T}, this selection is potentially dangerous as the uncertainty from the track fit grows roughly linearly as a function of muon energy

due to hit position resolution. However, in this analysis, we do not encounter muons with enough energy for this selection to be problematic. Nonetheless, this selection criteria is always checked for these reasons. See the discussion about Fig. 4.2 in Section 4.5 for further details.

- The scalar sum of p_{T} over all tracker tracks—excluding the muon tracker track itself—within a cone of $\Delta R = \sqrt{(\Delta\eta)^2 + (\Delta\phi)^2} = 0.3$ around the muon tracker track must be less than 10% of the muon Tracker track p_{T}.

  – Isolation suppresses muons originating from jets and heavy flavor decays. Track candidates used in the isolation sum in the numerator must have a longitudinal distance less than 0.2 cm with respect to the PV associated to the muon track, $|d_z| < 0.2\,\mathrm{cm}$.

No additional selection is made on the χ^2 of any of the muon track fits. As mentioned above, muons with very high energy have a larger probability to leave an electromagnetic shower in a muon detector, which can degrade the fit quality as a result. For a similar reason, no CMS calorimetry information is used in identifying high-p_{T} muons either, as muon showering due to bremsstrahlung can leave electromagnetic deposits in CMS calorimeters in the region adjacent to the muon track. This can then bias isolation quantities and cause high energy muons to self-veto.

We construct dimuon candidates and compute the kinematics of the dimuon system by performing a fit to a common vertex of the muon track candidates. This common vertex fit functions as a check that the two muons originate from the same primary vertex and as a guard against misassociating tracks from multiple pp interactions in an event. We then impose an additional set of selections on dimuon candidates:

- The muon pairs must have opposite sign.

  – For a muon with $p_{\mathrm{T}} = 1\,\mathrm{TeV}$ the charge misassignment rate is known to be roughly 5×10^{-5} in the barrel region and 8×10^{-4} in the endcap region. See above in Section 4.5 for more discussion on the charge misassignment probability.

- At least one muon is matched to a HLT candidate that passed at least one of our set of triggers within a cone of $\Delta R = 0.2$.

- The dimuon common vertex fit χ^2 divided by the number of degrees of freedom (dof) must be less than 20.

  - This selection ensures that the muon pair originates from the same PV and not from separate primary interactions in the event.

- The three-dimensional angle between the two muons' momenta must be less than $\pi - 0.02$ rad.

  - This selection suppresses high-energy cosmic muons that traverse the detector through the interaction region and are therefore nearly back-to-back.

If multiple dimuon candidates pass the entire selection in an event, then the pair with an invariant mass within 20 GeV of the Z-boson is selected. Otherwise, if no dimuon candidates are within this window, then the dimuon with the highest p_{T} sum is selected. In the 2016 iteration of the analysis, the pair with the highest p_{T} sum is selected. This new method has the advantage of reducing background with a Z candidate, such as those arising from the WZ and ZZ processes.

5.4 Background estimation

The primary background to the search for Z' resonances is Drell-Yan (DY) decay to dimuons, $pp \to Z/\gamma^* \to \mu^+\mu^-$. Dimuons from DY at invariant masses above the Z boson resonance are a steeply, but smoothly falling distribution. These dimuons are an irreducible background to dimuons from a Z' decay; that is, their detector signatures are identical.

The next largest background contribution of prompt muons comes from $t\bar{t}$ production. The $t\bar{t}$ contribution is also a non-resonant and smoothly falling as dimuon mass increases. Other sources of prompt dimuons listed in order of their relative contribution at high masses

are: diboson production WW, WZ, and ZZ; single-top tW^- and $\bar{t}W^+$ production; and Drell-Yan decay to tau pairs that then decay to muons. Among these, the DY, WZ, and ZZ backgrounds provide contributions to both the high-mass continuum and the Z resonance, as all of these processes can contain an on-shell Z.

Sources of dimuon pairs not associated with vector boson decay or with muons not coming from a primary vertex are the so-called non-prompt backgrounds or jet backgrounds, which we refer to as the jet background in all that follows. The jet background include muons from prompt heavy flavor decay (predominantly b-jet decay), hadrons reaching the inner CMS muons stations that are misidentified as muons, and hadronic decay-in-flight to muons. The dominant sources of these types of muons are processes associated with jet activity from QCD multi-jet processes and W +jets. The jet background source of dimuon production is a negligible contribution at high-mass but contributes to the background composition at low dimuon mass and at the Z resonance.

In this analysis, we use the SM background simulation for two purposes. The first is to determine the background shape to be used in the statistical analysis. For this purpose, the absolute prediction from simulation is unnecessary as the normalization is determined locally in the fit to the data at each test mass during the statistical procedure. The second purpose is to compare data to simulation. For this purpose, both the shape of the background and the absolute prediction are necessary. In the discussion that follows in this section, we describe how we determine both the shape and the absolute normalization for each simulated SM background process.

The DY, $t\bar{t}$, and single-top backgrounds are simulated with the POWHEG next-to-leading order (NLO) event generator [44] with parton showering and hadronization performed by the PYTHIA 8.2 program [45]. We use separate simulations for each decay mode of the WW, WZ, and ZZ background processes, which are generated with either the POWHEG generator mentioned above or the MADGRAPH NLO event generator [46]. All simulations considered are generated with the NNPDF3.1 next-to-next-to-leading order (NNLO) parton distribution functions (PDFs) [47] and the CP5 underlying-event (UE) tune [48]. Table 5.2 summarizes

the SM background simulations used. The first column gives the physical process and specific decay channel generated and the second column gives the Monte Carlo (MC) generator. The detector response is simulated with the GEANT4 [49] package. For the jet background, we do not use simulation. Instead we estimate the jet background with a data driven technique described below.

For the $t\bar{t}$ and WW simulations, we use the simulations generated and reconstructed for the 2017 data-taking year as 2018 versions were not ready in time for this document. We expect the behavior of reconstruction for 2017 and 2018 simulations to be similar for these two background processes as important conditions, such as detector alignment, were sufficiently similar and have a negligible effect on these backgrounds.

Process	Generator (order)
$Z/\gamma^* \to \mu^+\mu^-$	POWHEG (NLO)
$t\bar{t} \to bb\ell\ell\nu\nu$	POWHEG (NLO)
$WW \to \ell\ell\nu\nu$	POWHEG (NLO)
$WZ \to \ell\ell\ell\nu$	POWHEG (NLO)
$WZ \to llqq$	MADGRAPH (NLO)
$ZZ \to \ell\ell\ell\ell$	POWHEG (NLO)
$ZZ \to \ell\ell\nu\nu$	POWHEG (NLO)
$ZZ \to \ell\ell qq$	MADGRAPH (NLO)
tW^-	POWHEG (NLO)
$\bar{t}W^+$	POWHEG (NLO)
$Z/\gamma^* \to \tau^+\tau^-$	MADGRAPH (NLO)

Table 5.2: Summary of simulated background samples used in this analysis. The first column gives the physics process and specific decay channel generated and the second column gives the MC generator used.

An additional source of background dimuons are events that come from cosmic muons that traverse the detector near the interaction point. If these cosmic muons are also co-

incident with a collision, then the event can be triggered and then reconstructed as an opposite-sign dimuon. Dimuons from these events tend to be back-to-back in space. After we apply the selection on the three-dimensional angle described in Section 5.3, the cosmic muon background becomes negligible.

5.4.1 Drell-Yan background

5.4.1.1 Parton distribution functions considerations

As mentioned above, the DY simulation used for the analysis of 2018 (and also 2017) data was generated with the NNPDF3.1 NNLO PDF set and the CP5 UE tune. In the process of comparing the DY simulation to data collected in 2017 and 2018, we discovered numerous issues that were not present in the previous analysis of 2016 data and 2016 simulation. For the analysis of 2016 data, the DY simulation was generated with the NNPDF3.0 NLO PDF set [50] and the CUETP8M1 UE tune [51]. The CUETP8M1 tune is also referred to as the "Monash" tune. For brevity in the text that follows, we refer to the combination of the NNPDF3.1 NNLO PDF set and CP5 tune as "3.1-CP5" and the combination of NNPDF3.0 NLO PDF set and CUETP8M1 tune as "3.0-Monash". We have performed investigations into the 3.1-CP5 simulations for both high-mass ($m_{\mu^+\mu^-} > 120\,\text{GeV}$) and at the Z-peak (60–120 GeV) to both understand the issues related to 3.1-CP5 and also characterize the differences between 3.0-Monash and 3.1-CP5.

At high-mass we found that:

- The DY cross section predictions eventually become negative at extremely high masses ($m_{\mu^+\mu^-} > 6\,\text{TeV}$);
- The parton luminosity uncertainty becomes greater than 200% at 5 TeV;
- The Z-rapidity distribution for high-mass events has an unphysical drop near dimuon rapidity $y = 0$.

From the above list, Fig. 5.2 shows that for generated dimuons with mass greater than

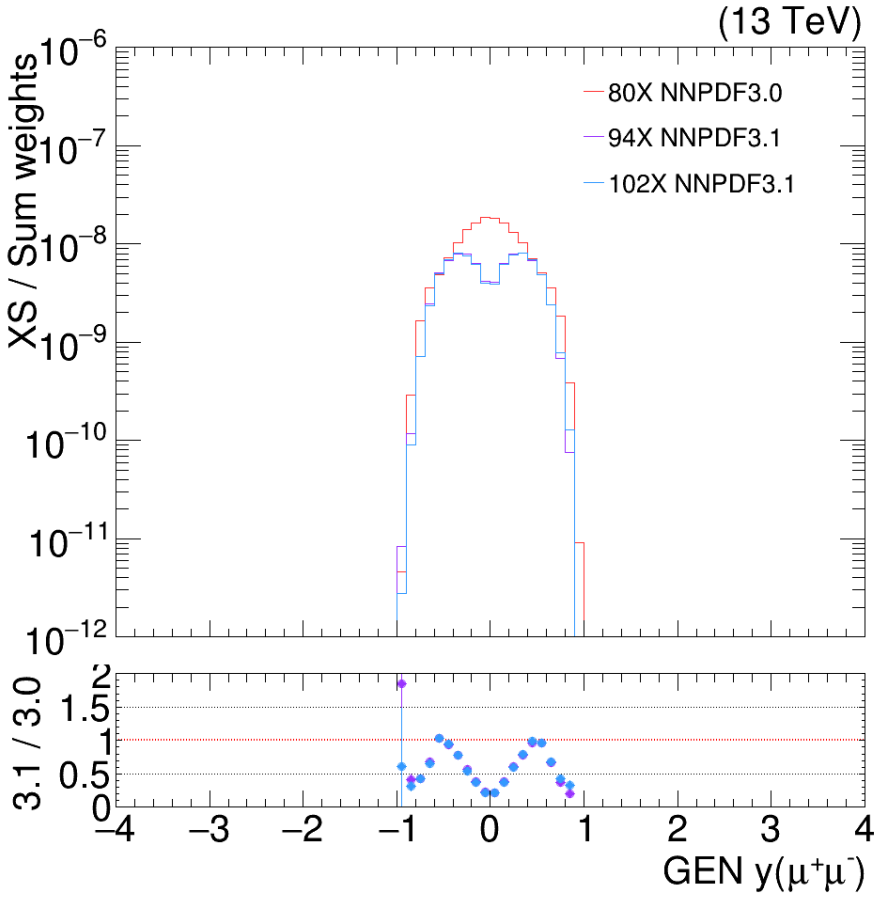

Figure 5.2: Histogram comparing the generated dimuon rapidity distributions for (red) 2016 3.0-Monash simulation, (purple) 2017 3.1-CP5 simulation, and (blue) 2018 3.1-CP5 simulation. The lower panel in the plot displays the ratio of the 3.1-CP5 simulations to the 3.0-Monash simulation.

5 TeV, fewer are generated with a rapidity near zero. This occurs because at high-mass, the DY process is dominated by the γ^* intermediate state, where u–$\overline{u}$ annihilation becomes the dominant production process. 3.1-CP5 predicts a drop in the $x\overline{u}(x, Q)$ structure function at high Bjorken x values, which reduces the available phase space for dimuons with rapidity close to zero to be produced at masses above 5 TeV.

Investigations into 3.1-CP5 at the Z-peak normalization region ($60 < m_{\mu^+\mu^-} < 120$ GeV) also showed issues:

- 3.1-CP5 predicts a 10% higher yield of Z-peak events for the same acceptance.
- 3.1-CP5 predicts an excess of events at low dimuon p_{T}.

Figure 5.3 compares the (left) acceptance and (right) yield of dimuons within acceptance in the DY simulations described. The acceptance is defined as both muons within $|\eta| < 2.4$ and generator-level muon $p_{\mathrm{T}} > 30\,\mathrm{GeV}$. The 3.1-CP5 simulation predicts an approximately 10% higher yield, despite both the 3.0-Monash and 3.1-CP5 showing similar acceptance fractions.

For the above features discovered in the simulation, it is currently unknown which are specifically caused by the NNPDF3.1 NNLO PDF set or by the CP5 UE tune relative to the 3.0-Monash baseline. Thus, for these reasons, we have decided to re-weight the high mass ($m_{\mu^+\mu^-} > 120\,\mathrm{GeV}$) 3.1-CP5 DY simulation to the distributions found in the 3.0-Monash DY simulation by applying a dimuon mass-dependent ratio of 3.0-Monash to 3.1-CP5. For the Z-peak, we have decided to re-weight these events according to the ratio of the leading generated muon p_{T} in 3.0-Monash to 3.1-CP5. Although it seems natural to choose to re-weight the Z-peak simulation by a Z-boson quantity, such as the Z-p_{T}, we chose to re-weight by leading generated muon p_{T} as it achieves the same result and does not introduce any additional acceptance corrections. For high and low mass, we calculate the re-weighting ratios separately for each analysis pseudorapidity category.

Figure 5.4 shows the ratio of 3.0-Monash to 3.1-CP5 for both 2017 and 2018 3.1-CP5 DY simulation in each analysis pseudorapidity category. For dimuon masses less than 1 TeV, the ratio is less than one, but for masses greater than 1 TeV the ratio is greater than one. As mass increases further, the ratio at 6 TeV is greater than 2. These ratios are parametrized with a 5th order polynomial, which are shown in the figure with a solid curve.

Figure 5.5 shows histograms comparing the leading muon reconstructed p_{T} spectrum for Z-peak data for 3.0-Monash and 3.1-CP5 and are compared with the 2018 Z-peak data. We correct the simulation predictions at the Z-peak by applying a re-weighting to the 3.1-CP5 DY simulation directly from histograms we obtain of the ratios of 3.0-Monash to 3.1-CP5.

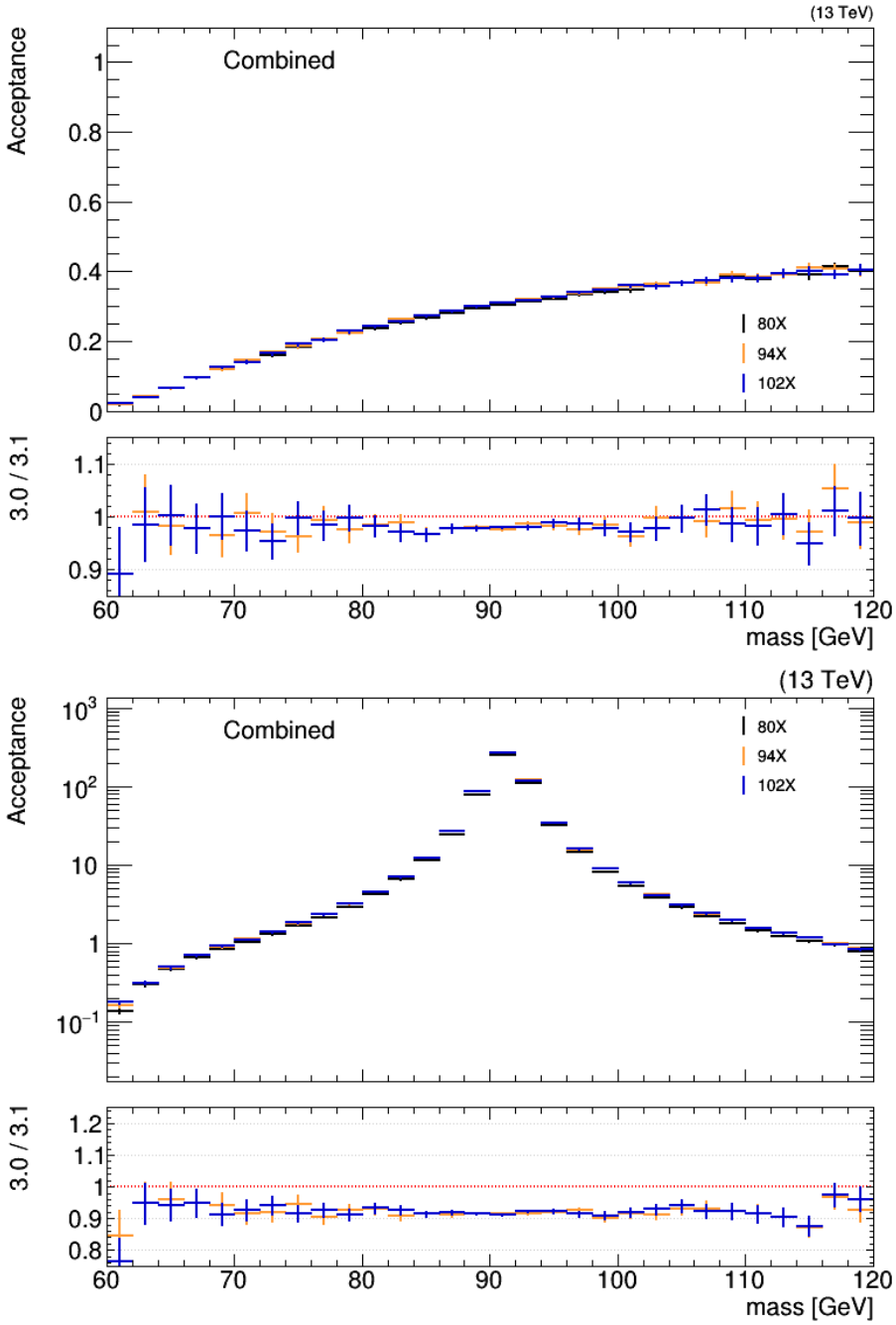

Figure 5.3: Comparison of normalization region DY simulation (top) acceptance fraction and (right) total event yield within acceptance as a function of dimuon invariant mass for the (black) 2016 3.0-Monash DY, (orange) 2017 3.1-CP5 DY, and (blue) 2018 3.1-CP5 DY. The 2016, 2017, and 2018 DY simulations are denoted 80X, 94X, and 102X respectively in the plot legends.

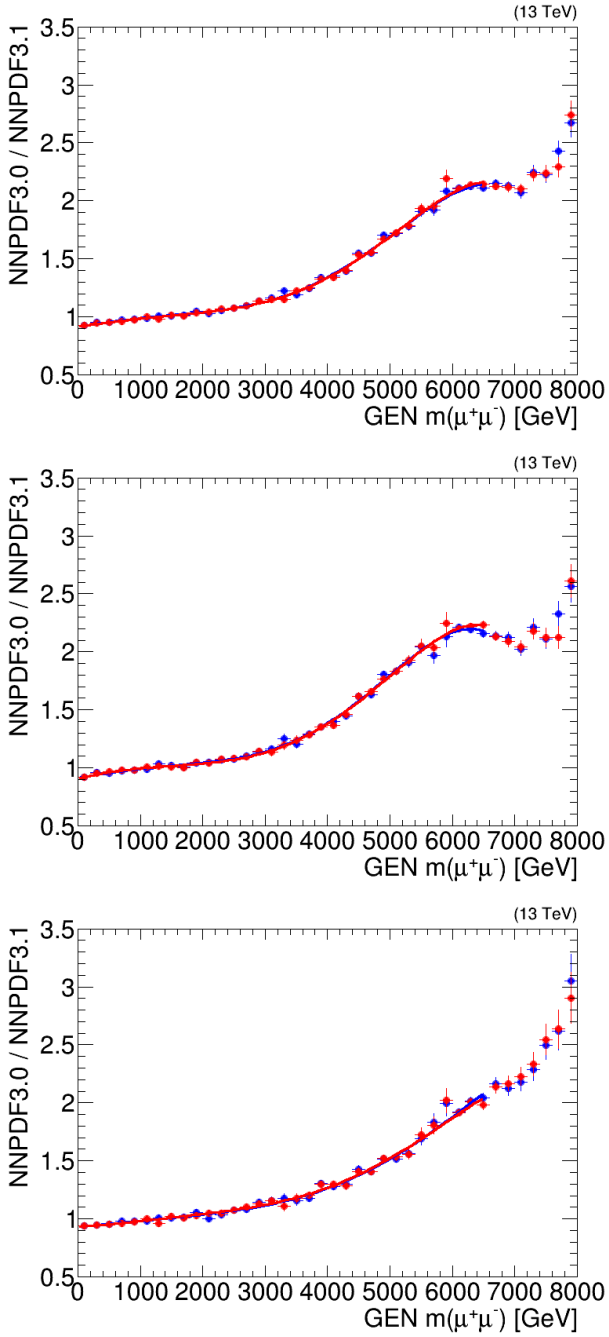

Figure 5.4: Ratio of predictions from 3.0-Monash DY simulation to 3.1-CP5 DY simulation for (blue) 2017 and (red) 2018 versus dimuon mass. Plotted is (top) inclusive category, (middle) BB category, and (bottom) BE+EE category acceptance categories. The solid curves in each plot represent a 5th order polynomial fit to the points.

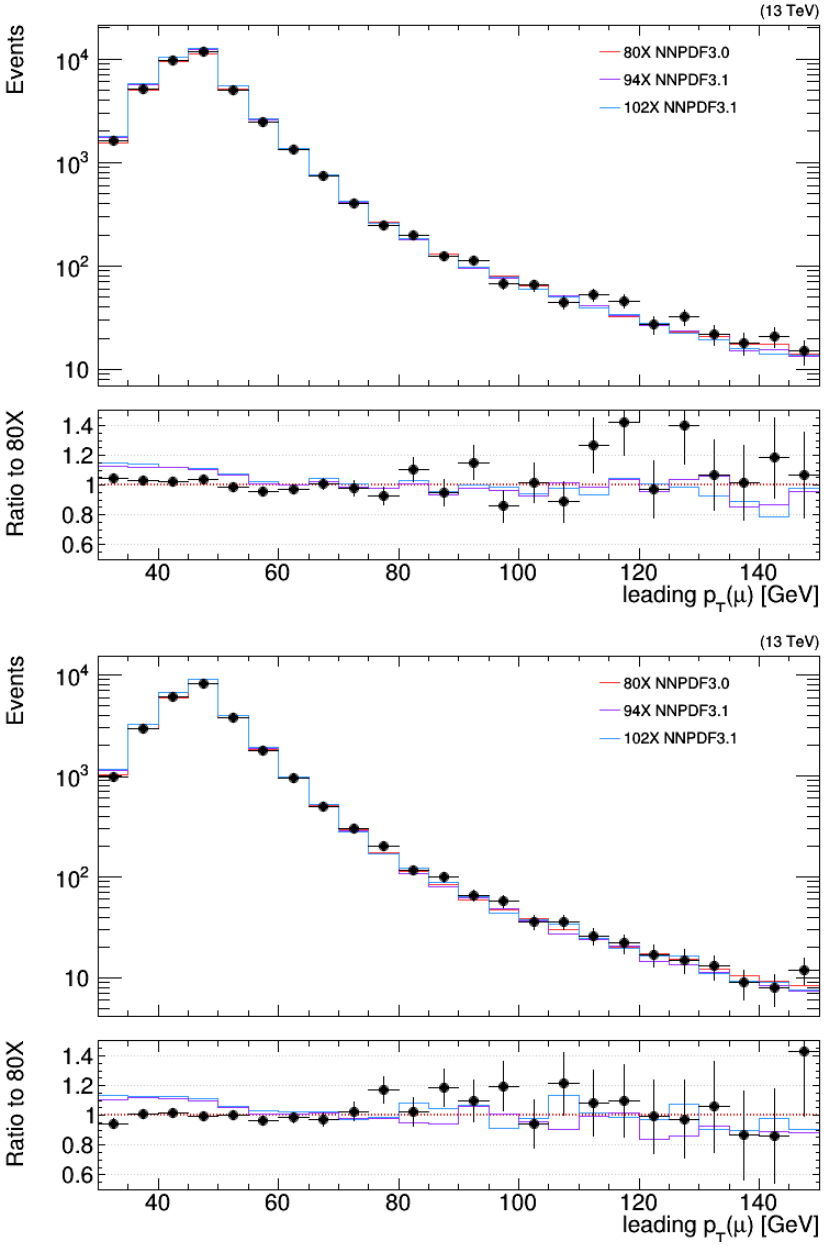

Figure 5.5: Comparison of the number of events from (red) 3.0-Monash DY simulation and 3.1-CP5 DY simulation in (purple) 2017 and (blue) 2018 with (black points) 2018 data versus leading muon p_{T}. Plotted is (left) barrel muons and (right) endcap muons. The simulations here are normalized by their cross sections and according to the integrated luminosity measured in 2018. The lower panel is a ratio of 2017 DY simulation, 2018 DY simulation, and 2018 data to 2016 DY simulation.

Further investigations into the NNPDF PDF sets, as well as the corresponding UE tune used with it, are on-going within the CMS collaboration, and with the NNPDF authors, to determine why the simulations produced with the 3.1-CP5 PDF set and UE tune do not behave as expected.

5.4.1.2 QCD NNLO, electroweak NLO, and photon-induced background corrections

In addition to the PDF choice, the DY spectrum is sensitive to other theoretical considerations. Here, we give a brief outline of the studies on effects on the DY continuum due to theory as discussed in Refs. [52, 53]. Considerations in these references include PDF uncertainties, PDF choice, strong coupling constant α_s dependence, QCD effects up to NNLO, renormalization factorization dependence, EWK effects up to NLO, and pure QED NLO effects.

The NLO cross sections obtained from POWHEG are corrected to NNLO in perturbative QCD, as well as corrected to include missing EWK effects at NLO, using a dilepton invariant mass dependent correction factor obtained using the FEWZ 3.1.b2 program [54]. The mass dependent correction factor is also referred to as a "k-factor". The k-factor we use is derived as the ratio of the FEWZ and 3.0-Monash DY simulation predictions. More clearly, we apply the k-factor after we rescale the DY simulation to the 3.0-Monash prediction described above.

We also account for pure QED effects, such as those that are due to the process known as the photon-induced (PI) background. The PI background arises from the photon component to the proton PDFs where both of the incoming protons emit a virtual $\gamma*$ that interact and produce a dilepton pair via a t or u channel process [52]. Figure 5.6 displays example Feynman diagrams of the PI production. The k-factor mentioned above uses the `LUXqed_plus_PDF4LHC15` PDF set [56], which combines the QCD PDFs based on the PDF4LHC [57] recommendations with the photon PDFs [53] to account for the PI background. At 2 TeV, the PI background is approximately 5% of the DY background [52].

Among these corrections, uncertainties like the intrinsic PDF uncertainty and the choice

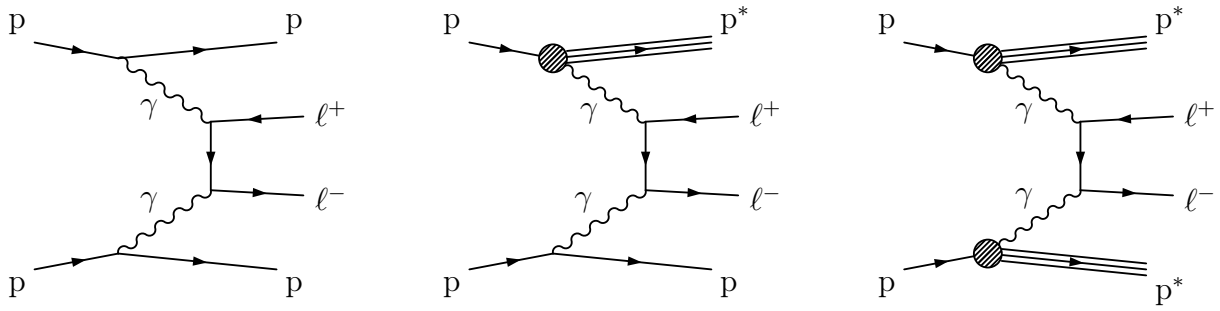

Figure 5.6: Feynman diagrams depicting the photon-induced production of dilepton pairs from pp collisions. Shown is are examples of the t-channel process with (left) both protons intact in the final state, (middle) one proton intact in the final state, and (right) neither proton intact in the final state. The figure is taken from Ref. [55].

of the PDF are the most important effects to consider in the high-mass DY continuum. Others, like those due to the strong coupling constant and the photon induced background, are comparatively small. The total uncertainty attributed to the PDF is approximately 6% at 4 TeV.

5.4.2 $t\bar{t}$ Background

The largest source of dimuon events not coming from DY is from leptonic decays of top quarks, where both W decay to a muon and a neutrino; $t\bar{t} \to WWbb \to \mu\mu\nu\nu bb$. As stated above, this background is estimated with simulation and is generated in separate bins of dilepton mass to improve the statistical precision at high mass. For the 2017 and 2018 analyses, the differences in the detector calibrations used for the simulation are small and have minimal impact on this background. Therefore, because we do not have simulations for the analysis of 2018 data, we use the 2017 simulation for the analysis of 2017 and 2018 data.

Like the DY simulation, the $t\bar{t}$ simulation is generated with NNPDF3.1 NNLO PDF set and the CP5 tune. We therefore perform similar checks on the comparison of the shape and rate of 3.0-Monash and 3.1-CP5 simulations. Figure 5.7 shows the ratio of the number

of events predicted by 3.0-Monash to 3.1-CP5. For each analysis pseudorapidity category, the ratio starts at unity for low mass and then decreases as mass increases. The ratios are similar for each analysis category, so we use the combined acceptance category to rescale all $t\bar{t}$ events simulated with 3.1-CP5. We parametrize the points with a third order polynomial. At a $m_{\mu^+\mu^-} = 3\,\text{TeV}$, the fitted ratio in the inclusive category is approximately 0.45.

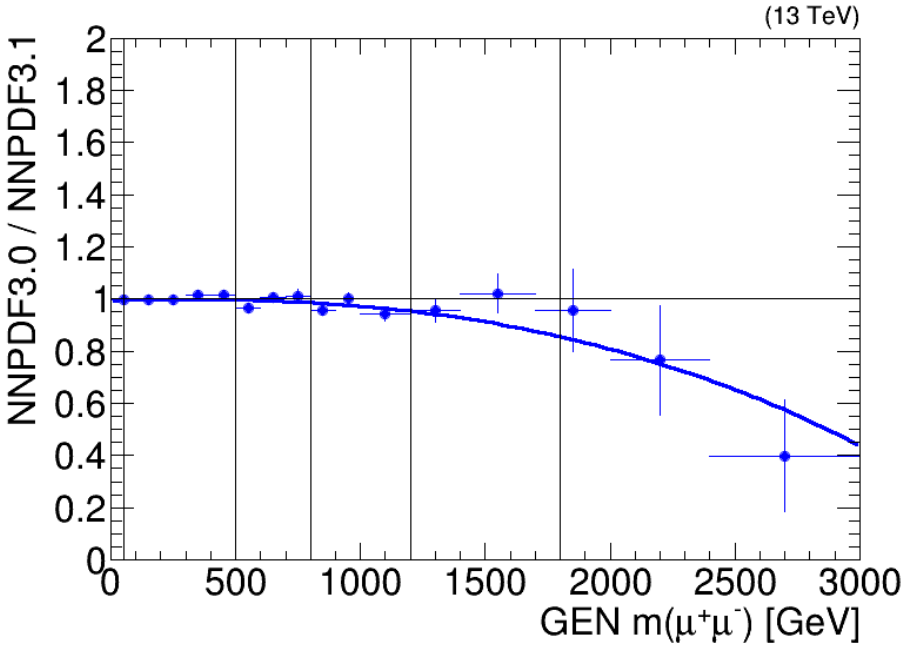

Figure 5.7: Ratio of $t\bar{t}$ simulation generated with 3.0-Monash to 3.1-CP5 for the 2017 simulation. Plotted is the ratio for the inclusive pseudorapidity category. The vertical lines denote the boundary between the $t\bar{t}$ simulations described in Table 5.2. The blue curves are third order polynomial fits to the points.

The predicted $t\bar{t}$ production cross sections are calculated to NNLO in perturbative QCD with the Top++2.0 program [58], which includes soft-gluon resummation to next-to-next-to-leading-log (NNLL), and assumes a top-quark mass $m_t = 172.5\,\text{GeV}$. An overall 6% uncertainty comes from the independent variation of the factorization and renormalization scales and variations in the PDF and strong coupling constant.

5.4.3 Other sources of prompt muons

For the $WW \to \mu\mu\nu\nu$ background, we simulate events with W bosons that decay leptonically and are binned in dilepton mass to improve the statistical precision at high mass. For this background, as the differences between detector conditions and reconstruction have minimal impact and we do not have dedicated 2018 simulations, we again use the same simulation used in the 2017 analysis. This simulation was also generated with 3.1-CP5 but was found to be consistent with the 3.0-Monash versions of the simulation, so we do not apply any rescaling to this simulation.

The $WZ \to \mu\mu\mu\nu$, $WZ \to \mu\mu\nu\nu$, $ZZ \to \mu\mu\ell\ell$, and $ZZ \to \mu\mu\nu\nu$ backgrounds we use simulations that are also generated with POWHEG at NLO, where ℓ denotes either μ or e. For the $WZ \to \mu\mu qq$ and $ZZ \to \mu\mu qq$ backgrounds, we use simulations generated with MADGRAPH (NLO) [46].

The remaining source of prompt dimuons coming from single-top backgrounds, $tW \to \ell\ell\nu\nu b$, are also estimated with simulation. The single top cross sections are computed up to NNLL accuracy [59].

5.4.4 Jet and QCD background

There is also a source of background dimuons coming from W+jets and QCD events where an object is misidentified as a muon candidate passing our selection. The leading contribution to this background comes from heavy flavor decay, typically where a b-jet decays to a muon. Pions or kaons decaying in flight to a muon or when a charged hadron (such as a pion) "punches through" the inner CMS calorimeters to the muon system and leaves a signature similar to that of a muon are also sources of background muons considered in this section.

Unlike the other backgrounds considered in this analysis, we do not use simulation to estimate the prompt muon misidentification background. This is because of the low number of events in available QCD and W+jets simulations that pass our selections. Instead we use a data-driven technique, colloquially referred to as the "fake rate method". This estimation

is performed by others in CMS for our analysis, so we only briefly describe the method here and quote the results in figures and tables to follow.

The central idea is to create a control region by loosening specific selection criteria that creates a data set of muon candidates that is both enriched in muons from jets or muons that do originate from a PV candidates and also orthogonal to the set of dimuons that pass the full analysis selection. The rate at which these muons mimic a prompt muon (rate denoted by f_R) is defined as the ratio of the number of muons in this region that pass the analysis selections to the total number of muon candidates as a function of muon p_{T}. Contamination from EWK processes evaluated by simulation and subtracted from both the numerator and denominator. We then parametrize the f_R by fitting the ratio to an arbitrary functional form that fits the data.

We use the single muon f_R to estimate both the single and double jet background dimuon contributions. For the single jet dimuon contribution, we use a control region where one muon candidate passes the full selection and the other passes a looser preselection but fails the full selection and weight these events by a factor of $f_R/(1-f_R)$ to extrapolate from the control region to our signal region. For the double jet dimuon contribution we use a control region where both muons fail the full selection but pass the looser preselection and weight these events by a factor of $f_{R1}/(1-f_{R1}) \times f_{R2}/(1-f_{R2})$, where the 1 and 2 denote that separate f_R are used according to the p_{T} for each muon. The sum of these two contributions constitute the full jet and QCD background. The uncertainty on this background is taken to be 100% based on the measurement on f_R at high mass. However, it has a negligible effect on the result as its contribution to the overall event yield is approximately 1–3%.

5.4.5 *Z*-peak ratio of data and simulation

As stated above, the primary measurement of this analysis is the ratio of the measured Z' cross section to the Z-peak cross section, where the Z-peak cross section is measured in the region of $60 < m_{\mu^+\mu^-} < 120\,\mathrm{GeV}$. We therefore normalize the simulation to the number of observed Z-peak events in data. The details of the procedure to count Z-peak events are

Before NNPDF re-weight			
Year (NNPDF PDF set)	All	BB	BE+EE
2016 (3.0)	0.9727 ± 0.0041	0.9842 ± 0.0057	0.9610 ± 0.0058
2017 (3.1)	0.9474 ± 0.0048	0.9500 ± 0.0067	0.9448 ± 0.0068
2018 (3.1)	0.9185 ± 0.0036	0.9254 ± 0.0051	0.9115 ± 0.0052
After NNPDF re-weight			
Year (NNPDF PDF set)	All	BB	BE+EE
2016 (3.0)	0.9727 ± 0.0041	0.9842 ± 0.0057	0.9610 ± 0.0058
2017 (3.0)	1.0282 ± 0.0052	1.0286 ± 0.0073	1.0278 ± 0.0068
2018 (3.0)	1.0062 ± 0.0040	1.0124 ± 0.0062	1.0017 ± 0.0052

Table 5.3: Ratios of Z-peak data to simulation for data taken in 2016, 2017, and 2018. The upper part of the table has ratios for the unscaled 3.1-CP5 simulation in 2017 and 2018 simulation and the lower part of the table has ratios for the scaled 2017 and 2018 simulation. The 2016 ratio of data to simulation are identical in the upper and lower parts of the table. Uncertainties are statistical only.

described in Section 5.7 and we only quote the results of that section here.

Here, we apply the ratio of the observed data to the simulation prediction from the Z-peak in the simulation predictions at high mass. By doing this we achieve two things. First, we remove uncertainties in the yield calculations that are common to both high mass and the Z-peak. This leaves us to consider only the uncertainties that vary in mass. This also scales the simulation prediction to the amount of data we measure at the Z-peak. Second, the ratio corrects the simulation for differences in reconstruction that exist between the Z-peak and high-mass. Therefore, we do not apply any additional efficiency scale factors (ratios of efficiencies in data to simulation) to the simulation.

Table 5.3 gives the Z-peak ratio of data to simulation in each analysis pseudorapidity category for each data-taking year in Run 2 separately. Ratios for both before and after applying the 3.0-Monash re-weighting are provided. After applying the re-weighting to 3.0-

Monash, the overall ratio of data to simulation becomes close to 1.0.

5.5 Comparison of data to simulation

In this section, we compare distributions of data and simulations described in the previous section, as a check on our understanding of the data, the detector, and the simulation. In addition, we perform checks on the efficiencies of individual selection criteria on dimuon events for the selection criteria described in Section 5.3. For all of the simulations shown here, we apply all of the relevant corrections as discussed in Section 5.4. Specifically, we apply corrections for the PDF set, for QCD NNLO, for EWK NLO, and for QED NLO effects. Unless otherwise stated, we present the sum of all the SM backgrounds.

As a check on the performance of individual selection criteria, we study their "N-1" efficiencies. To compute the N-1 efficiency we take the ratio of the number of events that pass the full selection criteria to the number of events that pass all but a single selection criteria. The selection criteria are explained in Section 5.3. In Fig. 5.8 and Fig. 5.9, we show comparisons the efficiencies for data and simulation for a selection of the N-1 selection efficiencies as a function of dimuon mass for events in the inclusive pseudorapidity category. For these studies we use approximately 99% of the full 2018 data set. We do not expect the missing 1% to significantly change the figures. Figure 5.8 shows N-1 efficiencies in simulation and data for muon and dimuon kinematic variables as a function of dimuon mass. Shown are the efficiencies for muon relative tracker isolation, relative muon track fit uncertainty, cosmic dimuon back-to-back selections, and dimuon vertex χ^2/dof probability. Figure 5.9 shows efficiencies for variables related to muon tracking as a function of dimuon mass. Shown are the efficiencies for valid pixel hits, valid tracker layers, valid muon hits, and matched muon stations. The N-1 efficiencies in data and simulation agree at a satisfactory level, which indicates that our understanding of our data set as well as the detector, offline reconstruction, and the simulation are all under control.

We also inspect distributions of low-level muon and dimuon kinematic quantities. Fig-

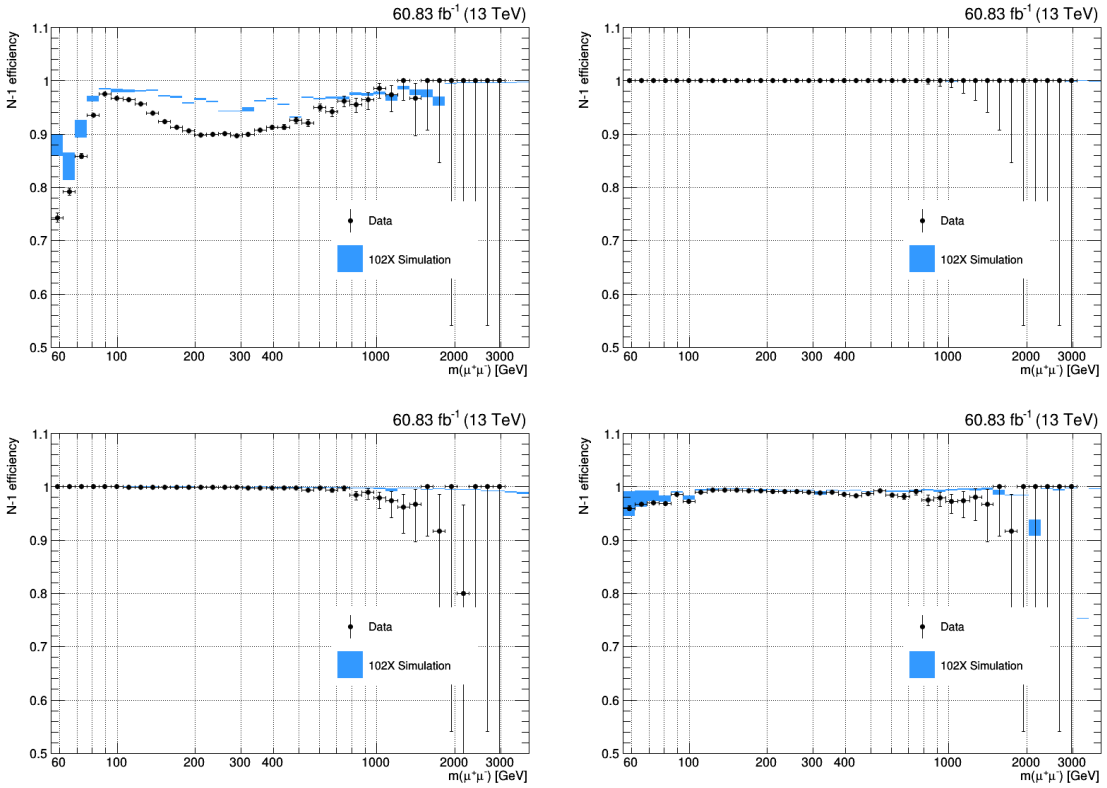

Figure 5.8: N-1 efficiencies for various selections in our muon and dimuon identification. Shown are the efficiencies as a function of dimuon mass on a logarithmic horizontal axis after removing (top left) relative tracker isolation, (top right) relative muon track fit uncertainty, (bottom left) back-to-back cosmic muon rejection, and (bottom right) dimuon vertex χ^2/dof selections.

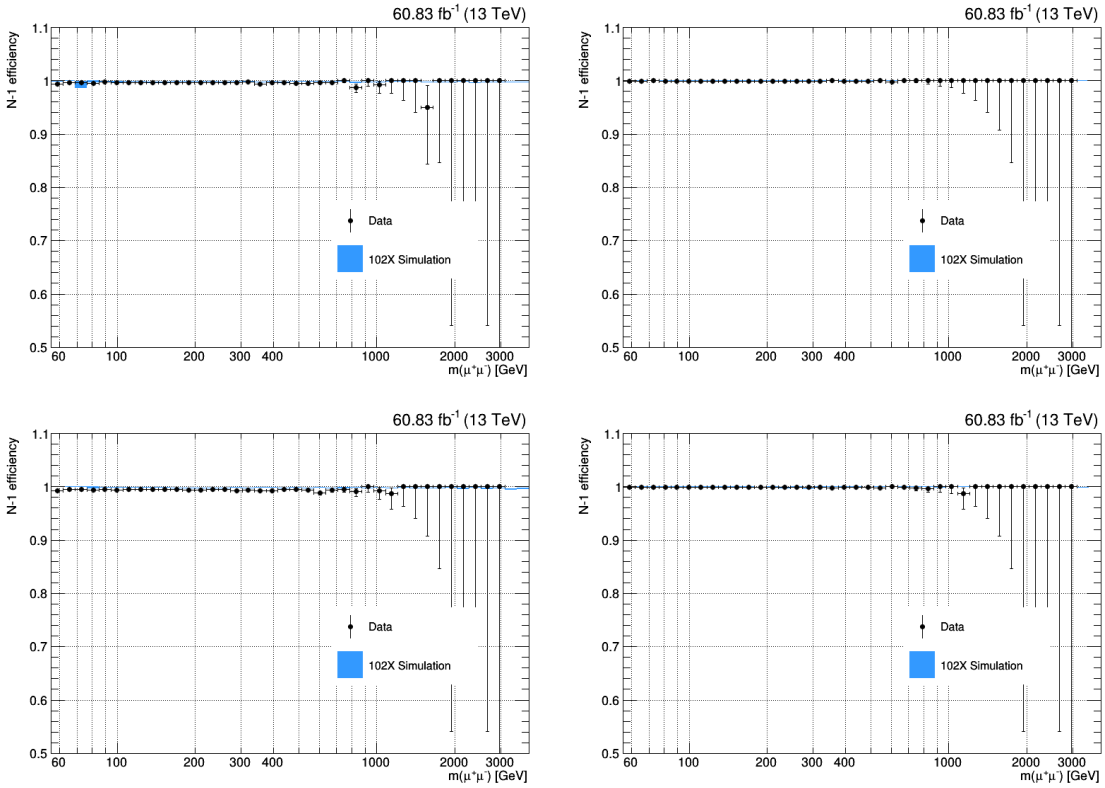

Figure 5.9: N-1 efficiencies for various muon track selections. Shown are the efficiencies as a function of dimuon mass on a logarithmic horizontal axis after removing the (top left) valid pixel hits, (top right) valid tracker layers, (bottom left) valid muon hits, and (bottom right) matched muon stations selections.

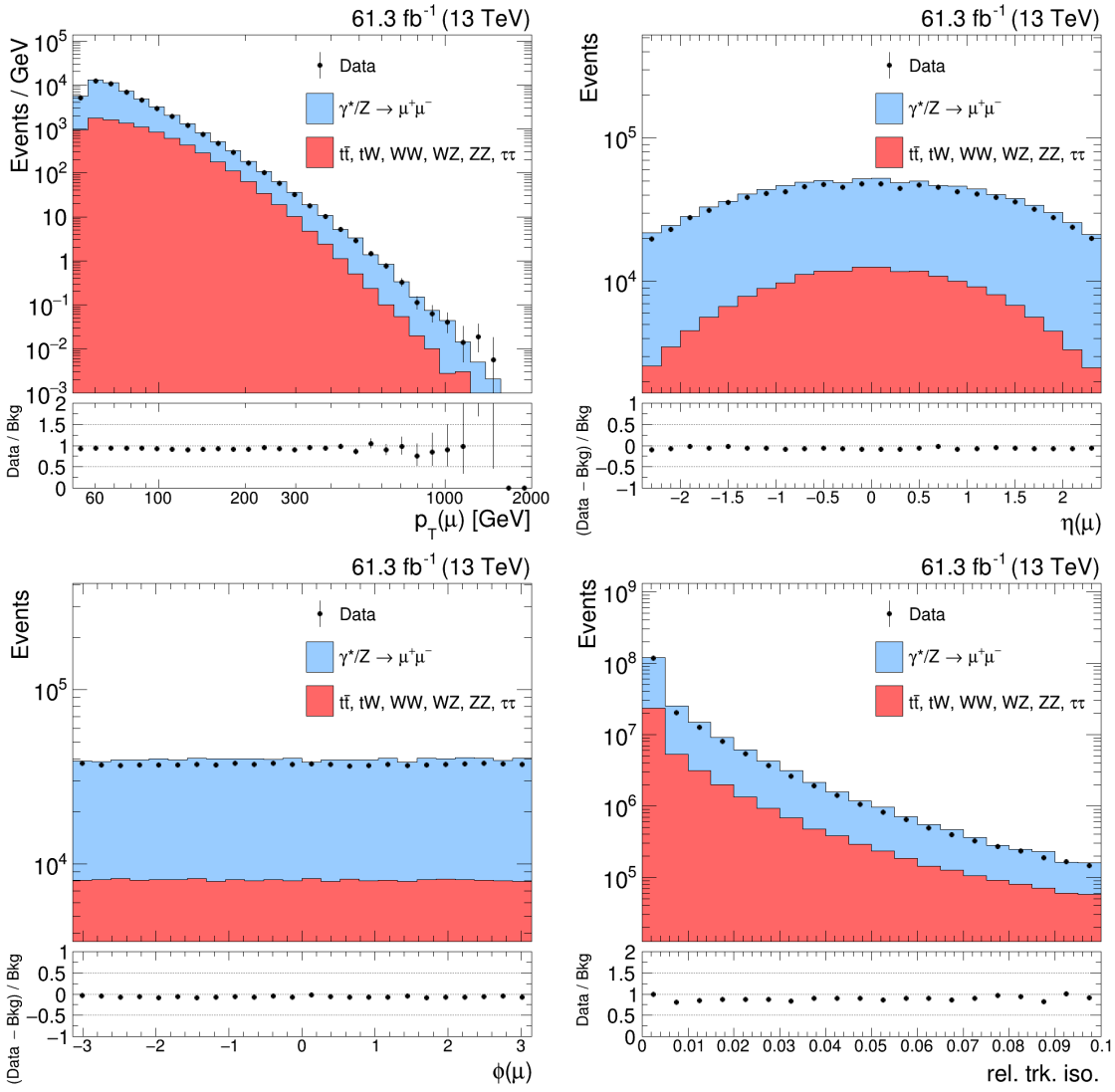

Figure 5.10: Comparison of data and simulation for events with $m_{\mu^+\mu^-} > 120\,\text{GeV}$ and in the inclusive pseudorapidity category. Shown are muon kinematic quantities: (top left) muon p_T, (top right) muon η, (bottom left) muon ϕ, and (bottom right) relative tracker isolation.

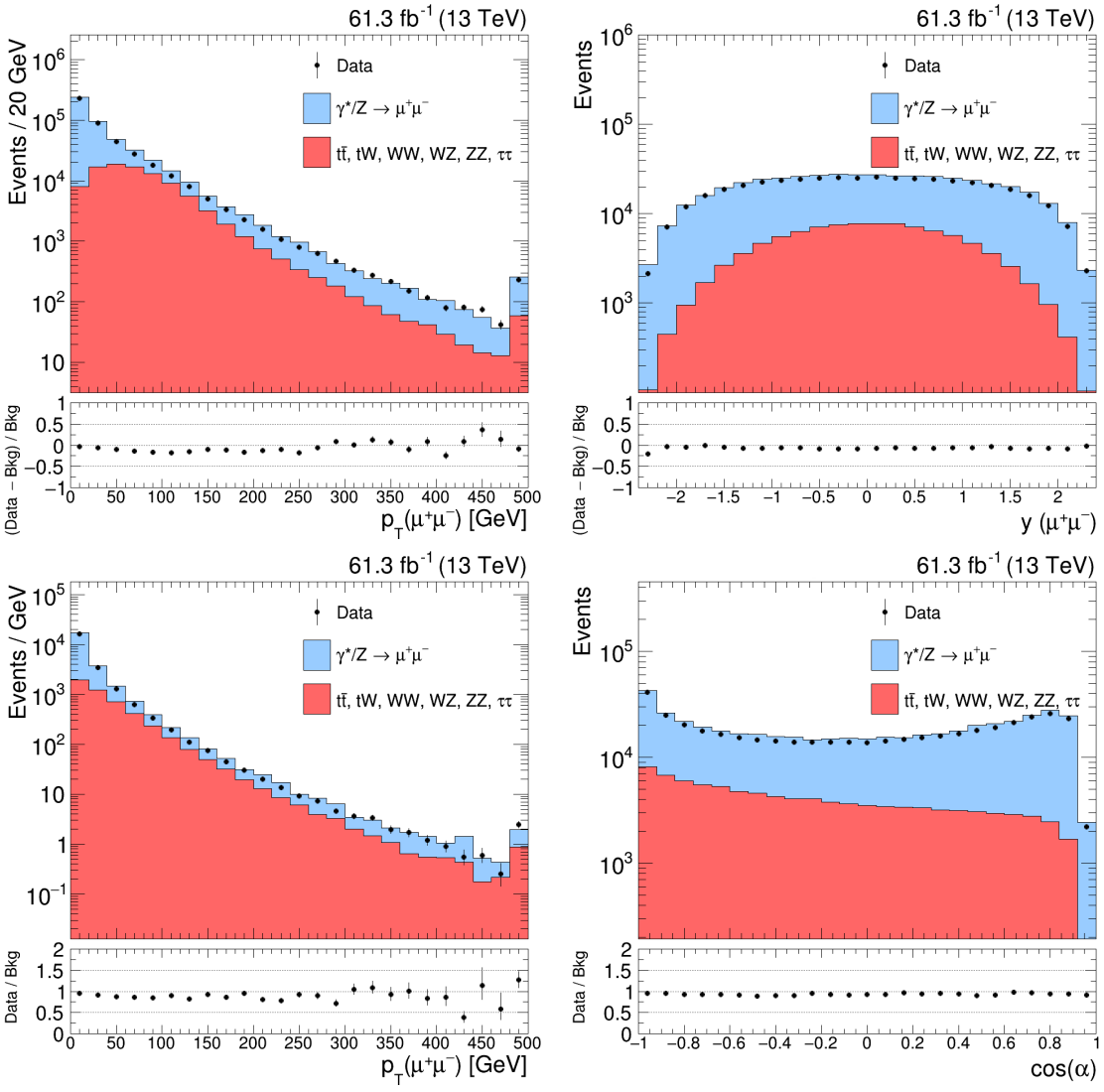

Figure 5.11: Comparison of data and simulation for events with $m_{\mu^+\mu^-} > 120\,\text{GeV}$ and in the inclusive pseudorapidity category. Shown are dimuon kinematic quantities: (top left) dimuon p_T, (top right) dimuon rapidity, (bottom left) dimuon p_T balance between the two muons, and (bottom right) cosine of the three-dimensional angle between the two muons.

ure 5.10 shows comparisons of data and simulation for the muon kinematic variables for events in the inclusive pseudorapidity category and $m_{\mu^+\mu^-} > 120\,\text{GeV}$: (top left) p_T, (top right) η, (bottom left) ϕ, and (bottom right) relative tracker isolation. Figure 5.11 shows dimuon kinematic quantities for events in the inclusive pseudorapidity category and $m_{\mu^+\mu^-} > 120\,\text{GeV}$: (top left) p_T, (top right) rapidity, (bottom left) lepton p_T balance, and (bottom right) cosine of the three-dimensional angle between the two muons.

$m_{\mu^+\mu^-}$ range [GeV]	Observed yield	Total background	$Z/\gamma^* \to \mu^+\mu^-$	$t\bar{t}$ + other backgrounds	Jets
120–400	432117	463000 ± 26700	370000 ± 21000	92300 ± 8300	1400 ± 1400
400–600	10625	11500 ± 696	7390 ± 430	4020 ± 360	85 ± 85
600–900	2479	2470 ± 148	1840 ± 110	600 ± 54	27 ± 27
900–1300	445	463 ± 28.1	381 ± 23	76.2 ± 6.8	5.8 ± 5.8
1300–1800	77	84.5 ± 5.36	74.8 ± 4.6	8.13 ± 0.76	1.6 ± 1.6
> 1800	21	19.2 ± 1.54	17 ± 1.1	1.16 ± 0.12	0.98 ± 0.98

Table 5.4: The number of dimuon events for 2018 in the inclusive category for selected dimuon mass ranges. The total background is the sum of all simulated SM processes considered. The yields from SM simulation are normalized to the expected cross section, the number of events generated, the NNPDF and NNLO correction factors, and normalized to the observed yield using the number of events in the mass window 60–120 GeV, acquired using a prescaled low threshold trigger. Uncertainties include both statistical and systematic components, summed in quadrature.

Finally, we show comparisons of data and simulation for the dimuon invariant mass distributions. Figure 5.12 displays the invariant mass in the inclusive pseudorapidity category on a logarithmic horizontal axis for both the (top) differential and (bottom) cumulative distributions. The cumulative distribution is constructed by setting each mass bin value equal to the sum of the number of events with an invariant mass equal to or greater than the mass value of the bin. Figure 5.13 displays the same distributions as Fig. 5.12 but on a linear horizontal axis with 25 GeV bin widths. Figures 5.14 and 5.15 show both log and

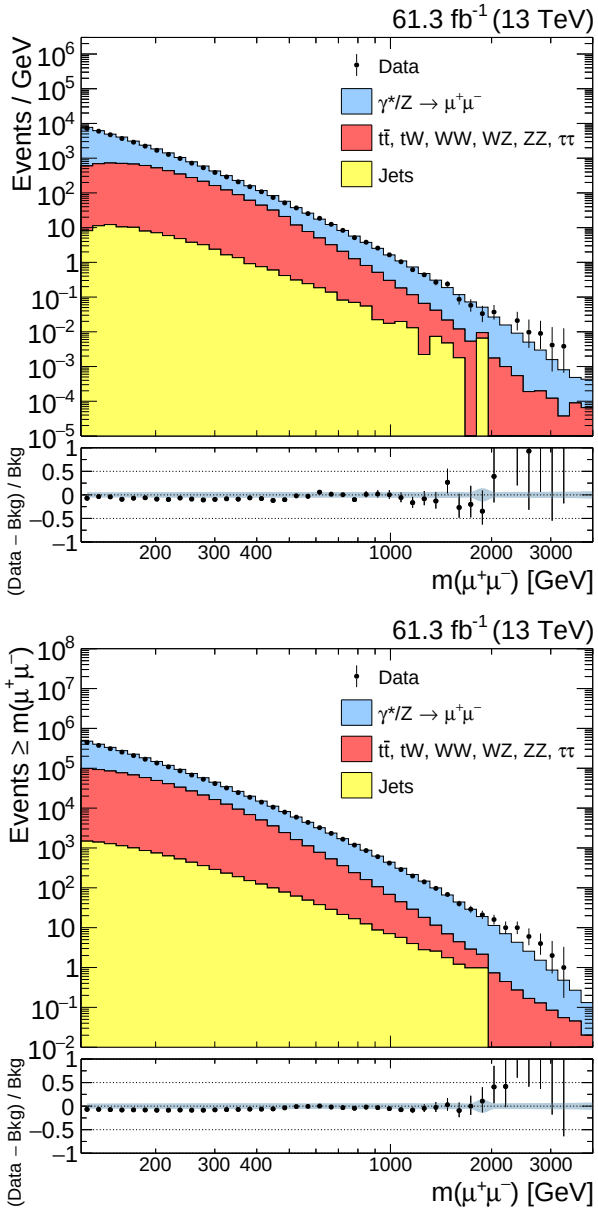

Figure 5.12: The observed opposite-sign dimuon invariant mass spectrum overlaid on the SM background prediction from simulation. Shown are the (top) differential and (bottom) cumulative distribution, both on a logarithmic horizontal axis. Each plot in the figure has a lower panel showing the ratio of data to simulation. Uncertainties in the data points are statistical only. The uncertainty band in the ratio plot includes the statistical and systematic uncertainties, summed in quadrature.

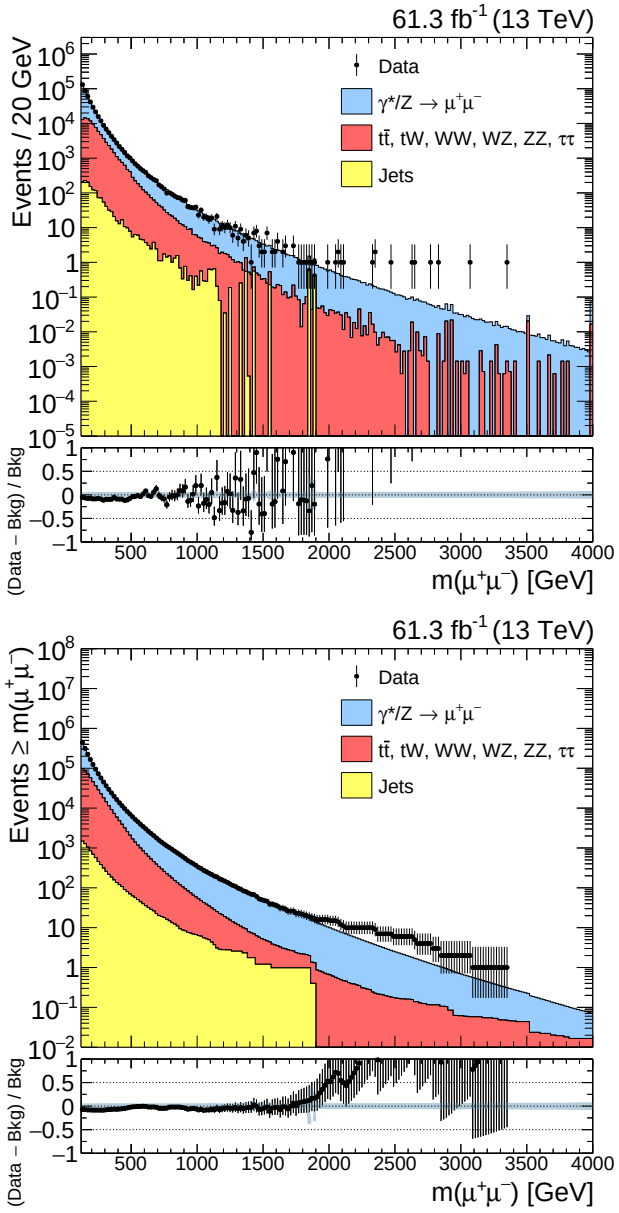

Figure 5.13: The observed opposite-sign dimuon invariant mass spectrum overlaid on the SM background prediction from simulation. Shown are the (top) differential and (bottom) cumulative distribution, both on a linear horizontal axis. Each plot in the figure has a lower panel showing the ratio of data to simulation. Uncertainties in the data points are statistical only. The uncertainty band in the ratio plot includes the statistical and systematic uncertainties, summed in quadrature.

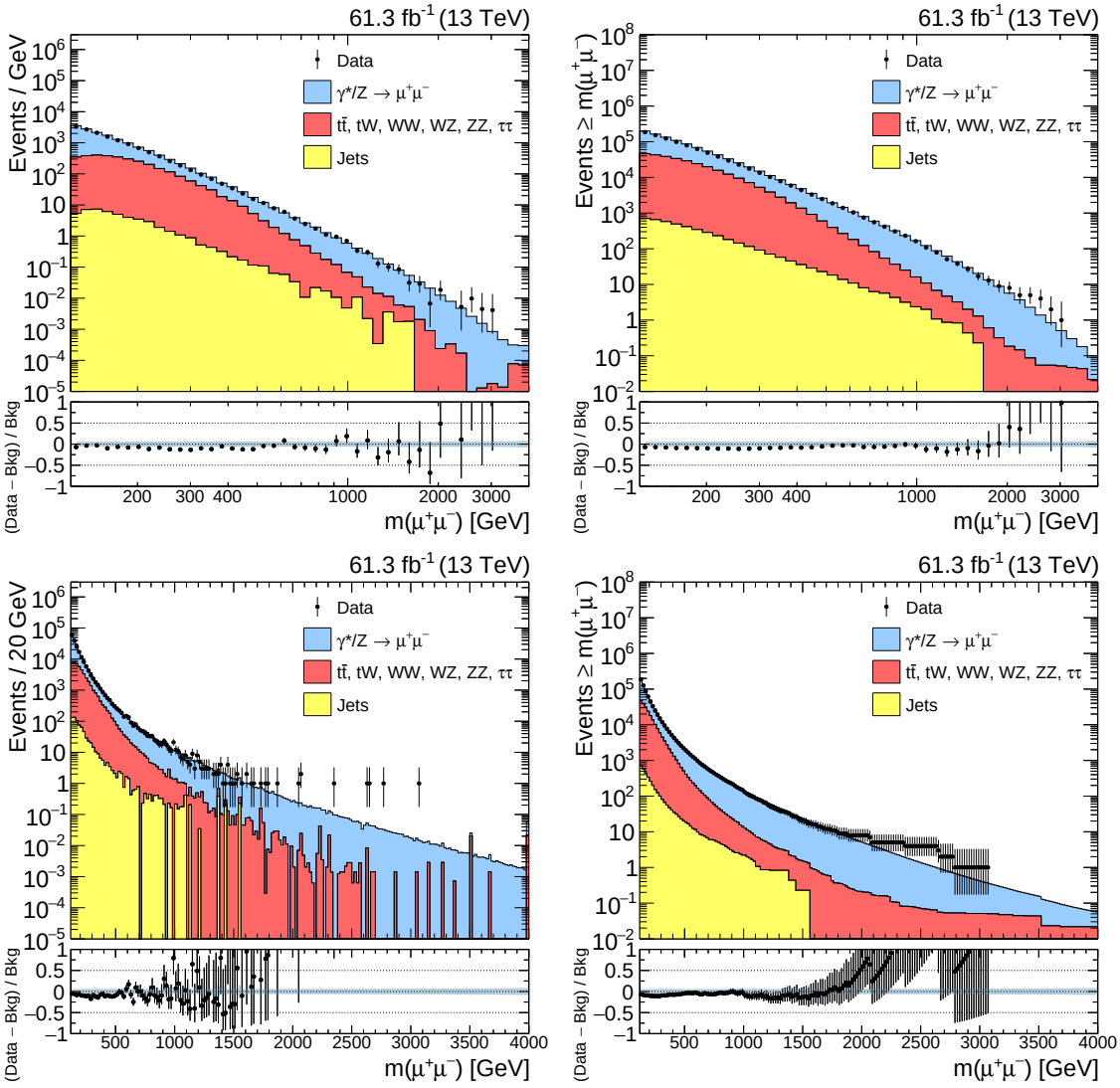

Figure 5.14: The observed opposite-sign dimuon invariant mass spectrum for the BB pseudorapidity category overlaid on the SM background prediction from simulation. Shown in the figures are the same data but with (top left) log and (bottom left) linear horizontal axes and for the cumulative distribution with (top right) log and (bottom right) linear horizontal axes. Each plot in the figure has a lower panel showing the ratio of data to simulation. The uncertainty band in the ratio plot includes the statistical and systematic uncertainties, summed in quadrature.

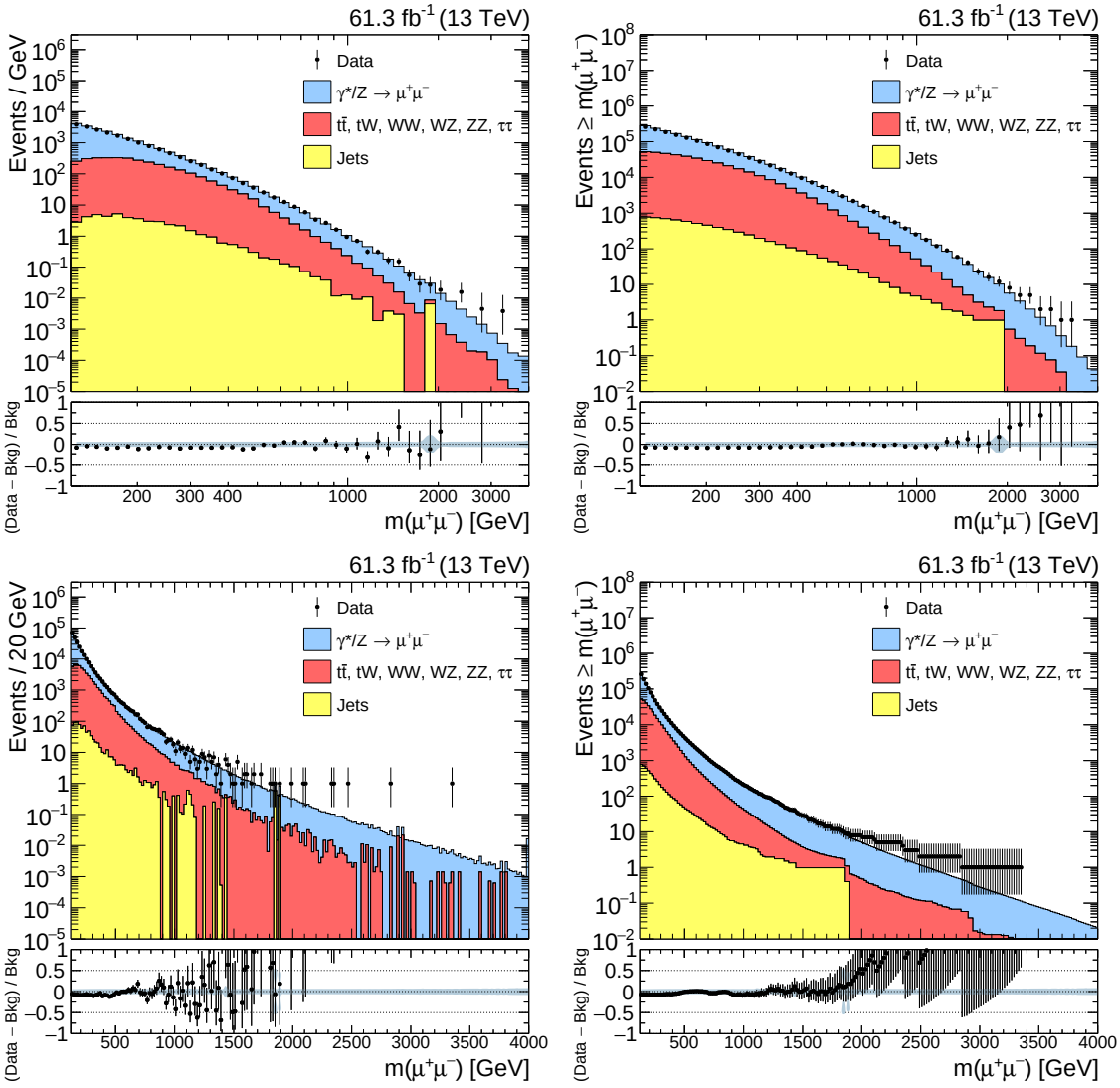

Figure 5.15: The observed opposite-sign dimuon invariant mass spectrum for the BE+EE pseudorapidity category overlaid on the SM background prediction from simulation. Shown in the figures are the same data but with (top left) log and (bottom left) linear horizontal axes and for the cumulative distribution with (top right) log and (bottom right) linear horizontal axes. Each plot in the figure has a lower panel showing the ratio data to simulation. The uncertainty band in the ratio plot includes the statistical and systematic uncertainties, summed in quadrature.

$m_{\mu^+\mu^-}$ range [GeV]	Observed yield	Total background	$Z/\gamma^* \to \mu^+\mu^-$	$t\bar{t}$ + other backgrounds	Jets
120–400	181423	195000 ± 11300	150000 ± 8500	44100 ± 3900	670 ± 670
400–600	3324	3650 ± 219	2500 ± 150	1120 ± 100	25 ± 25
600–900	759	797 ± 47.3	652 ± 39	138 ± 12	7.1 ± 7.1
900–1300	176	169 ± 10.2	150 ± 9	16.9 ± 1.5	2.0 ± 2.0
1300–1800	29	36.2 ± 2.35	33.3 ± 2.1	2.1 ± 0.21	0.8 ± 0.8
> 1800	9	8.91 ± 0.563	8.59 ± 0.55	0.296 ± 0.036	0.0 ± 0.0

Table 5.5: The number of dimuon events for 2018 in the BB category for selected dimuon mass ranges. The total background is the sum of all simulated SM processes considered. The yields from SM simulation are normalized to the expected cross section, the number of events generated, the NNPDF and NNLO correction factors, and normalized to the observed yield using the number of events in the mass window 60–120 GeV, acquired using a prescaled low threshold trigger. Uncertainties include both statistical and systematic components, summed in quadrature.

linear differential and cumulative mass distributions for the BB and BE+EE pseudorapidity categories. In each plot in the figures described above, the lower panel is the ratio of the observed data over the simulation prediction. The uncertainty bands in the ratio plots represent the systematic uncertainties in the background yields, which come from the dimuon mass scale, trigger efficiency, acceptance times reconstruction efficiency, Z-peak normalization, DY PDFs, the non-DY background cross sections, and jet background yield uncertainty. Overall, the agreement between data and simulation is consistent with the SM expectation and no sign of BSM physics is evident.

Tables 5.4, 5.5, and 5.6 report the yields in various $m_{\mu^+\mu^-}$-ranges for the 2018 data-taking for both data and simulation. The quoted uncertainties in the yield tables are computed in the same way as described above for the invariant mass plots.

In addition to the figures above, we also present a version of the invariant mass spec-

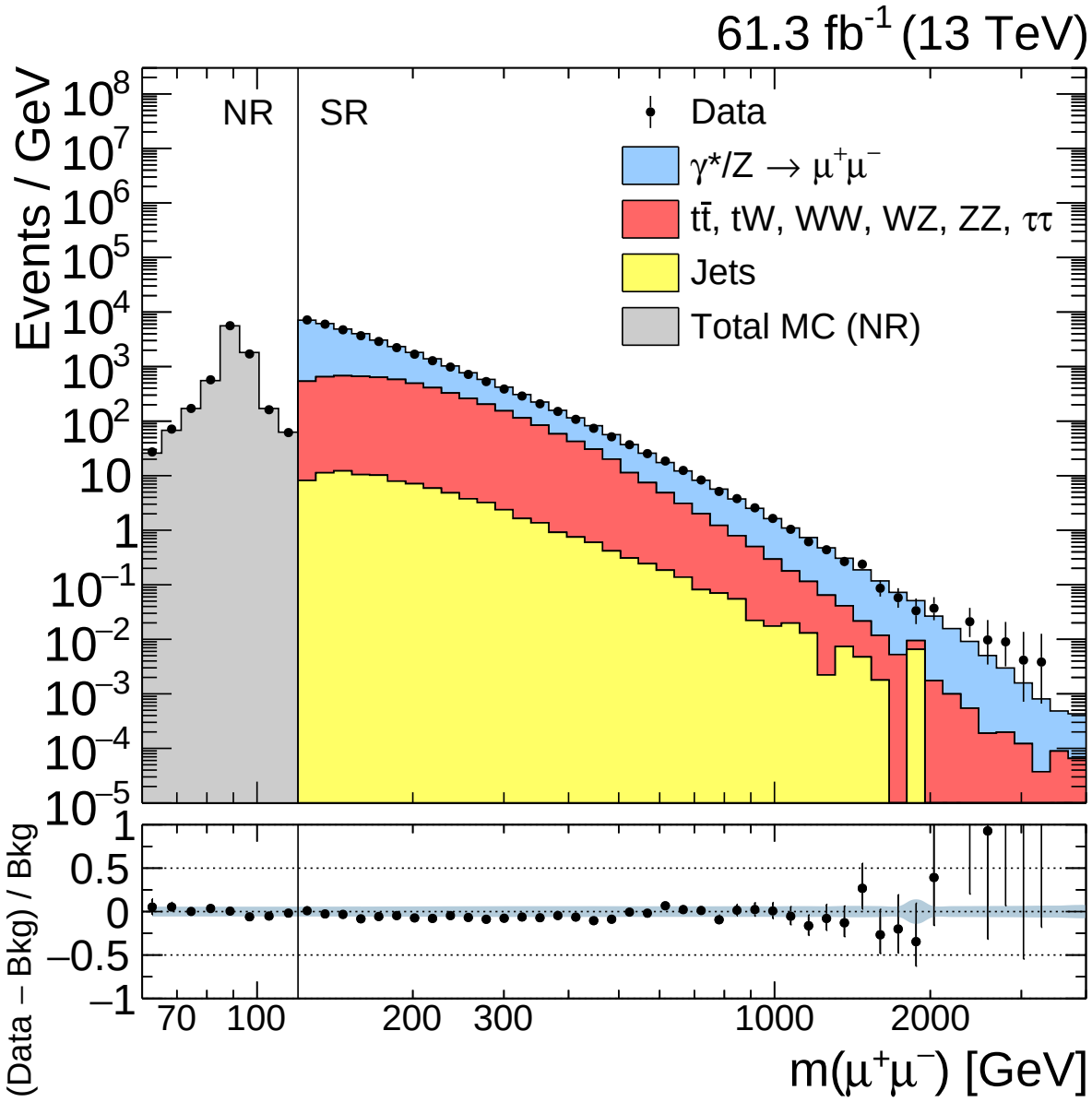

Figure 5.16: The observed opposite-sign dimuon invariant mass spectrum for the 2018 data set in the inclusive pseudorapidity category overlaid on the SM background prediction from simulation on a logarithmic horizontal axis. Shown in the figures are the Z-peak normalization region (NR) and the high-mass search region (SR). The NR data are collected with a lower threshold prescaled trigger as described in the text. The lower panel in the plot shows the ratio of data to simulation. The uncertainty band in the ratio plot includes the statistical and systematic uncertainties, summed in quadrature.

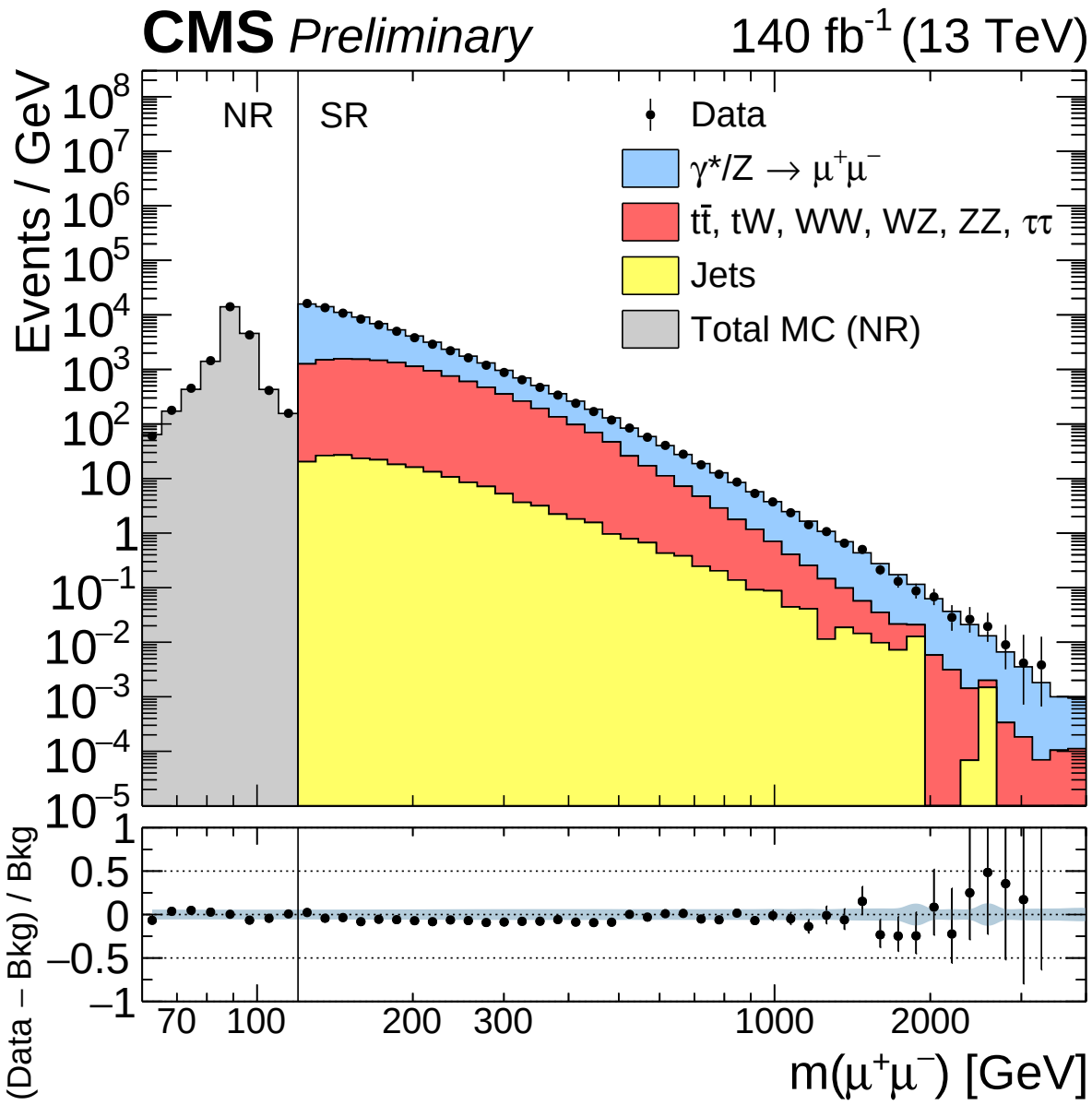

Figure 5.17: The observed opposite-sign dimuon invariant mass spectrum for the full Run 2 data set in the inclusive pseudorapidity category overlaid on the SM background prediction from simulation on a logarithmic horizontal axis. Shown in the figures are the Z-peak normalization region (NR) and the high-mass search region (SR). The NR data are collected with a lower threshold prescaled trigger as described in the text. The lower panel in the plot shows the ratio of data to simulation. The uncertainty band in the ratio plot includes the statistical and systematic uncertainties, summed in quadrature.

$m_{\mu^+\mu^-}$ range [GeV]	Observed yield	Total background	$Z/\gamma^* \to \mu^+\mu^-$	$t\bar{t}$ + other backgrounds	Jets
120–400	250694	270000 ± 15500	221000 ± 13000	48300 ± 4300	690 ± 690
400–600	7301	7860 ± 479	4910 ± 280	2890 ± 260	60 ± 60
600–900	1720	1670 ± 101	1190 ± 71	460 ± 41	20 ± 20
900–1300	269	295 ± 17.9	232 ± 14	59.2 ± 5.3	3.8 ± 3.8
1300–1800	48	48.4 ± 3.02	41.6 ± 2.6	6.01 ± 0.56	0.76 ± 0.76
> 1800	12	10.3 ± 1.16	8.48 ± 0.54	0.864 ± 0.08	0.98 ± 0.98

Table 5.6: The number of dimuon events for 2018 in the BE+EE category for selected dimuon mass ranges. The total background is the sum of all simulated SM processes considered. The yields from SM simulation are normalized to the expected cross section, the number of events generated, the NNPDF and NNLO correction factors, and normalized to the observed yield using the number of events in the mass window 60–120 GeV, acquired using a prescaled low threshold trigger. Uncertainties include both statistical and systematic components, summed in quadrature.

trum that combines the NR and SR regions onto one figure for the inclusive pseudorapidity category. Figure 5.16 displays NR and SR invariant mass spectra for the 2018 data and SM prediction. Figure 5.17 displays the combination of the 2016, 2017, and 2018 data sets and is the version presented in the CMS Physics Analysis Summary EXO-19-019 [41]. As stated above, the NR is the Z-peak region of 60–120 GeV and the high-mass SR as invariant masses above 120 GeV. The NR data are collected with a lower threshold prescaled trigger and the total NR simulation prediction is colored grey. In Section 5.7 we show the NR data and simulation prediction again as separate histograms. The high-mass SR data and simulation are in the same format as the above histograms.

$m_{\mu^+\mu^-}$ range [GeV]	Observed yield	Total background	$Z/\gamma^* \to \mu^+\mu^-$	$t\bar{t}$ + other backgrounds	Jets
120–400	977714	1050000 ± 60400	836000 ± 47000	210000 ± 19000	3100 ± 3100
400–600	24041	26100 ± 1580	16700 ± 970	9120 ± 820	210 ± 210
600–900	5501	5610 ± 339	4170 ± 250	1370 ± 120	74 ± 74
900–1300	996	1050 ± 65.5	863 ± 52	169 ± 15	20 ± 20
1300–1800	183	195 ± 13.6	169 ± 10	19.9 ± 1.8	6.7 ± 6.7
> 1800	42	44.3 ± 3.53	38.7 ± 2.5	3.27 ± 0.31	2.2 ± 2.2

Table 5.7: The number of dimuon events for Run2 in the inclusive category for selected dimuon mass ranges. The total background is the sum of all simulated SM processes considered. The yields from SM simulation are normalized to the expected cross section, the number of events generated, the NNPDF and NNLO correction factors, and normalized to the observed yield using the number of events in the mass window 60–120 GeV, acquired using a prescaled low threshold trigger. Uncertainties include both statistical and systematic components, summed in quadrature.

5.6 High-mass event scrutiny

In this section, we present studies on the of the highest-mass dimuon events collected in 2018. We scrutinize our highest mass events as a check to ensure that our reconstruction behaves well and to search for any unexpected features in the data. Table 5.10 provides some of the kinematic properties of the dimuons with mass larger than 2 TeV. We investigate many quantities of these events, but here we report on the dimuon mass, rapidity, and p_{T}. We also include the muon quantities; p_{T}, the TeV refit algorithm selected by the TuneP algorithm, and the η and ϕ.

Figure 5.18 is a collection of event displays for the highest mass event. The event has a mass of 3343 GeV. Both muons pass through the endcap chambers and do not leave any electromagnetic showers.

Figure 5.19 is a collection of event displays for the second-highest mass event. This event

$m_{\mu^+\mu^-}$ range [GeV]	Observed yield	Total background	$Z/\gamma^* \to \mu^+\mu^-$	$t\bar{t}$ + other backgrounds	Jets
120–400	412198	439000 ± 25400	338000 ± 19000	99900 ± 8900	1200 ± 1200
400–600	7539	8260 ± 494	5690 ± 330	2520 ± 230	51 ± 51
600–900	1735	1820 ± 108	1480 ± 88	313 ± 28	21 ± 21
900–1300	373	383 ± 23.9	340 ± 21	36.1 ± 3.2	7.1 ± 7.1
1300–1800	74	83 ± 5.83	75.1 ± 4.6	4.94 ± 0.48	2.9 ± 2.9
> 1800	15	21.6 ± 1.63	19.6 ± 1.3	0.954 ± 0.098	0.92 ± 0.92

Table 5.8: The number of dimuon events for Run2 in the BB category for selected dimuon mass ranges. The total background is the sum of all simulated SM processes considered. The yields from SM simulation are normalized to the expected cross section, the number of events generated, the NNPDF and NNLO correction factors, and normalized to the observed yield using the number of events in the mass window 60–120 GeV, acquired using a prescaled low threshold trigger. Uncertainties include both statistical and systematic components, summed in quadrature.

has a mass of 3071 GeV with one muon in the barrel and one in the endcap. Both muons appear to leave electromagnetic showers, which is evident by the extra reconstructed hits in the muon chambers (the extra red lines).

Figure 5.20 is a collection of event displays for the ninth-highest dimuon mass event, which is a potential high-mass $t\bar{t}$ candidate. The event has two clean muons that are located in the barrel and the endcap and has a mass of 2354 GeV. There are also two jet candidates that are both identified as potential b-jet candidates according to a dedicated b-jet identification algorithm developed by CMS. The event also has a missing transverse energy of 53 GeV. From the last line in Table 5.4 we expect approximately 1 non-DY background event for $m_{\mu^+\mu^-} > 1800$ GeV.

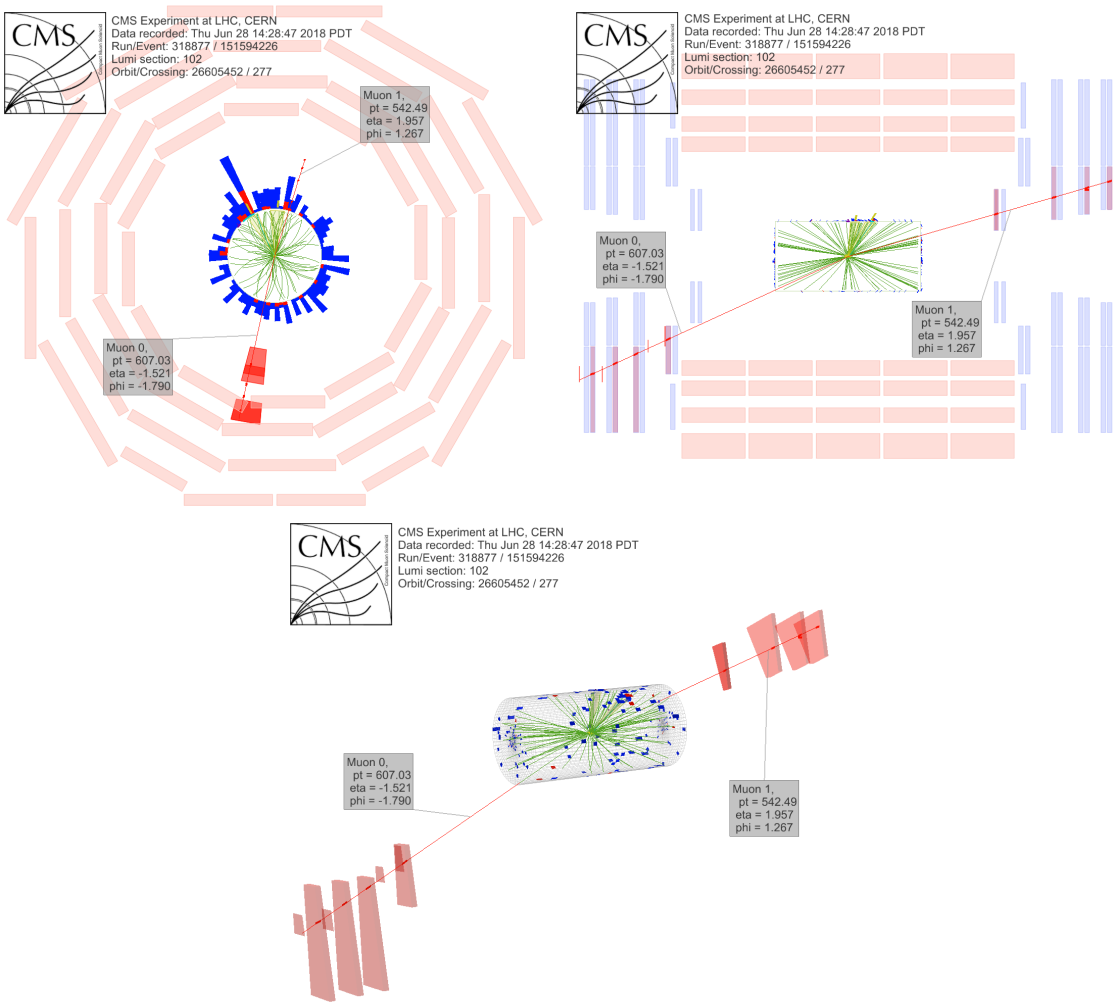

Figure 5.18: Event displays of the highest dimuon mass event collected in 2018, having an invariant mass of 3343 GeV. Shown are (top left) a $r - \phi$ view of the detector, (top right) a $r - \eta$ view of the detector, and (bottom) a three dimensional view of the detector. The red curves are the track fits of each muon. Grey boxes label the p_{T}, η, and ϕ of the muons.

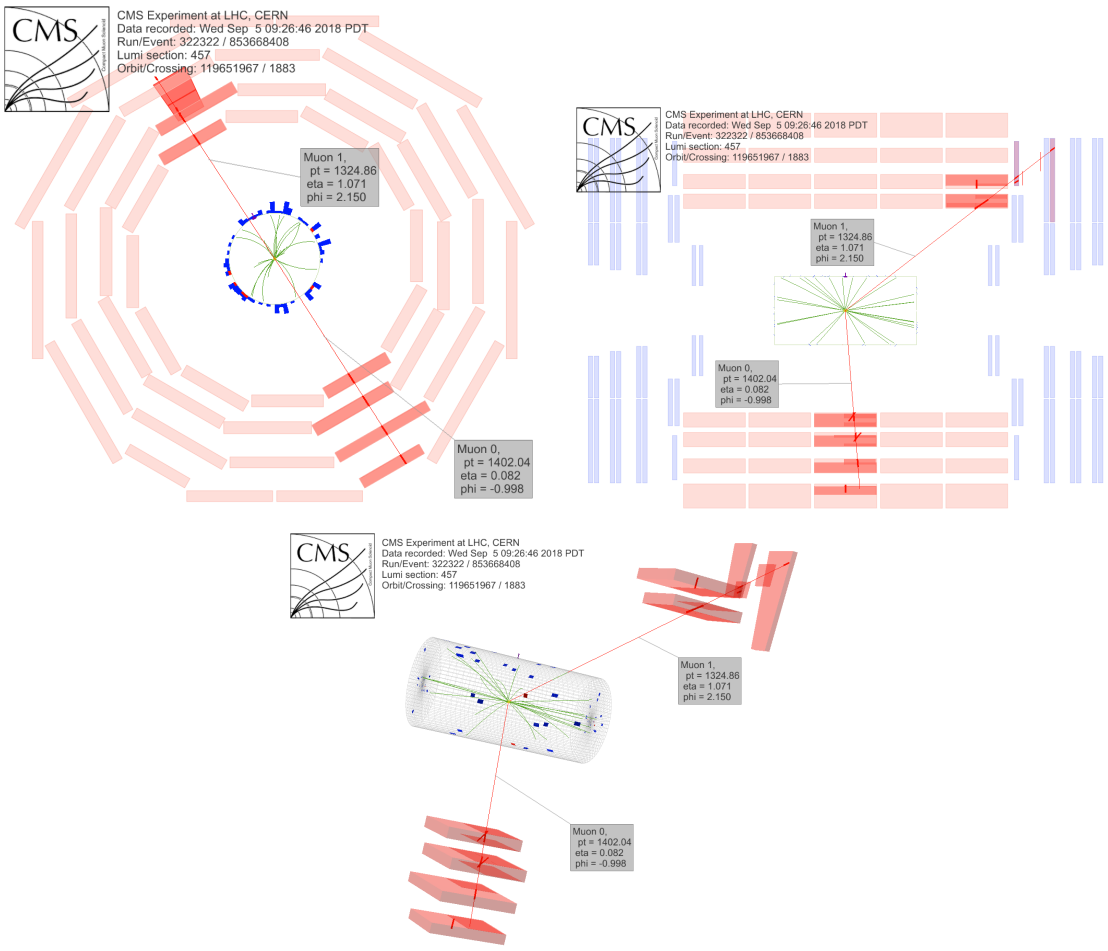

Figure 5.19: Event displays of the second-highest dimuon mass event collected in 2018, having an invariant mass of 3071 GeV. Shown are (top left) a $r-\phi$ view of the detector, (top right) a $r-\eta$ view of the detector, and (bottom) a three dimensional view of the detector. The red curves are the track fits of each muon. Grey boxes label the p_{T}, η, and ϕ of the muons.

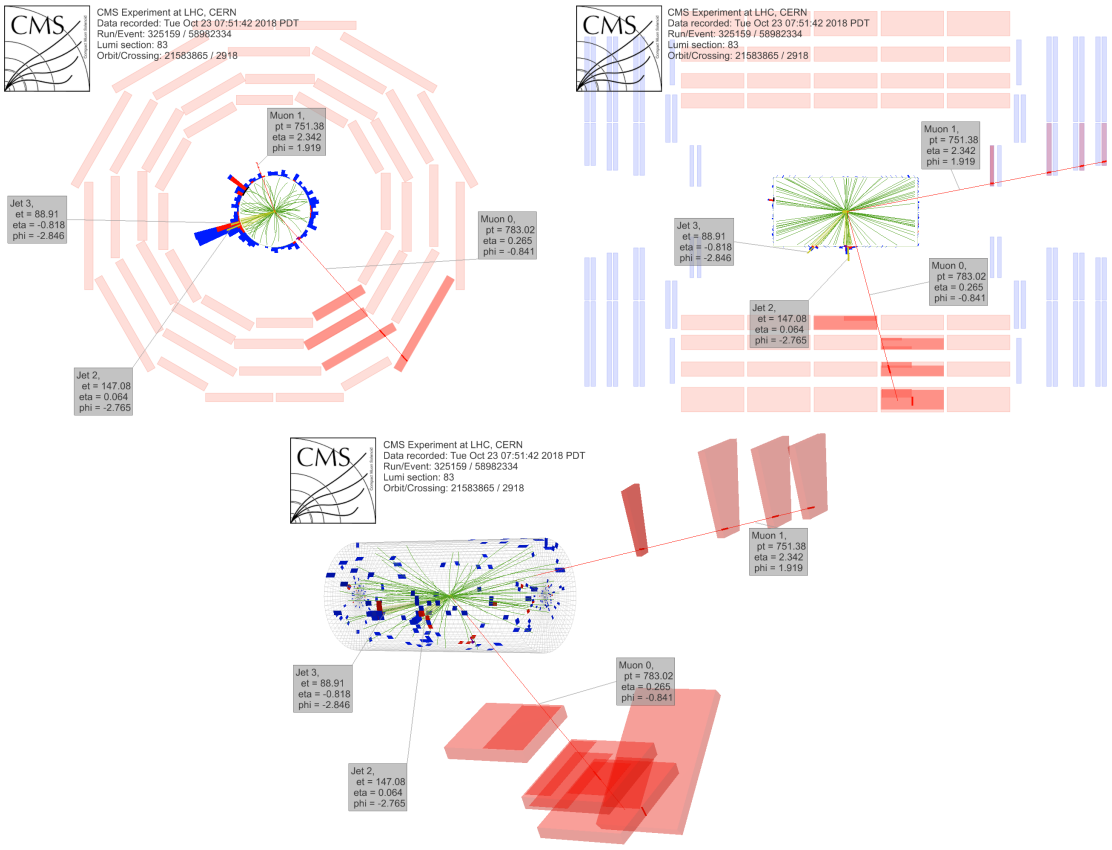

Figure 5.20: Event displays of the ninth-highest dimuon mass event collected in 2018, having an invariant mass of 2354 GeV, which is also a potential $t\bar{t}$ candidate. Shown are (top left) a $\rho - \phi$ view of the detector, (top right) a $\rho - \eta$ view of the detector, and (bottom) a three dimensional view of the detector. The red curves are the track fits of each muon. Grey boxes label the p_{T}, η, and ϕ of the muons. The yellow cones are the two b-jet candidates in the event and are also labeled with grey boxes. There is also missing transverse energy of 53 GeV in the event.

$m_{\mu^+\mu^-}$ range [GeV]	Observed yield	Total background	$Z/\gamma^* \to \mu^+\mu^-$	$t\bar{t}$ + other backgrounds	Jets
120–400	565516	611000 ± 35100	499000 ± 28000	110000 ± 9800	1900 ± 1900
400–600	16502	17800 ± 1090	11000 ± 640	6580 ± 590	160 ± 160
600–900	3766	3790 ± 231	2690 ± 160	1050 ± 94	53 ± 53
900–1300	623	668 ± 41.7	523 ± 32	132 ± 12	13 ± 13
1300–1800	109	112 ± 7.76	93.7 ± 5.8	14.9 ± 1.4	3.8 ± 3.8
> 1800	27	22.8 ± 1.91	19.2 ± 1.2	2.31 ± 0.21	1.3 ± 1.3

Table 5.9: The number of dimuon events for Run2 in the BE+EE category for selected dimuon mass ranges. The total background is the sum of all simulated SM processes considered. The yields from SM simulation are normalized to the expected cross section, the number of events generated, the NNPDF and NNLO correction factors, and normalized to the observed yield using the number of events in the mass window 60–120 GeV, acquired using a prescaled low threshold trigger. Uncertainties include both statistical and systematic components, summed in quadrature.

5.7 Normalization to Z resonance

As described above, the parameter of interest in this search is the ratio R_σ of the Z' cross section times branching fraction to dimuons to the the Z-peak cross section given by the full equation:

$$R_\sigma = \frac{\sigma(pp \to Z' + X \to \mu^+\mu^- + X)}{\sigma(pp \to Z + X \to \mu^+\mu^- + X)} = \frac{N(Z' \to \mu^+\mu^-)}{N(Z \to \mu^+\mu^-)} \times \frac{A(Z \to \mu^+\mu^-)}{A(Z' \to \mu^+\mu^-)} \times \frac{\epsilon(Z \to \mu^+\mu^-)}{\epsilon(Z' \to \mu^+\mu^-)} \tag{5.2}$$

where N is the number of events, A is the detector acceptance, and ϵ is the reconstruction efficiency.

To count the number of Z-peak events $N(Z \to \mu^+\mu^-)$ (shortened to $N(Z)$ in the text that follows) we use the count of reconstructed dimuons within the mass range of 60–120 GeV and use an identical selection criteria as described above for the high mass search, with one difference. Since the threshold of the main analysis trigger is more than half of the mass of

Dimuon quantities			μ^- quantities		μ^+ quantities	
$m_{\mu^+\mu^-}$ [GeV]	y	p_{T} [GeV]	p_{T} [GeV]	(η, ϕ)	p_{T} [GeV]	(η, ϕ)
3343 ± 172	0.165	81	D, 607 ± 29	(-1.52,-1.79)	P, 542 ± 53	(1.96,1.27)
3071 ± 134	0.563	78	D, 1325 ± 89	(1.07, 2.15)	D, 1402 ± 78	(0.08, -1.00)
2837 ± 106	-0.007	227	P, 610 ± 33	(-1.49, -2.65)	P, 677 ± 35	(1.38, 0.84)
2765 ± 161	-0.393	200	P, 1365 ± 63	(0.02, -0.81)	P, 1198 ± 156	(-0.86, 2.24)
2645 ± 113	-0.712	42	D, 1318 ± 83	(-0.86, 2.70)	P, 1296 ± 75	(-0.56, -0.47)
2632 ± 105	-0.482	355	D, 1422 ± 80	(-0.18, -1.62)	P, 1085 ± 62	(-0.87, 1.43)
2463 ± 343	-0.595	138	D, 312 ± 11	(1.33, 1.49)	D, 355 ± 86	(-2.40, -1.25)
2360 ± 111	0.686	120	P, 1013 ± 74	(1.14, 0.73)	D, 1133 ± 66	(0.27, -2.42)
2354 ± 198	1.288	293	P, 751 ± 134	(2.34, 1.92)	P, 783 ± 40	(0.27, -0.84)
2330 ± 112	0.997	189	P, 1045 ± 59	(0.74, 2.63)	P, 1229 ± 96	(1.22, -0.55)
2102 ± 90	-0.118	96	P, 409 ± 26	(-1.68, 0.66)	D, 472 ± 27	(1.32, -2.32)
2090 ± 86	0.188	144	P, 594 ± 34	(-1.01, 0.77)	P, 474 ± 28	(1.58, -2.52)
2078 ± 75	0.672	72	D, 1003 ± 59	(0.65, -2.49)	P, 1075 ± 45	(0.69, 0.65)
2064 ± 74	-0.467	104	D, 994 ± 52	(-0.47, 1.39)	P, 1083 ± 53	(-0.47, -1.81)
2044 ± 70	-0.187	94	P, 724 ± 37	(1.10, -1.19)	P, 650 ± 30	(-0.81, 2.04)

Table 5.10: List of 15 dimuon candidates with invariant mass above 2 TeV collected in 2018. Quantities listed in the table include the dimuon quantities; invariant mass, rapidity y, p_{T}, and muon quantities; p_{T}, η, and ϕ. Also quoted is the specific TeV refit selected by TuneP for each muon track; here P is for Picky and D is for DYT.

Prescale	Int. Lumi.	Prescaled Int. Lumi.
148	21.85	0.15
222	438.55	1.98
296	650.41	2.20
385	346.76	0.90
445	3962.37	8.90
500	55871.90	111.74
Total	61291.84	125.87

Table 5.11: List of prescale periods and corresponding unprescaled and prescaled integrated luminosities in units of pb^{-1}. Due to an error in the tool used to calculate the luminosity and prescale value, a set of runs and luminosity sections totaling $7\,\mathrm{pb}^{-1}$ (unprescaled) was excluded from this calculation.

the Z boson, it restricts the potential decay parameter space at the Z resonance. As this high trigger threshold requires that both muons have an offline p_{T} of at least 53 GeV, the dimuon candidates are consequently in a very boosted regime and the properties of the muons and dimuons become different between high- and low-mass. We also become vulnerable to incorrect modeling of the trigger turn-on threshold. We therefore use a lower-p_{T} threshold muon trigger and lower offline p_{T} selection to calculate the number of Z candidates for the ratio. The trigger used to count the Z candidates is an HLT algorithm similar to the trigger used to obtain the high mass data set, except with a p_{T} threshold of 27 GeV. The trigger is also prescaled, that is, only one event is kept in some fixed number of triggers that depends on specific data-taking conditions, such as the instantaneous luminosity. Trigger prescaling is done to keep the CMS trigger rate at a predefined rate, even at very high instantaneous luminosities. The offline p_{T} requirement is set at 30 GeV to be above the trigger p_{T} threshold. The Z acceptance A and reconstruction efficiency ϵ are computed at the Z-peak using the the same DY simulations listed in Table 5.2.

The list of prescales used during 2018 data-taking are reported in Table 5.11 as well as the corresponding prescaled and unprescaled integrated luminosities of each prescale period. To compute $N(Z)$ it is necessary to scale the count of dimuons by the prescale found. We compare three methods to compute $N(Z)$:

- Simple prescale correction

  Scale n_i, the number of Z candidates counted in each prescale period i, by each individual prescale p_i and sum over prescale periods. Table 5.12 reports the numbers $n_i(Z)$ for each prescale period i for the full pseudorapidity category and the two categories used in the analysis; BB and BE+EE.

$$N(Z) = \sum_i p_i n_i(Z) \tag{5.3}$$

- Lumi-Ratio Method

  Calculate average prescale by taking ratio of luminosities measured by unprescaled trigger, $\mathcal{L}_{50}$, and prescaled trigger, $\mathcal{L}_{27}$. The subscripts 50 and 27 denote the p_{T} thresholds of the nominal unprescaled muon trigger used for the high mass search and the prescaled muon trigger used for the Z-peak normalization, respectively. This method is also mathematically equivalent to computing a harmonic mean of the prescales p_i with a weight equal to the the unprescaled luminosity $\mathcal{L}_{50}$ of each prescale period i.

$$N(Z) = \frac{\mathcal{L}_{50}}{\mathcal{L}_{27}} \sum_i n_i(Z) \tag{5.4}$$

- Common Prescale Method

  Re-prescale data in all prescale periods to a chosen fixed prescale value, p^{common}. That is, we randomly drop events in the data set in all prescale periods (except the chosen prescale) such that the rate of events kept matches the rate defined by the chosen prescale. If a prescale exists at a higher value than the chosen prescale, then all of these events are not considered. For data collected in 2018, we choose $p_{\mathrm{common}} = 500$, which was both the highest prescale value and the prescale that roughly 90% of the

data was collected at.

$$N(Z) = p^{\text{common}} \sum_i n_i^{\text{common}}(Z) \tag{5.5}$$

Prescale	All	BB	BE+EE
148	78	30	48
222	1093	480	611
296	1151	485	666
385	446	181	265
445	4728	1992	2736
500	59646	24935	34711
Total	67142	28105	34711

Table 5.12: Counts of Z candidates in each prescale period for all dimuons and dimuons within the two analysis pseudorapidity categories.

	2016	2017	2018
$A(Z)$	0.2973	0.3034	0.3043
$\epsilon(Z)$	0.9132	0.9081	0.9140
$A(Z) \times \epsilon(Z)$	0.2715	0.2755	0.2782
Int. Lumi (pb^{-1})	36295	42037	61309
Simple	1900.14	2086.59	1917.04
Lumi-Ratio	1910.50	2087.76	1915.69
Common	1958.07	1979.43	1918.35

Table 5.13: Comparison of the measured Z-peak cross sections for all three data-taking years of the LHC Run 2 and for each method described above to compute $N(Z)$. Relevant uncertainties to the calculation include a roughly 0.5% statistical uncertainty, a 2.5% luminosity uncertainty, and a 1% uncertainty on acceptance times trigger and reconstruction efficiency.

Even though the Z-peak cross section itself is not directly used in the analysis, it is still useful to compute the measured value and compare to theoretical predictions and to

values obtained in previous data-taking years. Table 5.13 compares the results of the three prescale correction methods to compute $N(Z)$, the detector acceptance A, the reconstruction efficiency ϵ, the integrated luminosities, and also the corresponding Z-peak cross section for data taken in 2016, 2017, and 2018. The three methods give results that agree with each other to less than 0.1% in 2018 and agree over each data-taking year to within the approximately 0.5% statistical uncertainty and 2.5% integrated luminosity uncertainty.

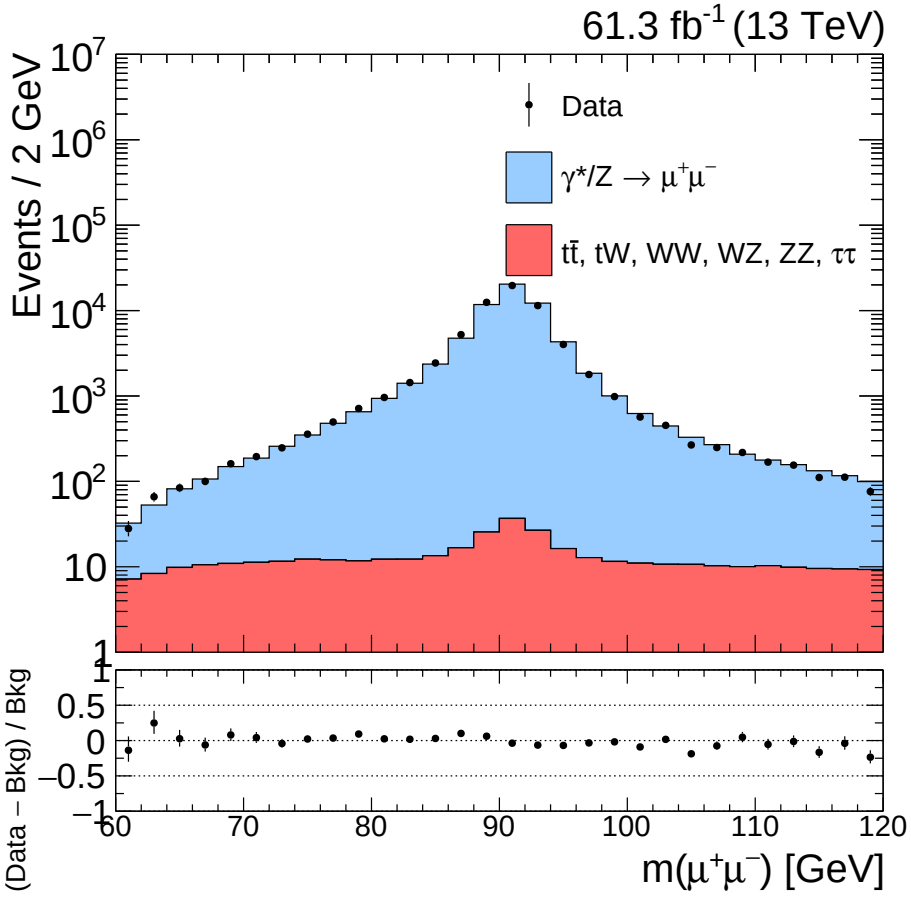

Figure 5.21: Histograms of 2018 Z-peak normalization region data and simulation after applying the 3.0-Monash scaling. The lower panel displays the ratio of data and simulation. Shown are dimuons from the inclusive pseudorapidity category.

For the analysis of Run 2 data, we use the Common Prescale method to compute the Z-peak normalization and cross sections. This method has the advantage of reducing any prescale-dependence effects that are caused by changes in instantaneous luminosity. It also

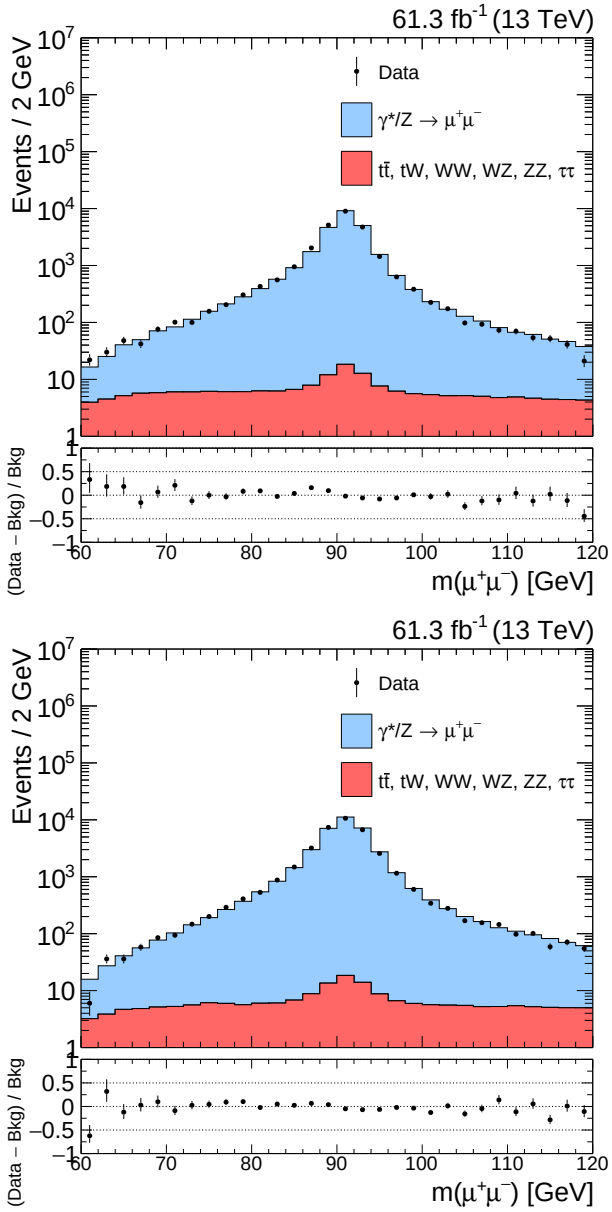

Figure 5.22: Histograms of 2018 Z-peak normalization region data and simulation after applying the 3.0-Monash scaling. The lower panel displays the ratio of data and simulation. Shown are dimuons from (top) the BB category and (bottom) the BE+EE dimuons.

simplifies the statistical uncertainty calculation because it reduces the number of prescales to one.

Figures 5.21 and 5.22 show the comparison of data and simulation at the Z-peak for the inclusive, BB, and BE+EE pseudorapidity categories. As discussed above, the Z-peak DY simulation is re-weighted to 3.0-Monash by leading generated muon p_{T}. These figures show the same data and simulation as the NR regions in Fig. 5.16 and Fig. 5.17. Table 5.3 gives the ratio of data to simulation R_Z as discussed above in Section 5.4. We do not compute a data-driven jet background for the Z-peak studies.

5.8 Statistical interpretation

In this section, we describe the formalism used to perform the statistical data analysis. First, the signal and background probability density functions (pdfs) are defined along with the relevant inputs to each. Next, we define the likelihood function used. Finally, we define the parameters of interest for limit-setting and for calculating the significance. We also describe the method used to perform the computation.

5.8.1 Signal model parametrization

We model the Z' signal shape as the convolution of a non-relativistic Breit-Wigner distribution with a double-sided Crystal-Ball distribution [60]. The non-relativistic Breit-Wigner distribution, defined in Eq. 5.6, models the intrinsic signal shape of the Z' resonance with parameters M'_Z and Γ'_Z describing the resonance mass value and resonance peak width. The set of widths considered are selected to be broadly applicable to a variety of BSM models that predict a Z' resonance. In this analysis we consider a width of $\Gamma'_Z/M'_Z = 0.6\%$. These narrow relative widths together with, as discussed later, the narrow fit window considered around the Breit-Wigner peak mean that the relativistic and non-relativistic Breit-Wigner functions are functionally equivalent. Without any relevant loss in precision, we choose to

use the non-relativistic formulation:

$$\texttt{BW}(m|M_{Z'},\Gamma_{Z'}) = \frac{N}{(m-M_{Z'})^2 + \left(\frac{\Gamma_{Z'}}{2}\right)^2}. \tag{5.6}$$

The double-sided Crystal-Ball distribution is defined in Eq. 5.7. We referred to this distribution as "DSCB" in the text and equations that follow. The DSCB is Gaussian distribution at its core, with parameter σ to describe the detector resolution, and μ for the mean. The tails are modeled as a power-law, with parameters α_L, n_L, α_R, and n_R to model the non-Gaussian tail effects on the reconstructed dimuon mass, like muon bremsstrahlung.

$$\texttt{DSCB}(m|\mu,\sigma,\alpha_L,n_L,\alpha_R,n_R) = N \cdot \left\{ \begin{array}{ll} \frac{\left(\frac{n_L}{\alpha_L}\right)^{n_L}\cdot\exp(-\alpha_L^2/2)}{\left(\frac{n_L}{\alpha_L}-\alpha_L-m\right)^{n_L}}, & \text{for } m < \alpha_L \\ \exp\left(-\frac{(x-\mu)^2}{2\sigma^2}\right), & \text{for } -\alpha_L \leq m \leq \alpha_R \\ \frac{\left(\frac{n_R}{\alpha_R}\right)^{n_R}\cdot\exp(-\alpha_R^2/2)}{\left(\frac{n_L}{\alpha_R}-\alpha_R-m\right)^{n_R}}, & \text{for } \alpha_R < m \end{array} \right\} \tag{5.7}$$

The full signal pdf is defined in Eq. 5.8:

$$f_{\text{sig}}(m_i|M'_Z,\Gamma'_Z,\sigma,\alpha_L,n_L,\alpha_R,n_R) = \texttt{BW}(m|M_{Z'},\Gamma_{Z'}) \otimes \texttt{DSCB}(m|\sigma,M_{Z'},\alpha_L,n_L,\alpha_R,n_R), \tag{5.8}$$

where the $\otimes$ symbol denotes the convolution of the two pdfs.

5.8.1.1 Mass resolution parametrization

We estimate the parameters of the DSCB function using the DY simulation described in Section 5.2. In bins of generated dimuon mass we fit the DSCB function to distributions of the dimuon mass relative residual,

$$R_{\text{RECO-GEN}} = \frac{m_{\text{RECO}} - m_{\text{GEN}}}{m_{\text{GEN}}}, \tag{5.9}$$

We perform the fit separately for the two analysis pseudorapidity categories, BB and BE+EE. As described above, the effects muon bremsstrahlung due to the additional material in the endcap region of the detector make splitting the resolution calculation into pseudorapidity

categories important, especially at high energy were these effects are more pronounced. Figure 5.23 displays example relative residuals, $R_{\text{RECO-GEN}}$, for (left) the BB category in a low mass bin and for (right) the BE+EE category in a high mass bin. These two distributions together represent a "best case" and a "worst case" scenario of the dimuon mass resolution. For the "best case" scenario shown the fitted Gaussian sigma represents a relative resolution of 1.25% and in the "worst case" the fitted sigma represents a relative resolution of 6.73%.

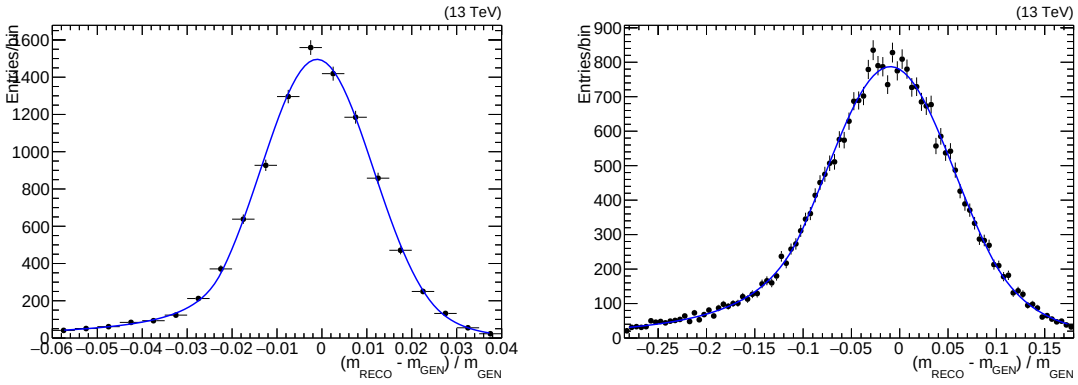

Figure 5.23: Relative mass residual, $(m_{\text{RECO}} - m_{\text{GEN}})/m_{\text{GEN}}$, distributions for dimuons (left) in the barrel-barrel pseudorapidity category and $120 \leq m_{\mu^+\mu^-} < 200\,\text{GeV}$ and (right) in the barrel-endcap + endcap-endcap pseudorapidity category and $4500 \leq m_{\mu^+\mu^-} < 5500\,\text{GeV}$ with the (blue curve) double-sided Crystal-Ball fits overlaid.

We evaluate the systematic uncertainty on the mass resolution by varying the `DSCB` fit windows and the bin widths of the relative residual distributions. We find that the fitted Gaussian σ (the resolution) changes by approximately 8.5%. We take this value as the systematic uncertainty. This systematic uncertainty is incorporated as an overall increase in the size of the uncertainty on the fitted Gaussian σ.

We also validate the mass resolution at the Z-peak by studying the Z-peak resolution as a function of muon p_{T} in data and simulation. In this method, we compare the residuals of the reconstructed mass and the resonance mass of the Z boson. Using this method, we find that the relative resolution measured in data is approximately 15% worse than the resolution in simulation for the the BE+EE category. The difference is negligible in the BB category.

The simulated dimuon masses in the BE+EE category of the DY simulation are therefore "smeared" by an additional 15% of the dimuon mass resolution so to match the resolution obtained in data. That is, event-by-event we smear the reconstructed dimuon masses by replacing the reconstructed dimuon mass with a new mass obtained by sampling Gaussian distribution with mean equal to the the event's dimuon reconstructed mass and a Gaussian sigma given by the formula,

$$\sigma_{\text{smear}} = \sqrt{\sigma^2_{\text{data}} - \sigma^2_{\text{MC}}} = \sqrt{(1.15 \times \sigma_{\text{MC}})^2 - \sigma^2_{\text{MC}}} = 0.568 \times \sigma_{MC}. \tag{5.10}$$

Here, σ_{MC} is evaluated according to the resolution parametrization curves defined by Eq. 5.11 before any additional smearing is applied.

We then plot the fitted relative mass resolutions (fitted Gaussian σ) extracted from the `DSCB` fits as a function of dimuon mass. For use with the statistical software, we parametrize the points using a fourth order polynomial given here:

$$\frac{\sigma(m)}{m} = A + B \cdot m + C \cdot m^2 + D \cdot m^3 + E \cdot m^4. \tag{5.11}$$

Figure 5.24 shows the dimuon mass resolution as a function of generated dimuon mass after applying the systematic uncertainties and additional Gaussian smearing for the (red) BB category and (green) BE+EE category. As expected, the mass resolution is worse in the BE+EE category than in the BB category.

5.8.1.2 Mass scale parametrization

The dimuon mass scale is sensitive to effects on the muon p_{T} scale. At high muon p_{T}, this implies that effects due to detector alignment and radiative losses have impacts on the calculation of the dimuon mass. To determine the muon p_{T} scale bias at high-p_{T} we use the GE method described in Section 4.4. This method produces a map of muon track curvature biases as a function of muon η and ϕ.

To compute the effect of the muon p_{T} scale bias on the dimuon mass, we perform pseudoexperiments where the values for each bin in the GE map are randomly chosen from a

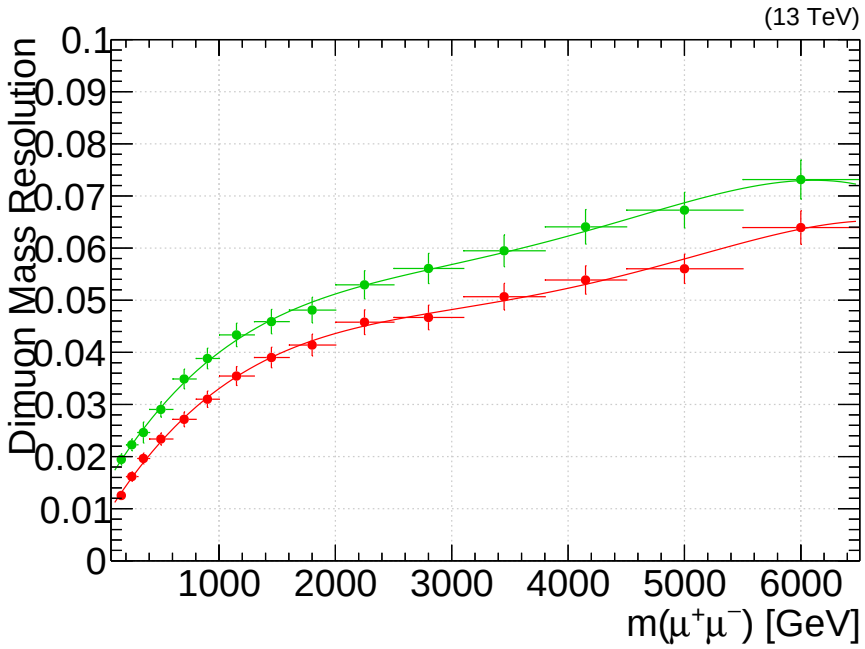

Figure 5.24: Relative dimuon mass resolution parametrization as a function of mass for (red) BB dimuons and (green) BE+EE dimuons. The BE+EE curves are those obtained post-smearing.

Gaussian distribution with mean equal to the measured bias κ_b and width equal to the uncertainty on the measured bias $\delta\kappa_b$. We also constrain the sign of the randomly sampled bias if both $\kappa_b + \delta\kappa_b$ and $\kappa_b - \delta\kappa_b$ have the same sign. The map is sampled individually for each muon and we calculate the dimuon mass with the corrected muon p_{T} values. For each pseudoexperiment we compute the mass scale uncertainty as the ratio of the corrected and uncorrected mass distributions as a function of the uncorrected mass. We perform 50 pseudoexperiments and take the mass scale uncertainty as the average scale bias over the individual pseudoexperiments. At 5 TeV, we observe that the mass scale is +1% and increases for both BB and BE+EE categories. Below 5 TeV, the mass scale bias is close to zero. We parametrize the mass scale uncertainty as a fifth-order polynomial.

5.8.1.3 Signal acceptance and efficiency parametrization

We evaluate the signal acceptance and efficiency by studying DY simulation. The acceptance for each pseudorapidity category is defined at generator-level as the number of dimuons that decay within the each category divided by the total number of generated dimuons. Efficiencies are defined as ability for CMS to trigger, reconstruct, and identify dimuon events. These efficiencies can be defined with respect to the acceptance, each other, or to the total number of simulated dimuons.

Figure 5.25 shows some of these curves separately for (left) the inclusive pseudorapidity category (both muons within detector acceptance, $|\eta| \leq 2.4$), (middle) the BB category (both muons within the barrel region of the detector, $|\eta| \leq 1.2$, and (right) the BE+EE category (at least one muon in the endcap region of the detector, defined as $1.2 < |\eta| \leq 1.2$). In the figure are curves for (blue) the fraction of generated dimuons within acceptance, (green) the fraction of dimuons that passed the trigger requirement with respect to dimuons in acceptance, (red) the fraction of dimuons that were reconstructed and passed the event selection with respect to the dimuons that triggered and were within acceptance, and finally (black) the combined fraction of dimuons within acceptance and satisfied the trigger, reconstruction, and selection requirements with respect to the total number of generated dimuons. The red curve is an ad-hoc fit to parametrize the total acceptance and efficiency curve (the black points). The trigger and selection criteria were described in Section 5.3. We use these acceptance and efficiency parametrizations all spin-1 Z' resonance interpretations.

We obtain systematic uncertainties of the dimuon trigger, selection, and reconstruction efficiencies by considering estimates of the corresponding muon uncertainties based on studies performed by the group dedicated to studying muon objects in CMS. For both the dimuon trigger and selection efficiencies, we assign a uniform $\pm 1\%$ systematic uncertainty for both the BB and BE+EE categories. For the dimuon reconstruction efficiency, we assign a one-sided uniform -1% systematic uncertainty for the BB category and a one-sided mass-dependent systematic uncertainty for the BE+EE category. For the BE+EE category, the dimuon reconstruction efficiency uncertainty is found to be -1% and at 2 TeV and -2% at 6 TeV.

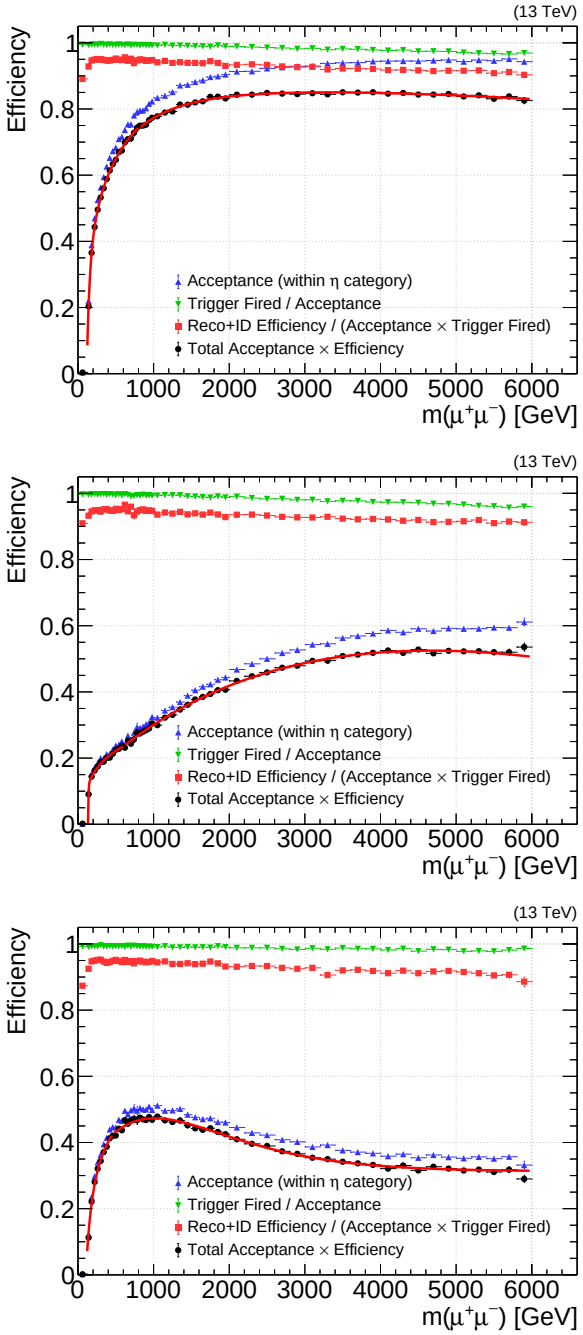

Figure 5.25: Curves for dimuon (blue) acceptance, (green) trigger efficiency, (red) reconstruction and selection efficiency, and (black) total acceptance plus trigger, reconstruction, and selection efficiency efficiency fractions for the (left) inclusive pseudorapidity category, (middle) BB category, and (right) BE+EE category.

We compute the total systematic uncertainty on the dimuon efficiency by summing these contributions in quadrature.

5.8.2 Background parametrization

The functional form of the background pdf is a smoothly falling curve chosen to describe the SM background predictions from simulation. For each analysis category, we fit the total background prediction with the fit separated into a low-mass region ($120 < m_{\mu^+\mu^-} < 500\,\text{GeV}$) and a high-mass region ($500 < m_{\mu^+\mu^-} < 6000\,\text{GeV}$). Equation 5.12 gives the definition of the functional form.

$$f_{bkg}(m|\alpha,\boldsymbol{\gamma},\beta,\boldsymbol{\delta}) = \begin{cases} m^{\alpha}\exp\left(\sum_{i=0}^{2}\gamma_i m^i\right), & \text{if } m \leq 500\,\text{GeV} \\ m^{\beta}\exp\left(\sum_{i=0}^{3}\delta_i m^i\right), & \text{if } m > 500\,\text{GeV} \end{cases} \tag{5.12}$$

Figures 5.26 and 5.27 show the results of the background pdf fits to Eq. 5.12 for the simulated SM backgrounds. In Fig. 5.26, we compare how the various corrections we apply to the simulation affect the background shape fit (see Section 5.4 for full details). In the figures the black curves are the result of the fit to the nominal simulation without any corrections applied; the green curves are the fits after re-weighting the DY and $t\bar{t}$ simulations to the 3.0-Monash predictions; and the purple curves are after the aforementioned 3.0-Monash re-weighting and also include the QCD NNLO, EWK NLO, and QED NLO corrections to the DY simulation. Coincidentally, the fits after applying all corrections (purple curves) are very similar to the uncorrected nominal simulation predictions (the black curves are underneath purple curves). In Fig. 5.27 we compare the background pdf fits in each analysis pseudorapidity category after applying all correction factors. The gap in the curves in both figures between the low and high mass fit functions at 500 GeV are an artifact of the software used to draw the fitted curves.

We evaluated the robustness of the upper limit on the cross section ratio with respect to changes in the background shape pdf by transforming the background shape pdf such

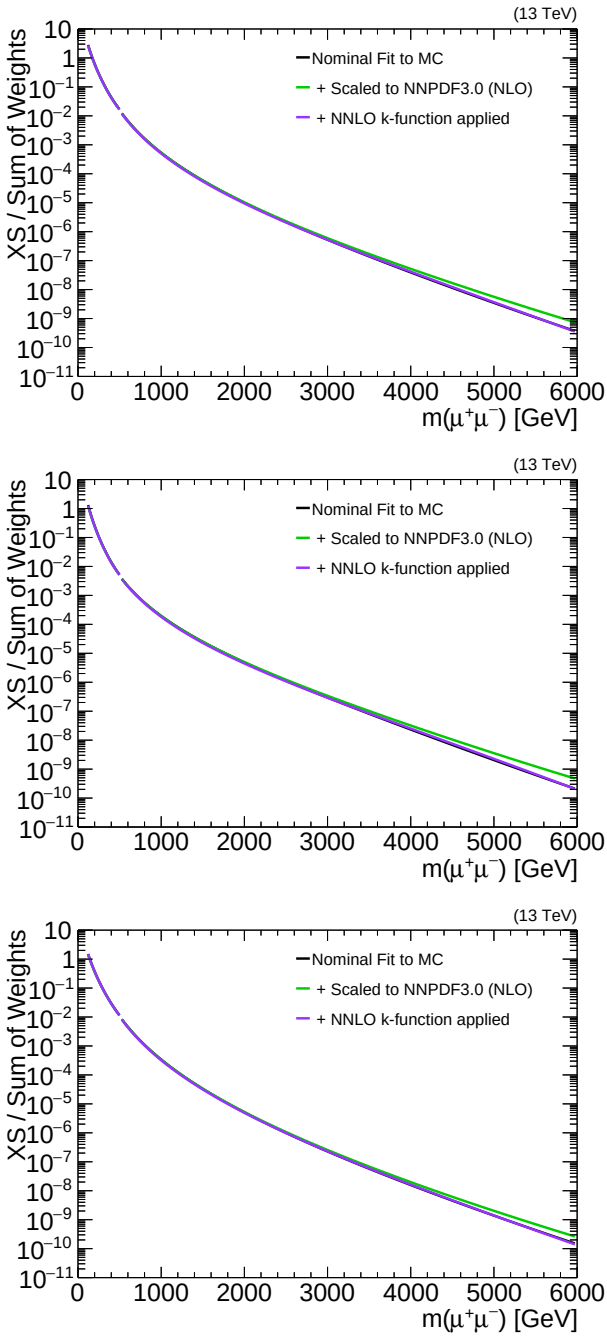

Figure 5.26: (Top row) Comparisons of the background shape fit while successively adding in the 3.0-Monash and NNLO correction factors described in the text. Shown are the (top) inclusive pseudorapidity category, (middle) BB category, and (bottom) BE+EE category.

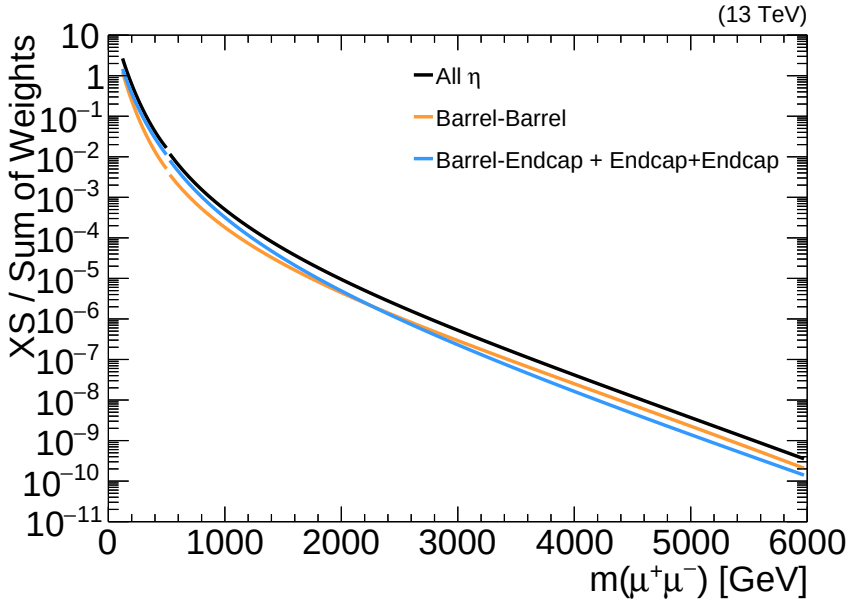

Figure 5.27: Comparison of fitted background shapes for all three analysis pseudorapidity categories with all corrections applied.

that there is zero change at the Z-peak and up to a $\pm 50\%$ linear increase/decrease in the background prediction at 3 TeV. We repeat the limit-setting procedure using these transformed background pdfs we find that the upper limits stay within $\pm 10\%$ of the nominal result using the original background pdf at low mass. At high mass, above where there is no data observed, there is a negligible change to the upper limits by altering the background shape. For the cases studied, as long as the assumption that the background shape remains monotonic and decreasing over the region where upper limits are set, the results are negligibly affected by any changes to the background shape.

5.8.3 Likelihood function

The full pdf that we use is the sum of the signal and background pdfs described above. Equation 5.13 gives the pdf,

$$f(m|\boldsymbol{\theta}_{\mathbf{sig}}, \boldsymbol{\theta}_{\mathbf{bkg}}, \boldsymbol{\nu}) = \mu_{\text{sig}} f_{\text{sig}}(m|\boldsymbol{\theta}_{\mathbf{sig}}, \boldsymbol{\nu}) + \mu_{\text{bkg}} f_{\text{bkg}}(m|\boldsymbol{\theta}_{\mathbf{bkg}}, \boldsymbol{\nu}) \tag{5.13}$$

where μ_{sig} is the signal event yield, μ_{bkg} is the background event yield, and μ is the total event yield is given by, $\mu = \mu_{\rm sig} + \mu_{\rm bkg}$. The vector $\boldsymbol{\theta}_{\mathbf{sig}}$ is the vector of signal model parameters described above: M'_Z, Γ'_Z, σ, α_L, n_L, α_R, and n_R and where $\boldsymbol{\theta}_{\mathbf{bkg}}$ is the vector of the background model parameters for low mass ($150 \leq m_{\mu^+\mu^-} < 500\,\text{GeV}$): γ_0, γ_1, γ_2, and α and for high mass ($m_{\mu^+\mu^-} \geq 500\,\text{GeV}$): δ_0, δ_1, δ_2, δ_3, and β. The vector $\boldsymbol{\nu}$ is the set of nuisance parameters.

We use an extended form of the unbinned likelihood using the sum of the signal and background pdfs;

$$\mathcal{L}(\mathbf{m}|\boldsymbol{\theta},\boldsymbol{\nu}) = \frac{\mu^N e^{-\mu}}{N!} \prod_{i=1}^{N} \left(\frac{\mu_{sig}(\boldsymbol{\theta},\boldsymbol{\nu})}{\mu} f_{sig}(m_i|\boldsymbol{\theta},\boldsymbol{\nu}) + \frac{\mu_{bkg}(\boldsymbol{\theta},\boldsymbol{\nu})}{\mu} f_{bkg}(m_i|\boldsymbol{\theta},\boldsymbol{\nu}) \right). \tag{5.14}$$

The product in the likelihood is taken over all events in the data set $\boldsymbol{m}$. We use the extended maximum likelihood (EML) formulation, which contains an explicit factor to estimate the Poisson mean, $\mu = \mu_{sig} + \mu_{bkg}$. In this formulation, the overall normalization of the likelihood and the shape parameters can be independently varied. For the pdf defined in Eq. 5.13, the estimates from the standard maximum likelihood and the EML will be identical [61].

The signal yield is a function of the parameter of interest, the ratio of the signal cross section to that of the Z:

$$\mu_{sig} = R_\sigma \frac{\epsilon_{Z'}}{\epsilon_Z} N_Z. \tag{5.15}$$

The calculation of the signal cross section is performed in a mass range of ± 6 times the the signal with, defined as the sum of the intrinsic width and mass resolution, about the hypothesized Z' resonance mass. We choose to fit to the data in a this narrow window for a few reasons. First, the narrow-window reduces BSM model-dependent effects, like effects due to $Z'/Z/\gamma^*$ interference or due to the PDFs. Thus, the measured signal cross sections correspond to the on-shell cross sections of a new resonance, and are therefore considered to a good approximation to be model-independent. Second, the narrow-window sets the level of the statistical uncertainty in the local background amplitude, which is chosen to dominate over the expected systematic uncertainties in the background shape. For cases where there are fewer than 100 events in the window, we symmetrically expand the window until there

are at least 100 events. As the mass spectrum at very high invariant masses falls with mass very rapidly, the events additional events come predominantly from the low mass side of the fit window as the window is expanded. Thus at high-mass, the minimum number of events is chosen to correspond a 10% statistical uncertainty in the background event yield, μ_{bkg}.

To quantify any excess in the observed data over the SM expectation, we scan over a range of hypothesized M'_Z masses with fixed hypothesized value of the width Γ'_Z and perform maximum-likelihood fits to the observed data and compute a significance estimator at each mass value. We use the following profile likelihood-ratio based significance estimator;

$$S_{\mathcal{L}} = \sqrt{-2\ln\lambda} = \sqrt{-2\ln\left(\frac{\mathcal{L}_B}{\mathcal{L}_{S+B}}\right)}, \tag{5.16}$$

where $\lambda = \mathcal{L}_B/\mathcal{L}_{S+B}$ is the profile likelihood ratio test statistic, $\mathcal{L}_{S+B} = \mathcal{L}(\hat{\mu}_{sig}, \hat{\boldsymbol{\nu}})$ denotes the likelihood function defined in Eq. 5.14 with the the profiled nuisance parameters $\hat{\boldsymbol{\nu}}$ for the maximum-likelihood estimate of the signal yield $\hat{\mu}_{sig}$, and $\mathcal{L}_B = \mathcal{L}(\mu_{sig} = 0, \hat{\hat{\boldsymbol{\nu}}})$ denotes the same likelihood function but under the background-only hypothesis with the profiled nuisance parameters $\hat{\hat{\boldsymbol{\nu}}}$ given the background-only hypothesis [62]. As we perform the scan over hypothesized mass values to compute the significance, both the mass hypothesis and the signal width are fixed in the likelihood function $\mathcal{L}_{S+B}$. Thus, as the nuisance parameters are independently profiled in the fits, $\mathcal{L}_{S+B}$ has one additional free parameter compared to $\mathcal{L}_B$: the signal yield μ_{sig}. By Wilk's theorem [63], $S^2_{\mathcal{L}}$ approaches a χ^2 distribution of one degree of freedom in the limit of large sample size. Thus, it follows that $S_{\mathcal{L}}$ is equivalent to the Gaussian tail probability in terms of the number of Gaussian standard deviations Z,

$$Z = S_{\mathcal{L}}. \tag{5.17}$$

Ref. [64] shows that this significance estimator reproduces Gaussian tail probabilities even in cases with small numbers of events. The corresponding p-value is then the fraction of the integral for which $\lambda > \lambda_{obs}$ from the distribution of λ generated from pseudoexperiments assuming the background-only hypothesis and λ_{obs} is the value obtained with the observed data for each mass hypothesis. The significance Z and the p-value are related by the equation,

$$Z = \sqrt{2}\,\mathtt{erf}^{-1}(1-2p), \tag{5.18}$$

where $\texttt{erf}^{-1}$ is the inverse error function.

Limits on the cross section defined by Eq. 5.2 are calculated at the 95% confidence level (CL) with Bayesian techniques known to have good frequentist properties. We use a positive uniform prior for the signal cross section. We model the the nuisance parameters for the uncertainties in efficiency, resolution, and mass scale with log-normal priors. The posterior pdf integration is performed by the Metropolis-Hastings Markov Chain Monte Carlo technique [65, 66] We also compute and compare to expected limits based on the SM background-only hypothesis. For the computation of both the significance and the upper limits on R_σ, we use the statistical framework developed for statistically combining the Higgs boson searches [67], which is based on the RooStats package [68].

As a technical device for the numerical integration, we choose a log-normal prior pdf with a width of 40% for the background yield. This prior pdf is a smooth and slowly varying function designed to ensure that the posterior pdf from the Bayesian calculation is dominated by the likelihood function. However, during studies of the robustness of our results to various choices, the 40% width of the log-normal prior on the background yield was found to be too large at low masses where the the width of the likelihood is much narrower than the width of this prior. statistical uncertainties. This leads to inefficient sampling of the posterior pdf in our Bayesian calculation. For this, we have decided to use a log-normal prior with a width of ± 3 times the statistical uncertainty for the background yield prior.

Specific signal model R_σ curves are constructed by dividing the LO cross section, calculated using the pythia 8.2 program with the NNPDF2.3 (NLO) PDF set [69], by the NNLO Z boson cross section of $1928 \pm 78\,\text{pb}$ calculated using the fewz 3.1 program [54]. As the limits we present correspond to the on-shell cross-section and the pythia event generator includes off-shell effects, we follow the recommendations in Ref. [70] and calculate the signal cross sections in a window of $\pm 5\% \sqrt{s}$ of the resonance mass. We account for NNLO QCD effects in the signal model cross section by multiplying by a mass independent k-factor, which was estimated at a dilepton mass of 4.5 TeV and found to be consistent with unity.

As discussed above, we use a mass window of ± 6 times the signal width to compute the

signal cross section in the observed data. The size of this sideband window is a choice made that is designed to ensure that the statistical uncertainty is dominant over any systematic uncertainties on the background pdf shape, such as those due to PDFs, the dimuon mass resolution, and the dimuon mass scale. However, with the amount of data we collected in 2018, the statistical uncertainty is no longer the dominant source of uncertainty at low mass. For example, in the 2018 data at a resonance mass of 400 GeV in the BB category the statistical uncertainty is approximately 1% while the systematic uncertainty is at the level of a few percent. Due to this small statistical uncertainty, we do not compute values of the significance for the low-mass region, $M'_Z < 800\,\text{GeV}$, which requires a more careful treatment of the systematic uncertainty of the background shape than we have available at this time. The CMS Z' analysis team is currently investigating methods to ensure the uncertainty on the background shape is properly treated.

5.9 Results

Figure 5.28 displays results computed using the 2018 data set in the dimuon decay channel (top) the significance scan and (bottom) the limit setting on R_σ. The largest local significance for $M_{Z'} > 1\,\text{TeV}$ occurs at $M_{Z'} = 2.7\,\text{TeV}$ corresponding to approximately $Z = 2.3$. The estimates of the local significance do not account for the so-called "look-elsewhere effect" (LEE) which takes into account the probability to observe a signal as large or larger than the one present in the data in the entire search range. We find the LEE-corrected or "global" significance by performing pseudoexperiments, which are drawn from the background-only pdf for $m_{\mu^+\mu^-} > 800\,\text{GeV}$. The global significance is then the fraction of pseudoexperiments with a significance equal to or greater than the local signifiance found in the data. For 150 pseudoexperiments, we find that 27% result in a significance of $Z = 2.3$ or higher, which corresponds to a global significance of $Z = 0.6$.

Figure 5.29 displays results computed using the full Run 2 data set in the dimuon decay channel (top) the significance scan and (bottom) the limit setting on R_σ. With the full Run 2 data set the largest local significance is observed at $M_{Z'} = 2.7\,\text{TeV}$ in the 2018 data set

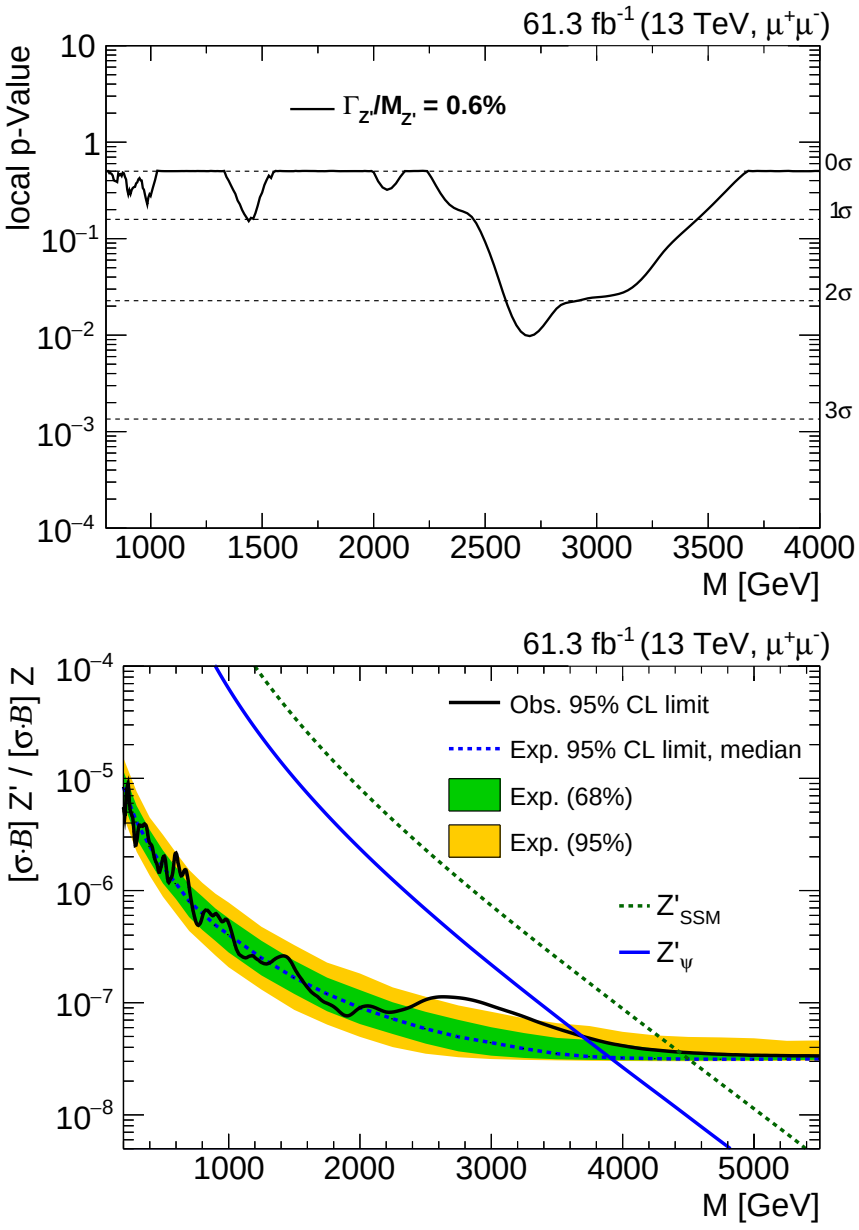

Figure 5.28: Results for the 2018 data set in the dimuon channel. Shown are (top) the observed local significance and (bottom) 95% CL upper limits on the production cross section times branching fraction. The results are computed assuming a relative width $\Gamma_{Z'}/M_{Z'} = 0.6\%$. The shaded bands in the bottom plot correspond to the 68% and 95% quantiles for the expected limits. Theoretical predictions for two benchmark models, Z'_{SSM} and Z'_{ψ} are shown for comparison.

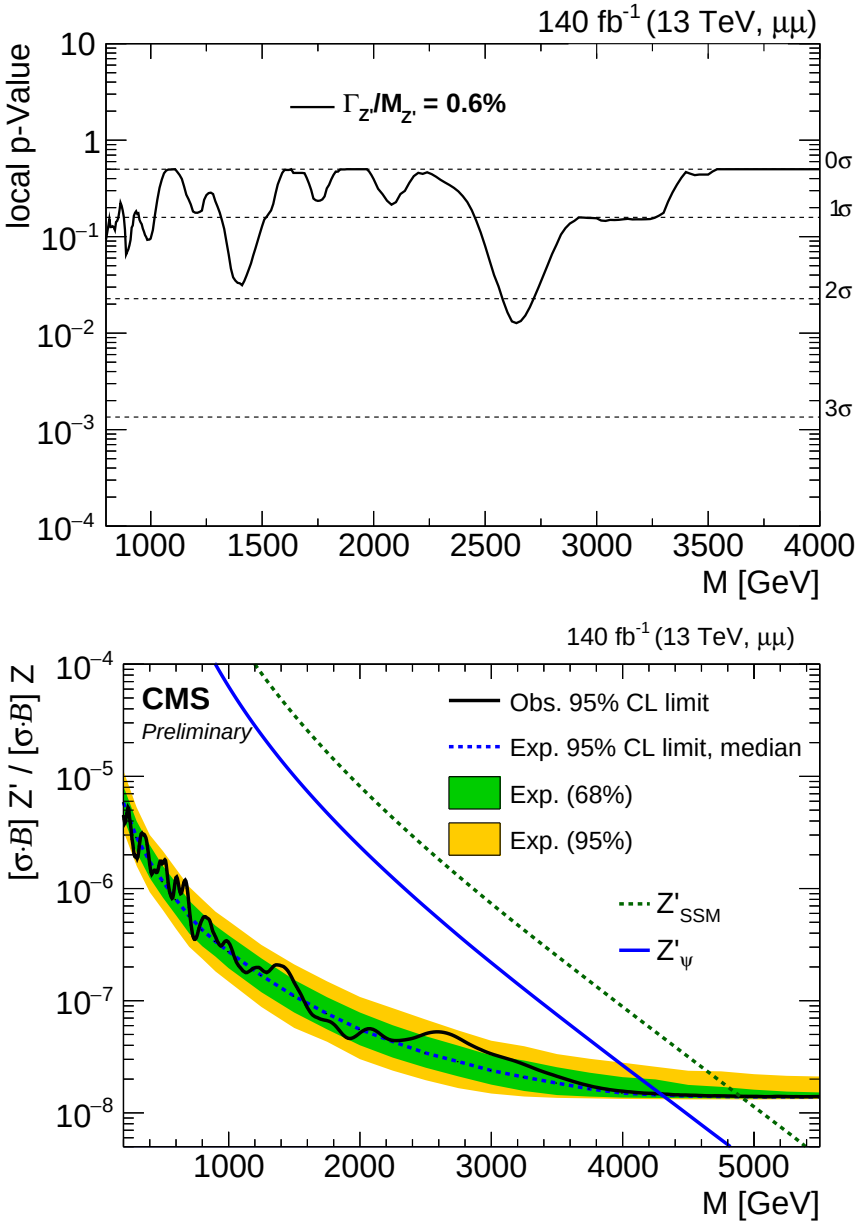

Figure 5.29: Results for the full Run 2 data set in the dimuon channel. Shown are (top) the observed local significance and (bottom) 95% CL upper limits on the production cross section times branching fraction. The results are computed assuming a relative width $\Gamma_{Z'}/M_{Z'} = 0.6\%$. The shaded bands in the bottom plot correspond to the 68% and 95% quantiles for the expected limits. Theoretical predictions for two benchmark models, Z'_{SSM} and Z'_{ψ} are shown for comparison. The bottom figure is reproduced from Ref. [41].

shrinks to approximately $Z = 1.6$.

We also compute the results including the dielectron channel, which we do not discuss here. Figure 5.30 displays results using the full Run 2 dataset in the combined dimuon and dielectron decay channels of (top) the significance scan and (bottom) the limit setting on R_σ. The largest local significance at high mass in the combined dielectron and dimuon Run 2 data set occurs at $M'_Z = 3.4\,\text{TeV}$ corresponding to approximately $Z = 2.3$.

Channel	Z'_{SSM}		Z'_ψ	
	Obs. [TeV]	Exp. [TeV]	Obs. [TeV]	Exp. [TeV]
$\mu^+\mu^-$	4.89	4.90	4.29	4.30
$ee + \mu^+\mu^-$	5.15	5.14	4.56	4.55

Table 5.14: The observed and expected 95% CL lower limits on the masses of the two benchmark models, Z'_{SSM} and Z'_ψ. Shown are the limits for the dimuon channel and the combination with the dielectron channel. The limits are rounded to the nearest 10 GeV. This table is reproduced from Ref [41] with the dielectron-only results removed.

The corresponding 95% CL expected and observed lower mass limits for the two benchmark models with the Run 2 data sets, Z'_ψ and Z'_{SSM}, are shown in Table 5.14. For Z'_ψ and Z'_{SSM}, the lower mass limits from the combined dielectron and dimuon data sets from Run 2 are 4.56 TeV and 5.15 TeV, respectively.

5.10 Z' interference studies

Partially inspired by a deficit of high-mass events in the analysis of 2016 data [36] and also by the lack of a new high-mass dimuon resonance, we look to other methods to discover signs of a new Z' resonance. One such method is to use the $Z'/Z/\gamma^*$ interference structure. In this method, if a new resonance exists, but is beyond the reach of LHC collisions, then it is possible that we may observe a continuum deficit or a continuum excess of events in data compared to the SM background prediction.

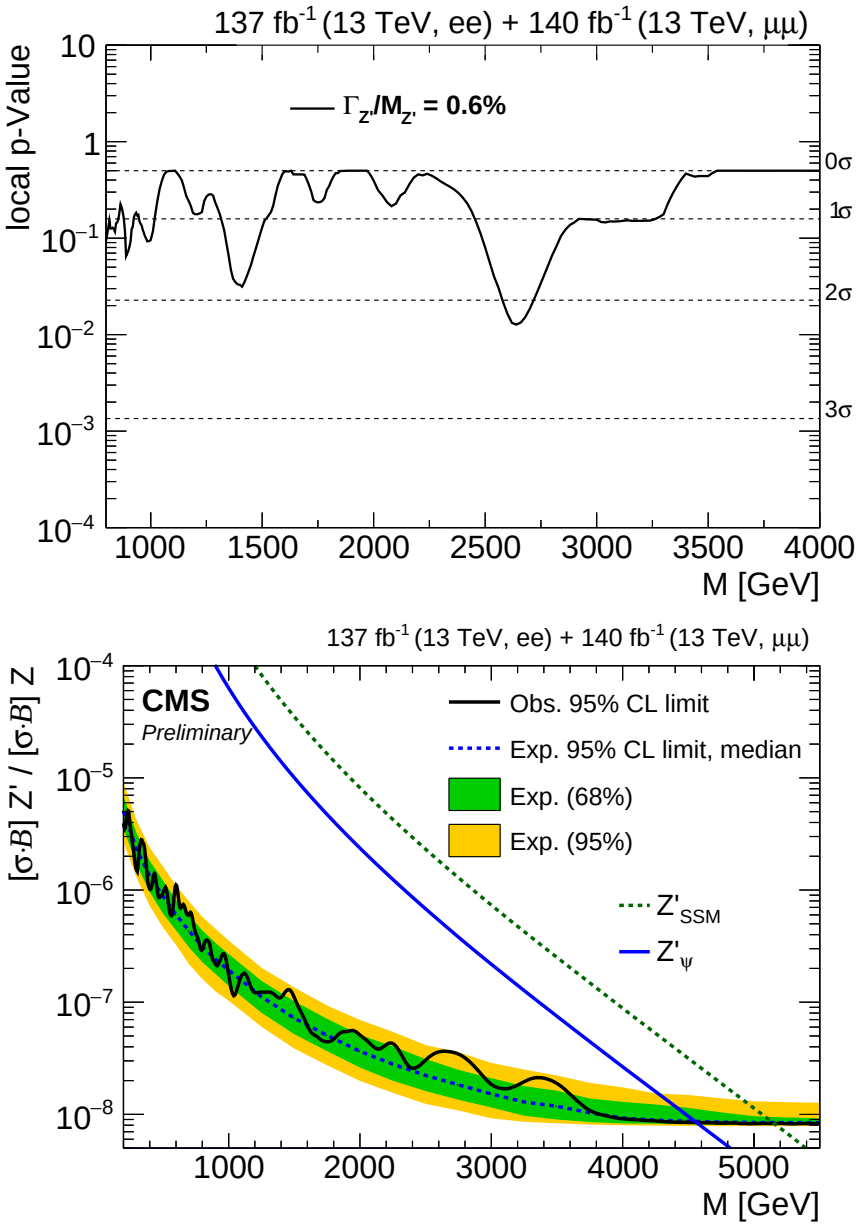

Figure 5.30: Results for the full Run 2 data set in the combined dimuon and dielectron channel. Shown are (top) the observed local significance and (bottom) 95% CL upper limits on the production cross section times branching fraction. The results are computed assuming a relative width $\Gamma_{Z'}/M_{Z'} = 0.6\%$. The shaded bands in the bottom plot correspond to the 68% and 95% quantiles for the expected limits. Theoretical predictions for two benchmark models, Z'_{SSM} and Z'_{ψ} are shown for comparison. The bottom figure is reproduced from Ref. [41].

In the study outlined in this section, we side-step many of the details necessary for a full result, and, instead, present a qualitative study of the feasibility of using $Z'/Z/\gamma^*$ interference as a complementary tool to the resonance search for discovery of BSM physics.

In this study we do not rely on the explicit presence of a resonance in the data, rather, it involves studying the high-mass dimuon continuum. Thus, many of the assumptions made in the resonance search described above are not valid. These include, but are not limited to, a precise knowledge of both the shape and the rate of the SM DY prediction, as well as from other SM backgrounds. In particular, EWK corrections are important as they can be different for DY and Z'. Also, as described in Section 2.2, uncertainties from the PDFs play an important role in both the DY and Z' prediction at high mass.

In general, interference from a Z' is highly model dependent as the size of the effect has dependence on the model-specific couplings to up- and down-type quarks for both left and right handedness, as well as the mass of the Z' resonance. Many models exist on the market that span much of the parameter space of couplings, but for the purposes of this study we restrict ourselves to the set of models described in Section 2.3. More discussion can be found elsewhere [10, 11, 12, 13].

We generate simulations of the full $Z'/Z/\gamma^*$ interference structure for several values of resonance mass for each model. The generation is done with PYTHIA and we use the NNPDF3.0 (NLO) PDF set with the CUETP8M1 UE tune. We also generate a DY-only simulation that is consistent with the Z' samples with the full interference.

Figure 5.31 displays a comparison of the mass distribution for a selected set of Z' models with the DY-only prediction for three different resonance masses: (top) 4 TeV, (middle) 6 TeV, and 8 TeV. The bottom panel in each of the plots is the ratio of the full $Z'/Z/\gamma^*$ prediction to Z/γ^*-only prediction. Shown are the Z'_{B-L}, Z'_Q, Z'_{T3L}, Z'_{SSM}, and Z'_ψ (denoted Z'_{SI} in the legend in the figure) models decaying to dimuons. To simulate the detector response, we smear each generated dimuon mass by the resolution obtained in the 2016 analysis. These models represent a set of models that exhibit "large" interference (Z'_Q), "medium" interference (Z'_{B-L}, Z'_{T3L}, and Z'_{SSM}), and "small" interference (Z'_ψ).

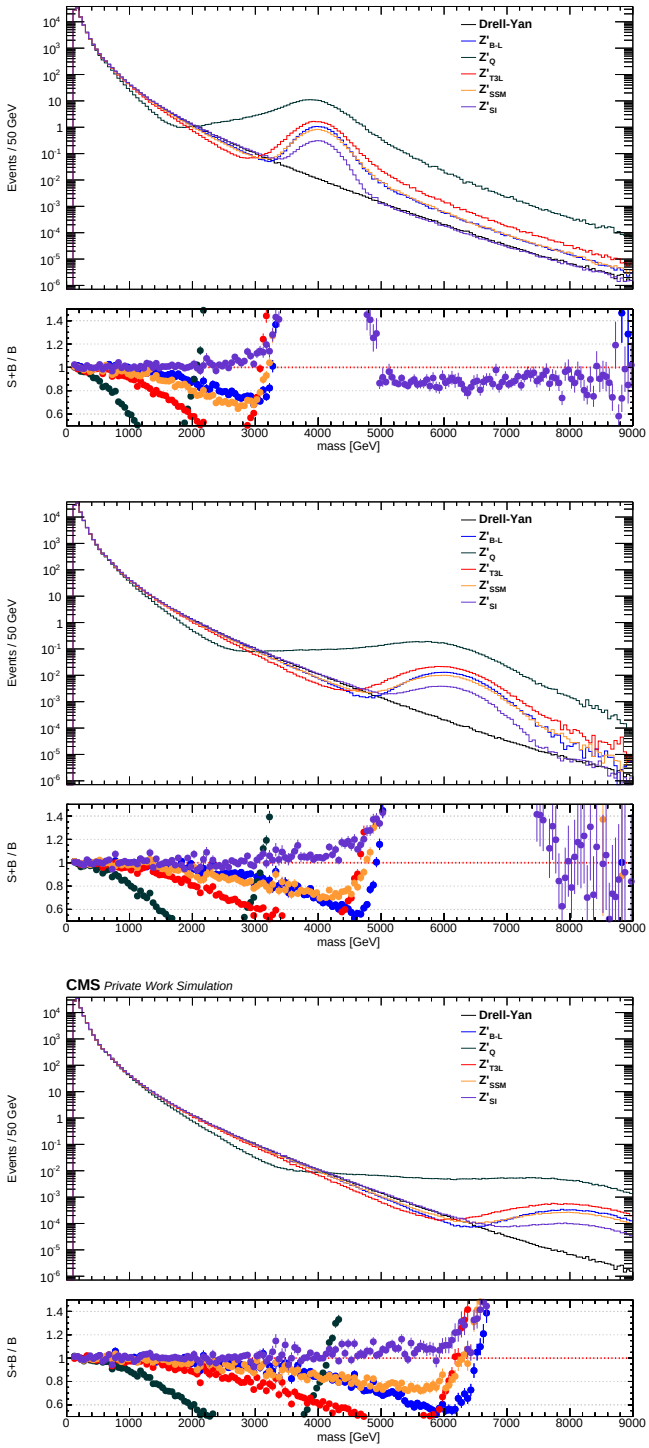

Figure 5.31: Comparison of a selected set of Z' models with full $Z'/Z/\gamma^*$ interference (colored curves) with the Z/γ^*-only prediction (black curve).

Among these models, we choose to narrow our focus on finding model that satisfies the following criteria:

- Destructive interference is visible (i.e. large) in mass range where we observe data, namely, 1–2 TeV and
- No events are visible from the resonance peak.

The two models that have the largest interference effect are the Z'_Q and Z'_{T3L}. To estimate the visibility of the interference effect we study pseudoexperiments generated from each of these models. For the following pseudodatasets, we generate enough data to be representative of the amount of data collected in the 2016 and 2017 data-taking years.

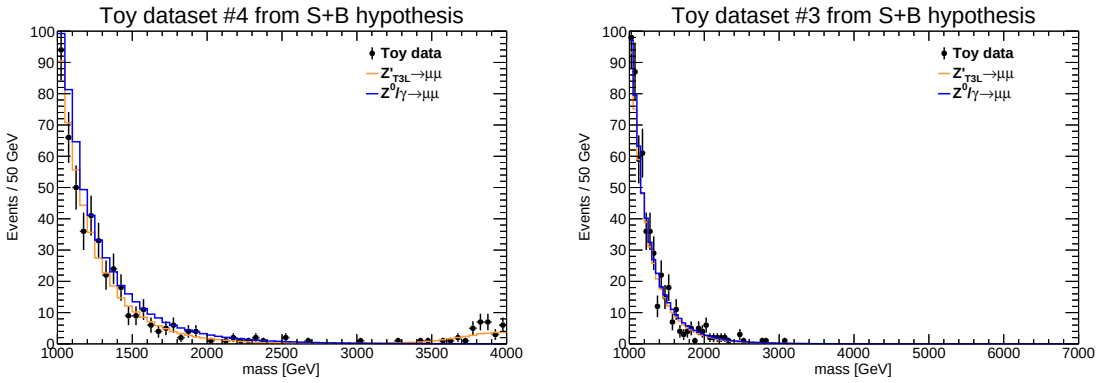

Figure 5.32: Comparison of (black data points) pseudodata generated with (orange curve) the Z'_{T3L} model with full interference and (blue curve) the DY-only prediction. Shown is pseudodata for a (left) 4 TeV resonance and (right) a 7 TeV resonance. The amount of pseudodata generated is taken to be representative of the amount of data collected in the 2016 and 2017 data taking years. Note the different horizontal axis ranges in the left and right figures.

Figure 5.32 shows two example pseudoexperiments for the Z'_{T3L} model. For a 4 TeV resonance (shown left), the interference effect is approximately 10–25% in the mass range 1–2 TeV. This would be an observable interference effect, however, the mass is still low enough such that this model would have been observed in the current observed data. If we raise the

resonance mass to 7 TeV (shown right), such that the peak is no longer visible in the current data, then the interference effect becomes negligible. Thus, Z'_{T3L} is not a good candidate to study interference with the current data.

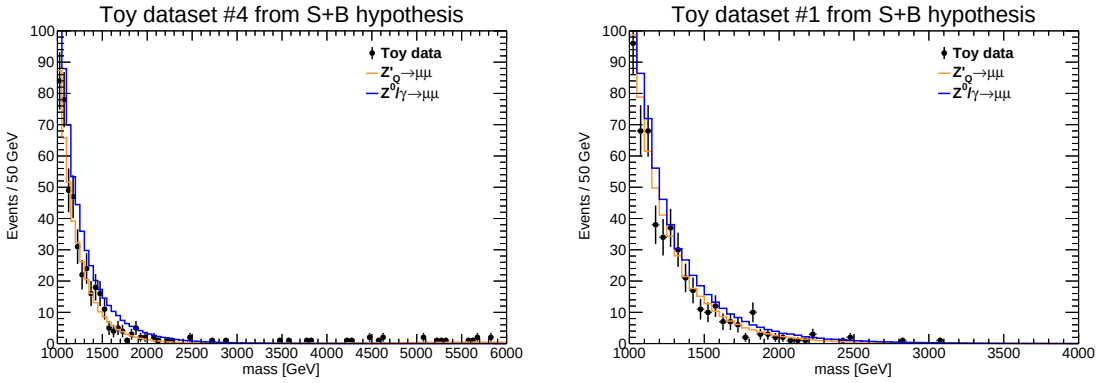

Figure 5.33: Comparison of (black data points) pseudodata generated with (orange curve) the Z'_Q model with full interference and (blue curve) the DY-only prediction. Shown is pseudodata for a (left) 6 TeV resonance and (right) a 9 TeV resonance. The amount of pseudodata generated is taken to be representative of the amount of data collected in the 2016 and 2017 data taking years. Note the different horizontal axis ranges in the left and right figures.

Figure 5.33 shows two example pseudoexperiments for the Z'_Q model. For a 6 TeV resonance (shown left), the interference effect is approximately 15–50% in the mass range 1–2 TeV. Like the case above, this would be an observable interference effect, however, the mass is still low enough such that this model would have been observed in the current data. If we raise the resonance mass to 9 TeV (shown right), then the interference effect changes to 10–40% in the mass range 1–2 TeV. Unlike any of the cases above, this mass is high enough such that we would not observe the resonance peak in the current data. For the 9 TeV resonance mass, the highest generated dimuon mass is approximately 3.1 TeV in this particular pseudoexperiment. Thus, Z'_Q is a good candidate to study interference with the current data.

Figure 5.34 shows a selection of resonance masses for the Z'_Q model. The lavender curve

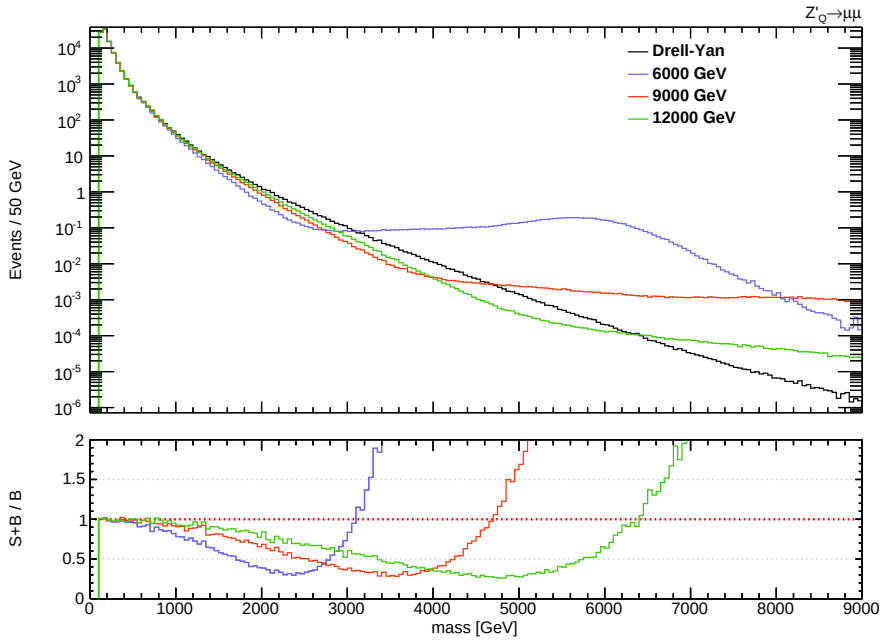

Figure 5.34: Comparison of the Z'_Q model for various resonance masses. Shown is (lavender curve) a 6 TeV resonance, (red curve) a 9 TeV resonance, and (green curve) a 12 TeV resonance.

shows a 6 TeV resonance, which is an example of a model that would have too many peak events. The red curve shows a 9 TeV resonance, which is an example of a model with the "optimal" sensitivity, which in this context means that the interference effect is large enough to be detectable without also observing the resonance peak. The green curve shows a 12 TeV resonance, which is an example of a model with too little interference.

As mentioned above, PDF sets can play an important role in DY and Z' predictions at high mass. Figure 5.35 (top panel) compares the prediction of the interference structure for various PDF sets for the Z'_Q model at 9 TeV and (bottom panel) compares the ratios of the interference structures to the NNPDF3.0 (NLO) prediction. The top plot compares predictions for the NNPDF3.0 (NLO), CT10 (NLO), and CT14 (NLO) PDF sets each generated with PYTHIA and the CUETP8M1 UE tune. The bottom plot compares predictions for the same NNPDF3.0 (NLO) PDF set with two versions of the NNPDF3.1 PDF set; an NLO version produced with the CP3 tune [48] and a special NNLO version with the CP5 tune

that contains only positive PDF replicas. (The details of the positive-replica only NNPDF3.1 (NNLO) PDF set are unimportant for this study.) Although the absolute prediction due to the PDFs and the UE tune can be different (not shown), each PDF set predicts a similar interference structure for a similar model.

We conclude with an eye toward future studies that are possible with the full Run 2 data set, as well as the data that is expected from the high-luminosity upgrade to the LHC. We have shown that a potential model, Z'_Q, exhibits features that enable future study; it has a large-enough interference effect for large-enough resonance masses such that it is not detectable with the current Run 2 data set.

5.11 Summary

In this chapter we present a search for a new high-mass resonance in the dimuon invariant mass spectrum in proton-proton collisions at $\sqrt{s} = 13\,\text{TeV}$ corresponding to an integrated luminosity of $61.3\,\text{fb}^{-1}$ taken in 2018. We also present results for the full Run 2 data set corresponding to an integrated luminosity of $139.7\,\text{fb}^{-1}$, as well as their combination with the dielectron channel. The observations are consistent with standard model prediction for all results shown. We set upper limits at the 95% confidence level on the ratio of the cross section times branching fraction for a new resonance to the cross section times branching fraction of the standard model Z boson. Corresponding lower mass limits are set for two benchmark models, the sequential standard model Z'_{SSM} and the E_6 gauge group inspired Z'_ψ at 5.1 TeV and 4.5 TeV, respectively. We also consider possible future studies complementary to the resonance search. We discuss studying the $Z'/Z/\gamma^*$ interference structure in the high-mass continuum as a tool for indirectly observing the presence of a resonance to large in mass to directly observe at current LHC collision energies.

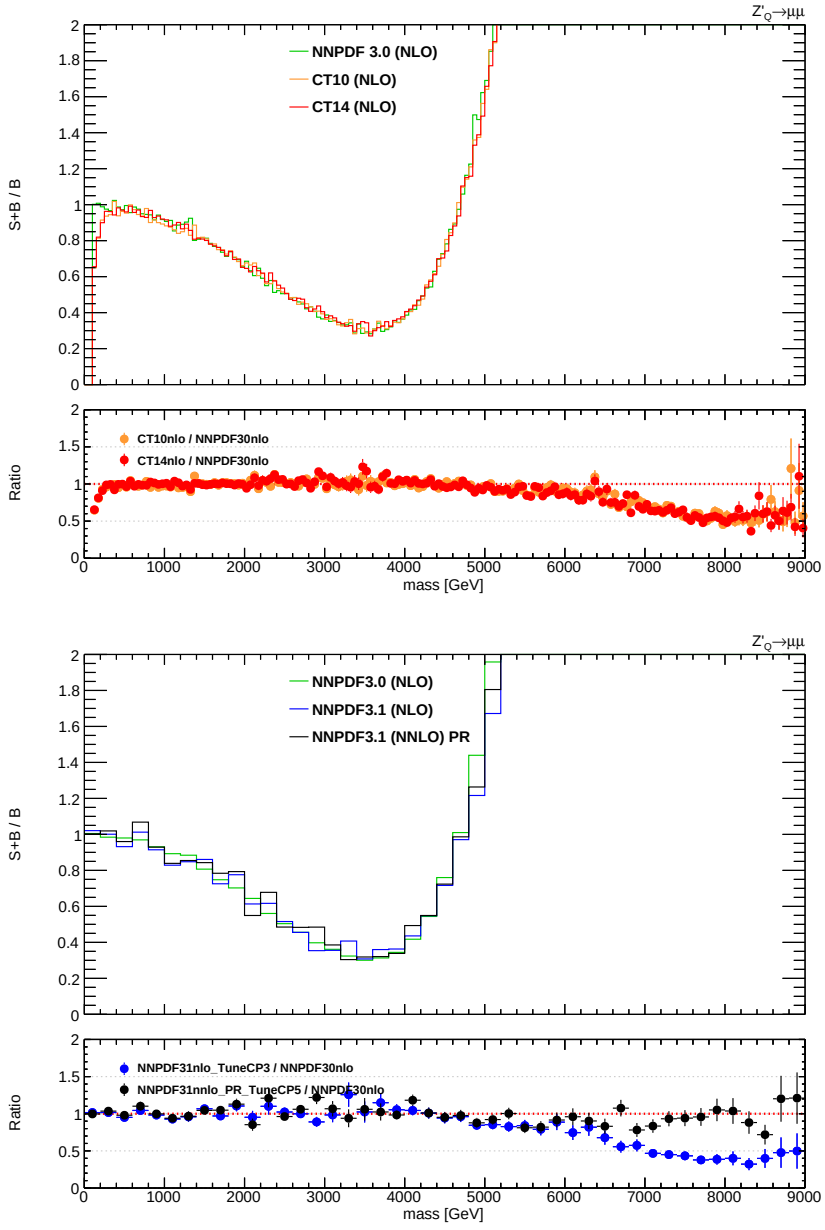

Figure 5.35: Comparison of the Z'_Q model at a 9 TeV resonance generated with various PDF sets. Plotted is (top panel) the ratio of the full $Z'/Z/\gamma^*$ simulation with interference to the Z/γ^*-only prediction and (bottom panel) the ratio of various PDF set predictions to the NNPDF3.0 (NLO) prediction. Shown are comparisons for (top figure) NNPDF3.0 (NLO), CT10 (NLO), and CT14 (NLO); and (bottom figure) NNPDF3.0 (NLO), NNPDF3.1 (NLO), and a special version of NNPDF3.1 (NNLO) that contains positive-only PDF replicas.

APPENDIX A

Study of neutron-induced background hits in CMS endcap muon detectors

Foreword

The work described in this appendix was performed in full collaboration with fellow UCLA graduate student Abhigyan Dasgupta under the supervision of our common advisor, Prof. Robert Cousins. Together the two students wrote a detailed draft internal CMS Detector Note DN-2017/019, reproduced below. Prof. Cousins also provided editing assistance, particularly in Section A.5. Abhigyan Dasgupta presented this work in a poster session [71] at 2017 European Physical Society Conference on High-Energy Physics (EPS-HEP), and wrote a conference note for the Proceedings [72]. Christian Schnaible presented this work in a talk at the the 2017 American Physical Society Meeting of the Division of Particles & Fields (APS-DPF) [73].

Abstract of the Appendix

Among the many challenges to be brought by the high luminosities of the HL-LHC is the impact of increased hit rates in the cathode strip chambers of the CMS endcap muon system. These chambers are used for all levels of trigger as well as offline reconstruction. Neutrons induce background hits via nuclear interactions and capture, followed by gamma emission and (mainly) Compton scatter off electrons that subsequently ionize the chamber gas. This note describes recent efforts to improve the understanding of such neutron-induced back-

ground through detailed comparison of CMS pp collision data, GEANT4 simulation, and the response of CMS detectors placed in the CERN high-intensity gamma irradiation facility, GIF++. Projections for the effect of such neutron-induced background hits on trigger and reconstruction at the HL-LHC are described.

A.1 Introduction

The high-luminosity upgrade to the CERN LHC (HL-LHC) will bring not only increased access to discovering new physics but increased background rates in CMS muon chambers [15, 74]. This note focuses on the study of neutron-induced background hits in CMS endcap cathode strip chambers (CSCs) due to their large active volume and forward placement in CMS [75, 76]. Neutrons induce hits in CSCs by producing photons, via either nuclear scattering or capture. These photons produce or scatter electrons, via Compton scattering, the photoelectric effect, or pair production; this ionization can either corrupt hits from desirable tracks in the event, or add extra background hits. This note describes efforts to quantify and characterize the effects of this neutron-induced ionization through analysis of Monte Carlo (MC) simulation of neutrons in CMS, as well as of CMS proton-proton (pp) collision data. The results are tied to analyses of muon test beam data at the CERN Gamma Irradiation Facility (GIF++), which allows us to study the effects of high background radiation on CSC performance and project the effects of neutron-induced background at the HL-LHC.

In minimum-bias pp collisions, forward hadronic interactions liberate neutrons from CMS calorimeters, shielding, and various other detector structures. These neutrons can carry several GeV or more of kinetic energy, propagating throughout the experimental cavern, detector materials, and shielding. They lose kinetic energy through many scattering interactions over the course of several milliseconds, and if not captured sooner, are eventually cooled to thermal equilibrium with the cavern environment, carrying kinetic energies of around 0.025 eV (300 K). There are three main processes by which neutrons lead to photons: inelastic scattering, resonant capture on nuclei, and thermal capture on nuclei [77].

Neutrons with several MeV of kinetic energy may scatter inelastically with detector and shielding material, producing one or more photons. In addition to undergoing inelastic scattering, neutrons may be captured by various nuclei, including iron, copper, and free hydrogen, resulting in excited isotopes of the original capturing nuclei with energies typically a few MeV greater than that of their ground states. The excited isotopes reach their ground states by emitting one or more photons. Resonant capture occurs when the kinetic energy of a neutron (typically of order keV) is such that the sum of the total neutron and target nucleus energies matches the total energy of a discrete excited state of the final-state isotope. For example, ^{56}Fe has a resonant neutron capture cross section at a neutron kinetic energy of 1.1 keV [77]. Thermal capture occurs when neutrons have reached sub-eV thermal energies, in a regime where the cross section for capture increases with decreasing neutron velocity. Throughout this note, any reference to neutron capture refers to both thermal and resonant neutron capture unless otherwise specified.

The photons produced from inelastic scattering and nuclear capture are typically of order MeV in energy. Once produced, the photons can propagate inside the gas volume of a CMS muon chamber where they predominantly scatter off electrons, but also produce electrons via pair production and the photoelectric effect. These scattered electrons can ionize the chamber gas and subsequently leave background hits.

Such hits contribute to aging of muon chambers as well as increased background rates. This note focuses on the effect that these increased background rates have on muon triggering and offline measurement and reconstruction of muons.

The identification of neutron-induced hits in CMS data is complicated by the fact that data from a CSC is read out only if the CSC trigger electronics identify a potential muon track (trigger primitive) in that CSC [78, 79, 80]. A muon leading to a trigger primitive can induce other hits in the CSC via e.g. bremsstrahlung or delta rays, or be accompanied by other charged particles from a jet in which the muon is embedded. Precision measurements of the ionization charge are read out through the main CMS data acquisition (DAQ) system only for a small fraction of the area of the CSC that is near the triggering muon, and are

particularly vulnerable to hits from these extra particles. Thus, for most of the studies in this paper, we use instead the diagnostic information for the whole chamber that is passed to the DAQ by the trigger electronics (the so-called "trigger path"). These trigger path data are much less precise than the high-precision charge data read out by the main DAQ [81], but since they include information from the entire chamber, they allow us to look for neutron-induced hits in areas of the chamber that are further away from the triggering muon. With various additional selection criteria, sufficient samples of neutron-induced hits are obtained for detailed studies of rates in CMS, for comparison to simulated CMS data and GIF++ data.

Section A.2 is a brief overview of cathode strip chambers and the on-chamber trigger electronics in the CMS detector. Section A.3 describes GEANT4 simulation of pp collisions, including neutron-induced hits. Section A.4 describes the selections we use to isolate a sample of neutron-induced hits in CMS data. Section A.5 describes the procedure by which we normalize our neutron-induced hits counts into hit rates. Sections A.6 and A.7 describe studies of GIF++ data and CMS data from which we predict the effect of increased radiation in HL-LHC-like conditions.

A.2 Cathode Strip Chambers in the CMS Detector

A.2.1 Cathode Strip Chambers and Trigger Electronics

The CSC system in the endcap muon detection system of CMS [79] contains 540 chambers in the endcaps. Each endcap has 4 stations numbered from 1 to 4, and each station contains two or three rings of chambers. A chamber is uniquely specified by a string of the form ME$\pm S/R/C$, where $\pm$ refers to either the $+$ or $-$ endcap, S is the station number, R is the ring number, and C is the chamber number, e.g. ME+1/1/36. Part of this notation may be omitted when referring to groups of chambers; for example, we refer to ME1/1 or ME2/1 chambers, i.e. chambers in the innermost ring of the first or second stations, respectively, in either endcap.

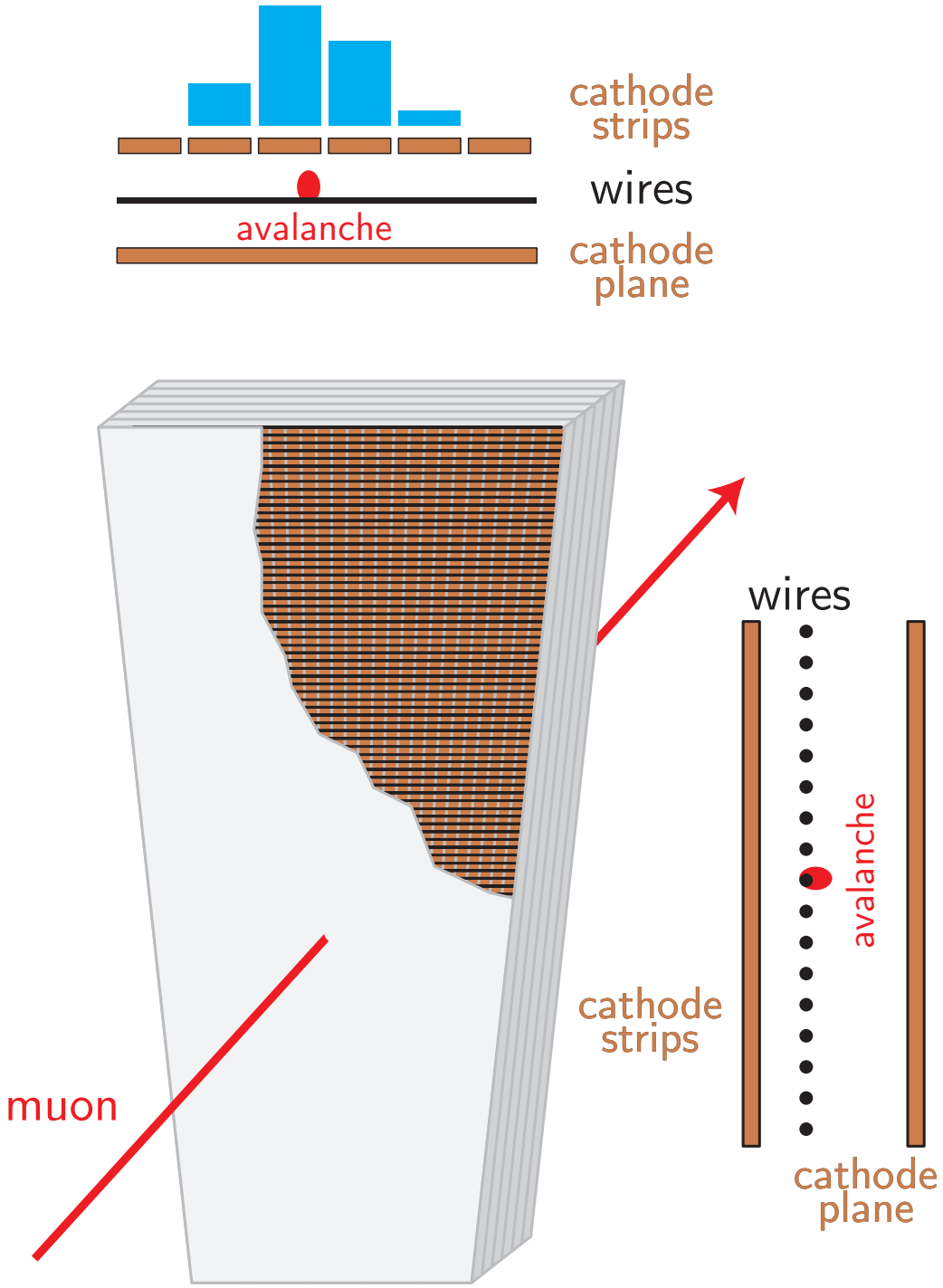

Figure A.1: Diagram and principle of operation of a CSC endcap muon chamber in CMS

The chambers in each station are arranged within a circle perpendicular to the z axis of CMS, with the narrow end of their trapezoidal shapes closer to the beam line. Figure A.1 contains a diagram illustrating the principle of operation of a CSC. Each CSC is a multi-wire proportional chamber consisting of 6 layers, with each layer lying in an r-ϕ plane of CMS. Each layer contains an ionization gas layer consisting of 50% CO_2, 40% Ar, and 10% CF_4 in between a plane of copper cathode strips and a plane of anode wires. The strips extend from the narrow end to the wide end, along the r direction, at constant z and ϕ coordinates; the wires extend parallel to the narrow and wide ends, approximately along the ϕ direction, at constant z and approximately constant r coordinates. The wires are spaced 2.5–3.5 mm apart, arranged in groups of 5–16 mm (wire groups, or WG), and kept at a high voltage of 2900–3600 V with respect to the cathode strips.

A muon ionizes the gas, and the resulting electrons drift towards the wires, causing an avalanche of charge that induces an opposite charge on the cathode strips. The notable feature of a CSC is excellent position resolution in the ϕ direction achieved by precision cathode charge readout and interpolation. A comparator network provides half-strip hit position resolution at hardware trigger level. Cathode comparator hits give the layer and half-strip position and anode wire group hits give the layer and wire group number. A general digitized detector hit – a cathode strip hit or a wire group hit – is referred to as a digi, and therefore the strip (or half-strip) number or wire group number may also generally be referred to as a digi number. A digi may refer to a hit at trigger level or at offline level [78, 81, 80].

As illustrated in Fig. A.2, the anode wire group hits and comparator half-strip hits are transmitted to circuits that perform low-level local pattern recognition on the hits in the six layers of a chamber. Candidate tracks from charged particles are identified separately in the cathode strips and anode wires and then combined. Anode local charged tracks (ALCTs) are formed by ALCT boards, which receive data for each plane from anode front end boards (AFEBs). Cathode local charged tracks (CLCTs) are formed in two steps within the trigger motherboard (TMB) from data transmitted by cathode front end boards (CFEBs). First,

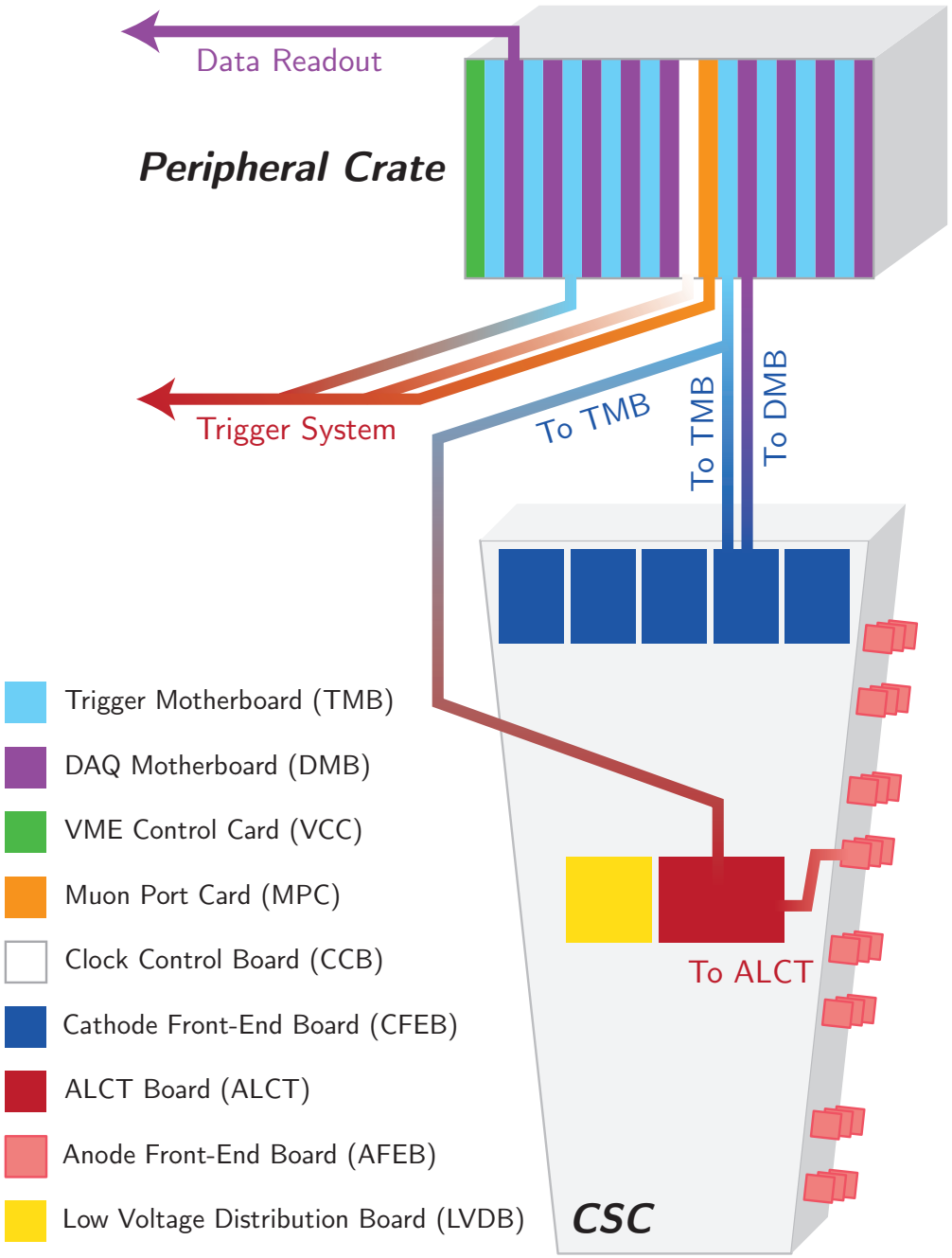

Figure A.2: Diagram of the CSC electronics system in CMS

a set of loose requirements, for example on the number of layers hit, are applied to the CFEB data. These are known as the pre-trigger, and a candidate track that passes these requirements is called a pre-CLCT. Then, a set of tighter requirements are applied, and a pre-CLCT that passes these requirements becomes a CLCT. The TMB also receives ALCTs from the ALCT boards and combines coincidences of ALCTs and CLCTs to create local charged tracks (LCTs). The CSC firmware has programmable requirements for the various pattern recognition steps, e.g. for the number of layers hit, the spatial distribution of the hits, the temporal distribution of the hits, and the time window for coincidence of the ALCTs and CLCTs.

These trigger data, referred to as trigger primitives, are transmitted to the endcap muon trigger system and also inserted into the DAQ stream via the DAQ motherboard (DMB). For offline use, the DMB also reads out the high-precision analog-to-digital converter (ADC) charge measurement for each cathode strip when the CSC trigger electronics receive and accept a signal from the CMS Level-1 trigger. However, these ADC charge measurement data are read only from CFEBs for which a pre-CLCT was formed, which constitute only a fraction of a chamber. As noted above, muon-induced background hits make these data of limited use in our current studies of neutron-induced hits.

When the TMB reads out data, both early and late detector hits with respect to the triggering muon are inserted into the DAQ stream. Hit times with respect to the muon are binned into 16 readout time bins of 25 ns each, with the muon usually inducing hits in time bins 7 or 8. The chamber electronics can thus read out detector hits that occur approximately 200 ns (8 time bins) before and after the muon hits.

A.3 Geant4 MC Simulation for Neutron Studies

A.3.1 Geant4 MC Simulation Setup

To better understand the basic nuclear interactions that may result in background hits in CSCs, we turn to simulation. We used the GEANT4 simulation package to privately simulate

minimum-bias proton-proton (pp) collision events [82, 49, 83, 84]. To study neutron background effectively, a few specific modifications to the default CMS simulation configurations were necessary [85].

- To accommodate the long lifetimes of the neutrons under study, we extended the tracking time of all particles to 10 s.
- To accommodate the low energies of the neutrons under study, we removed any particle energy thresholds where they existed.
- To properly model low-energy neutrons, we enabled a feature in the GEANT4 thermal neutron scattering routine that models nuclei at room temperature. The standard GEANT4 routine models the temperature of the nuclei in the detector at 0 K and as a result artificially cools neutrons down to well below thermal energies. Figure A.3 displays histograms of the kinetic energy of neutrons just before their capture on a nucleus, before and after the new feature was enabled. The dashed line is at 0.025 eV; without the feature enabled, the low energy peak of captured neutrons is well below thermal energies, whereas with it enabled, the low energy peak is at thermal energies.
- To retain all simulated electronics signals in simulated CSCs, we assigned simulated hits produced after times longer than 200 ns a time of 200 ns in the CSC digitization simulation module. This is to ensure that all hits from a single simulated pp collision are retained, rather than just the hits that occur within the simulated detectors' limited time readout window of 400 ns.

Two versions of GEANT4 neutron interaction packages are compared:

- HP: "High Precision" package that parametrizes existing experimental nuclear data for neutron interaction cross sections
- XS: intended for CPU optimization, derived from HP by approximating detailed parameterizations in HP with averages

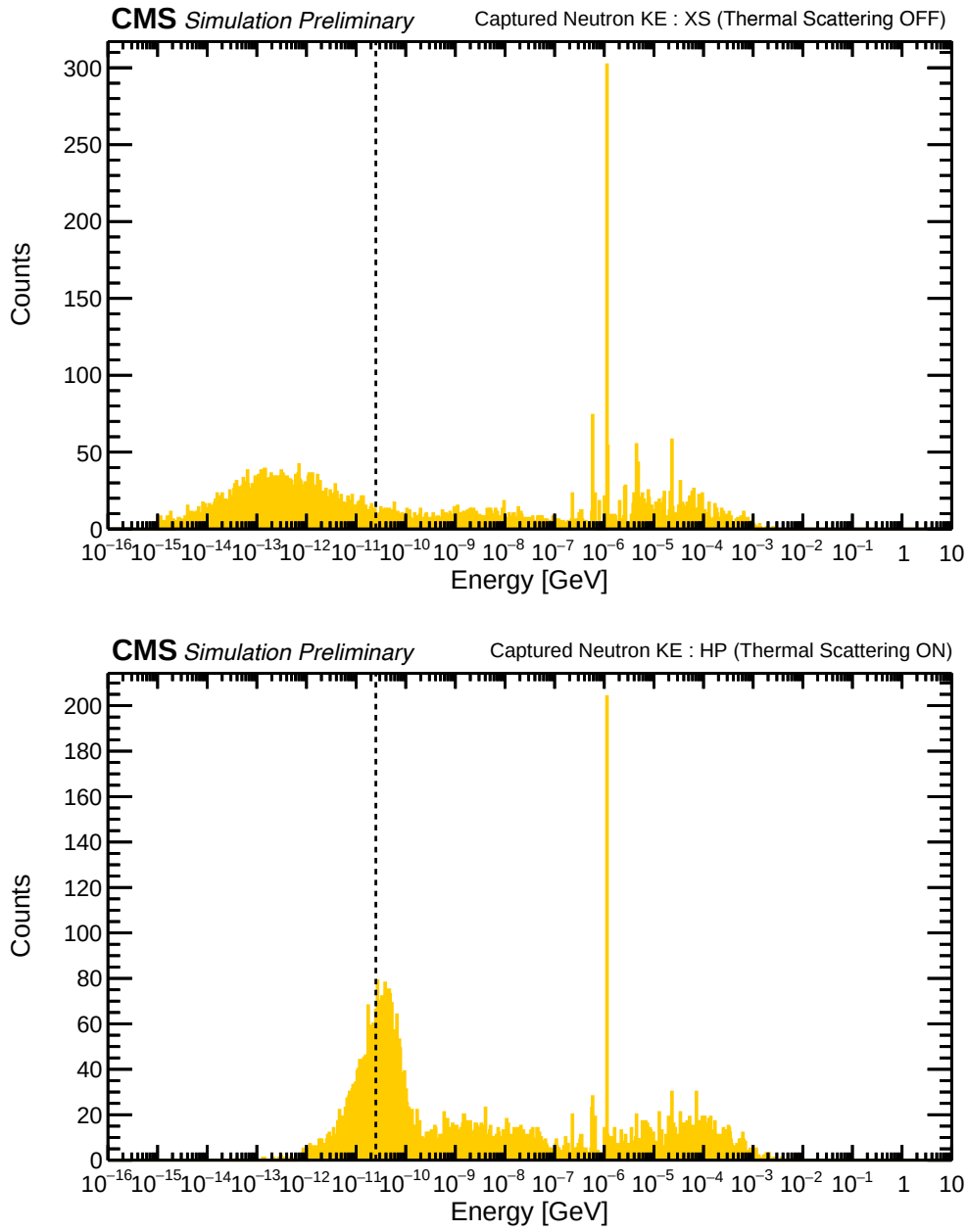

Figure A.3: Histogram of neutron kinetic energy just before nuclear capture, (top) before and (bottom) after enabling thermal treatment of detector nuclei. The dashed line indicates 0.025 eV. Before enabling the new feature, the low energy peak of captured neutrons is several orders of magnitude below thermal energies; after enabling the feature, the low energy peak is at thermal energies. Also visible are the resonant capture peaks on, for example, ^{56}Fe, in the keV range.

A.3.2 Results from MC Simulation

In examining these simulated events, we find that each *pp* collision can lead to three broad categories of neutron-induced hits:

- Hits on the time scale of 100 ns after the *pp* collision, induced by "fast" neutrons whose energies have degraded over time to a few MeV and higher. The neutrons interact inelastically with nuclei, giving some ionization from protons or nuclear fragments, but primarily resulting in nuclear de-excitation photons that give rise to ionizing electrons, primarily from Compton scattering.

- Hits on the time scale of several μs after the *pp* collision, induced by neutrons whose energies have degraded over time to a few keV of energy. The neutrons are resonantly captured on various types of nuclei, also resulting in nuclear de-excitation photons that give rise to ionizing electrons.

- Hits on the time scale of several ms or longer after the *pp* collision, induced by thermal neutrons whose energies have degraded over time to be at thermal equilibrium with the experimental cavern. The neutrons are captured on nuclei, also resulting in nuclear de-excitation photons that give rise to ionizing electrons.

Figure A.4 displays plots of the final energy of simulated neutrons vs. the time (since the *pp* collision) of the corresponding simulated detector hits (SimHits) in CSCs. The final energy of the neutron refers to the energy of the neutron at the moment it gives rise to the photon that eventually gives rise to the electron that produced the SimHit. Visible on the top plot are the three populations of hits as mentioned above: two groups of red dots that are hits induced by neutron captures; and blue dots that are hits induced by neutron inelastic scatters. The bottom plot in Fig. A.4 shows the same quantities for all neutron-related SimHits, including the photon-induced hits as well as hits from ions (green) and protons (magenta).

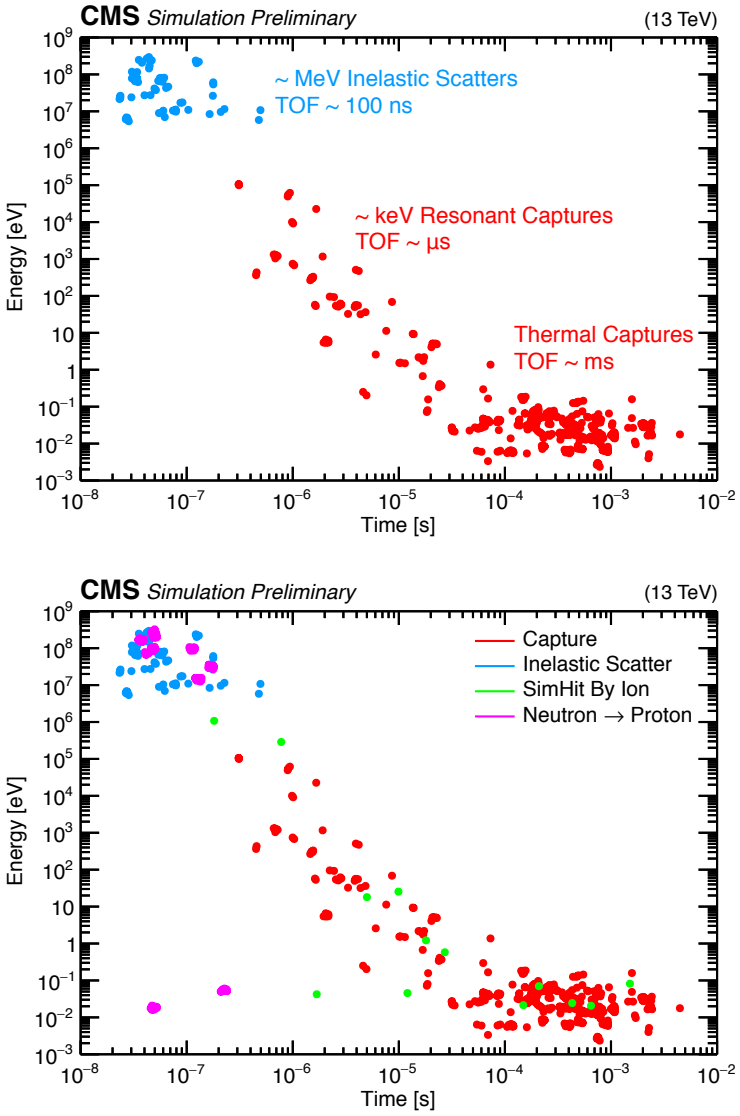

Figure A.4: Final energy of simulated neutron vs. the time since *pp* collision of simulated detector hit, for hits in CSCs. Hits are induced by electrons that are produced from photons that are produced from neutron capture or from neutron inelastic scattering. Red dots indicate simulated hits induced by neutron captures, and blue dots indicate simulated hits induced by neutron inelastic scatters. The top plot shows hits from photons only, coming from inelastic scattering and nuclear capture; the bottom plot shows all neutron-related hits, including those induced by protons and nuclear fragments, shown in magenta and green dots, respectively.

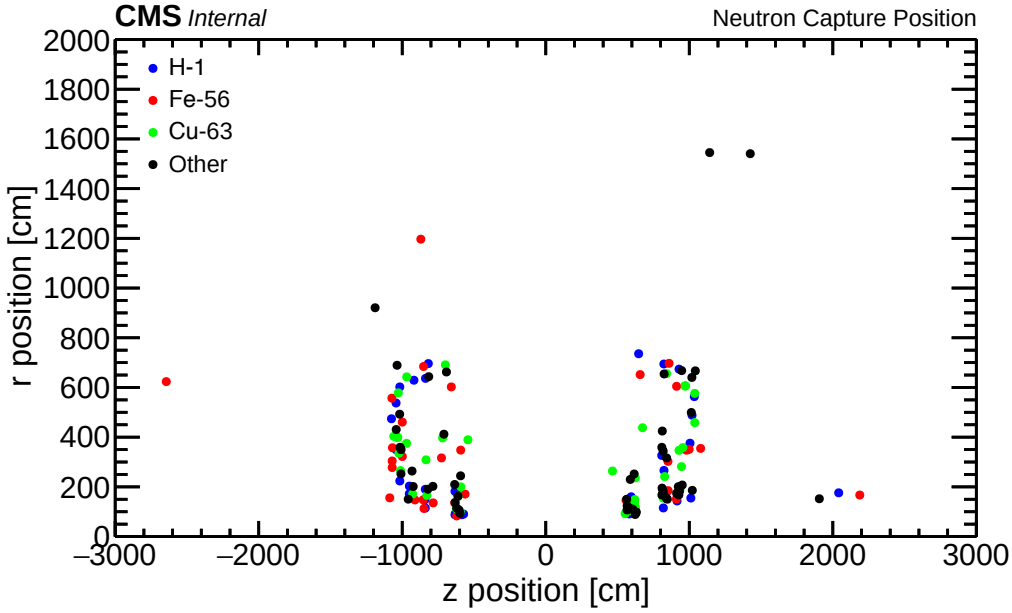

Figure A.5: r-z view of CMS cavern showing the locations of the specific neutron captures that led to SimHits in the CSCs.

Since the time scales from when the neutrons are created to when neutron capture induces hits are much longer than time scales of LHC bunch train gaps [15], hits occur in chambers uniformly at all times during an LHC fill. In simulation, we distinguish hits from neutron capture in CSCs from hits from prompt and fast neutrons by selecting the simulated hits that occur after a sufficiently long time after the pp collision.

Figure A.5 is an r-z view of the CMS cavern showing the location of neutron captures that lead to SimHits in the CSCs, each dot colored according to the capturing nucleus. Neutrons are mainly captured on ^{56}Fe (red), ^{63}Cu (green), and free hydrogen (blue) within the CMS endcap muon system, CMS calorimeters, and LHC shielding.

Of additional interest are the processes by which photons produce the electrons that result in SimHits. Fig. A.6 is a histogram of the simulated photon energy emitted by nuclear de-excitations from both inelastic scattering and neutron capture that lead to SimHits, stacked by the specific production or scattering process that created the electron responsible. Photons that lead to SimHits predominantly have energies in the hundreds of keV to several

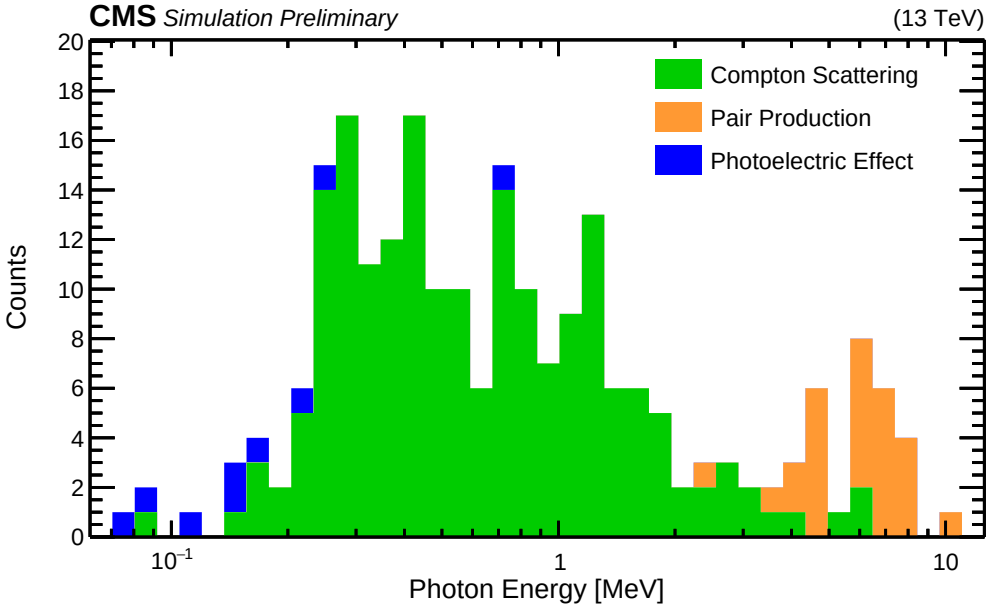

Figure A.6: Stacked histogram of the final energy of simulated photons at the time they produce simulated electrons that lead to simulated detector hits. The photons are categorized by the process by which the electrons are created or scattered. The most common process by which electrons that eventually lead to simulated hits are formed is Compton scattering.

MeV, and the most common process that leads to SimHits is Compton scattering.

A.4 Selection and Isolation of Neutron-Induced Hits in CMS Data

To obtain a sample of events in pp collision data suitable for studying the neutron background, we first select events with Z boson candidates decaying to two opposite sign muons from the SingleMuon dataset from Run 2016H, corresponding to approximately $9\,\mathrm{fb}^{-1}$ of integrated luminosity. Events are chosen with at least two muons of opposite sign where the muon leading in p_T is required to have $p_\mathrm{T} > 30\,\mathrm{GeV}$, and the subleading muon is required to have $p_\mathrm{T} > 20\,\mathrm{GeV}$. In addition, muon candidate tracks are required to have at least one hit in the pixel detector, hits in at least six silicon-strip tracker layers, and matched segments in two or more muon stations. To suppress non-prompt muons, the sum of the p_T of charged tracks within a cone of $\Delta R = 0.3$ around the muon is required to be less than 10% of the muon p_T. Also, the muon is required to have a transverse impact parameter of less than 2 mm and a longitudinal distance of less than 5 mm with respect to the primary vertex. The Z boson dimuon candidates are selected within an invariant mass window of 60–120 GeV. This provides us with a sample of prompt muons with reduced hadronic activity near the muon candidate. Finally, at least one of the muons is required to have passed through at least one CSC, by requiring that an LCT in at least one CSC was matched to the muon candidate track.

We then look for evidence of neutron-induced hits in cathode comparator half-strip hits and anode wire group hits in the data of each CSC thus selected. To reduce potential muon-induced contamination of our selection of candidate neutron-induced hits, we require that there be exactly one LCT occurring in a one-sixteenth corner of a chamber and consider only comparator half-strip or wire group hits occurring in the opposite half of the chamber from the LCT. Figure A.7 displays an example diagram of a CSC with a muon (indicated by the black arrow) passing through a chamber corner (shaded in red) and the corresponding opposite half of the chamber (shaded in blue) where we look for hits. This ensures that any potential muon-induced background is at least a quarter chamber spatially separated from

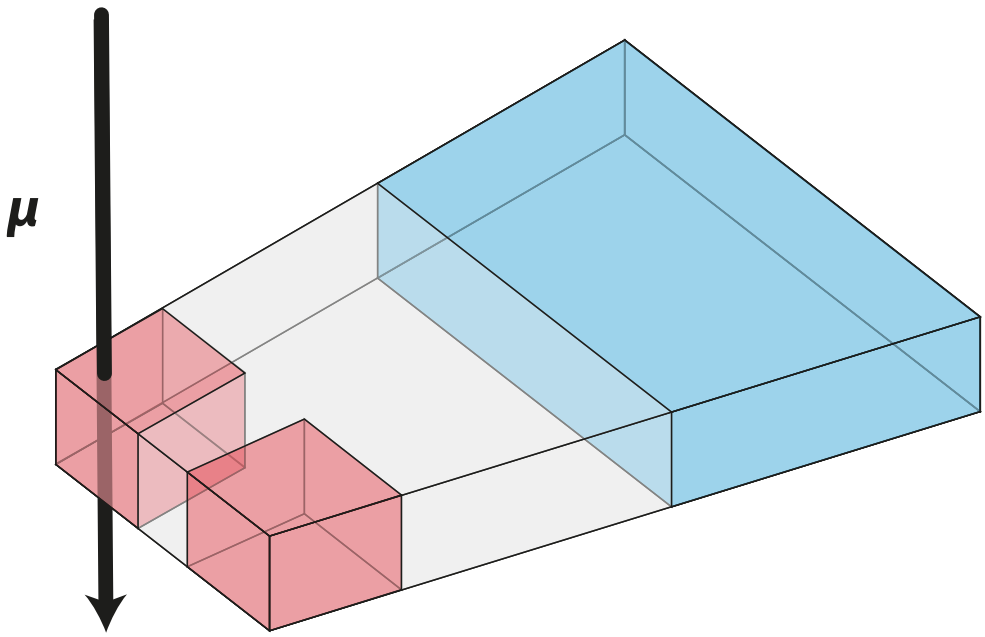

Figure A.7: Opposite half selection for neutron-induced hits in CSCs

the region of the chamber in which we search for candidate neutron-induced hits.

As a precise clarification of what is meant by a one-sixteenth corner and an opposite half, an example definition of a chamber corner area is the overlap region between wire groups 1 through $N_{\mathrm{WG}}/4$ and comparator half-strips 1 through $N_{\mathrm{HS}}/4$, where N_{WG} and N_{HS} are the total number of anode wire groups and comparator half-strips in a chamber, respectively. The corresponding area for the opposite half of the chamber in which we search for candidate neutron-induced wire group hits is the area defined by wire groups $N_{\mathrm{WG}}/2$ through N_{WG}, and similarly for candidate neutron-induced comparator half-strip hits is the area defined by $N_{\mathrm{HS}}/2$ through N_{HS}. All four definitions of a chamber corner and their corresponding opposite halves are considered and used in this analysis.

Since the rate of trigger muons varies over the CSC system, the number of times we look in each half-chamber varies for each half-chamber in the CSCs and with each event, and the hit rates vary with luminosity. We introduce some rather tedious bookkeeping to compute rates in the next section, with an indicator function used to specify when we look.

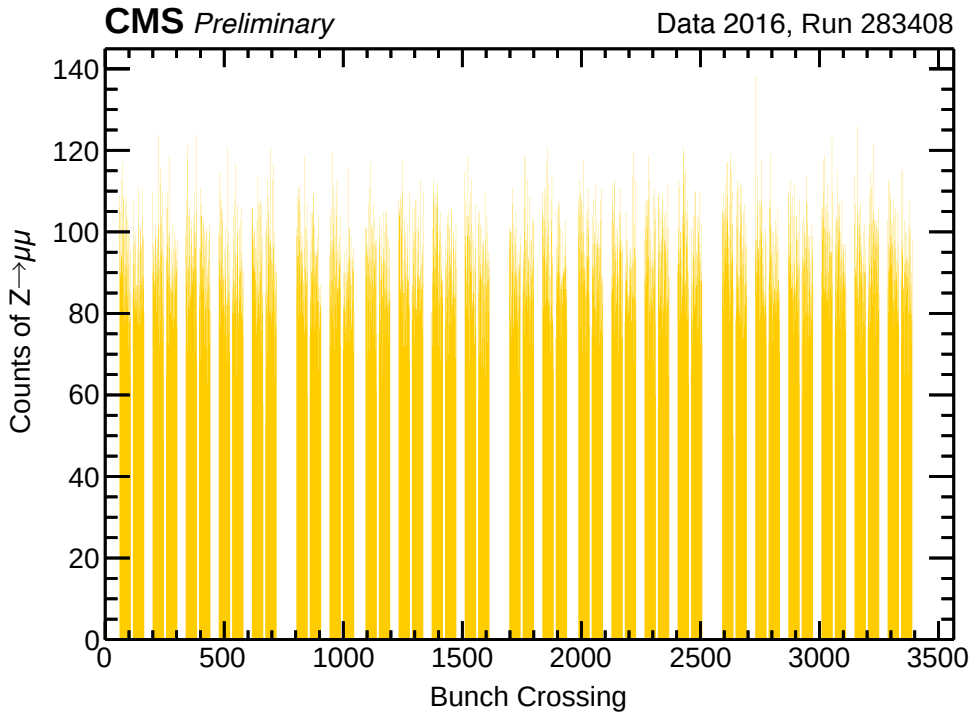

Figure A.8: Histogram of bunch crossing number in a particular CMS data taking period during LHC proton-proton collisions in 2016, showing the gaps of various sizes in the LHC bunch structure.

The LHC proton beam has 3564 bunch places, with a bunch spacing of 25 ns. Not every bunch place has protons in it; rather, consecutive bunches of protons occur in trains, separated by gaps [15]. Proton-proton collisions occur in CMS when bunches of protons cross, called bunch crossings (BX). Figure A.8 is a histogram of the LHC bunch place numbers that are filled with *pp* collisions taken during a high statistics run, displaying the LHC bunch structure. In this run, trains with protons are exactly 48 bunches long and the trains are separated by bunch gaps of 8 to 35 bunch places, with the final train followed by the LHC abort gap of approximately 200 bunch places.

In each event read out by the CMS DAQ, anode wire hits are read out from CSCs in 16 time bins of 25 ns. As mentioned in Section 2, hits in time with the muon occur in the middle of the readout window in time bin 8; time bins before time bin 8 then correspond to earlier bunch places. Hits from these early-time time bins where the readout was triggered by a muon from pp collisions in the first BX after a gap correspond to times within the gap. That is, these hits occur during bunch places without any pp collisions. Thus, they must arise from pp collisions from before the start of the gap (apart from the rare cosmic or noise hit), and we attribute them to be neutron-induced hits from long-surviving neutrons, i.e. from neutron capture. Events with muons that are triggered in the first few BXs after a gap can also be used to identify neutron-induced hits as long as the early-time time bins are early enough to occur within the gap.

Similarly, events with muons that are triggered at the end of a bunch train have late-time time bins that correspond to times within the beginning of the next bunch gap. As the LHC bunch trains often have 48 consecutive BX with collisions between gaps, for convenience we consider only bunch trains that are exactly 48 BX long and that occur after gaps of at least 35 bunch places.

Figure A.9 is a 2D histogram of the CSC anode wire hits (intensity given by color code) as a function of the number of bunch crossings after a gap on the y axis and the digi readout time bin on the x axis. Both BX and time bins are 25 ns wide. Time bin 8 is in-time with the muon that triggered readout of the chamber.

The region bounded by the lower left red outlined triangle contains early readout time hits in early bunch places, i.e. hits recorded near the end of an LHC bunch gap. This triangle contains neutron capture induced hits with negligible contribution from cosmic muons. The excess hits in readout time bin 0 contain hits from the previous bunch crossing due to the length of electronic pulses and are therefore not considered. We use the time windows selected within the lower left triangle as the final step in isolating neutron capture induced hits.

The central red outlined rectangle is a region delineating early readout time hits in bunch places contained completely within a bunch train. Hits from these bunch crossings contain, in addition to neutron capture induced hits, hits induced by fast neutrons and hits in time with *pp* collisions from other bunch crossings occurring in out-of-time readout time bins. The upper right red outlined triangle is a region delineating hits in late bunch places, i.e. hits recorded at the beginning of an LHC bunch gap. Hits from these bunch crossings contain not only neutron capture induced hits, but also hits induced by fast neutrons (neutrons which have not yet lost enough energy to be captured) that occur within a few bunch crossings of a *pp* collision. Table A.1 summarizes the time windows for each of the three regions outlined in Fig. A.9.

In summary, we select neutron capture induced hits in CMS data using the following criteria:

- Triggering muons must be from $Z \rightarrow \mu\mu$ candidates in SingleMuon Run 2016H
- Exactly one LCT must be in a one-sixteenth corner of a chamber
- Digis must be in the opposite half of the chamber from the LCT
- Digis must be found at early times in events occurring in the first few bunch places in a train of size exactly 48 bunch places, after a bunch gap of at least 35 bunch places

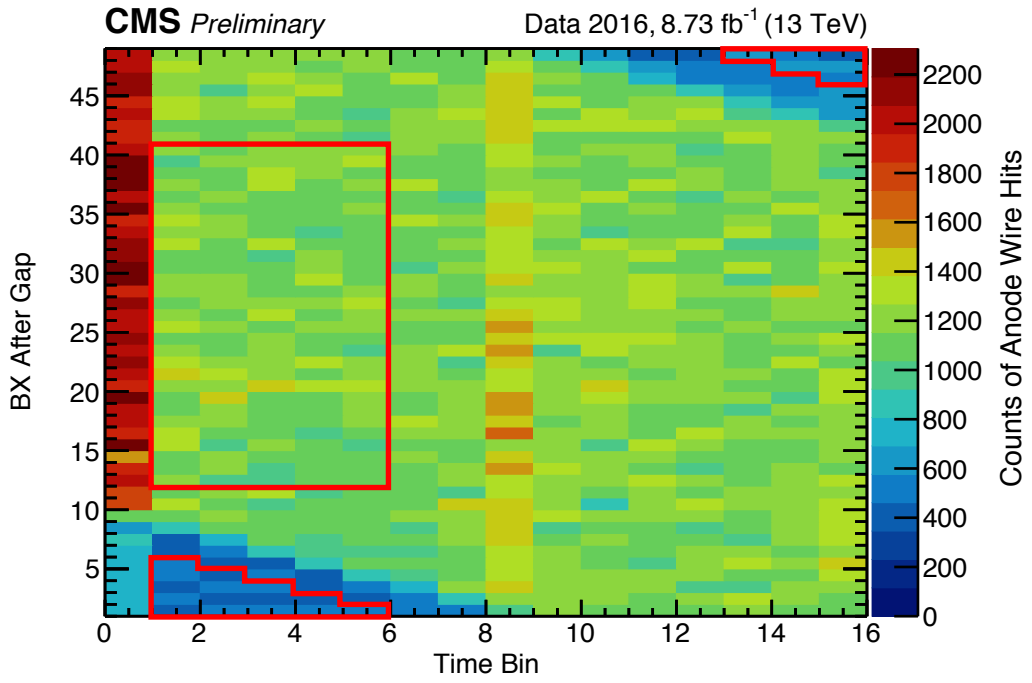

Figure A.9: 2D histogram of number of anode wire hits from CSCs in the inner ring of the first station (ME1/1) of the CMS endcap muon system. The histogram is plotted as a function of the chamber readout time bin, and of number of bunch crossings (BX) after an LHC bunch gap of at least 35 BX in bunch trains that are exactly 48 BX in length. Hits in readout time bin 0 are contaminated with an artifact of anode wire readout electronics and are therefore not considered.

Region	BX After Gap	Readout Time Bins	
	b	$T(b)$	$N_{T(b)}$
Lower left triangle (neutron capture only)	1	1–5	5
	2	1–4	4
	3	1–3	3
	4	1–2	2
	5	1	1
Total 2D bins in region			**15**
Central rectangle (neutron capture, fast neutrons, and hits from pp collisions)	12–40	1–5	5
Total 2D bins in region			**145**
Upper right triangle (neutron capture and fast neutrons)	46	15	1
	47	14–15	2
	48	13–15	3
Total 2D bins in region			**6**

Table A.1: Enumeration of time windows used for each region in Fig. A.9, listed by digi readout time bins and bunch places after the gap.

A.5 Results and Comparison of CMS Data with MC Simulation

A.5.1 Computation of Neutron-Induced Hit Rates

With the selection of neutron-induced hits in CMS data as well as the understanding gained from neutron simulation at CMS, we examine the local r and ϕ distributions of neutron-induced hits within a given chamber type, as well as the neutron-induced hit rate for a given chamber as a function of instantaneous luminosity [86, 42]. Directly comparing CMS data and MC simulation requires careful normalization of the digi counts. This section describes how the samples of neutron-induced hits obtained using the procedures discussed in Section A.4 are normalized, and various neutron-induced hit rates are defined.

As discussed in Section A.4, neutron captures typically occur many bunch places after the pp collisions that created the neutrons, so that, to a good approximation, neutron-induced hits uniformly populate all bunch places in the LHC. Observation of early-time neutron-induced hits during a particular triggering bunch crossing necessarily implies contributions from many pp collisions in many previous bunch crossings at CMS. In the steady state of approximately constant instantaneous luminosity, we can associate the aggregate number of all neutron-induced hits to the aggregate number of all pp collisions, even though the pp collisions are not uniformly spaced in time at CMS, having significant gaps between bunch trains. This association is the basis for all our rate calculations.

Since we connect rates of neutron-induced hits to approximately constant instantaneous luminosity, it is convenient to use the instantaneous luminosity as measured over a "lumi section," a time interval of data taking at CMS of about 23 s. We consider any changes in instantaneous luminosity within a lumi section to be negligible. We further consider edge effects from neutrons created during one lumi section but detected during another to be negligible. (The effects on the two ends of the a lumi section tend to cancel in any case.)

As further discussed in Section A.4, the neutron-induced hits that we observe are a random sample of the steady stream of hits, where the number of samples varies from half-chamber to half-chamber within CMS and with each event, according to the selection criteria

described. Thus, in order to normalize our neutron-induced hit rates, we keep track of the number of times we look for hits in each half chamber as well as the steady state rate of pp collisions at the times we look.

The bookkeeping accounts for each 2D bin in Fig. A.9, each readout time bin and bunch place after the gap. The details are described in the next sections; here we define some variables to be used.

Each ring specifies a different chamber type, represented by c. These chamber types contain different numbers and sizes of wire groups and half-strips; we let d (for digi) represent a particular wire group or half-strip within a given chamber type. The counts also vary with the particular bunch place b after a gap and the particular readout time bin τ in which we look.

A.5.1.1 Computation of Neutron Hit Rate in CMS Data

To determine the neutron-induced hit rate in CMS data, we count the number of selected digis found in particular bunch places after a gap and particular time bins in one of the red outlined regions in Fig. A.9. These regions consist of a set B of bunch places after a gap, and a set $T(b)$ of time bins for each particular bunch place $b \in B$ after a gap. Table A.1 enumerates each of the bunch places after a gap considered in each region, consisting of a bunch place set B, the set of time bins $T(b)$ for each bunch place, and the total number of time bins $N_{T(b)}$ for each bunch place. For all b not in the table, $T(b)$ is the empty set.

We process our data as a series of DAQ events, as described in Section A.4. In the following, "event" refers to a DAQ event, which corresponds to a trigger at a particular bunch crossing leading to a complete readout of the detector. The event data of course contains hits from many pp collisions, including (in the out-of-time time bins) hits from pp collisions in other bunch crossings.

We formalize our notation for counting the number of neutron-induced digis in a somewhat tedious manner in order to help with the bookkeeping that follows for keeping track of

the associated pp collisions.

Let $N_{\text{events}}^{\text{CMS}}$ be the number of events in the data set used; we let the index i run over the events considered, so that $i = 1, \ldots, N_{\text{events}}^{\text{CMS}}$.

Let $b(i)$ be the number of the bunch place after a gap for event i.

Then $T(b(i))$ is the set of time bins examined in event i, either the bins listed in Table A.1 for the region under study, or the empty set. (For example, if the region under study is the "Lower left triangle", then $T(b(i))$ is the empty set for $b(i) > 5$.)

A chamber type c represents multiple chambers in a ring; let c_j represent the jth chamber in chamber type c, and let N_c represent the total number of chambers of type c, so that $j = 1, \ldots, N_c$.

Let $I_{\text{look}}(i, c_j, d)$ denote an indicator function representing whether or not we looked in wire group or half-strip d of chamber j of chamber type c in event i. That is, $I_{\text{look}}(i, c_j, d)$ is 1 whenever d is in a half chamber in which we looked in event i, and 0 otherwise.

Let $I_{\text{hits}}(i, c_j, d, \tau)$ denote an indicator function representing whether or not a hit is present in time bin τ of wire group or half-strip d in chamber j of chamber type c in event i. That is, $I_{\text{hits}}(i, c_j, d, \tau)$ is 1 whenever a hit was found, and 0 otherwise.

The product of the two indicator functions is 1 whenever we look for hits and find them. For each event i, we sum the product of the indicator functions over the time bins examined for event i, then over chambers of type c, and then further sum over events.

We thus obtain $N_{\text{hits}}^{\text{CMS}}(c, d)$, the number of digis found in the data set in the examined time bins of chamber type c and wire group or half-strip d:

$$N_{\text{hits}}^{\text{CMS}}(c, d) = \sum_{i=1}^{N_{\text{events}}^{\text{CMS}}} \sum_{j=1}^{N_c} \sum_{\tau \in T(b(i))} I_{\text{look}}(i, c_j, d) \times I_{\text{hits}}(i, c_j, d, \tau). \tag{A.1}$$

As is evident, this sums over all chambers of type c. One may divide by N_c to get the average number of hits in one chamber of type c.

We also formalize our notation for counting the number of pp collisions to be associated

with the hits found. This is complicated by the varying luminosity (or equivalently, varying pileup and/or fraction of LHC filled with bunches).

Given the association between the steady state number of *pp* collisions and the steady state number of hits, the number of *pp* collisions associated with event i is given by the mean number of *pp* collisions during the time interval in which we look. The time interval in which we look in one time bin τ is the that of a time bin in the CSC readout, namely 25 ns. This is also the length in time of a bunch place in the LHC. Thus the associated number of *pp* collisions in event i is given by the mean number of *pp* collisions *per bunch place*, averaged over all bunch places at CMS (including empty bunch places), when event i was acquired. The latter is a product of two quantities: the mean number of *pp* collisions per *bunch crossing* P_i (also referred to as pileup) for event i, as reported by the CMS lumi group; and the fraction of filled bunch places (bunch places that have bunch crossings), which we call f_{fill}, and which is approximately 0.62 for the data used in this analysis.

We let $N_{pp}^{\text{CMS}}(c,d)$ be the total number of associated *pp* collisions in the data set at wire group or half strip d in chamber type c. It is the number of associated *pp* collisions, summed over all events:

$$N_{pp}^{\text{CMS}}(c,d) = \sum_{i=1}^{N_{\text{events}}^{\text{CMS}}} \sum_{j=1}^{N_c} \sum_{\tau \in T(b(i))} I_{\text{look}}(i, c_j, d) \times P_i \times f_{\text{fill}} \tag{A.2}$$

As in Eq. A.1, this sums over all chambers of type c, and one may divide by N_c to get the average for one chamber of type c.

The sum over τ in Eq. A.2 counts the same *pp* collisions more than once in an event i; this is because we may look in more than one time bin, and the goal is to have a normalization for each time bin, and hence for hits found.

Dividing Eq. A.1 by Eq.A.2, we obtain the number of hits per *pp* collision *per wire group or half-strip* d in chamber type c:

$$\text{hits per } pp \text{ per } d = \frac{N_{\text{hits}}^{\text{CMS}}(c,d)}{N_{pp}^{\text{CMS}}(c,d)}. \tag{A.3}$$

To convert Eq. A.3 to a per area quantity, we divide by the area subtended by each wire

group or half-strip d in a chamber type c, denoted $A_{\text{digi}}(c,d)$. The neutron background hit rate per pp collision per area at CMS is given by

$$\text{hits per } pp \text{ per area at } d = \frac{1}{A_{\text{digi}}(c,d)} \, \frac{N_{\text{hits}}^{\text{CMS}}(c,d)}{N_{pp}^{\text{CMS}}(c,d)} \tag{A.4}$$

The average neutron background hit rate per area for the entire chamber type c is obtained by summing Eq. A.3 over the set of possible wire groups and half-strips in a chamber type, denoted $D(c)$, and dividing by the chamber area $A_{\text{CSC}}(c)$:

$$\text{hits per } pp \text{ per area, avg over } c = \frac{1}{A_{\text{CSC}}(c)} \sum_{d \in D(c)} \frac{N_{\text{hits}}^{\text{CMS}}(c,d)}{N_{pp}^{\text{CMS}}(c,d)} \tag{A.5}$$

To convert Eqs. A.4 and A.5 to per time quantities, we choose a reference luminosity $\mathcal{L}_0$ and multiply by the mean pp collision rate per time at that luminosity, N_{pp}^{CMS}/t. That is,

$$\text{hits per } pp \text{ per area per time at } d = \frac{1}{A_{\text{digi}}(c,d)} \, \frac{N_{\text{hits}}^{\text{CMS}}(c,d)}{N_{pp}^{\text{CMS}}(c,d)} \, \left. \frac{N_{pp}^{\text{CMS}}}{t} \right|_{\mathcal{L}_0} \tag{A.6}$$

and similarly for the number of hits in the entire chamber,

$$\text{hits per } pp \text{ per area per time, avg over } c = \frac{1}{A_{\text{CSC}}(c)} \sum_{d \in D(c)} \frac{N_{\text{hits}}^{\text{CMS}}(c,d)}{N_{pp}^{\text{CMS}}(c,d)} \, \left. \frac{N_{pp}^{\text{CMS}}}{t} \right|_{\mathcal{L}_0} \tag{A.7}$$

We obtain the mean pp collision rate, N_{pp}^{CMS}/t, via two related methods. In the first method, we multiply the measured pp interaction cross section and the instantaneous luminosity:

$$\left. \frac{N_{pp}^{\text{CMS}}}{t} \right|_{\mathcal{L}_0} = \sigma_{pp} \, \mathcal{L}_0 \tag{A.8}$$

In the second method, we multiply the mean pileup P_0 at a reference luminosity $\mathcal{L}_0$ by the fill fraction f_{fill}, and divide by 25 ns, the bunch spacing interval.

$$\left.\frac{N_{pp}^{\mathrm{CMS}}}{t}\right|_{\mathcal{L}_0} = \frac{f_{\mathrm{fill}}\ P_0}{25\,\mathrm{ns}}\ \frac{10^9\,\mathrm{ns}}{\mathrm{s}}. \tag{A.9}$$

Both methods for measuring N_{pp}^{CMS}/t should give the same answer if we use the same cross section as used by the CMS BRIL group when computing pileup numbers. We favor the second method of because it uses only quantities which are directly provided by the by CMS BRIL.

In either case, the pp collision rate can in principle be scaled to other luminosities:

$$\left.\frac{N_{pp}^{\mathrm{CMS}}}{t}\right|_{\mathcal{L}} = \left.\frac{N_{pp}^{\mathrm{CMS}}}{t}\right|_{\mathcal{L}_0} \frac{\mathcal{L}}{\mathcal{L}_0}. \tag{A.10}$$

Consistency checks are shown in Figs. A.10 and A.11.

Figure A.10 is a plot of the measured N_{pp}^{CMS}/t vs. instantaneous luminosity via the second method described above. In the plot, each black dot in the plot represents a single luminosity section and the slope of this line corresponds to the pp interaction cross section, σ_{pp}. From Fig. A.10 we read off the pp collision rate at any instantaneous luminosity. At the reference luminosity $10^{34}\,\mathrm{cm}^{-2}\,\mathrm{s}^{-1}$, $N_{pp}^{\mathrm{CMS}}/t \approx 7 \times 10^8\,pp/\mathrm{s}$.

Figure A.11 shows a plot of instantaneous luminosity vs. mean pileup. Each dot in the plot represents a single luminosity section and is color coded according to the f_{fill} for that data taking period. Approximately 95% of the data collected corresponds to $f_{\mathrm{fill}} = 0.62$. As a check that the two methods for calculating N_{pp}^{CMS}/t are equivalent, lines are drawn according to the f_{fill} of various data taking conditions and the measured pp interaction cross section [87, 88].

A.5.1.2 Computation of Neutron Hit Rate in CMS as a Function of Luminosity

The above hit rates per pp collision are independent of luminosity, and the per time rates are with respect to a reference luminosity. In this section we check the implicit assumption of linearity of rates with luminosity. We count the number of neutron hits, binned by the

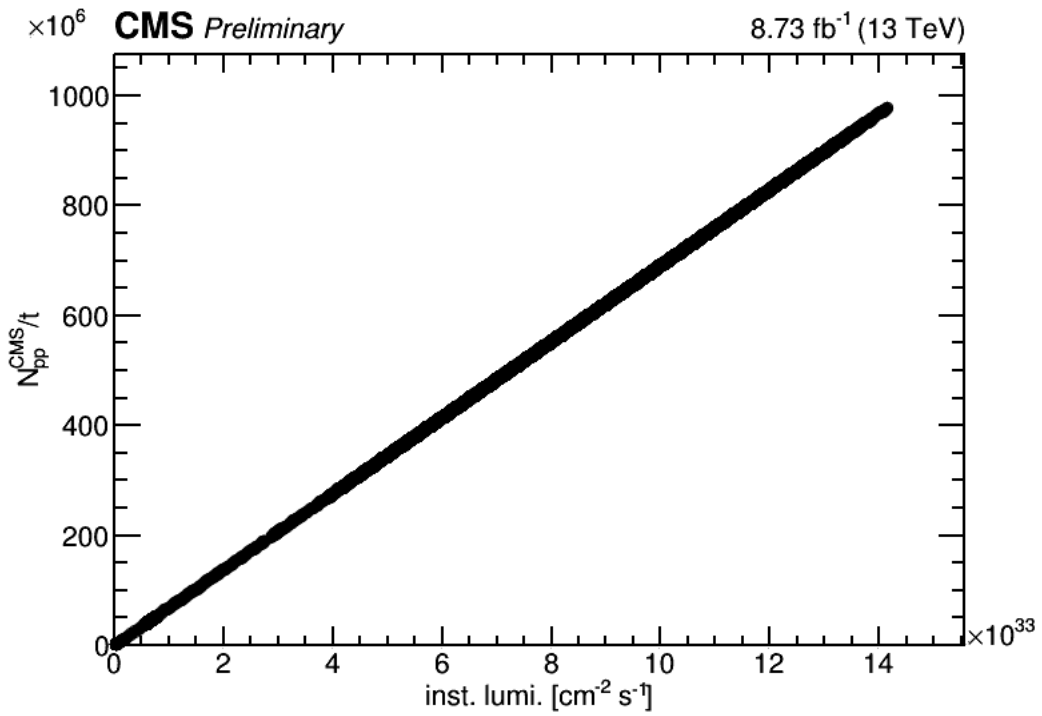

Figure A.10: Plot of N_{pp}^{CMS}/t vs. instantaneous luminosity. Each dot denotes single luminosity section.

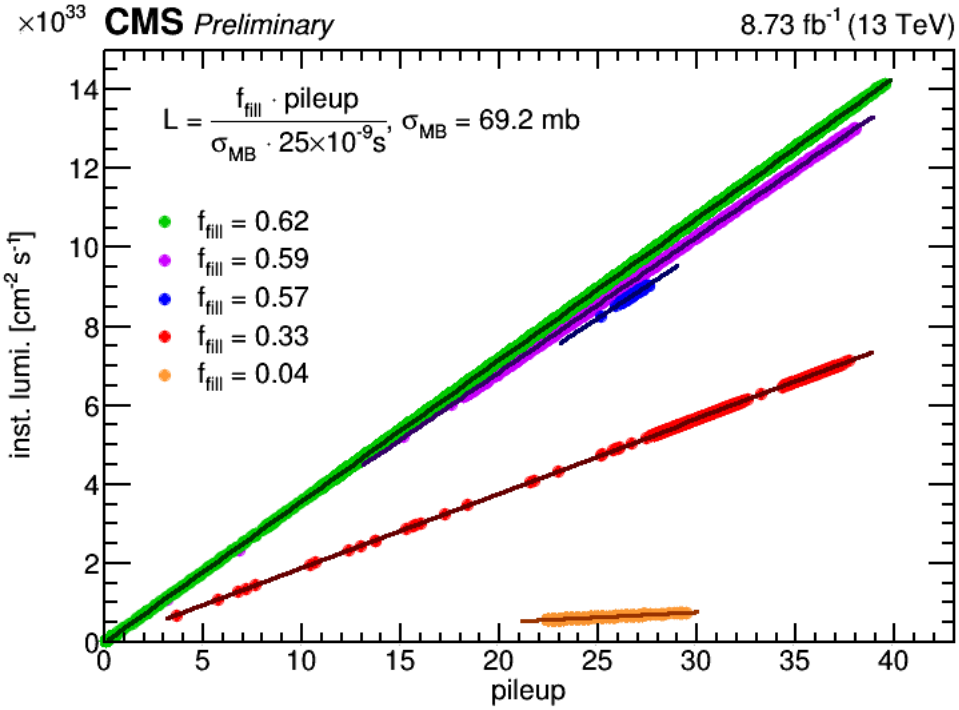

Figure A.11: Plot of instantaneous luminosity vs. mean pileup. Each dot denotes single luminosity section and the color denotes the fraction of filled bunches, f_{fill}, during which that data were collected.

luminosity of the event in which the triggering muon occurred, and normalize to the number of times we look, binned by luminosity.

At the risk of confusion, we let $\mathcal{L}$ refer to a luminosity *bin* centered on $\mathcal{L}$, and let $I_{\text{lumi}}(i, \mathcal{L})$ denote an indicator function representing whether or not event i occurred with a luminosity within luminosity bin $\mathcal{L}$. Then the computation of hit rates within lumi bins is the same as in Eq. A.1, with the addition of an indicator function to specify the lumi bin.

We thus obtain $N^{\text{CMS}}_{\text{hits}}(c, d, \mathcal{L})$ the number of digis found in the data set in the examined time bins of chamber type c and wire group or half-strip d, in lumi bin $\mathcal{L}$:

$$N^{\text{CMS}}_{\text{hits}}(c, d, \mathcal{L}) = \sum_{i=1}^{N^{\text{CMS}}_{\text{events}}} \sum_{j=1}^{N_c} \sum_{\tau \in T(b(i))} I_{\text{look}}(i, c_j, d) \times I_{\text{hits}}(i, c_j, d, \tau) \times I_{\text{lumi}}(i, \mathcal{L}). \tag{A.11}$$

The normalization for each lumi bin, $N^{\text{CMS}}_{\text{looks}}(c, d, \mathcal{L})$, is the sum of the number of times we looked in the lumi bin as in Eq. A.2, without the factors counting pp collisions:

$$N^{\text{CMS}}_{\text{looks}}(c, d, \mathcal{L}) = \sum_{i=1}^{N^{\text{CMS}}_{\text{events}}} \sum_{j=1}^{N_c} \sum_{\tau \in T(b(i))} I_{\text{look}}(i, c_j, d) \times I_{\text{lumi}}(i, \mathcal{L}). \tag{A.12}$$

Then we can define rates similar to those defined in Eqs. A.3–A.5 that are functions of luminosity:

$$\text{hits per } pp \text{ per } d = \frac{N^{\text{CMS}}_{\text{hits}}}{N^{\text{CMS}}_{\text{looks}}}(c, d, \mathcal{L}) \tag{A.13}$$

$$\text{hits per } pp \text{ per area at } d = \frac{1}{A_{\text{digi}}(c, d)} \, \frac{N^{\text{CMS}}_{\text{hits}}}{N^{\text{CMS}}_{\text{looks}}}(c, d, \mathcal{L}) \tag{A.14}$$

$$\text{hits per } pp \text{ per area, avg over } c = \frac{1}{A_{\text{CSC}}(c)} \sum_{d \in D(c)} \frac{N^{\text{CMS}}_{\text{hits}}}{N^{\text{CMS}}_{\text{looks}}}(c, d, \mathcal{L}) \tag{A.15}$$

To convert Eqs. A.14 and A.15 to per time quantities, we observe that each time we look corresponds to a 25 ns time interval readout time bin, and also one bunch space. Therefore, the neutron hit rate in chamber type c as a function of luminosity is simply Eq. A.15 multiplied by the conversion from time bin to ns:

$$\text{hits per } pp \text{ per area per time, avg over } c = \frac{1}{A_{\rm CSC}(c)} \sum_{d \in D(c)} \frac{N^{\rm CMS}_{\rm hits}}{N^{\rm CMS}_{\rm looks}}(c,d,\mathcal{L}) \; \frac{\text{time bin}}{25\,\text{ns}} \; \frac{10^9\,\text{ns}}{\text{s}} \tag{A.16}$$

A.5.1.3 Computation of Neutron Hit Rate in MC Simulation

In MC simulation, we identify the neutron capture induced hits in each simulated event by the long time that is recorded since the pp collision of the event. In the rest of this section, when we refer to hits or digis, we refer to those with late enough times to be identified as being induced by neutron capture.

There is no need for a selection process as described for the CMS data (with LCTs in a corner, etc). All digis in all chambers in all simulated events are examined. We again invoke the approximation described in Sec. A.5 that we can associate the aggregate number of all neutron-induced hits to the aggregate number of all *pp* collisions, even though the *pp* collisions are not uniformly spaced in time at CMS. Thus we need not be concerned with recording the hit-by-hit time bin of simulated hits, but rather work with totals and averages.

At CMS, this steady-state number of neutron-induced hits per *pp* collision at CMS, measured in one time bin (25 ns), is the sum of hits induced by neutrons originating from all previous pp collisions. A key point is that it is not necessary to attempt such a sum, which would be awkward computationally. Rather, we note that this sum is equal to the sum of all simulated neutron-induced hits (in all future time bins) coming from a single simulated pp collision.

Let $N^{\rm MC}_{\rm events}$ be the number of simulated events considered.

Let $N^{\rm MC}_{\rm hits}(c,d)$ be the total number of hits in $N^{\rm MC}_{\rm events}$ at wire group or half-strip d (for digi) in chamber type c. In analogy with Eq.A.1, we can write, using all hits in all times bins,

$$N^{\rm MC}_{\rm hits}(c,d) = \sum_{i=1}^{N^{\rm MC}_{\rm events}} \sum_{j=1}^{N_c} \sum_{\text{all } \tau} 1 \tag{A.17}$$

As with data, this sums over all chambers of type c. One may divide by N_c to get the average number of hits in one chamber of type c.

We let $N_{pp}^{\mathrm{MC}}(c)$ be the normalization to pp collisions for this hit total. (We suppress the argument d since unlike data, all wire groups and half strips are examined in every event.) While one MC event corresponds to a single simulated pp collision, the sum over N_c chambers in Eq. A.17 means that a factor of N_c is needed to consistently normalize, i.e.,

$$N_{pp}^{\mathrm{MC}}(c) = N_{\mathrm{events}}^{\mathrm{MC}}\ N_c \tag{A.18}$$

Then the number of hits per pp collision at d is then

$$\text{hits per } pp \text{ per } d,\ \mathrm{MC} = \frac{N_{\mathrm{hits}}^{\mathrm{MC}}(c,d)}{N_{pp}^{\mathrm{MC}}(c)} \tag{A.19}$$

As in data, we convert $N_{\mathrm{hits}}^{\mathrm{MC}}(c,d)/N_{pp}^{\mathrm{MC}}(c)$ to a per area quantity by dividing by $A_{\mathrm{digi}}(c,d)$. The neutron hit rate per pp collision in MC simulation is thus given by:

$$\text{hits per } pp \text{ per area at } d,\ \mathrm{MC} = \frac{1}{A_{\mathrm{digi}}(c,d)}\ \frac{N_{\mathrm{hits}}^{\mathrm{MC}}(c,d)}{N_{pp}^{\mathrm{MC}}(c)} \tag{A.20}$$

and similarly for the number of simulated hits in the entire chamber,

$$\text{hits per } pp \text{ per area, avg over } c,\ \mathrm{MC} = \frac{1}{A_{\mathrm{CSC}}(c)}\ \frac{1}{N_{pp}^{\mathrm{MC}}(c)}\ \sum_{d\in D(c)} N_{\mathrm{hits}}^{\mathrm{MC}}(c,d) \tag{A.21}$$

Finally, we convert Eq. A.20 and A.21 to per time quantities by choosing a reference luminosity $\mathcal{L}_0$ and multiplying by the pp collision rate per time at that luminosity, N_{pp}^{MC}/t:

$$\text{hits per } pp \text{ per area per time at } d,\ \mathrm{MC} = \frac{1}{A_{\mathrm{digi}}(c,d)}\ \frac{N_{\mathrm{hits}}^{\mathrm{MC}}(c,d)}{N_{pp}^{\mathrm{MC}}(c)}\ \frac{N_{pp}^{\mathrm{MC}}}{t} \tag{A.22}$$

and

$$\text{hits per } pp \text{ per area per time, avg over } c,\ \mathrm{MC} = \frac{1}{A_{\mathrm{CSC}}(c)}\ \frac{1}{N_{pp}^{\mathrm{MC}}(c)}\ \sum_{d\in D(c)} N_{\mathrm{hits}}^{\mathrm{MC}}(c,d)\ \frac{N_{pp}^{\mathrm{MC}}}{t} \tag{A.23}$$

A.5.2 Results

Figures A.12 and A.13 display plots of neutron-induced wire group hit rate without normalizing to *pp* collisions (as in Eq. A.16) vs. luminosity, for hits that occur at the end of LHC bunch gaps (lower left triangle from Fig. A.9) and hits that occur during CMS *pp* collisions (rectangle in Fig. A.9), for ME1/1 and ME2/1 chambers, respectively. We plot the hit rate that is not normalized to *pp* collisions, a quantity that is a function of luminosity, in order to see any potential linear dependence of hits vs. luminosity. Indeed, these plots show a relationship that is linear to the eye and intercepts the origin. This suggests that we have succeeded in isolating neutron capture induced hits, because contamination from muon-induced background would result in a positive offset on the y axis. Fluctuations in the data points are presumably due to changes in data taking conditions; however, the size of the χ^2/dof from the fit suggest that there are some systematic uncertainties that are not understood.

Figures A.14 and A.15 display histograms of the neutron-induced wire group hit rate for CMS data and MC, Eq.s A.6 and A.22, as a function of wire group number, in ME1/1 and ME2/1 chambers, respectively. We plot the hit rates that have been multiplied by N_{pp}^{MC}/t for a reference luminosity of $10^{34}\,\mathrm{cm}^{-2}\,\mathrm{s}^{-1}$ so as to compare data and MC, as in Eqs. A.6 and A.22. Rates normalized to area and time for both MC simulation and CMS data are shown, for both the XS and HP cross section libraries. The agreement is good to a factor of 2, depending on chamber type. The agreement in the HP plot of ME2/1 is anomalously good, presumably by chance.

In preliminary results in 2017 for the neutron induced hit rates, we incorrectly normalized the number of hits we counted with respect to the number of pp collisions in CMS data. Specifically in Eq. A.2, we omitted the fill factor, which changes the result for data by about a factor of 0.62 with respect to MC simulation. In addition, the way we expressed the rates per time was ambiguous and confusing; we trust that the current methodology is more clear.

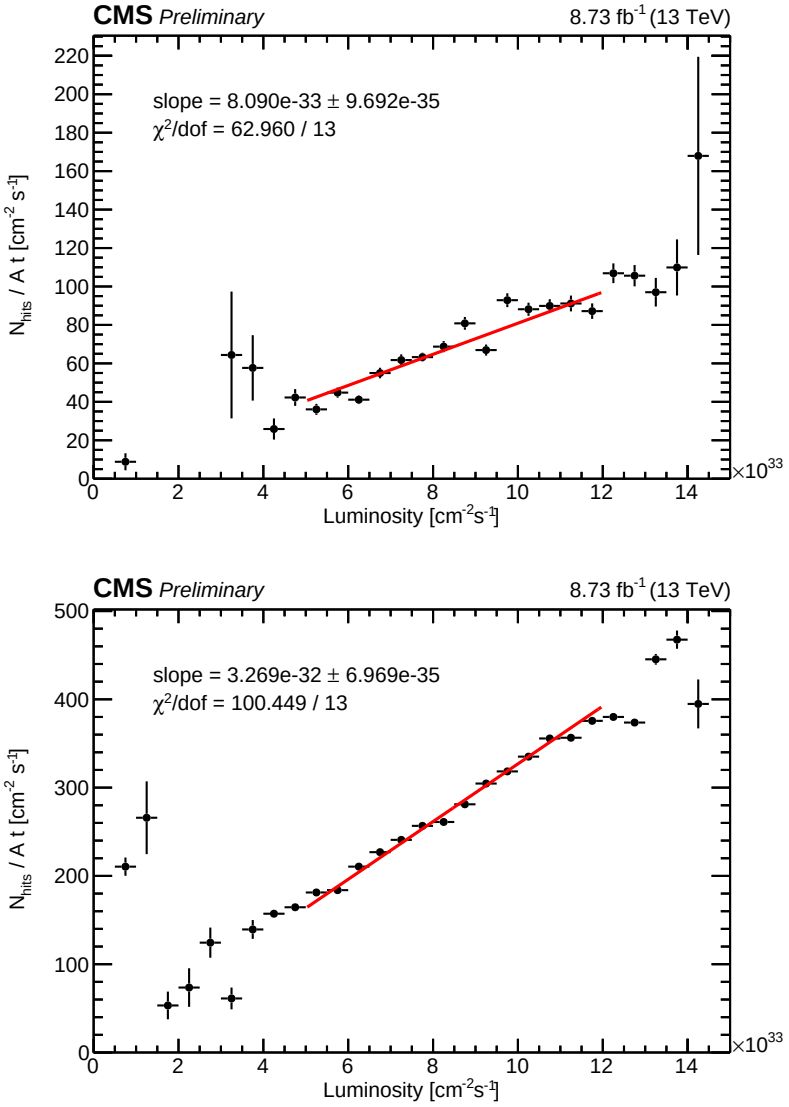

Figure A.12: Plot of hits per time per area as a function of luminosity as calculated in Eq. A.16 for ME1/1 chambers, (top) for hits that occur at the end of LHC gaps (candidate neutron capture induced hits) and (bottom) for hits that occur during *pp* collisions. The red line is a linear fit constrained to go through the origin and fit over the central region of luminosity.

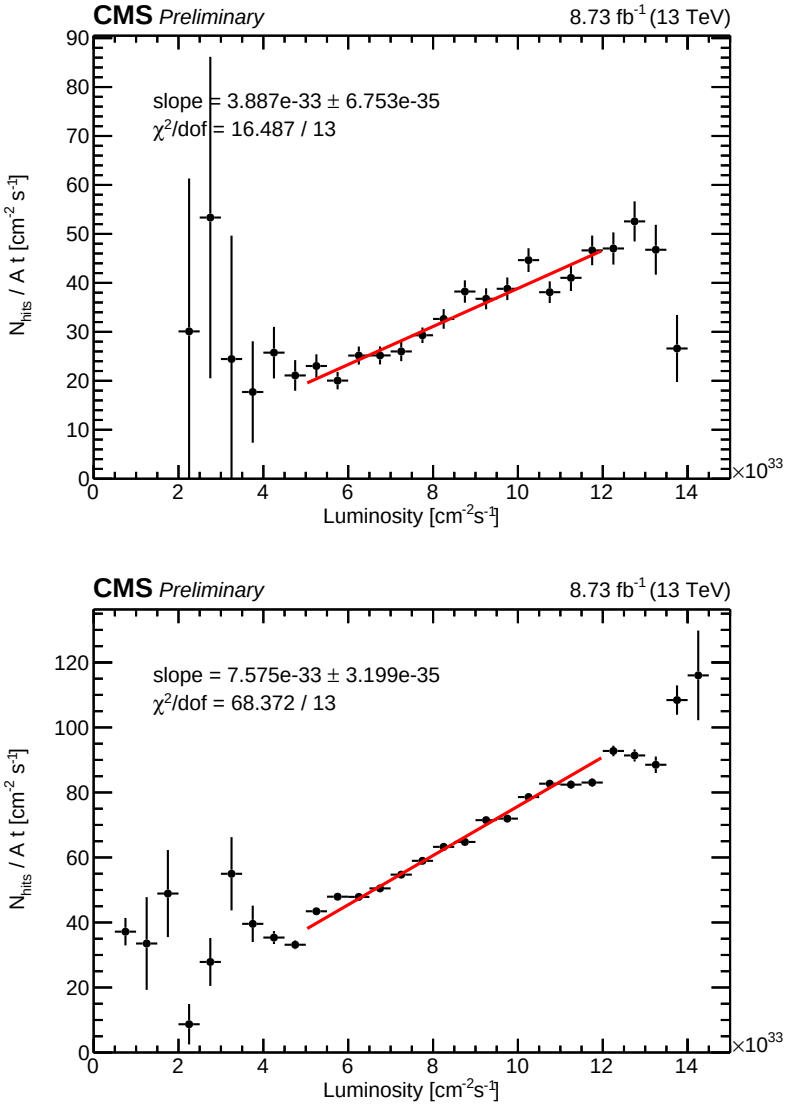

Figure A.13: Plot of hits per time per area as a function of luminosity as calculated in Eq. A.16 for ME2/1 chambers, (top) for hits that occur at the end of LHC gaps (candidate neutron capture induced hits) and (bottom) for hits that occur during *pp* collisions. The red line is a linear fit constrained to go through the origin and fit over the central region of luminosity.

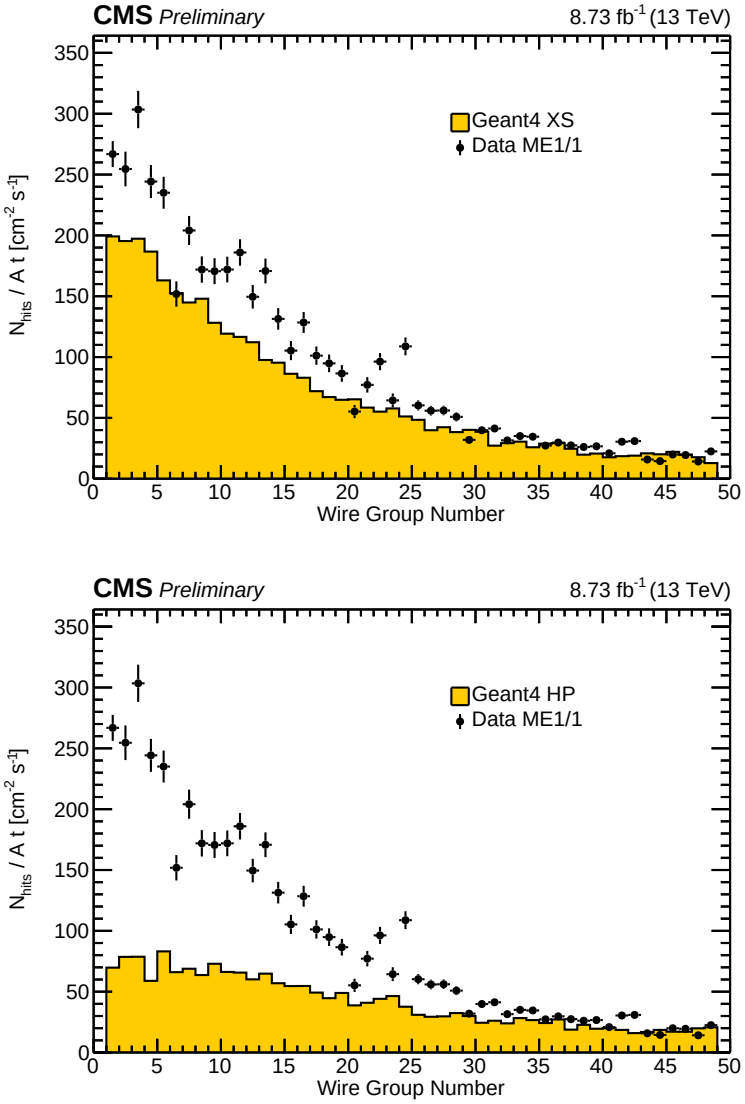

Figure A.14: Histogram of neutron capture induced anode wire hits per time per area for CMS data (as calculated in Eq. A.6) and for MC simulation (as calculated in Eq. A.22) for ME1/1 chambers for a reference luminosity of $10^{34}\,\mathrm{cm}^{-2}\,\mathrm{s}^{-1}$. CMS data are compared to results from GEANT4 (top) XS and (bottom) HP neutron interaction cross section libraries in CMS MC simulation of minimum-bias proton-proton collisions at 13 TeV.

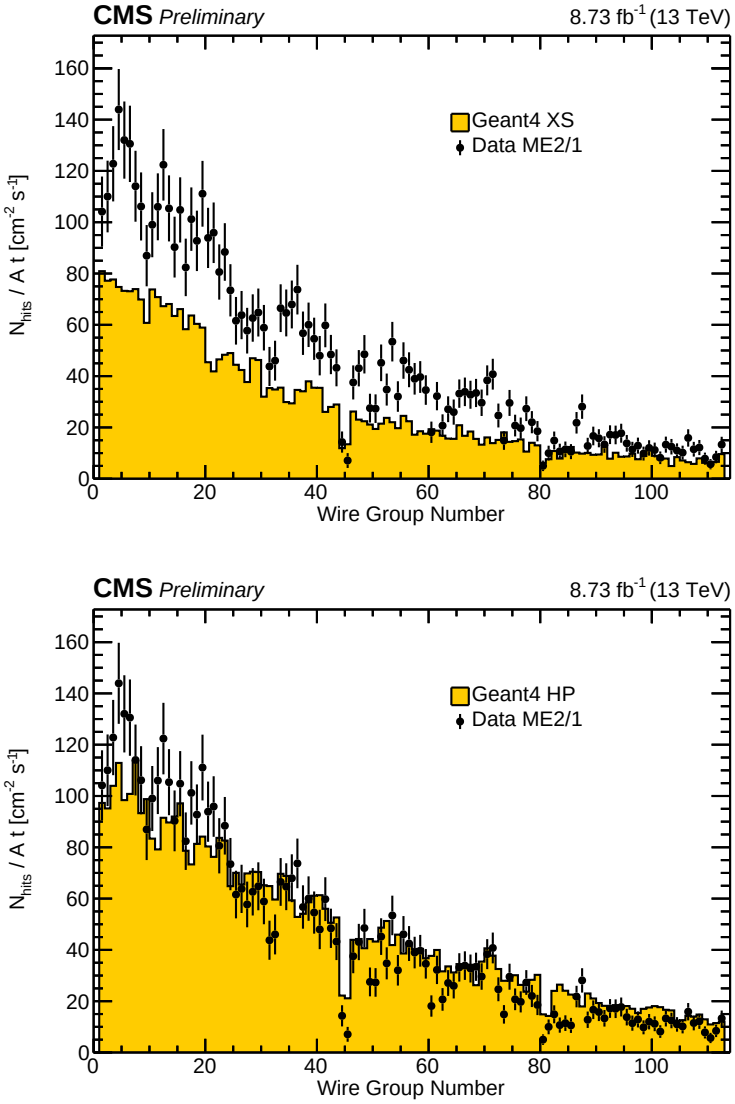

Figure A.15: Histogram of neutron capture induced anode wire hits per time per area for CMS data (as calculated in Eq. A.6) and for MC simulation (as calculated in Eq. A.22) for ME2/1 chambers for a reference luminosity of $10^{34}\,\mathrm{cm}^{-2}\,\mathrm{s}^{-1}$. CMS data are compared to results from GEANT4 (top) XS and (bottom) HP neutron interaction cross section libraries in CMS MC simulation of minimum-bias proton-proton collisions at 13 TeV.

A.5.3 Neutron Hit Patterns

A neutron-induced electron that leaves hits in more than one strip or layer is potentially more disruptive to reconstruction than one that leaves a single isolated hit. It is of interest to see if the MC simulation reproduces digi patterns of single, double, and triple hits found in CMS data. From the selected neutron digis, we consider contiguous clusters of at most 3 half-strips $\times$ 3 layers, i.e. ϕ-z patterns, and study patterns for both CMS data and MC simulation.

Figure A.16 displays histograms of the neutron-induced hit ϕ-z pattern distribution for CMS data and MC simulation. The x axis bin labels each show a representation of the half-strip vs. layer pattern; the horizontal direction in each is half-strips, and the vertical direction in each is layers. The sections of plots are colored by the number of hits in each pattern; on the far left in green is the only 1-hit pattern, followed by all possible 2-hit patterns in blue, and finally all possible 3-hit patterns in orange. The shaded histogram bins indicate patterns that have comparators on adjacent half-strips on the same layer. Since trigger electronics only report comparator hits on adjacent half-strips if they are in different time bins, the occupancy of these patterns should be suppressed compared to patterns to which they are otherwise geometrically similar. Comparing the shaded histogram bins in Fig. A.16 to the unshaded histogram bins suggests that this is indeed the case.

The distribution of neutron-induced hit patterns is overwhelmingly single, isolated hits. Both the occupancy of each pattern type and the relative ratio between singles, doubles, and triples, as well as to each other, show rough agreement between CMS data and MC simulation.

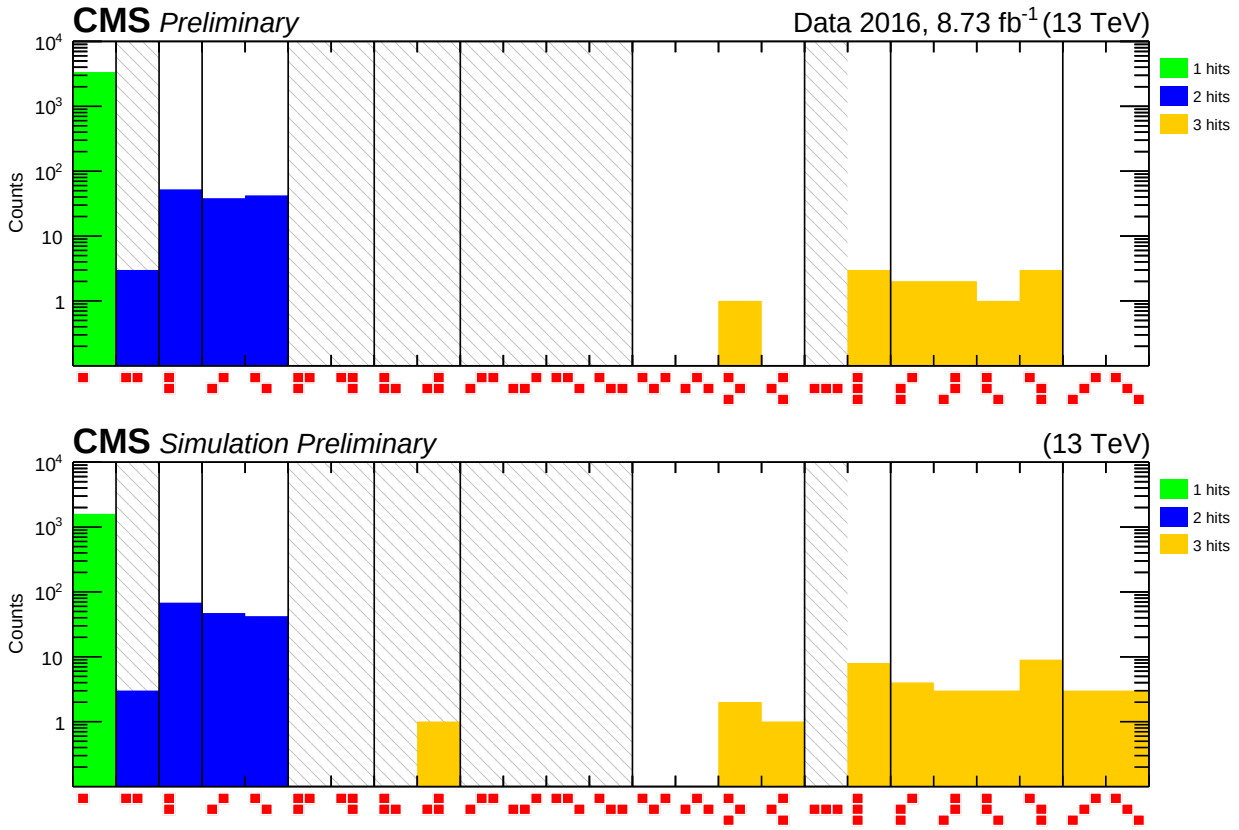

Figure A.16: Distribution of candidate neutron capture induced patterns in (top) 2016 CMS data and (bottom) CMS simulation. The patterns shown here are 1, 2, and 3-hit clusters only. For each red 3×3 pattern, the horizontal direction represents cathode half-strips and the vertical direction represents a layer in the CSC. The red boxes in a pattern indicate the presence of a candidate neutron capture induced hit in a cathode half-strip and layer. The shaded histogram bins correspond to patterns that are suppressed by CSC firmware electronics.

A.6 Muon Test Beam Studies at GIF++

A.6.1 The GIF++ Experimental Setup

The CERN Gamma Irradiation Facility (GIF++) is located on the CERN Prévessin site in the H4 beam line extracted from the Super Proton Synchrotron (SPS) [89]. The SPS delivers a beam of 400 GeV protons on a fixed target, providing a charged particle beam

of hadrons decaying to a beam primarily consisting of muons with a broad momentum spectrum around 100 GeV. The facility includes a 13.9 TBq ^{137}Cs gamma ray irradiation source emitting primarily 662 keV photons with the means to attenuate the source over a large range. Two CSCs (one ME1/1 and one ME2/1) are placed within the facility. This setup is used for studying aging, gas gain, high-luminosity conditions, etc., in preparation for the HL-LHC.

Level-1 Trigger Accepts (L1As) from muons, triggering chamber readout, can be produced in one of two ways. The first way is by self-trigger, where L1As are produced by chamber electronics forming Local Charged Tracks (LCTs) using coarsely correlated anode wire and cathode strip hits. Variables under control in the experimental setup include the chamber anode high voltage, the gamma ray source intensity (via attenuating filters, allowing a range of intensities from fully open to nearly closed as well as completely off), and the firmware of the controlling electronics, which defines various settings such as hit multiplicity thresholds. The second way to produce L1As is by external trigger, where L1As are produced by the triple coincidence of three scintillators in the beam: one upstream of the source, one downstream of the source, and one that is mounted in the path of the beam just in front of the chambers. The GIF++ data used in this note are externally triggered data taken during a muon test beam over a large range of GIF++ source intensities with CMS-like firmware parameters, and with a set of high voltages intended to equalize gas gain across all layers.

A.6.2 LCT Efficiency and RecHit Displacement at GIF++

To measure the LCT efficiency, we begin by counting the fraction f of L1As that have at least one LCT within the area shadowed by the middle scintillator mounted in front of the chambers. Due to issues of precisely defining the shadow and dealing with events with more than one muon, we do not attempt to define an absolute efficiency. Instead, we define a relative efficiency dividing the value of f taken at higher source intensities by the value of f with the GIF++ source off, denoted f_{off}. We estimate the scintillator area boundary empirically using a position scatter plot of LCTs, and count those LCTs whose layer 3

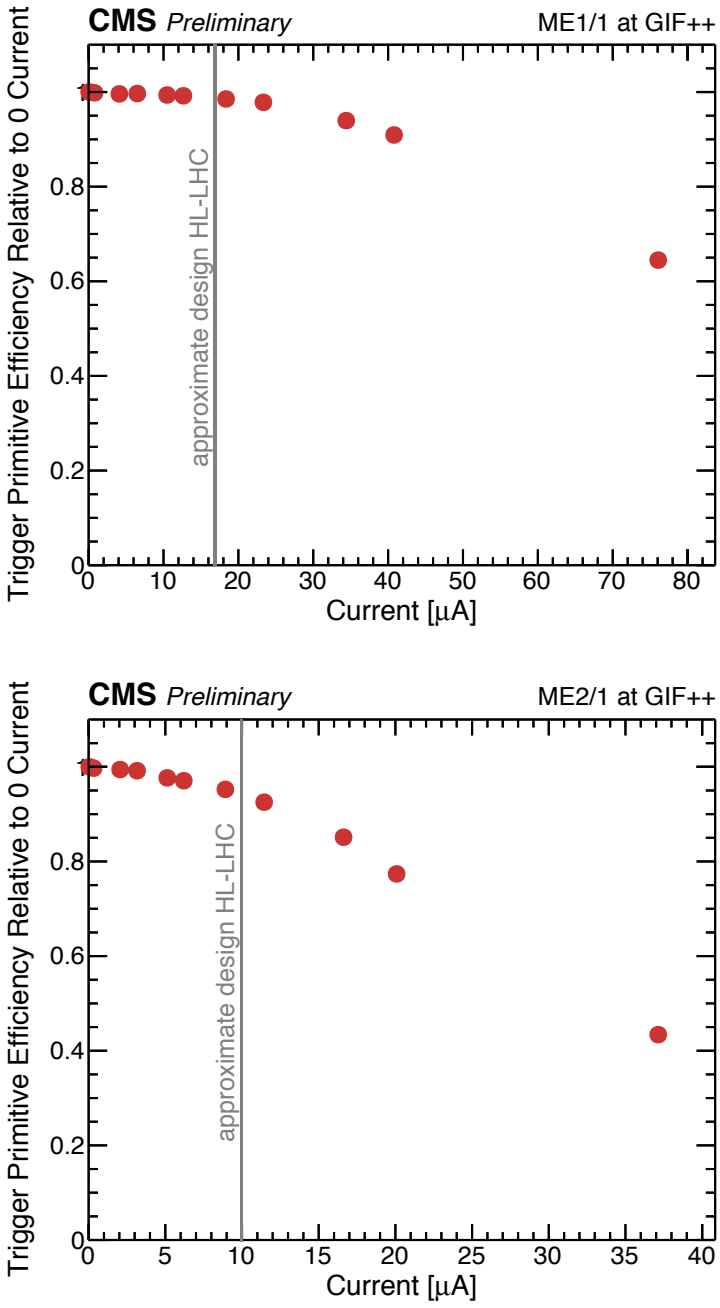

Figure A.17: Plot of LCT efficiency divided by the efficiency at minimum HV current (irradiation source turned off), for the (top) ME1/1 and (bottom) ME2/1 chambers at GIF++. LCT efficiency is defined as the number of LCTs created within a scintillator shadow, divided by the number of scintillator triggers received. As the source intensity is increased (chamber anode HV current is increased), the LCT efficiency drops. The gray line indicates an approximate equivalent HV current corresponding to design HL-LHC luminosity.

half-strip and wire group number fall within this boundary. Figure A.17 displays plots of the LCT relative efficiency, f/f_{off}, as a function of chamber anode HV current induced by increasing the GIF++ source intensity for the ME1/1 and ME2/1 chambers at GIF++. As the gamma source intensity is increased, the number of photon-induced noise hits increases, and the number of LCTs constructed decreases.

One possible cause for the loss of signal muon LCTs is the corruption of muon hits induced by background. To understand the characteristics of hit corruption, we examine CSC event displays such as in Fig. A.18. These event displays show wire group hits, comparator half-strip hits, and strip ADC counts with the layer on the vertical axis and the digi number on the horizontal axis. The color for the wire groups and comparators indicates the digi time bin, while the color for the strip ADC counts indicates the ADC counts. The comparator hit plot has an overlay in black rectangular outline of the LCT pattern that was used to identify the LCT.

This particular event display illustrates a way that a photon-induced hit may cause loss of LCTs, and consequently, loss of offline reconstructed segments. The display shows a muon triggering readout and forming a 4-hit LCT, whose comparator pattern can be seen in half-strips 9–13. The strip ADC counts show a large energy deposit that we attribute to a photon-induced hit in strips 3–4 in layer 3. The corresponding comparator hit in half-strip 7 is shifted away from what would have been its correct position in approximately half-strip 11. This results in what would have been a 5-hit LCT deteriorating to a 4-hit LCT. This ability of photon hits to displace hits can in this way cause loss of LCTs as well as deterioration of their quality.

Figure A.19 is a display of the corresponding offline reconstructed hits (RecHits) [90], along with an overlay of the muon segment constructed from them. The RecHits that contributed to the segment are shown in red. The shifted comparator hit and the photon energy deposit resulted in a RecHit that was displaced to the left, resulting in its exclusion from the segment. This directly results in a deterioration of segment reconstruction resolution.

Figure A.20 displays stacked plots of the fraction of reconstructed muon segments spa-

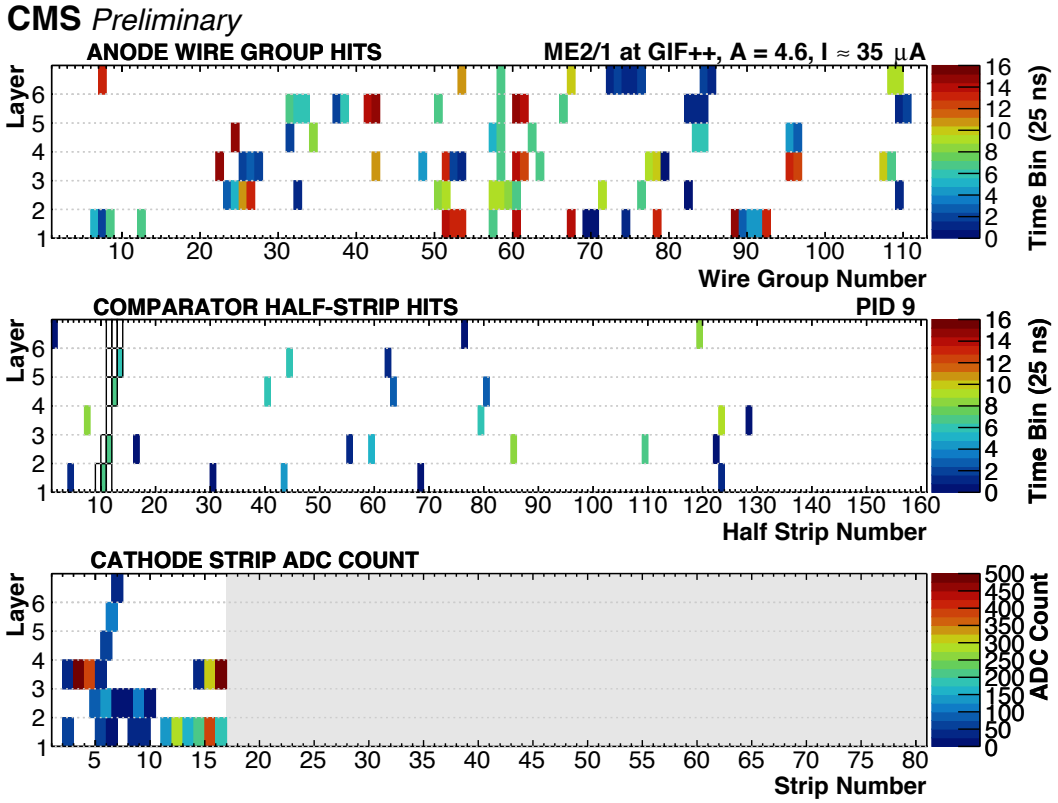

Figure A.18: Display of an event collected during a muon test beam at the CERN Gamma Irradiation Facility (GIF++) with a CSC from ME2/1, showing digitized detector responses: anode wire (r coordinate) responses (wire group hits), cathode half-strip (ϕ coordinate) responses (comparator half-strip hits), and cathode strip analog-to-digital-converter (ADC) counts proportional to deposited charge. Each display is organized by the gas gap layer and the strip or wire number in which the response occurred. The quantity A represents the attenuating factor applied to the 13.9 TBq ^{137}Cs gamma irradiation source and I is the chamber anode wire HV current. This display illustrates a mechanism by which a photon hit can displace a muon hit; the large amount of deposited charge seen at the left edge of the ADC counts resulted in a corresponding shifted comparator hit.

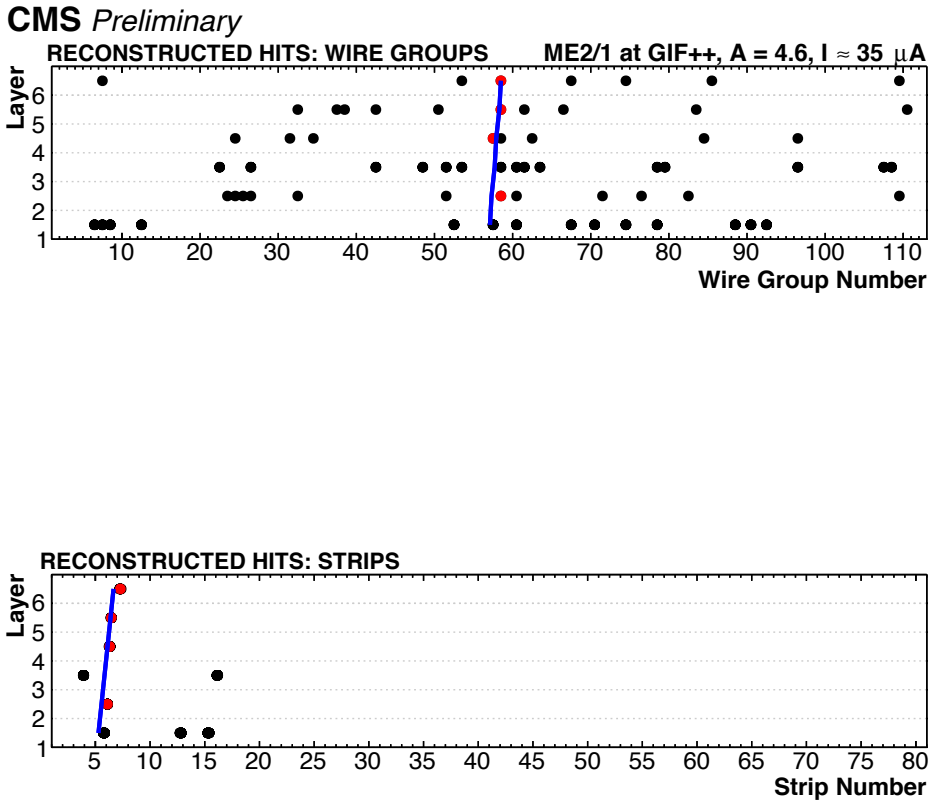

Figure A.19: Display of the same event as Fig. A.18, showing offline reconstructed detector responses (RecHits), projected along the anode wire axis and the cathode strip axis (black dots). Blue lines indicate the offline reconstructed muon segment created by a straight-line fit to the red highlighted RecHits. This display illustrates a mechanism by which a photon hit can displace a muon hit; the reconstructed hit in layer 3 was displaced and subsequently excluded from the segment fit.

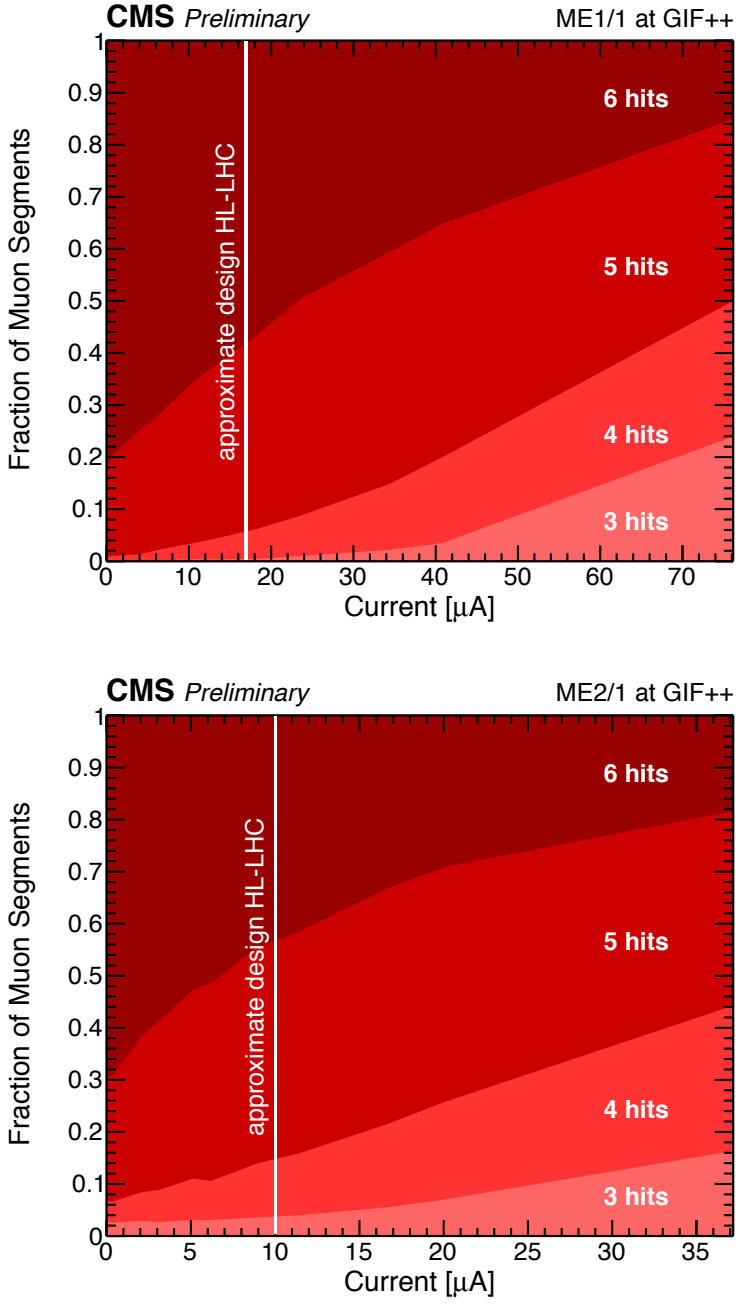

Figure A.20: Stacked plot of fraction of offline reconstructed muon segments, categorized by the number of reconstructed hits used to form them, vs. chamber anode HV current, for the (top) ME1/1 and (bottom) ME2/1 at GIF++. As the source intensity is increased (chamber anode HV current is increased), the fraction of good quality 6 hit segments decreases, while the fraction of lower quality 3 hit segments increases. The white line indicates an approximate equivalent HV current corresponding to design HL-LHC luminosity.

tially closest to muon LCTs within the scintillator acceptance area, categorized by the number of hits used to form that segment, as a function of chamber anode HV current for the ME1/1 and ME2/1 chambers at GIF++. The plot shows that the fraction of high quality segments formed with 6 hits decreases as the source intensity is increased, while the fraction of lower quality segments formed by 3 hits increases. This confirms that LCT loss can be caused by a loss of hits, and demonstrates the mechanism by which neutron-induced hits can potentially disrupt CSC detector performance.

A.7 Charge per Hit Studies at GIF++ and in CMS Data and Simulation

As discussed in Section A.6, the GIF++ facility allows us to study the performance of CSC online and offline reconstruction under conditions that potentially correspond to the radiation environment expected at the HL-LHC. To investigate the correspondence between GIF++ source intensity and LHC instantaneous luminosity, we examine the CSC anode HV current as measured by an ammeter in the CSC HV power supply (HVPS) of both CSCs at GIF++ and for similar chamber types at CMS.

Differences in radiation environments produced from the GIF++ source and from LHC *pp* collisions necessitate understanding the validity of using anode HV current for the correspondence between GIF++ and CMS. As noted in Section A.6 above, GIF++ photons are emitted with a maximum energy of 662 keV by the ^{137}Cs source, and the resulting ionizing electrons are primarily from Compton scattering and the photoelectric effect. In contrast, photons originating from the neutron background in CMS can carry up to several MeV in energy and thus, in addition to more energetic electrons from Compton scattering and the photoelectric effect, ionizing electrons and positrons can arise from pair production. Because of these differences and to explore any others, we measure the charge/hit of background hits that are expected to be the dominant source of charge in the anode HV current by measuring the ratio of the anode HV current to the anode wire group hits/s in both CMS data and

GIF++ data.

A.7.1 Computation of charge/hit from CMS data

A.7.1.1 ME1/1

To calculate charge/hit in ME1/1 chambers using CMS data, we take the ratio of the measured HV current (charge/s) and the anode wire group hits/s. Each of the measured HV current and anode wire group hits/s are calculated at a fixed reference luminosity intended to be representative of a typical measured values of the HV current and hits/s. We choose $10^{34}\,\mathrm{cm}^{-2}\,\mathrm{s}^{-1}$ as the reference luminosity.

We use anode HV current data collected by the HVPS and stored in an external database during LHC fills to calculate the HV current at the reference luminosity, which we refer to as the reference HV current. We read the HV current data offline from the database and correlate each HV current measurement by time to the corresponding measured LHC luminosity. In ME1/1 chambers, each layer constitutes an HV channel. We retrieve the HV current measurements for all ME1/1 HV channels, for all LHC fills during data taking period Run 2016H. We then study plots of anode HV current vs. luminosity and attempt to calculate the reference HV current by performing a two-parameter linear fit to the data and reading off the value of the fit at $10^{34}\,\mathrm{cm}^{-2}\,\mathrm{s}^{-1}$.

However, since the HVPSs for the ME1/1 chambers at CMS are known to measure a non-zero offset of HV current at zero luminosity, some adjustment of the HV current is necessary. In addition, in some ME1/1 HV channels, the HVPS can produce very noisy measurements of the anode HV current, resulting in data that are inconsistent with a straight line fit. Figure A.21 displays three plots of anode HV current vs. luminosity. The top plot is an example of a well-behaved ME1/1 channel that does not have an offset in the vertical intercept, so that we can use it to calculate the reference HV current. The middle plot is an example of ME1/1 channels that have a large offset of $0.46\,\mu$A that needs to be corrected when calculating the reference HV current. The bottom plot is an example of a noisy HV

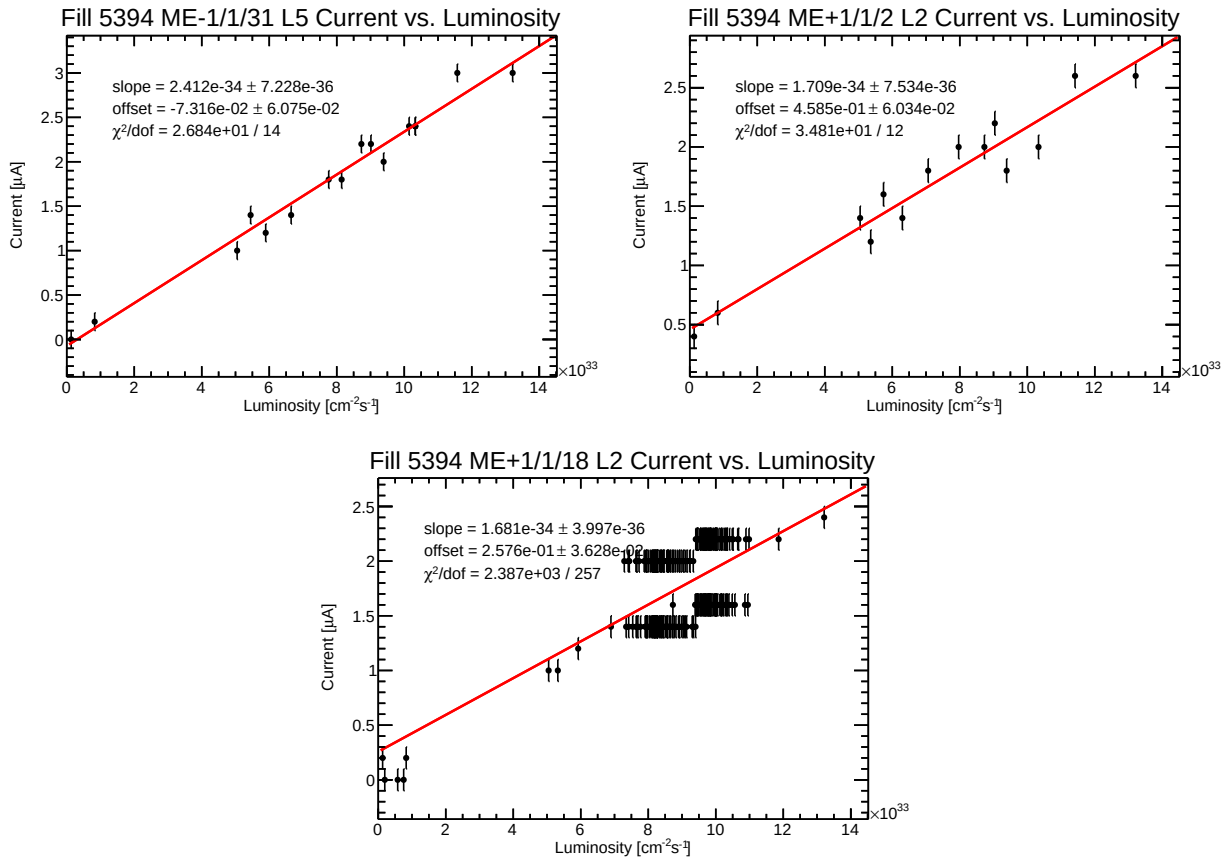

Figure A.21: Plot of anode HV current vs. LHC luminosity with a two-parameter linear fit for (top) a well-behaved ME1/1 channel, (middle) an ME1/1 channel with a large fitted offset, and (bottom) a noisy ME1/1 channel.

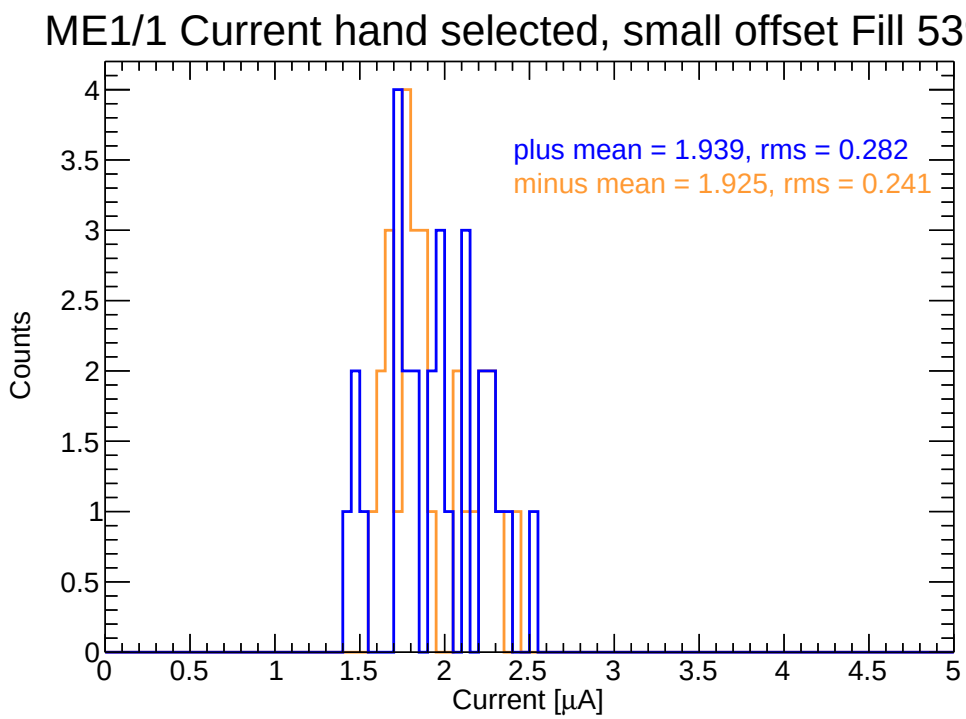

Figure A.22: Histogram of offset-corrected reference HV currents from ME1/1 HV channels that pass the hand selection color-coded by endcap.

channel where the HVPS reads out hundreds of values of the HV current within a short period of time where the measured values oscillate between two values separated by 0.6 μA and is not consistent with the model of a straight line fit.

To avoid problems such as large offsets and many oscillating values, we scanned through all 432 ME1/1 HV channels in LHC fill 5394. We selected what we thought were the best channels, similar in appearance to the top plot in Fig. A.21, based on fit χ^2, number of degrees of freedom, and our own judgment. We applied this list of 157 (out of 432 possible) selected channels for use in all other LHC fills considered. We considered a total of 23 fills in this study.

Figure A.22 is a histogram of reference HV current values at the reference luminosity from hand-selected channels with the offset required to be less than $\pm 0.1\,\mu$A. To obtain one characteristic HV current value for each fill, we take the average of the plus and minus

endcaps. Then to combine the measurements over all fills, we take the average of the HV currents in each fill during Run 2016H, with each fill weighted by its integrated luminosity. The averaged HV current is then multiplied by 6 because each CSC chamber has six HV channels (one per chamber layer) which operate independently. The resulting total ME1/1 chamber HV current is

$$I_{\mathrm{ME1/1}} = 11.3\,\mu A \tag{A.24}$$

at the reference luminosity.

To obtain the reference rate of anode wire group hits, we start by calculating the values of the hits/s at the reference luminosity $10^{34}\,\mathrm{cm}^{-2}\,\mathrm{s}^{-1}$ from the slopes of one-parameter linear fit to plots of hits/s vs. luminosity in Fig. A.23. The top plot in Fig. A.23 is the ME1/1 wire group hits/s vs. LHC luminosity (from Eq. A.7 but without the $1/A_{\mathrm{CSC}}$ factor) for wire group hits that occur in LHC bunch gaps (lower left triangle from Fig. A.9); the bottom plot is the same but for wire group hits that occur during pp collisions (middle rectangle from Fig. A.9). The reference rate of anode wire group hits/s is sum of the hit rates of hits occurring in LHC gaps, $H_{\mathrm{LHC\ gap}}$, and during LHC bunch trains, $H_{pp\text{-coll}}$, weighted by the LHC bunch fill fraction, $f_{\mathrm{fill}} = 0.62$,:

$$\begin{aligned} H_{\text{WG-ME1/1}} &= f_{\mathrm{fill}}\ H_{pp\text{-coll}} + (1 - f_{\mathrm{fill}})\ H_{\mathrm{LHC\ gap}} \\ &= 0.62\ 10.1 \times 10^{6}\,\mathrm{hits/s} + 0.32\ 2.5 \times 10^{5}\,\mathrm{hits/s} \\ &= 7.2 \times 10^{6}\,\mathrm{hits/s}. \end{aligned} \tag{A.25}$$

The charge/hit is then calculated by dividing the anode HV current by the anode wire group hits/s:

$$\text{charge/hit} = I_{\mathrm{ME1/1}}/H_{\text{WG-ME1/1}} = (11.3\,\mu A)/(7.2 \times 10^{6}\,\mathrm{hits/s}) = 1570\,\mathrm{fC/hit}. \tag{A.26}$$

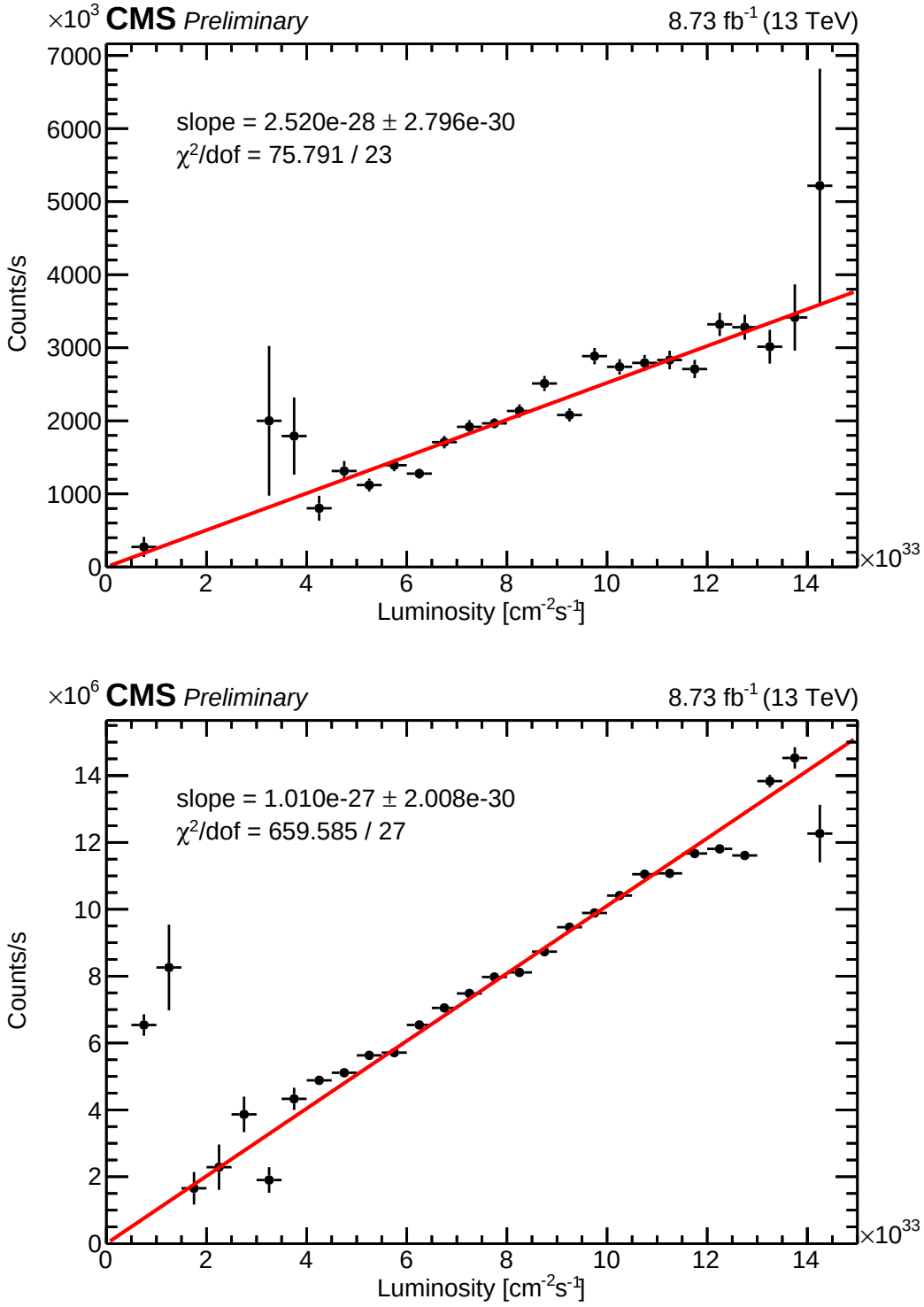

Figure A.23: Plot of ME1/1 wire group $N_{\text{hits}}^{\text{CMS}}/t$ vs. LHC luminosity with a one-parameter linear fit for hits that occur (top) during LHC bunch gaps and (bottom) during pp collisions.

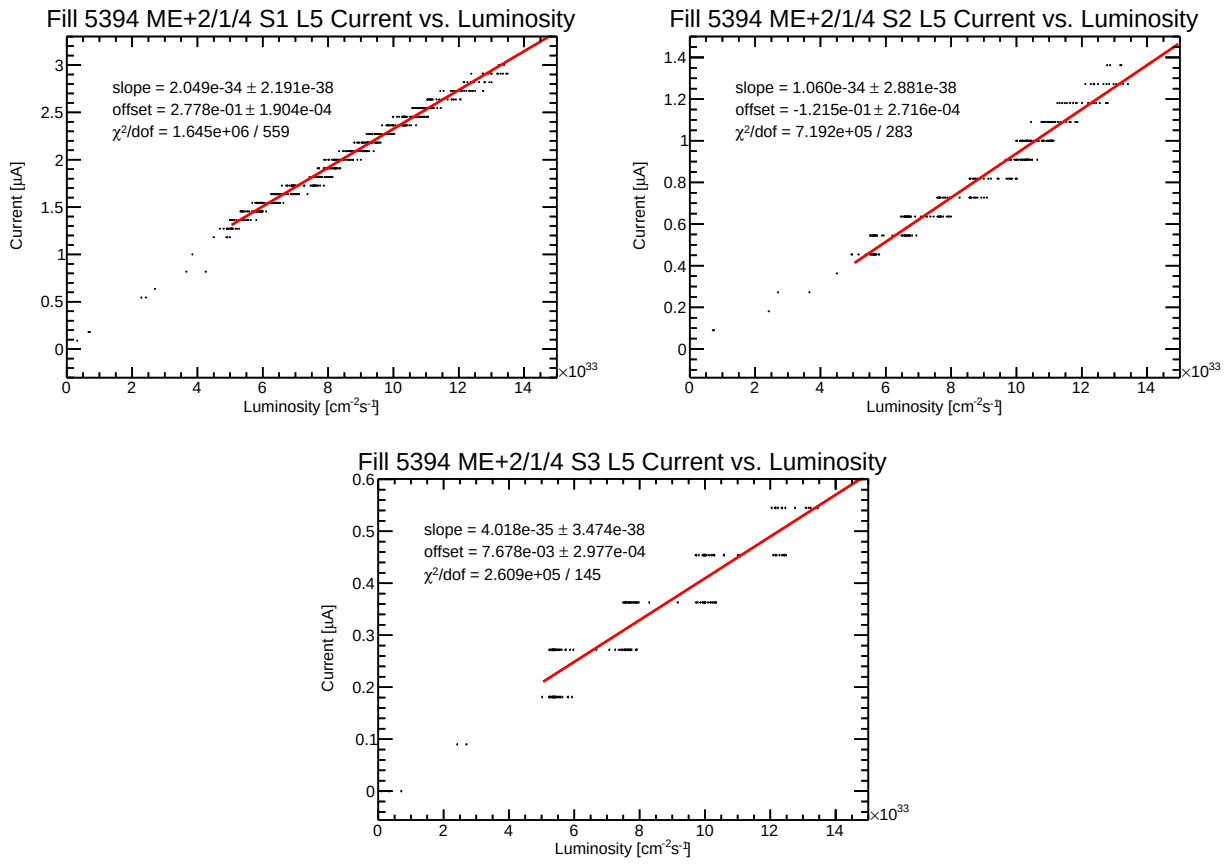

Figure A.24: Plot of current vs. luminosity for ME+2/1/04 layer 5 for HV Segment (top) 1, (middle) 2, and (bottom) 3, with a two-parameter linear fit. The least count of approximately 0.1 μA is most evident in HV segment 3.

A.7.1.2 ME2/1

ME2/1 chambers each have 18 independent HV channels. Each of a chamber's six layers is divided into three HV segments: one HV segment, through which passes the highest current, is close to the beam line; one HV segment, through which passes a lower current, is in the center of the chamber; and one HV segment, through which passes the lowest current, is at the end of the chamber furthest from the beam line. Figure A.24 displays plots of the anode HV current vs. luminosity for a representative example of ME2/1 chambers, ME+2/1/04 Layer 5, for all three HV segments.

We start by calculating the rate of wire group hits in ME2/1 for the full chamber in the same way as ME1/1. Figure A.25 displays plots of the rate of ME2/1 wire group hits second for hits occurring at the end of LHC bunch gaps and during pp collisions with a one-parameter linear fit through the origin. The slopes are again used as the reference hit rate and are combined according to Eq. A.25. This gives an estimate of the hit rate in hits/s for ME2/1, denoted as $H_{\text{WG-ME2/1}}$.

We then count the number of hits that occur within each HV segment. This number divided by the total number of hits in the chamber is the fraction of hits $f_{\text{ME2/1-}s}$ that occur in each HV segment, where s =1, 2, or 3 for each HV segment. The boundaries of HV segments are visible in Fig. A.26 as dips in the occupancy plot at wire groups 45 and 81. HV segment 1 is taken as wire group numbers 1–45, HV segment 2 as 46–81, and HV segment 3 as 82–112. Table A.2 reports the hit fractions calculated from Fig. A.26. The rate of wire group hits in each HV segment at the reference luminosity is then obtained by multiplying the hit fraction for each HV segment to the full ME2/1 rate of wire group hits,

$$H_{\text{WG-ME2/1-}s} = f_{\text{ME2/1-}s}\ H_{\text{WG-ME2/1}}. \tag{A.27}$$

These hit rates are also reported in Table A.2.

The next step we take is to convert the luminosity values of all points in Fig. A.24 to

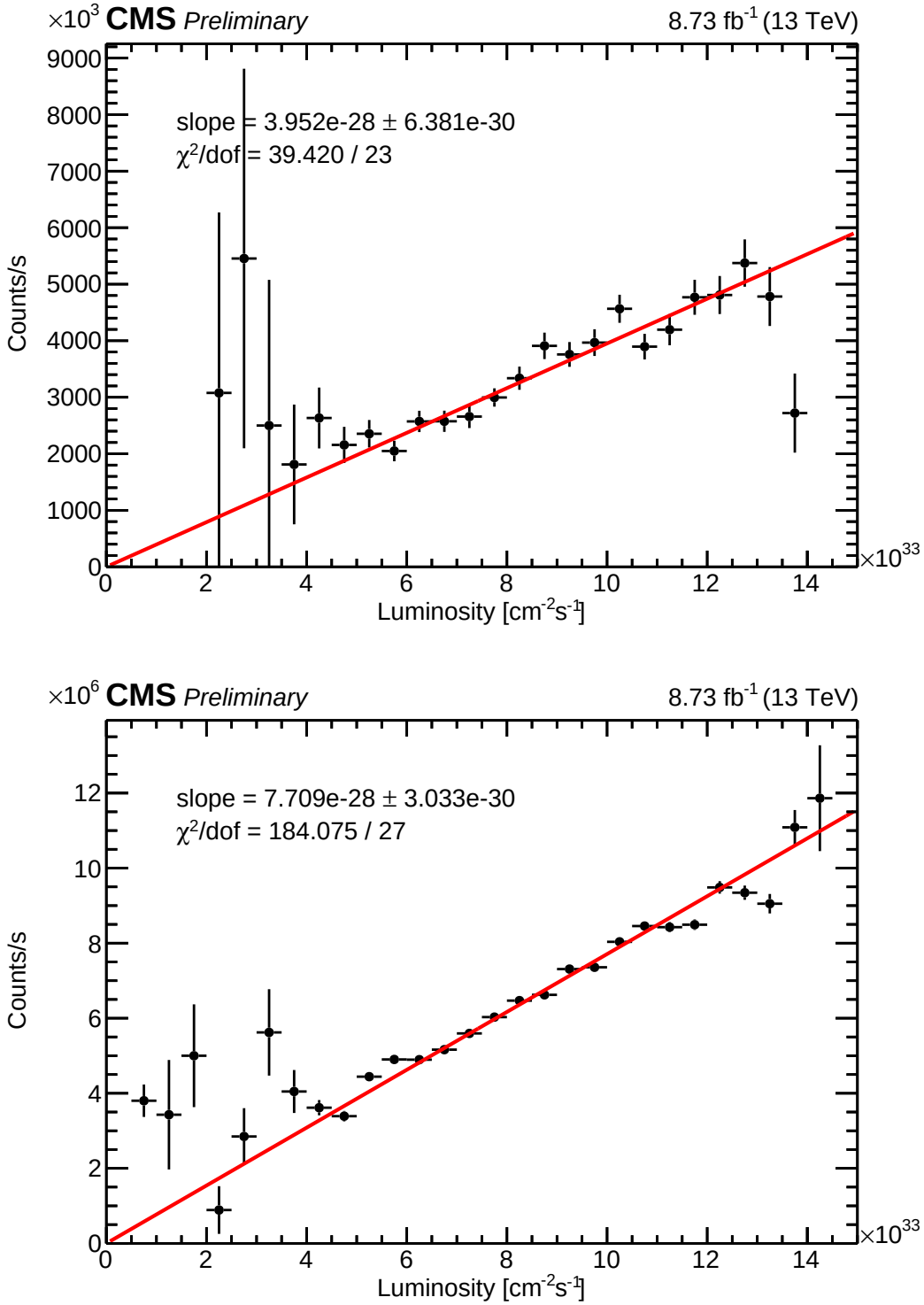

Figure A.25: Plot of ME2/1 wire group $N_{\text{hits}}^{\text{CMS}}/t$ vs. LHC luminosity for hits that occur (top) during LHC bunch gaps and (bottom) during pp collisions, with a one-parameter linear fit.

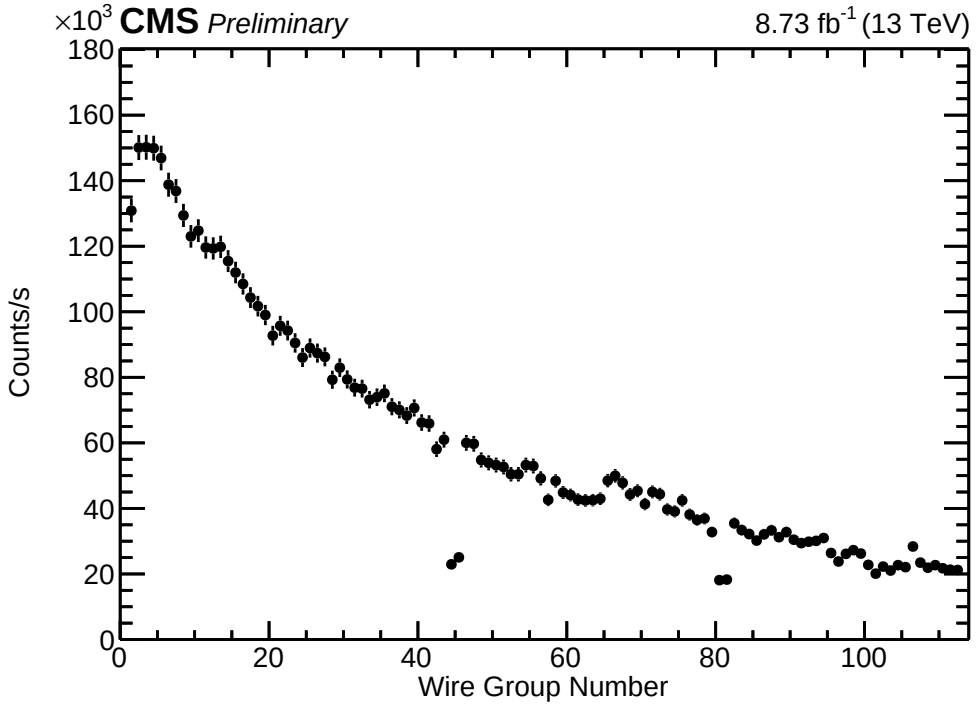

Figure A.26: Plot of anode wire group $N_{\text{hits}}^{\text{CMS}}(d)/t$ that occur during pp collisions in ME2/1. HV segment 1 is wire group numbers 1–45, HV segment 2 is wire group numbers 46–81, and HV segment 3 is wire group numbers 82–112.

	$f_{\text{ME2/1-}s}$	$H_{\text{WG-ME2/1-}s}$ [hits/s]
ME2/1	-	6.3×10^6
ME2/1 S1	0.63	3.9×10^6
ME2/1 S2	0.25	1.5×10^6
ME2/1 S3	0.12	0.8×10^6

Table A.2: Values of wire group hit fraction and hit rate in each ME2/1 HV segment

equivalent hits/s. To do this, we multiply the luminosity value of each point, denoted $\mathcal{L}$, by the hits/s at $10^{34}\,\mathrm{cm}^{-2}\,\mathrm{s}^{-1}$, $H_{\text{WG-ME2/1-}s}$, in each HV segment.

$$\text{hits/s} = \mathcal{L} \times H_{\text{WG-ME2/1-}s} \tag{A.28}$$

This transformation from luminosity to equivalent hits/s gives us the HV current as a function of hits/s in each ME2/1 segment individually. Figure A.27 displays example HV current vs. hits/s for ME+2/1/04 Layer 5 and Layer 6.

At CMS, the non-ME1/1 chambers use a different HVPS system than the ME1/1 chambers. When the non-ME1/1 HVPS were commissioned in CMS, each HV channel in the non-ME1/1 chambers was independently calibrated from each other. As a check of this, we study plots of current vs. luminosity and we verify that it is not necessary to correct for fitted offsets when computing the fitted reference current values. However, we observe that for some non-ME1/1 chambers, there are layer-by-layer differences in current in a given chamber and given LHC fill at the same hit rate. Figure A.27 displays example HV current vs. hits/s plots for ME+2/1/04 Layer 5 and Layer 6. The top plot (Layer 5) shows that when different HV segments in the same chamber have similar hits/s, they do have similar HV currents. However, for some channels, a noticeable jump is observed in the HV current at similar hits/s, as in the bottom plot (Layer 6). This discrepancy might be caused by some amount of miscalibration of the HVPS conversion of ADC to μA. To avoid channels with possible miscalibration, we scan through plots of HV current vs. hits/s for all layers of ME2/1 chambers and search for subjectively defined smooth transitions in HV current and hits/s between each segment.

We then calculate charge/hit by dividing the y axis value (HV current) by the x axis value (hits/s) of each data point in the HV current vs. hits/s plots for all three HV segments in each selected chamber layer. Each charge/hit value is collected into a histogram for each LHC fill during run period H of 2016. One entry in this histogram is a single data point from plots of HV current vs. hits/s in chamber layers that pass our selection. Figure A.28 is an example of the charge/hit histogram of selected chamber layers for each HV segment

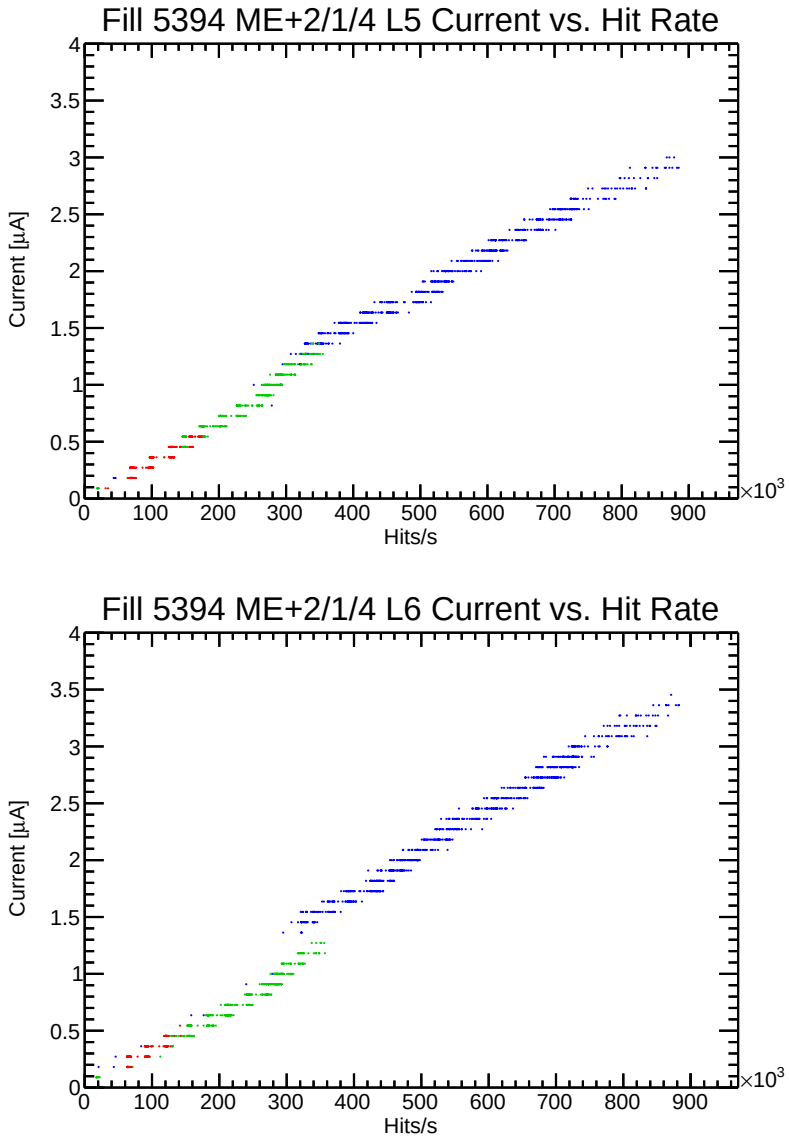

Figure A.27: Plot of HV current vs. hits/s for a ME2/1 layer (top) with smooth transitions in current and hits/s between HV segments and (bottom) Plot of HV current vs. hits/s for a ME2/1 layer with a jump in HV current and hits/s between HV segments 1 and 2. Segment 1 is in blue, segment 2 is in green, and segment 3 is in red.

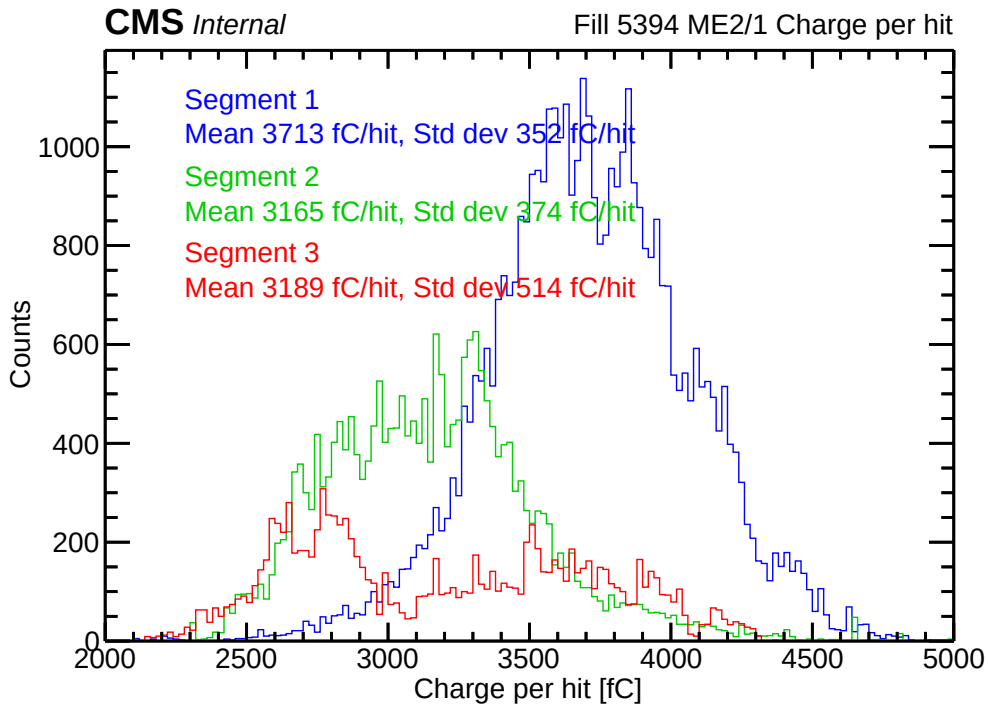

Figure A.28: Histogram of values of charge/hit in fC in ME2/1 for LHC Fill 5394.

for LHC Fill 5394. (Fill 5394 was used to determine the selection of good ME2/1 layers.) HV segment 1 is the blue histogram, HV segment 2 is the green histogram, and HV segment 3 is the red histogram. HV segment 3 is bi-modal because at very low HV current (less than approximately 0.6 μA) the HV current ADC least count of approximately 0.1 μA is the dominant source of uncertainty which causes measured values of the HV current to fluctuate between the two closest least count values.

To obtain a charge/hit value in each fill and HV segment, we use the mean of each of the charge/hit histogram. Then finally, just as the HV current measurements in ME1/1 were combined, the charge/hit for each HV segment in each LHC fill is averaged with a weighting according to the integrated luminosity of each fill considered. For HV segment 3 this procedure gives a 4% larger charge/hit than by computing the ratio of the HV current averaged over fills and the hits/s from Table A.2.

A.7.2 Computation of charge/hit from GIF++ data

At GIF++, the charge/hit for background hits is obtained by measuring the anode HV current and the rate of early time anode wire groups hits in externally triggered data at each source attenuation. Figure A.29 displays plots of the measured anode HV current as a function of the total number of anode wire group hits that occur in readout time bins 1–5 for the ME1/1 and ME2/1 chambers at GIF++ respectively. Each dot represents a single source attenuation, where the lowest source intensity yields the lowest HV current and lowest background hits/s, and increasing the source intensity also increases the HV current and anode wire hits/s roughly linearly. The slopes of the fitted lines represent the measured charge/hit of each CSC. For ME2/1, only the first 8 points are used to calculate the slope, because at higher source intensities, the high HV currents passing through the internal resistance result in a non-negligible drop in the HV at the anode wire.

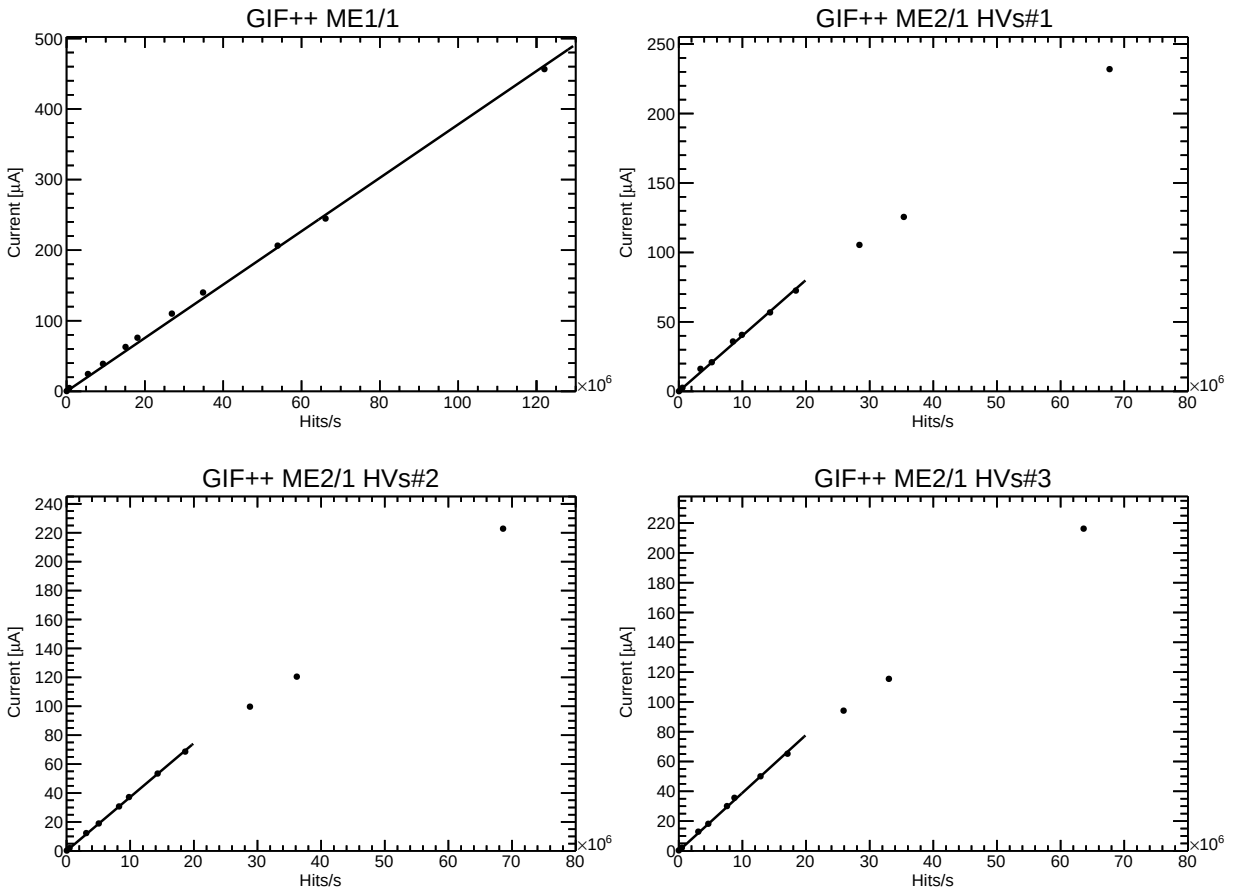

Figure A.29: Plot of anode HV current vs. hits/s at GIF++ for (top left) ME1/1 and ME2/1 HV segment (top right) 1, (bottom left) 2, and (bottom right) 3.

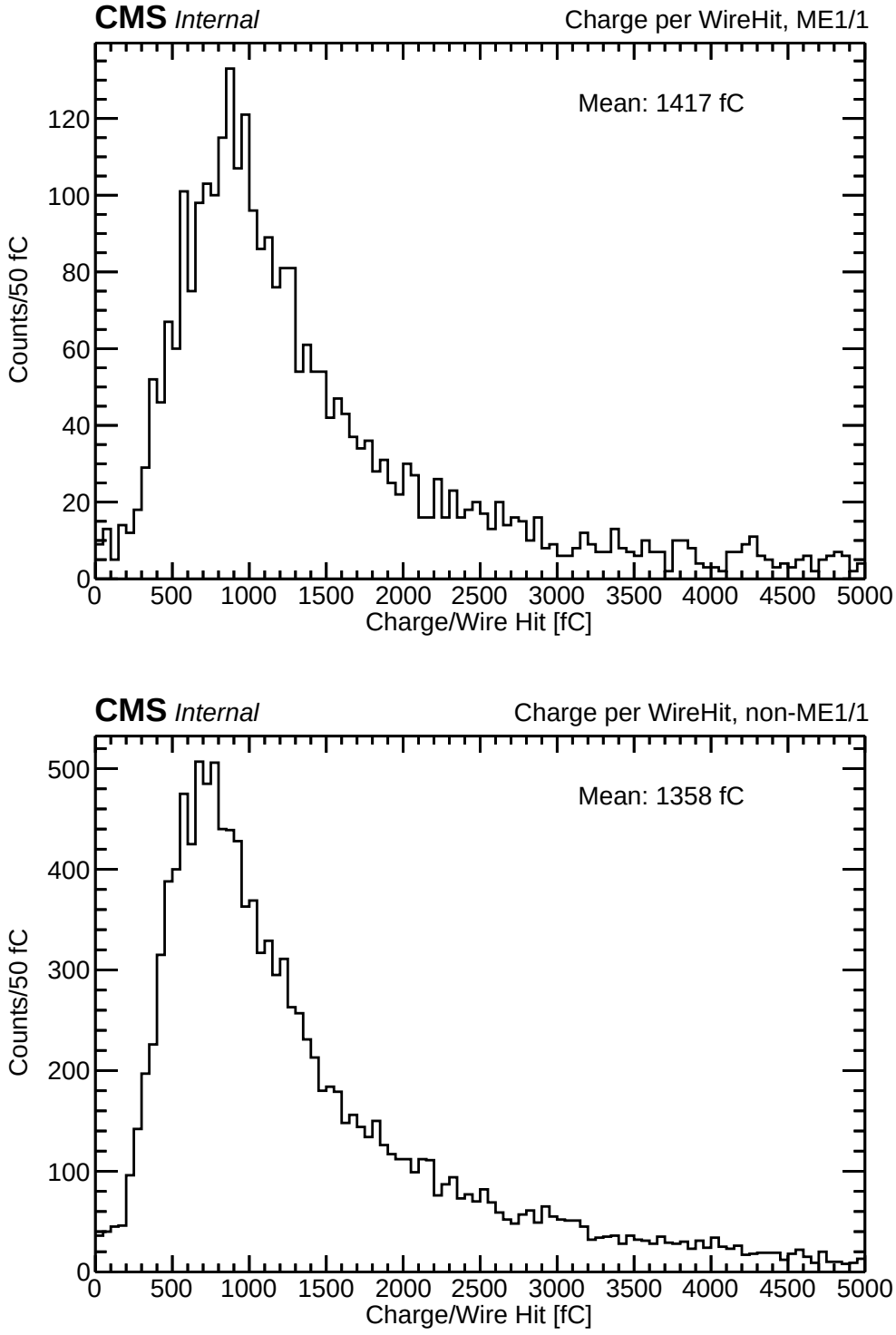

Figure A.30: In simulation of CMS data, histogram of the avalanche charge per simulated wire hit for (top) ME1/1 and (bottom) non-ME1/1 chambers

[fC/hit]	CMS	GIF++	MC
ME1/1	1570	3780	1360
ME2/1 S1	3451	4010	1420*
ME2/1 S2	3274	3720	
ME2/1 S3	3166	3890	

Table A.3: Values of charge/hit in ME1/1 and each HV segment of ME2/1 in units of fC/hit. All non-ME1/1 chamber charge/hit were observed to be similar. Therefore, the charge/hit was measured by averaging all non-ME1/1 chambers; the * in the ME2/1 MC charge/hit measurements indicates this.

A.7.3 Computation of charge/hit from CMS simulation

In the HP neutron simulation as described above, each simulated wire hit can be associated to a quantity of simulated avalanche charge produced from the gas ionization. Figure A.30 displays histograms of the simulated avalanche charges for ME1/1 and non-ME1/1 simulated wire hit. We take the mean of these histograms of total avalanche charge per simulated wire hit as a measure of charge/hit in MC simulation for neutron-induced hits.

A.7.4 Comparison of charge/hit

Table A.3 is the collection of all charge/hit calculations in units of fC/hit for ME1/1 and ME2/1 for CMS data, GIF++ data, and CMS simulation.

To summarize the results:

- ME1/1 charge/hit at GIF++ is roughly a factor of 2.5 higher than at CMS
- ME1/1 MC charge/hit matches ME1/1 charge/hit at CMS within 15%
- ME2/1 charge/hit is a factor of 2–3 higher than ME1/1 charge/hit at CMS
- ME2/1 charge/hit at GIF++ is 20–30% higher at GIF++ than at CMS
- ME2/1 MC charge/hit is roughly 2–2.5 lower than ME2/1 charge/hit at CMS

These results are important for reconstruction studies, where the total hits/s is the strongest indicator of trigger and software performance. This means that at equal hits/s for CSCs at GIF++ and CMS (effects on muon reconstruction are roughly the same), the HV current will differ by the same amount as charge/hit. So, when using HV current for correspondence between GIF++ source intensities and ME1/1, these results at face value imply that at an equal hits/s the chamber at GIF++ will have a factor of 2.5 larger HV current than chambers in CMS. Similarly, for the ME2/1 chamber correspondence, the ME2/1 at GIF++ will have a 20–30% larger HV current than the chambers in CMS assuming an equal hits/s (depending on HV segment). However, further understanding of possible mis-calibration of HV current ADC to μA conversion is necessary in the calculation of ME2/1 charge/hit.

A.8 Acknowledgments of the appendix

We would like to thank everyone on the CSC GIF++ team, the CMS UCLA group, and everyone whose work we have built on or partially reproduced and who have contributed valuable knowledge and advice, including Cameron Bravo, Tim Cox, Alice Florent, Jay Hauser, Misha Ignatenko, Vladimir Ivantchenko, Evaldas Juska, Alexey Kamenev, Andrey Korytov, Katerina Kuznetsova, Armando Lanaro, Paul Lujan, Alex Madorsky, Nick McColl, Hualin Mei, Yuriy Pakhotin, Vladimir Palchik, Victor Perelygin, Jian Wang, Wells Wuslin, and Piet Verwilligen. This work was partially supported by the U.S. Department of Energy under Award Number DE–SC0009937.

Reference [85] contains brief a history of the measurement of the neutron background in CMS with links to previous work done dating back to 1994.

REFERENCES

[1] J. J. T. M. F.R.S., "XL. Cathode Rays", *The London, Edinburgh, and Dublin Philosophical Magazine and Journal of Science* **44** (1897) 293, doi:10.1080/14786449708621070.

[2] CMS Collaboration, "Observation of a new boson at a mass of 125 GeV with the CMS experiment at the LHC", *Phys. Lett. B* **716** (2012) 30, doi:10.1016/j.physletb.2012.08.021, arXiv:1207.7235.

[3] ATLAS Collaboration, "Observation of a new particle in the search for the standard model Higgs boson with the ATLAS detector at the LHC", *Phys. Lett. B* **716** (2012) 1, doi:10.1016/j.physletb.2012.08.020, arXiv:1207.7214.

[4] J. E. Augustin et al., "Discovery of a narrow resonance in e^+e^- annihilation", *Phys. Rev. Lett.* **33** (1974) 1406, doi:10.1103/PhysRevLett.33.1406.

[5] J. J. Aubert et al., "Experimental observation of a heavy particle J", *Phys. Rev. Lett.* **33** (1974) 1404, doi:10.1103/PhysRevLett.33.1404.

[6] S. W. Herb et al., "Observation of a dimuon resonance at 9.5 GeV in 400 GeV proton-nucleus collisions", *Phys. Rev. Lett.* **39** (1977) 252, doi:10.1103/PhysRevLett.39.252.

[7] UA1 Collaboration, "Experimental observation of lepton pairs of invariant mass around 95 GeV/c^2 at the CERN SPS Collider", *Phys. Lett. B* **126** (1983) 398, doi:10.1016/0370-2693(83)90188-0.

[8] UA2 Collaboration, "Evidence for $Z^0 \to e^+e^-$ at the CERN $\bar{p}p$ Collider", *Phys. Lett. B* **129** (1983) 130, doi:10.1016/0370-2693(83)90744-X.

[9] A. Hebecker, "Grand Unified Theories", Ch. 114 in Particle Data Group, C. Patrignani et al., "Review of particle physics", *Phys. Rev. D* **98** (2018) 030001, doi:10.1103/PhysRevD.98.030001.

[10] J. L. Hewett and T. G. Rizzo, "Low-energy phenomenology of superstring-inspired E_6 models", *Phys. Rept.* **183** (1989) 193, doi:10.1016/0370-1573(89)90071-9.

[11] P. Langacker, "The physics of heavy Z' gauge bosons", *Rev. Mod. Phys.* **81** (2009) 1199, doi:10.1103/RevModPhys.81.1199, arXiv:0801.1345.

[12] M. Cvetic and S. Godfrey, "Discovery and identification of extra gauge bosons", doi:10.1142/9789812830265_0007, arXiv:hep-ph/9504216.

[13] E. Accomando et al., "Z' physics with early LHC data", *Phys. Rev. D* **83** (2011) 075012, doi:10.1103/PhysRevD.83.075012, arXiv:1010.6058.

[14] E. Mobs, "The CERN accelerator complex - August 2018. Complexe des accélérateurs du CERN - Août 2018",. General Photo. https://cds.cern.ch/record/2636343.

[15] L. Evans and P. Bryant, "LHC machine", *JINST* **3** (2008) S08001, doi:10.1088/1748-0221/3/08/S08001.

[16] CMS Collaboration, "The CMS experiment at the CERN LHC", *JINST* **3** (2008) S08004, doi:10.1088/1748-0221/3/08/S08004.

[17] CMS Collaboration, "Performance of the CMS muon detector and muon reconstruction with proton-proton collisions at $\sqrt{s} = 13\,\text{TeV}$", *JINST* **13** (2018) P06015, doi:10.1088/1748-0221/13/06/P06015, arXiv:1804.04528.

[18] A. Saha, "Phase 1 upgrade of the CMS pixel detector", *JINST* **12** (2017) C02033, doi:10.1088/1748-0221/12/02/c02033.

[19] CMS Collaboration, "Interactive slice of the CMS detector",. http://cds.cern.ch/record/2205172.

[20] CMS Collaboration, "Performance of CMS muon reconstruction in *pp* collision events at $\sqrt{s} = 7\,\text{TeV}$", *JINST* **7** (2012) P10002, doi:10.1088/1748-0221/7/10/P10002, arXiv:1206.4071.

[21] CMS Collaboration, "Performance of the reconstruction and identification of high-momentum muons in proton-proton collisions at $\sqrt{s} = 13\,\text{TeV}$", (2019).

[22] H. Bichsel, "Passage of Particles Through Matter", Ch. 33 in Particle Data Group, C. Patrignani et al., "Review of particle physics", *Phys. Rev. D* **98** (2018) 030001, doi:10.1103/PhysRevD.98.030001.

[23] R. Frühwirth, "Application of Kalman filtering to track and vertex fitting", *Nucl. Instrum. Meth. A* **262** (1987) 444, doi:https://doi.org/10.1016/0168-9002(87)90887-4.

[24] A. Bodek et al., "Extracting muon momentum scale corrections for hadron collider experiments", *Eur. Phys. J. C* **72** (2012) 2194, doi:10.1140/epjc/s10052-012-2194-8, arXiv:1208.3710.

[25] R. N. Mohapatra, "Unification and Supersymmetry". Springer, Berlin, 1986. doi:10.1007/978-1-4757-1928-4, ISBN 9781475719307, 9781475719284,

[26] G. Altarelli, B. Mele, and M. Ruiz-Altaba, "Searching for new heavy vector bosons in $p\bar{p}$ colliders", *Z. Phys. C* **45** (1989) 109, doi:10.1007/BF01556677.

[27] L. Randall and R. Sundrum, "A large mass hierarchy from a small extra dimension", *Phys. Rev. Lett.* **83** (1999) 3370, doi:10.1103/PhysRevLett.83.3370, arXiv:hep-ph/9905221.

[28] N. Arkani-Hamed, S. Dimopoulos, and G. Dvali, "Phenomenology, astrophysics and cosmology of theories with sub-millimeter dimensions and TeV scale quantum gravity", *Phys. Rev. D* **59** (1999) 086004, doi:10.1103/PhysRevD.59.086004, arXiv:hep-ph/9807344.

[29] CMS Collaboration, "Search for resonances in the dilepton mass distribution in pp collisions at $\sqrt{s} = 7\,\text{TeV}$", *JHEP* **05** (2011) 093, doi:10.1007/JHEP05(2011)093, arXiv:1103.0981.

[30] CMS Collaboration, "Search for narrow resonances in dilepton mass spectra in pp collisions at $\sqrt{s} = 7\,\text{TeV}$", *Phys. Lett. B* **714** (2012) 158, doi:10.1016/j.physletb.2012.06.051, arXiv:1206.1849.

[31] ATLAS Collaboration, "Search for dilepton resonances in pp collisions at $\sqrt{s} = 7$ TeV with the ATLAS detector", *Phys. Rev. Lett.* **107** (2011) 272002, doi:10.1103/PhysRevLett.107.272002, arXiv:1108.1582.

[32] CMS Collaboration, "Search for heavy narrow dilepton resonances in pp collisions at $\sqrt{s} = 7\,\text{TeV}$ and $\sqrt{s} = 8\,\text{TeV}$", *Phys. Lett. B* **720** (2013) 63, doi:10.1016/j.physletb.2013.02.003, arXiv:1212.6175.

[33] CMS Collaboration, "Search for physics beyond the standard model in dilepton mass spectra in proton-proton collisions at $\sqrt{s} = 8\,\text{TeV}$", *JHEP* **04** (2015) 025, doi:10.1007/JHEP04(2015)025, arXiv:1412.6302.

[34] ATLAS Collaboration, "Search for high-mass dilepton resonances in pp collisions at $\sqrt{s} = 8\,\text{TeV}$ with the ATLAS detector", *Phys. Rev. D* **90** (2014) 052005, doi:10.1103/PhysRevD.90.052005, arXiv:1405.4123.

[35] CMS Collaboration, "Search for narrow resonances in dilepton mass spectra in proton-proton collisions at $\sqrt{s} = 13\,\text{TeV}$ and combination with 8 TeV data", *Phys. Lett. B* **768** (2017) 57, doi:10.1016/j.physletb.2017.02.010, arXiv:1609.05391.

[36] CMS Collaboration, "Search for high-mass resonances in dilepton final states in proton-proton collisions at $\sqrt{s} = 13\,\text{TeV}$", *JHEP* **06** (2018) 120, doi:10.1007/JHEP06(2018)120, arXiv:1803.06292.

[37] ATLAS Collaboration, "Search for high-mass new phenomena in the dilepton final state using proton-proton collisions at $\sqrt{s} = 13\,\text{TeV}$ with the ATLAS detector", *Phys. Lett. B* **761** (2016) 372, doi:10.1016/j.physletb.2016.08.055, arXiv:1607:03669.

[38] ATLAS Collaboration, "Search for new high-mass phenomena in the dilepton final state using $36.1\,\text{fb}^{-1}$ of proton-proton collision data at $\sqrt{s} = 13\,\text{TeV}$ with the ATLAS detector", *JHEP* **10** (2017) 182, doi:10.1007/JHEP10(2017)182, arXiv:1707.02424.

[39] ATLAS Collaboration, "Search for high-mass dilepton resonances using $139\,\text{fb}^{-1}$ of pp collision data collected at $\sqrt{s} = 13\,\text{TeV}$ with the ATLAS detector", *Phys. Lett. B* **796** (2019) 68, doi:10.1016/j.physletb.2019.07.016, arXiv:1903.06248.

[40] CMS Collaboration, "CMS luminosity measurement for the 2018 data-taking period at $\sqrt{s} = 13\,\text{TeV}$", technical report, CERN, Geneva, 2019. http://cds.cern.ch/record/2676164.

[41] CMS Collaboration, "Search for a narrow resonance in high-mass dilepton final states in proton-proton collisions using $140\,\text{fb}^{-1}$ of data at $\sqrt{s} = 13\,\text{TeV}$", technical report, CERN, Geneva, 2019. http://cds.cern.ch/record/2684757.

[42] CMS Collaboration, "CMS luminosity measurements for the 2016 data taking period", CMS Physics Analysis Summary CMS-PAS-LUM-17-001, CERN, 2017. https://cds.cern.ch/record/2257069.

[43] CMS Collaboration, "CMS luminosity measurement for the 2017 data-taking period at $\sqrt{s} = 13\,\text{TeV}$", technical report, CERN, Geneva, 2018. http://cds.cern.ch/record/2621960.

[44] S. Frixione, P. Nason, and C. Oleari, "Matching NLO QCD computations with Parton Shower simulations: the POWHEG method", *JHEP* **11** (2007) 070, doi:10.1088/1126-6708/2007/11/070, arXiv:0709.2092.

[45] T. Sjöstrand et al., "An introduction to PYTHIA 8.2", *Comput. Phys. Commun.* **191** (2015) 159, doi:10.1016/j.cpc.2015.01.024, arXiv:1410.3012.

[46] J. Alwall et al., "The automated computation of tree-level and next-to-leading order differential cross sections, and their matching to parton shower simulations", *JHEP* **07** (2014) 079, doi:10.1007/JHEP07(2014)079, arXiv:1405.0301.

[47] NNPDF Collaboration, "Parton distributions from high-precision collider data", *Eur. Phys. J. C* **77** (2017) 663, doi:10.1140/epjc/s10052-017-5199-5, arXiv:1706.00428.

[48] CMS Collaboration, "Extraction and validation of a new set of CMS PYTHIA8 tunes from underlying-event measurements", arXiv:1903.12179.

[49] J. Allison et al., "Geant4 developments and applications", *IEEE Trans. Nucl. Sci.* **53** (2006) 270, doi:10.1109/TNS.2006.869826.

[50] NNPDF Collaboration, "Parton distributions for the LHC Run II", *JHEP* **04** (2015) 040, doi:10.1007/JHEP04(2015)040, arXiv:1410.8849.

[51] CMS Collaboration, "Event generator tunes obtained from underlying event and multiparton scattering measurements", *Eur. Phys. J. C* **76** (2016) 155, doi:10.1140/epjc/s10052-016-3988-x, arXiv:1512.00815.

[52] D. Bourilkov, "Exploring the LHC landscape with dileptons", (2016). arXiv:1609.08994.

[53] D. Bourilkov, "Photon-induced background for dilepton searches and measurements in pp collisions at 13 TeV", (2016). arXiv:1606.00523.

[54] Y. Li and F. Petriello, "Combining QCD and electroweak corrections to dilepton production in FEWZ", *Phys. Rev. D* **86** (2012) 094034, doi:10.1103/PhysRevD.86.094034, arXiv:1208.5967.

[55] CMS, TOTEM Collaboration, "Observation of proton-tagged, central (semi)exclusive production of high-mass lepton pairs in pp collisions at 13 TeV with the CMS-TOTEM precision proton spectrometer", *JHEP* **07** (2018) 153, doi:10.1007/JHEP07(2018)153, arXiv:1803.04496.

[56] A. Manohar, P. Nason, G. P. Salam, and G. Zanderighi, "How bright is the proton? a precise determination of the photon PDF", *Phys. Rev. Lett.* **117** (2016) 242002, doi:10.1103/PhysRevLett.117.242002, arXiv:1607.04266.

[57] J. Butterworth et al., "PDF4LHC recommendations for LHC Run II", *J. Phys. G* **43** (2016) 023001, doi:10.1088/0954-3899/43/2/023001, arXiv:1510.03865.

[58] M. Czakon and A. Mitov, "Top++: a program for the calculation of the top-pair cross-section at hadron colliders", *Comput. Phys. Commun.* **185** (2014) 2930, doi:10.1016/j.cpc.2014.06.021, arXiv:1112.5675.

[59] N. Kidonakis, "Two-loop soft anomalous dimensions for single top quark associated production with a W^- or H^-", *Phys. Rev. D* **82** (2010) 054018, doi:10.1103/PhysRevD.82.054018, arXiv:1005.4451.

[60] M. Oreglia, "A Study of the Reactions $\psi' \to \gamma\gamma\psi$". PhD thesis, SLAC, 1980.

[61] R. J. Barlow, "Extended maximum likelihood", *Nucl. Instrum. Meth. A* **297** (1990) 496, doi:10.1016/0168-9002(90)91334-8.

[62] G. Cowan, "Statistics", Ch. 39 in Particle Data Group, C. Patrignani et al., "Review of particle physics", *Phys. Rev. D* **98** (2018) 030001, doi:10.1103/PhysRevD.98.030001.

[63] S. S. Wilks, "The large-sample distribution of the likelihood ratio for testing composite hypotheses", *Annals Math. Statist.* **9** (1938) 60, doi:10.1214/aoms/1177732360.

[64] CMS Collaboration, "Detection of Z' gauge bosons in the dimuon decay mode in CMS", CMS NOTE CMS-NOTE-2005/002, 2005. https://cms-secr.web.cern.ch/cms-secr/documents/05/note05_002.pdf.

[65] N. Metropolis et al., "Equation of state calculations by fast computing machines", *J. Chem. Phys.* **21** (1953) 1087, doi:10.1063/1.1699114.

[66] W. K. Hastings, "Monte carlo sampling methods using markov chains and their applications", *Biometrika* **57** (1970) 97. http://www.jstor.org/stable/2334940.

[67] The ATLAS Collaboration, The CMS Collaboration, The LHC Higgs Combination Group, "Procedure for the LHC Higgs boson search combination in Summer 2011", CMS Note/ATLAS Physics Public Note CMS-NOTE-2011-005/ATL-PHYS-PUB-2011-11, CERN, Geneva, 2011. https://cds.cern.ch/record/1379837.

[68] L. Moneta et al., "The RooStats Project", in *13th International Workshop on Advanced Computing and Analysis Techniques in Physics Research (ACAT2010)*. SISSA, 2010. arXiv:1009.1003. PoS(ACAT2010)057.

[69] R. D. Ball et al., "Parton distributions with LHC data", *Nucl. Phys. B* **867** (2013) 244, doi:10.1016/j.nuclphysb.2012.10.003, arXiv:1207.1303.

[70] E. Accomando et al., "Z' at the LHC: Interference and finite width effects in Drell-Yan", *JHEP* **10** (2013) 153, doi:10.1007/JHEP10(2013)153, arXiv:1304.6700.

[71] A. Dasgupta, "Study of neutron-induced background hits in the CMS endcap muon system, and implications for the HL-LHC", (2017). Poster at The European Physical Society Conference on High Energy Physics, Venice, Italy, 5–12 July, 2017. https://indico.cern.ch/event/466934/contributions/2590728/.

[72] A. Dasgupta, "Study of neutron-induced background hits in the CMS endcap muon system", in *Proceedings of The European Physical Society Conference on High Energy Physics*. Venice, Italy, 2017. PoS(EPS-HEP2017)782. doi:10.22323/1.314.0782.

[73] C. Schnaible, "Study of neutron-induced background hits in the CMS endcap muon chambers, and implications for the HL-LHC", (2017). Contributed talk at APS Division of Particles and Fields meeting, Fermilab, 31 July–4 August, 2017. https://indico.fnal.gov/event/11999/session/11/contribution/46.

[74] G. Apollinari et al., "High-luminosity large hadron collider (HL-LHC): Preliminary design report". CERN Yellow Reports: Monographs. CERN, Geneva, 2015. https://cds.cern.ch/record/2116337.

[75] CMS Collaboration, "The CMS Muon Project: Technical Design Report", *CERN-LHCC-97-032, CMS-TDR-3* (1997). http://cds.cern.ch/record/343814.

[76] CMS Collaboration, "Commissioning of the CMS experiment and the cosmic run at four tesla", *JINST* **5** (2010) T03001, doi:10.1088/1748-0221/5/03/T03001, arXiv:0911.4845.

[77] J. Kopecky et al., "Atlas of neutron capture cross sections", *International Nuclear Data Committee (IAEA Nuclear Data Section)* **362** (1997). https://www-nds.iaea.org/publications/indc/indc-nds-0362/.

[78] J. Hauser et al., "Experience with trigger electronics for the CSC system of CMS", in *Proceedings of the 10th workshop on electronics for LHC and future experiments*. Boston, USA, 2004. doi:10.5170/CERN-2004-010.292.

[79] D. Acosta et al., "Design features and test results of the CMS endcap muon chambers", *Nucl. Instrum. Meth. A* **494** (2002) 504, doi:10.1016/S0168-9002(02)01540-1.

[80] D. Acosta et al., "Efficiency of finding muon track trigger primitives in CMS cathode strip chambers", *Nucl. Instrum. Meth. A* **592** (2008) 26, doi:10.1016/j.nima.2008.03.118.

[81] M. Baarmand et al., "Spatial resolution attainable with cathode strip chambers at the trigger level", *Nucl. Instrum. Meth. A* **425** (1999) 92, doi:10.1016/S0168-9002(98)01390-4.

[82] S. Agostinelli et al., "GEANT4—a simulation toolkit", *Nucl. Instrum. Meth. A* **506** (2003) 250, doi:10.1016/S0168-9002(03)01368-8.

[83] J. Allison et al., "Recent developments in GEANT4", *Nucl. Instrum. Meth. A* **835** (2016) 186, doi:10.1016/j.nima.2016.06.125.

[84] T. Sjöstrand, S. Mrenna, and P. Skands, "PYTHIA 6.4 physics and manual", *JHEP* **05** (2006) 026, doi:10.1088/1126-6708/2006/05/026, arXiv:hep-ph/0603175.

[85] P. Verwilligen, "CMS Twiki: Neutron Background in the Muon System". https://twiki.cern.ch/twiki/bin/viewauth/CMS/MuonNeutronBackground.

[86] R. Cousins, J. Mumford, and S. Valuev, "CSC trigger primitive rates in ORCA", Technical Report CMS-NOTE-2002-007, CERN, Geneva, Feb, 2002. http://cds.cern.ch/record/687399.

[87] T. A. Bawej et al., "The new CMS DAQ system for run 2 of the LHC", Technical Report CMS-CR-2014-082, CERN, Geneva, May, 2014. https://cds.cern.ch/record/1711011.

[88] CMS Collaboration, "Measurement of the inelastic proton-proton cross section at $\sqrt{s} = 13\,\text{TeV}$", *JHEP* **07** (2018) 161, doi:10.1007/JHEP07(2018)161, arXiv:1802.02613.

[89] D. Pfeiffer et al., "The radiation field in the gamma irradiation facility GIF++ at CERN", *Nucl. Instrum. Meth. A* **866** (2017) 91, doi:10.1016/j.nima.2017.05.045, arXiv:1611.00299.

[90] CMS Collaboration, "Fast algorithm for track segment and hit reconstruction in the CMS cathode strip chambers", *Nucl. Instrum. Meth. A* **589** (2008) 383, doi:10.1016/j.nima.2008.02.096.